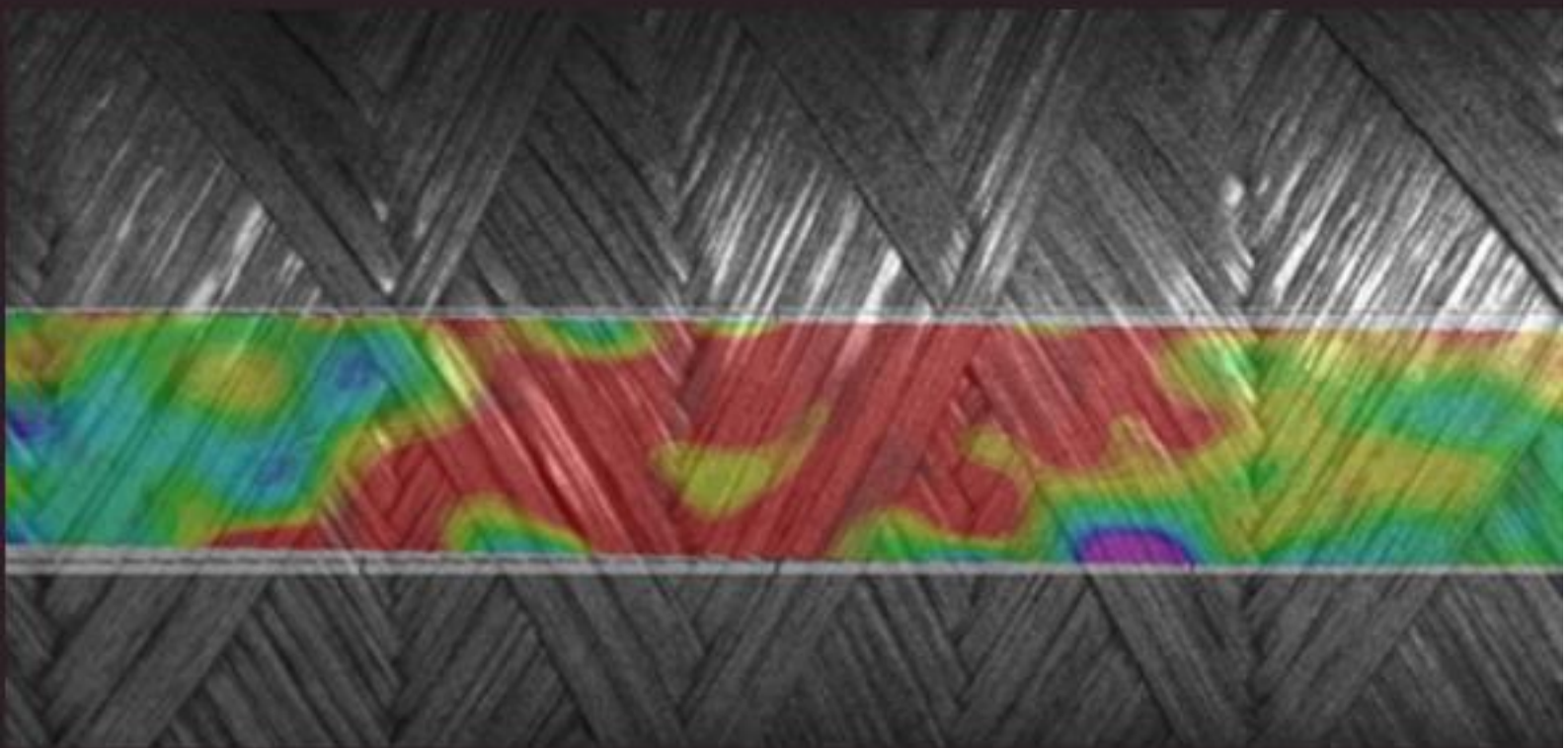




**IAMaC2023**

**2<sup>nd</sup> IBERO-AMERICAN CONFERENCE  
ON COMPOSITE MATERIALS**

**20<sup>st</sup> and 21<sup>th</sup> of July, 2023**



São Carlos School of Engineering  
University of São Paulo, Brazil



**EESC · USP**  
Escola de Engenharia de São Carlos  
Universidade de São Paulo

**U. PORTO**

**FEUP** FACULDADE DE ENGENHARIA  
UNIVERSIDADE DO PORTO

# **2<sup>nd</sup> Ibero-American Conference on Composite Materials**

## **IAMaC 2023**

**20<sup>th</sup> and 21<sup>st</sup> July 2023**

**Proceedings of the 2<sup>nd</sup> Ibero-American  
Conference on Composite Materials  
IAMaC 2023**

**Editors**

Volnei Tita  
Ricardo de Medeiros

**SÃO CARLOS-SP  
EESC | USP  
2023**

University of Sao Paulo  
Sao Carlos School of Engineering  
Dean: Professor Fernando Martini Catalano  
Deputy-Dean: Professor Antônio Néilson Rodrigues da Silva

Catalog card prepared by Library Service at  
"Prof. Dr. Sergio Rodrigues Fontes" at EESC/USP

I61p.2  
2023

Ibero-American Conference on Composite Materials (2. : 2023 :  
São Carlos)  
Proceedings of the 2nd Ibero-American Conference on Composite  
Materials [electronic resources] / Editors: Volnei Tita,  
Ricardo de Medeiros. -- São Carlos : EESC/USP, 2023.  
165 p. - Electronic date  
ISBN 978-65-86954-32-6

1. Composite Materials. I. Tita, Volnei. II. Medeiros,  
Ricardo de. III. IAMaC (2. : 2023 : São Carlos). IV. Title.

*Flávia Helena Cassin – CRB-8/5812*

ISBN 978-65-86954-32-6  
Page: 165  
Electronic version in PDF available at Portal de Eventos Científicos da EESC-  
USP  
<http://eventos.eesc.usp.br/iamac2023>  
Size and dimensions: 21 cm x 29.7 cm (paper sheet A4)

## **Technical information**

Publication of the São Carlos School of Engineering of the  
University of São Paulo (EESC-USP).

## **Editors**

**Volnei Tita**

Department of Aeronautical Engineering - Sao Carlos School of Engineering  
University of Sao Paulo

**Ricardo de Medeiros**

Department of Mechanical Engineering – Center of Technological Sciences  
Santa Catarina State University

## **Organizing Committee**

**Volnei Tita (Chairman)**

EESC/University of São Paulo (USP)

**Ricardo de Medeiros (Co-Chairman)**

CCT/Santa Catarina State University (UDESC)

## **International Scientific Committee**

**Alberto Barroso**

Universidad de Sevilla, Spain

**Alejandro Ureña**

Universidad Rey Juan Carlos, Spain

**Alfredo B. de Morais**

Universidade de Aveiro, Portugal

**Augustín Chiminelli**

Instituto Tecnológico de Aragón, Spain

**Aurélio Araujo**

Universidade de Lisboa, Portugal

**Carlos Santiuste**

Universidad Carlos III de Madrid, Spain

**Cristovão Mota Soares**

Universidade de Lisboa, Portugal

**Edson C. Botelho**  
Universidade Estadual Paulista, Brazil

**Filipe S. Silva**  
Universidade do Minho, Portugal

**Humberto B. Santana**  
Universidad Tecnológica Metropolitana, Chile

**João Correia**  
Universidade de Lisboa, Portugal

**João Reis**  
Universidade Federal Fluminense, Brazil

**José D. D. Melo**  
Universidade Federal do Rio Grande do Norte, Brazil

**Humberto Almeida Jr.**  
Aalto University, Finland

**José M. Guedes**  
Universidade de Lisboa, Portugal

**José R. Tarpani**  
Universidade de São Paulo, Brazil

**Juan C. Del Real**  
Universidad Ponticia Comillas Madrid, Spain

**Julian Bravo-Castillero**  
Universidad Nacional Autónoma de México, Mexico

**Leonel Chiacchiarelli**  
Instituto Tecnológico de Buenos Aires, Argentina

**Luís F. M. Menezes**  
Universidade de Coimbra, Portugal

**Marcelo L. Ribeiro**  
Universidade de São Paulo, Brazil

**Mariana D. Banea**  
Centro Federal de Educação Tecnológica Celso Suckow da Fonseca, Brazil

**Maurício Donadon**  
Instituto Tecnológico de Aeronáutica, Brazil

Michele Bacciocchi  
Università di San Marino, San Marino

Nicholas Fantuzzi  
Università di Bologna, Italy

Nicolae Crainic  
Politecnica Timisoara, Romania

Nuno Silvestre  
Universidade de Lisboa, Portugal

Reinaldo Rodríguez Ramos  
Universidad de La Habana, Cuba

Renato Hunter  
Universidad de la Frontera, Chile

Rui M. Guedes  
Universidade do Porto, Portugal

Sandro C. Amico  
Universidade Federal do Rio Grande do Sul, Brazil

Silvio R. de Barros  
Centro Federal de Educação Tecnológica Celso Suckow da Fonseca, Brazil

Sofia T. de Freitas  
TU Delft, Neetherlands

Túlio H. Panzera  
Universidade Federal de São João del-Rei, Brazil

### **Publisher**

Library Service - Sao Carlos School of Engineering - University of Sao Paulo  
Researcher Support Section

**Our Address:** Av. Trab. São Carlense, 400 - Parque Arnold Schimidt, São Carlos - SP,  
Brazil

**Email Us:** [iamac@eesc.usp.br](mailto:iamac@eesc.usp.br)

## ORGANIZATION



## PREFACE

The Editors are grateful to all authors for their effort in writing the papers in time and acknowledge the outstanding work of all people involved with the organization of II Ibero-American Conference on Composite Materials (IAMaC 2023), mainly the students and technicians, who helped in direct or indirect way the publication of the present Proceedings.

The Editors also would like to thank CETEPE of Sao Carlos School of Engineering of USP for the support provides to have an edition of the Ibero-American Conference on Composite Materials (IAMaC) in Sao Carlos, which is very important conference on composite materials in the international scenario.

The IAMaC 2023 was the first edition in hybrid format. To enrich the debates and exchange of knowledge, IAMaC 2023 had international presence as the keynote lecture given by Prof. Jandro L. Abot, professor at the Catholic University of America (USA), who brought the topic "Integrated Multifunctional Sensing Using Carbon Nanotube Fibers: Progress and Challenges". In addition, there was the keynote lecture given by Prof. Reinaldo Rodríguez-Ramos, from the Universidad de La Habana (Cuba), with the topic "Analysis of effective properties for heterogeneous media with imperfect adhesion".

The two-day conference (20th and 21st of July, 2023) at CETEPE (Sao Carlos School of Engineering of USP) covered a wide range of topics that are part of the universe of composite structures and materials, from manufacturing, testing and computational methods, to aeronautical structures in composite materials, nanocomposites, inspection and optimization techniques, composite materials intelligent systems, up to monitoring the integrity of aeronautical structures through solid-state batteries. The event had around 50 participants and featured works involving co-authors from different countries, such as: Brazil, Portugal, France, Italy, USA, England, China, Mexico, Cuba and Canada, including professors and post-doctoral researchers, as well as PhD's, master's and undergraduate students.

Volnei Tita  
Ricardo de Medeiros  
*The Editors*



## TABLE OF CONTENTS

### ANÁLISE NUMÉRICA DO COMPORTAMENTO DE ENRIJECIMENTO À TRAÇÃO E FORMAÇÃO DE FISSURAS EM ELEMENTOS DE CONCRETO ARMADO

Matheus Machado Costa, Ederli Marangon, Leandro Ferreira Friedrich

### ANALYSIS OF THE ASYMPTOTIC HOMOGENIZATION METHOD IN A BILAMINATE ACOUSTIC MEDIUM

Erika Torres Figueiras, Reinaldo Rodríguez Ramos, Panters Rodríguez Bermúdez,  
Yoanh Espinosa Almeyda

### ANALYSIS OF GFRP COMPOSITES REPAIRED WITH ADHESIVELY BONDED STEEL PATCH

Alex Sousa Lassé, João Marciano Laredo Dos Reis, Heraldo Silva Da Costa Mattos

### ANALYTICAL MODEL FOR BISTABLE DEPLOYABLE COMPOSITE BOOM

Tian-Wei Liu, Jiang-Bo Bai, Nicholas Fantuzzi

### ARBITRARILY SHAPED LAMINATED THIN PLATES IN GRADIENT ELASTICITY: A FINITE ELEMENT SOLUTION

Michele Baccocchi, Nicholas Fantuzzi, Ana M.A. Neves, Antonio J.M. Ferreira

### A BRIEF OUTLINE ON PREVIOUS RESULTS OF FLEXURAL MODULUS ESTIMATION FOR ASYMMETRIC SANDWICH STRUCTURES

Rodrigo José da Silva, Túlio Hallak Panzera, Fabrizio Scarpa, Júlio Cesar dos Santos,  
Fabiano Bianchini Batista, André Luis Christoforo

### CARACTERIZAÇÃO DO TALO DA CARNAÚBA E A INFLUÊNCIA DA SUA INCORPORAÇÃO EM COMPÓSITOS DE PEAD

Laura Nunes de Menezes, José Roberto Moraes d'Almeida

### COMPUTATIONAL ANALYSIS OF 2D-DCB BONDED COMPOSITE JOINTS USING TRAPEZOIDAL TRACTION SEPARATION LAW

Jailto A.P. da Silva, Rafael Beck, Lucas F.M. da Silva Volnei Tita, and Ricardo de  
Medeiros

### CRACK PROPAGATION DUE TO ANISOTROPIC DAMAGE IN ORTHOTROPIC MATERIALS

Carlos L. C. S. Esteves, Jose L. Boldrini, Marco L. Bittencourt

DISPERSION PROBLEMS FOR A ONE-DIMENSIONAL PERIODIC MEDIUM  
USING THE THREE-SCALE HOMOGENIZATION METHOD Carlos Núñez  
Almaguera , Laura Saez Lombira, Reinaldo Rodríguez-Ramos, Raúl Guinovart-Díaz,  
Humberto Brito Santana

DYNAMIC ASYMPTOTIC HOMOGENIZATION FOR MAGNETO ELECTRO-  
ELASTIC PERIODIC LAYERED COMPOSITE WITH IMPERFECT INTERFACE  
Mriganka Shekhar Chaki, Julián Bravo-Castillero

EFFECTS OF THERMAL ACTIVATION ON GEOPOLYMERIZATION OF SLAG-  
BASED PURE GEOPOLYMER  
Lais Alves, Nordine Leklou, João dos Santos, Fábio de Souza, Silvio de Barros

FATIGUE LIFE PREDICTIONS UNDER VARIABLE AMPLITUDE LOADING FOR  
COMPOSITE MATERIALS  
Jorge Alberto Rodriguez Duran, Panters Rodriguez Bermudez, Reinaldo Rodriguez  
Ramos

FIBER-MATRIX INTERFACE INFLUENCE FOR IN-PLANE SHEAR LOAD – A  
NOVEL MICROMECHANICAL APPROACH  
Lucas L. Vignoli, Marcelo A. Savi, Pedro M.C.L. Pacheco, Alexander L. Kalamkarov

GENERATION OF IRREGULAR COMPOSITE MICROSTRUCTURES THROUGH  
OPTIMIZATION  
Matheus Urzedo Quirino, Volnei Tita, Marcelo Leite Ribeiro

MECHANICAL BEHAVIOR OF CFRP STRENGTHENED TUBULAR STEEL  
STRUCTURES  
Bárbara Thaís Jacques Minosso, Rogério José Marczak

MECHANICAL CHARACTERIZATION OF JUTE/CARBON HYBRID EPOXY  
COMPOSITES  
Henrique Queiroz, Vitor Pastor, Anna Mendonça, Jorge Neto, Daniel Cavalcanti,  
Mariana Banea

MECHANICAL PROPERTIES CHARACTERIZATION OF POLYURETHANE  
BASED BIO-BASED ADHESIVES IN ZERO THICKNESS BOND  
Shahin Jalali, Catarina da Silva Pereira Borges, Eduardo André de Sousa Marques,  
Ricardo João Camilo Carbas Carbas, L.F.M. da Silva

MECHANICAL RESPONSE OF COMPOSITE LAMINATES CONTAINING  
ELASTOMERIC LAYERS

Amanda Pereira Peres, Rogerio José Marczak

NUMERICAL ANALYSIS OF A MULTI-MATERIAL DAM VIA IGABEM AND  
THE SUBREGIONS TECHNIQUE

Deborah C. Nardi, Edson Denner Leonel

ON THE OBTAINANCE OF DAMAGE EVOLUTION LAWS FOR COMPOSITE  
LAMINATES VIA CYCLIC TESTING

Gabriel S. C. Souza, Behzad V. Farahani, Rui M. Guedes, Eduardo Gerhardt, Sandro C. Amico, Volnei Tita

REDUCTION OF PLATE FLEXIBILITY BY THE PROGRESSIVE APPLICATION  
OF REINFORCEMENTS WITH OPTIMIZED PATHS

Eduardo da Rosa Vieira, Daniel Milbrath de Leon, Rogério José Marczak

STUDY OF FILAMENT WOUND CYLINDERS WITH VAT IN ELASTIC  
CONDITIONS

Maísa Milanez Ávila Dias Maciel, Bruno Cristhoff, Sandro Amico, Eduardo Gehardt, Nuno Viriato Ramos, Paulo Tavares, Rui Miranda Guedes, Volnei Tita

A TECHNIQUE FOR STRUCTURAL FINITE ELEMENT MODELING OF FIBER-  
REINFORCED RUBBER COMPOSITE USED IN FLEXIBLE COUPLINGS

Bruno Cavalli Vieceli, Katulo Rossi De Martini Moraes, Daniel Pacheco e Silva, João Moreira Lopes, Lourenço de Siqueira Daudt, Filipe Paixão Geiger, Rogério José Marczak

A 3D COMPUTATIONAL HOMOGENIZATION APPROACH FOR PREDICTING  
THE EFFECTIVE ELASTIC CONSTITUTIVE TENSOR OF PERIODIC POROUS  
MATERIALS

Wanderson Ferreira dos Santos, Sergio Persival Baroncini Proença

ON THE USE OF A NOVEL ALL-SOLID-STATE BATTERY AS A COMPOSITE  
STRUCTURE DAMAGE SENSOR

Denys Eduardo Teixeira Marques, Bruno Guilherme Christoff, Maísa Milanez Maciel, Pouria Ataabadi, João Paulo Carmo, Maria Helena Braga, Rui Guedesb, Marcílio Alves, Volnei Tita

VERTICAL TWO-PHASE FLOW WITH A NON-NEWTONIAN PHASE IN  
LAMINAR HETEROGENEOUS POROUS MEDIA  
Lucas Constantino Mendonça, Panters Rodríguez-Bermudez, Alexandre Santos  
Francisco, Isamara Landim Nunes Araujo, Jorge A. Rodríguez Durán

# ANÁLISE NUMÉRICA DO COMPORTAMENTO DE ENRIJECIMENTO À TRAÇÃO E FORMAÇÃO DE FISSURAS EM ELEMENTOS DE CONCRETO ARMADO

Matheus Machado Costa<sup>a</sup>, Ederli Marangon<sup>a</sup>, Leandro Ferreira Friedrich<sup>b</sup>

<sup>a</sup>Programa de Pós-Graduação em Engenharia, Grupo de pesquisa de Materiais Aplicados à Engenharia Civil, Universidade Federal do Pampa  
Av. Tiaraju 810, 97456-550 – Alegrete-RS, Brasil  
[matheuscosta.aluno@unipampa.edu.br](mailto:matheuscosta.aluno@unipampa.edu.br)/[ederlimarangon@unipampa.edu.br](mailto:ederlimarangon@unipampa.edu.br)

<sup>b</sup>Curso de Engenharia Mecânica, Universidade Federal do Pampa  
Av. Tiaraju 810, 97456-550 – Alegrete-RS, Brasil  
[leandrofriedrich@unipampa.edu.br](mailto:leandrofriedrich@unipampa.edu.br)

**Palavras-chave:** concreto armado, transferência de tensões, ANSYS, MEF e LDEM-DYNA.

## 1. INTRODUÇÃO

O concreto é um compósito cimentício amplamente empregado na construção civil, devido à sua boa resistência à compressão. No entanto, o material estrutural apresenta comportamento frágil e baixa resistência à tração. A fim de contornar as limitações citadas, barras de aço podem ser convenientemente embebidas nos locais onde ocorrem os fluxos de tração [1]. A associação das barras de aço ao concreto gera o material compósito denominado de concreto armado.

Outra adaptação do compósito cimentício com o intuito de beneficiá-lo, é a produção de misturas com maior fluidez e homogeneidade, chamadas de concreto autoadensável (CAA). O CAA possui uma maior capacidade de preencher todos os espaços das formas sem necessitar de vibração e independentemente da quantidade de obstáculos a serem transpostos. Diante disso, melhorando o envolvimento dos reforços (barras de aço) e conseqüentemente a aderência entre as fases do compósito [2].

A existência do concreto armado depende diretamente do trabalho conjunto da barra de aço e do concreto na reação aos esforços, o que é propiciado pela propriedade de aderência. O mecanismo é responsável pela transferência de tensões e convergência de deformações entre os materiais. A ligação interfacial, e conseqüentemente, a transferência de tensões e formação de fissuras podem ser estudados por diversos tipos de ensaio, tal como ensaio de tirante [3].

Devido à complexidade no entendimento de tal mecanismo, é necessária uma grande quantidade de ensaios com alto controle das condições de teste, o que torna o estudo custoso em termos de tempo, materiais e estruturas de laboratório envolvidas. Diante disso, as análises numéricas têm se mostrado excelentes alternativas em relação aos testes experimentais, pois permitem estudar em tempo hábil e custo reduzido [4].

O presente trabalho visa estudar numericamente a aderência, o mecanismo de transferência de tensões e a formação de fissuras no concreto, usando modelos híbridos através da união do Método dos Elementos Discretos formado por barras (LDEM) e o Método dos Elementos Finitos (MEF), chamado a seguir de LDEM-DYNA. Os resultados experimentais de Jucá (2020) [5], o qual ensaiou tirantes com barras de 20mm embebidas em concreto autoadensável, são utilizados para validação dos resultados numéricos.

## 2. ADERÊNCIA, TRANSFERÊNCIA DE TENSÕES E FORMAÇÃO DE FISSURAS

O mecanismo de aderência é responsável por garantir o comportamento unitário do concreto e das barras de aço na reação aos esforços solicitantes, e além disso, pela transferência de tensões e

convergência de deformações entre os dois materiais. A aderência, pode ser dividida em três parcelas [6,7]:

- Aderência por adesão (Figura 1a): Gerada pelas ligações físico-químicas entre os materiais, em outras palavras, efeito de colagem;
- Aderência por atrito (Figura 1b): Oriunda da resistência de atrito entre o aço e o concreto, desde que haja pressões transversais ( $P_t$ ) na armadura;
- Aderência mecânica (Figura 1c): Devida ao engrenamento mecânico entre a matriz e o reforço. O concreto circunvizinho às saliências da barra é submetido ao corte, criando assim uma resistência ao deslizamento da armadura.

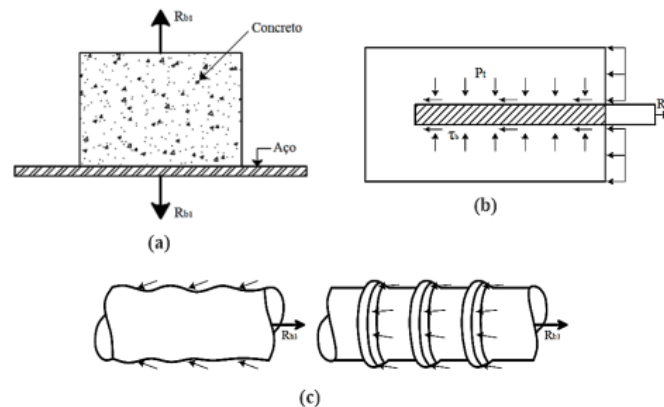


Figura 1 – Aderência: (a) por adesão, (b) por atrito e (c) mecânica [6].

Nas estruturas de concreto armado, quando as solicitações não são suficientes para atingir a tensão de ruptura do concreto à tração  $f_{ct}$ , ou seja,  $\sigma_{ct} < f_{ct}$ , o concreto não possui fissuras e as tensões no concreto e armadura são uniformes, como mostra a Figura 2. Na sequência com o aumento das solicitações, ocorre o surgimento de fissuras (ver os pontos A e B da Figura 2). Nesse caso, a tensão no concreto se anula e a solicitação que estava presente é absorvida pela armadura. Convém lembrar que essa transferência somente é possível devido a aderência existente entre o concreto e o aço. Portanto, enquanto existir tensões de aderência que possam ser mobilizadas, novas fissuras poderão surgir em outros pontos do elemento cimentício [6].

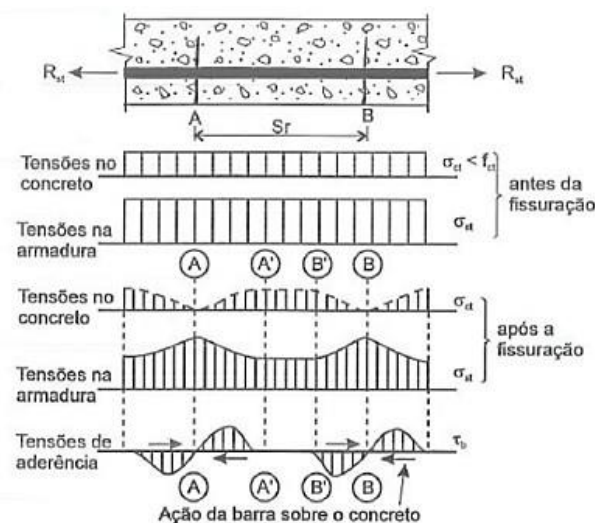


Figura 2 – Fissuração no concreto submetido à tração [6].

### 3. O ENSAIO DE TIRANTE

O ensaio de tirante consiste em um bloco prismático de concreto com uma barra embebida no centro da sua seção transversal, a qual é aplicado o esforço de tração nos seus extremos, exemplificado no esquema da Figura 3. O experimento é destinado à análise do comportamento de enrijecimento à tração de concretos. Os resultados obtidos possibilitam analisar a interação aço-matriz ao longo da formação e propagação de fissuras, bem como os mecanismos de fissuração distribuída [3].

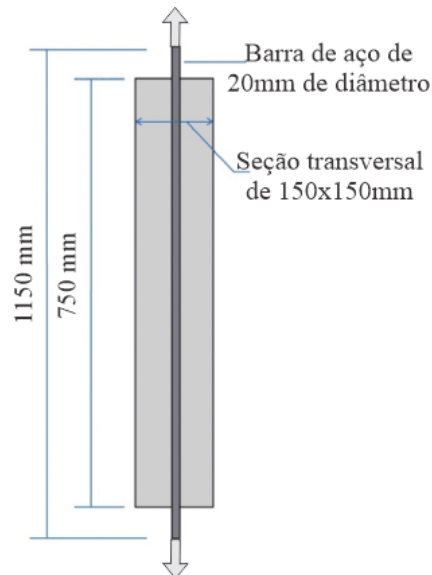


Figura 3 – Configuração do ensaio de tirante e dimensões dos elementos [3,5].

O comportamento do enrijecimento à tração apresenta quatro fases, apresentadas na Figura 4: fase elástica, múltipla fissuração, estabilização das fissuras e escoamento do aço. No trecho de pré-fissuração, fase elástica (trecho a), a carga é distribuída para matriz e armadura, o trabalho é conjunto dos materiais. Ao surgir a primeira fissura, o material não sofre uma falha catastrófica, no entanto ocorre a redistribuição de cargas entre a matriz e o reforço, e posteriormente surgem outras fissuras adicionais (trecho b). Após a múltipla fissuração, qualquer deformação adicional gera o descolamento, deslizamento e estiramento da barra de aço. Portanto, após a múltipla fissuração a curva se aproxima da curva da barra de aço isolada (como visto nos trechos c e d), pois o concreto não contribui mais [3,8].

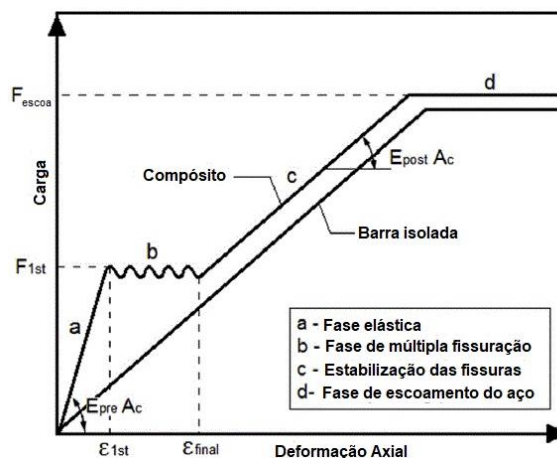


Figura 4 – Descrição esquemática do comportamento de enrijecimento à tração no ensaio de tirante [3,8].

#### 4. MÉTODOS DOS ELEMENTOS FINITOS E MÉTODO DOS ELEMENTOS DISCRETOS FORMADOS POR BARRA

O Método dos Elementos Finitos (MEF) é uma excelente ferramenta no estudo de problemas complexos da mecânica do contínuo e fluídos. A solução pelo método consiste em dividir o domínio em subdomínios com menores complexidades, possíveis de serem resolvidos. Ao associar as parcelas obtêm-se a solução do problema complexo inicial. Detalhes da formulação do MEF podem ser encontrados em referências clássicas como Reddy (1993) [9].

O MEF possui uma grande versatilidade, porém não é indicado para tratar problemas onde se deseja modelar a iniciação e propagação de trincas, uma vez que o método é baseado nos fundamentos da mecânica do contínuo. Ao contrário do MEF, o Método dos Elementos discretos formados por barras (*Lattice Discrete Element Method - LDEM*) permite estudar o processo de dano em materiais, em termos de nucleação, propagação e interação de fissuras [10].

No LDEM, a discretização de um sólido contínuo é realizada através de um arranjo de barras dispostas com massas concentradas nos seus nós (Figura 5a) [11]. A disposição é ordenada, formando um módulo cúbico básico, que se repete ao longo de todo elemento modelado. Ademais, cada barra é caracterizada por uma lei constitutiva bilinear, como pode ser vista na Figura 5b, que relaciona a força interna com a deformação na barra.

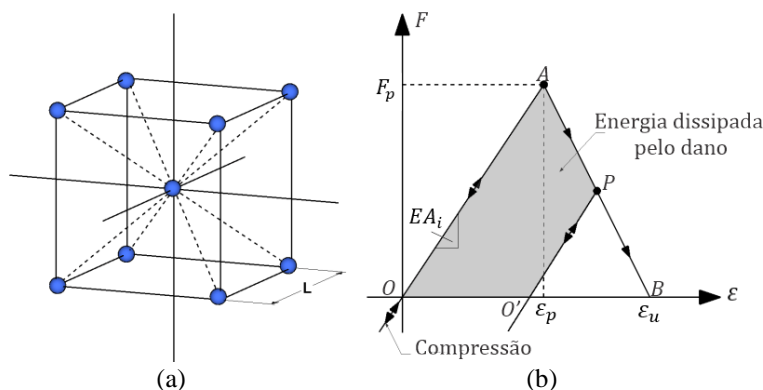


Figura 5 – LDEM: (a) módulo cúbico básico; (b) lei constitutiva bilinear [10].

##### 4.1. LDEM-DYNA

O LDEM pode ser implementado no programa de elementos finitos ANSYS, no ambiente ANSYS LS-DYNA. Dessa forma, é possível o desenvolvimento de modelo híbrido, denominado de LDEM-DYNA. Mais precisamente, a região susceptível a fratura é modelada por elementos discretos e o restante do modelo é analisado por elementos finitos. As barras (ver Figura 5a) são modeladas por elementos discretos de mola (COMBI165) e nos nós são aplicados elementos de massa (MASS166). As possíveis heterogeneidades e imperfeições do material são levadas em consideração através da variação estatística das propriedades do material. Neste estudo e nos demais presentes na literatura, utiliza-se campos aleatórios para representar a distribuição da energia de fratura do material [10,12].

O método LDEM-DYNA foi proposto por Colpo, Iturrioz e Friedrich (2019) [13], onde os autores estudaram a fratura de corpos de prova de poliestireno expandido sob tração. Mais recentemente, outras aplicações do LDEM-DYNA foram apresentadas em Zanichelli et al. (2021) [10] que estudaram numericamente o comportamento à fratura de painéis sanduíche sob flexão em três e quatro pontos, e em Friedrich et al. (2022) [12], que investigaram a evolução do dano em placas de aço galvanizadas.

#### 5. METODOLOGIA

O LDEM-DYNA é aqui empregado para simular o comportamento de enrijecimento a tração baseado nos ensaios experimentais de Jucá (2020). A abordagem numérica é realizada a partir de um



modelo 3D, com as dimensões iguais ao experimento. O elemento de concreto tem seção transversal de 150x150mm e comprimento de 750mm. O compósito cimentício é modelado usando elementos discretos, enquanto a barra de aço é modelada usando elementos finitos de viga (BEAM161), exemplificado no corte da Figura 6. As condições de contorno também são apresentadas na Figura. Vale ressaltar que foram estudados quatro campos aleatórios de energia de fratura, mesma quantidade de espécimes experimentais ensaiadas.

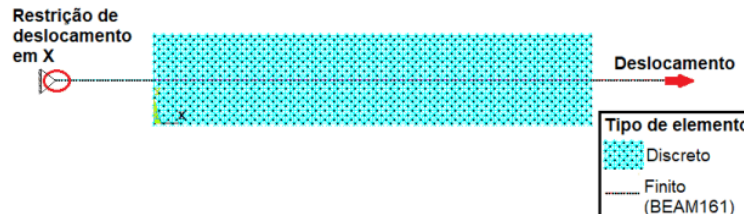


Figura 6 – Discretização e condições de contorno do modelo numérico 3D.

O aço é caracterizado pela curva de tensão-deformação típica de uma barra de 20mm (valores disponibilizados em Jucá (2020)) e o compósito cimentício é definido, a partir das propriedades apresentadas na Tabela 1, obtidos de Jucá (2020) [5] e Marangon (2011) [14].

Tabela 1 – Propriedades mecânicas e parâmetros de entrada para o concreto do LDEM.

Propriedade/Parâmetro	Propriedades mecânicas			Dados de entrada LDEM	
	$E$ (GPa)	$\rho$ (kg/m <sup>3</sup> )	$\sigma_p$ (MPa)	$\epsilon_p$ (%)	$G_f$ (N/m)
Concreto	37,98	2.400	4,45	0,0117	42,74

## 6. RESULTADOS

Na Figura 7, os resultados numéricos (ver curvas coloridas), considerando quatro campos aleatórios diferentes, são comparados à faixa de valores experimentais obtidas por Jucá (2020) [5]. Os dados numéricos apresentaram boa correlação aos determinados em laboratório. Além disso, é possível identificar as quatro fases características do ensaio: fase elástica (pré-fissuração), múltipla fissuração, estabilização das fissuras e escoamento do aço.

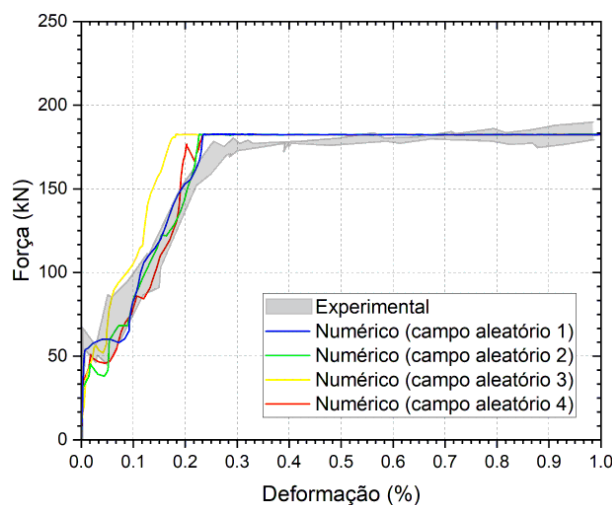


Figura 7 – Comparação entre os dados experimentais e numéricos, considerando quatro campos aleatórios de  $G_f$ .

A Figura 8 mostra um comparativo entre a curva experimental típica do ensaio de enrijecimento por tração obtidas por Jucá (2020) [5] e a curva numérica para o campo aleatório 1 (resultado numérico mais próximo da curva média experimental, comparando os valores de força e deformação nos pontos de transição entre as fases (apresentadas na Figura 4)), utilizando o LDEM-DYNA. Com base na Figura 8, quatro pontos, indicados na Figura, são analisados usando o *Digital Image Correlation* (DIC), no caso do experimento, e as configurações de ruptura visualizadas numericamente. A comparação da ruptura do espécime experimental e da simulação numérica é apresentada na Figura 9.

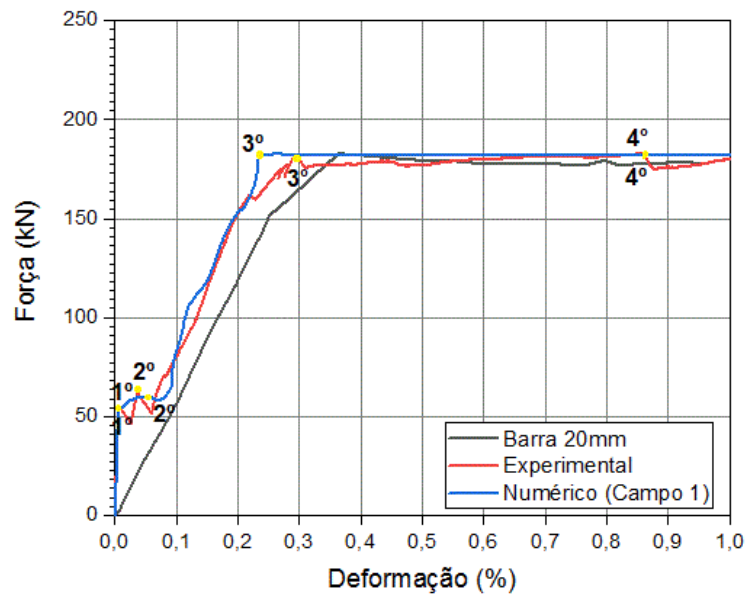


Figura 8 – Curva típica dos ensaios experimentais e a numérica para o campo aleatório 1.

Na Figura 9 é possível notar a ocorrência do fendilhamento na parte inferior do tirante, tendo o mecanismo iniciado ao fim do trecho de múltipla fissuração. Ademais, houve presença de fissuras transversais simétricas nos corpos de prova. No resultado numérico, trincas transversais e fissuras por fendilhamento também são observadas.

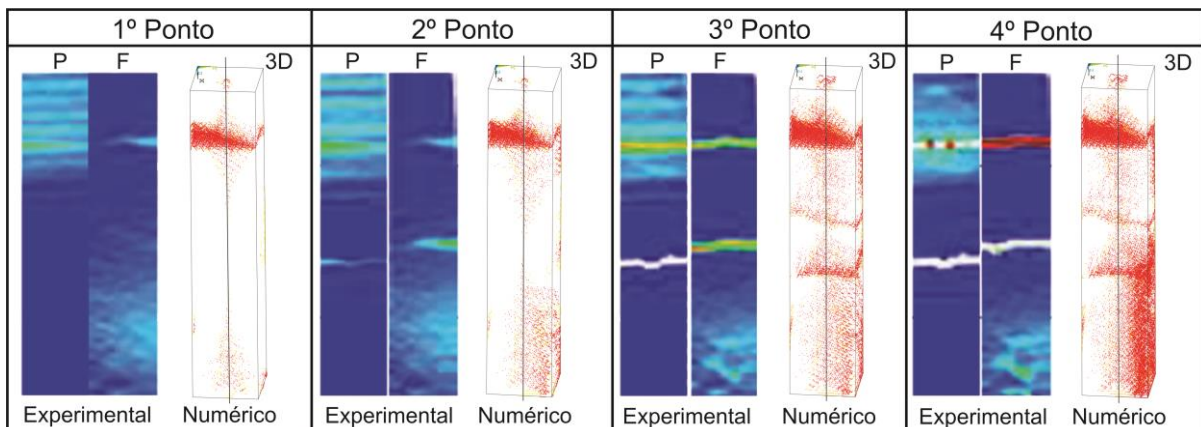


Figura 9 – Comparação da configuração de ruptura dos resultados experimental e numérico.

## 7. CONCLUSÕES

Neste trabalho, um modelo numérico é desenvolvido para investigar o comportamento por enrijecimento à tração do concreto armado e o processo de fissuração até a ruptura. A partir dos resultados obtidos, é possível concluir que o modelo híbrido desenvolvido no LDEM-DYNA consegue reproduzir com satisfatória acurácia os resultados experimentais, como mostrado no comparativo entre as curvas força *versus* deformação axial. A configuração de ruptura também é bem reproduzida pelo modelo numérico.

## AGRADECIMENTOS

Os autores agradecem à Coordenação de Aperfeiçoamento de Pessoal de Nível Superior (CAPES) e à Universidade Federal do Pampa (UNIPAMPA) pelo apoio financeiro, sem o qual não seria possível a realização deste trabalho.

## REFERÊNCIAS

- [1] D. Y. Yoo, et al. Effects of fiber shape, aspect ratio, and volume fraction on flexural behavior of ultra-high-performance fiber-reinforced cement composites. *Composite Structures*, v. 174, p. 375-388. (2017).
- [2] EFNARC. Specification and guidelines for self-compacting concrete. In: *EFNARC - European Federation for Specialist Construction Chemicals and Concrete Systems*. Norfolk, UK, 2002.
- [3] C. S. Rangel, et al. Tension stiffening approach for interface characterization in recycled aggregate concrete. *Cement and Concrete Composites*, v. 82, p. 176-189. (2017).
- [4] M. Congro, D. Roehl, C. Mejia. Mesoscale computational modeling of the mechanical behavior of cement composite materials. *Composite Structures*, v. 257, p. 113137. (2021).
- [5] P. H. D. O. Jucá. *Avaliação do mecanismo de transferência de tensões e formação de fissuras no concreto autoadensável com reforço híbrido*. Dissertação. Universidade Federal do Pampa, Alegrete (2020).
- [6] P. B. Fusco. *Técnica de armar as estruturas de concreto*. 1. ed. São Paulo: Pini, 1995. 382 p.
- [7] F. Leonhardt, E. Mönnig. *Construções de concreto: princípios básicos do dimensionamento de estruturas de concreto armado*. 2. reimp. ed. Rio de Janeiro: Interciência, 2008. v. 1. 336 p.
- [8] J. Aveston, G.A. Cooper, A. Kelly. *The properties of fiber composites*. In: Conference Proceedings of the National Physical Laboratory, Guildford: IPC Science and Technology Press Ltd., p. 15–26. (1971).
- [9] J.N. Reddy. *An introduction to the finite element method*. 2. ed., McGraw-Hill, 1993.
- [10] A. Zanichelli, et al. A Novel Implementation of the LDEM in the Ansys LS-DYNA Finite Element Code. *Materials*, v.14, n. 24, p. 7792. (2021).
- [11] A. H. Nayfeh, M. S. Hefzy. Crack propagation in elastic solids using the truss-like discrete element method. *AIAA Journal*, v. 16, n. 8, p. 779–787. (1978).
- [12] L. F. Friedrich, et al. Combination of discrete and finite element method to simulate damage in galvanised steel. *Procedia Structural Integrity*, v. 41, p. 254–259. (2022).
- [13] A. Colpo, I. Iturrioz, L. Friedrich. Implementation of the lattice discrete element method in the ansys ls-dyna software. In: *ENIEF 2019: XXIV Congresso sobre Métodos Numéricos y sus Aplicaciones*, 2019
- [14] E. Marangon. *Caracterização Material e Estrutural de concretos autoadensáveis reforçados com fibras de aço*. Tese. Universidade Federal do Rio de Janeiro. (2011).

# ANALYSIS OF THE ASYMPTOTIC HOMOGENIZATION METHOD IN A BILAMINATE ACOUSTIC MEDIUM

Erika Torres Figueiras <sup>a</sup>, Reinaldo Rodríguez Ramos <sup>a, b</sup>, Panters Rodríguez Bermúdez <sup>c</sup>,  
Yoanh Espinosa Almeyda <sup>d</sup>

<sup>a</sup> Faculty of Mathematics and Computing Science, University of Havana  
San Lázaro y L, Vedado, Havana, CP 10400, Cuba  
[erikafig804@gmail.com](mailto:erikafig804@gmail.com)

<sup>b</sup> PPG-MCCT, Universidade Federal Fluminense  
Av. dos Trabalhadores 420, Vila Sta. Cecília, CP 27255-125 Volta Redonda, RJ, Brazil  
[reinaldo@matcom.uh.cu](mailto:reinaldo@matcom.uh.cu), [reinaldorr@id.uff.br](mailto:reinaldorr@id.uff.br)

<sup>c</sup> Departamento de Ciências Exactas, Universidade Federal Fluminense  
Av. dos Trabalhadores 420, Vila Sta. Cecília, CP 27255-125 Volta Redonda, RJ, Brazil  
[pantersrb@id.uff.br](mailto:pantersrb@id.uff.br)

<sup>d</sup> Instituto de Ingeniería y Tecnología, Universidad Autónoma de Ciudad Juárez  
Av. Del Charro 450 Norte, Cd. Juárez, Chihuahua, CP 32310, México  
[yoanhealmeyda1209@gmail.com](mailto:yoanhealmeyda1209@gmail.com)

**Keywords:** asymptotic homogenization, metafluid, effective equation.

## 1. INTRODUCTION

The homogenization process stands out in the search for the effective properties of composite materials. As it is suggested in Refs. [1,2,3,4], the homogenization method consists of finding effective equations that govern the response at the macroscale from partial differential equations with coefficients of rapid oscillation associated with a microscale,.

In this work, we are interested in the Asymptotic Homogenization Method (AHM), which is used to characterize a composite material with periodic microstructure. By working with two-scale asymptotic expansions and solving the problems in different orders while taking into account the boundary conditions, the corresponding effective wave equation, the homogenized equations of motion, and the homogenized constitutive relation are obtained.

## 2. BILAMINATE COMPOSITE SYSTEM

The Fig. 1 (a) shows the laminate structure of a material made of two plane-parallel layers of different fluids that are repeated periodically. Following [1,2], the fluid phases are assumed as perpendicular to the  $x$  axis and the symbols  $\rho_j$  and  $\kappa_j$  are the density and bulk modulus of fluid  $j$ , respectively. Fluids 1 and 2 have thickness  $R$  and  $\ell - R$ , respectively, where  $\ell$  is the period of the system. The Fig. 1 (b) shows the periodic unit cell at microstructure, where  $D_j$  denotes the domain of the fluid  $j$  ( $j=1,2$ ) and  $r = 1 - R/\ell$  is the interface. Let  $X = (x, y)$  be the macroscopic coordinates and  $\xi = (\xi_1, \xi_2) = (x/\ell, y/\ell)$  the microscopic coordinates, such that the small parameter  $\varepsilon = \ell/L \ll 1$ , where  $L$  is the length of the composite and the wavelength in each fluid is much larger than the period of the microscale  $\ell$ .

Linearized constitutive relationships and equations of motion relating pressure acoustic  $p$  and the velocity  $v$  in each fluid, for harmonic excitations proportional to  $e^{-i\omega t}$ , are given by the following equations

$$p = \frac{\kappa_j}{i\omega} \left( \frac{\partial v_x}{\partial x} + \frac{\partial v_y}{\partial y} \right), \quad v = \frac{1}{i\rho_j \omega} \left( \frac{\partial p}{\partial x}, \frac{\partial p}{\partial y} \right), \quad (1)$$

where  $v_x$  and  $v_y$  are the components of the velocity. Let  $k_j = \omega/c_j$  and  $c_j = (\kappa_j/\rho_j)^{1/2}$  be the wave number and acoustic wave velocity of fluid  $j$ , respectively.

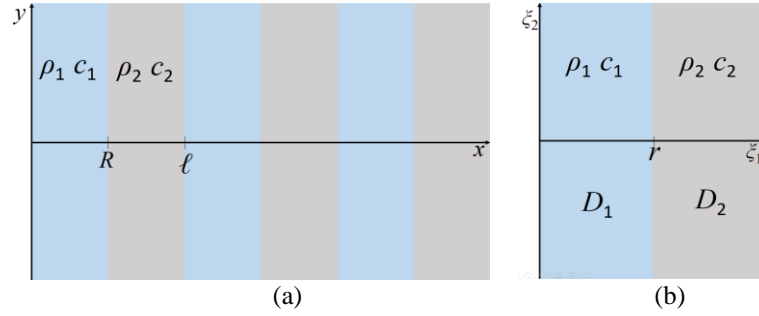


Figure 1 – (a) Heterostructure of the composite material; (b) Unit cell for different types of fluids occupying domains  $D_1$  and  $D_2$ .

## 2.1. Application of the AHM

It is assumed that  $p$  and  $v$  are both functions of the macroscopic and microscopic coordinates. Expanding the derivatives, taking into account the chain rule, we have

$$\frac{\partial f}{\partial (X_s)} = \frac{\partial f}{\partial (X_s)} + \frac{1}{\varepsilon} \frac{\partial f}{\partial (\xi_s)}, \quad (2)$$

where  $f$  is an arbitrary function that depends on the macroscopic and microscopic coordinates and  $s = x, y$ .

Now, substituting into the expressions of Eq. (1) the expansions of the derivatives in Eq. (2) and  $\kappa_j = m_j^2 c_j^2 \rho_2^2 / \alpha_j^2 \rho_j$  and  $\omega = m_j c_2 \rho_2 / \rho_j$ , where  $\alpha_1 = \alpha = k_1/k_2 = c_2/c_1$ ,  $\alpha_2 = 1$ ,  $m_1 = m = \rho_1/\rho_2$ , and  $m_2 = 1$  are dimensionless parameters, this leads to the constitutive relations

$$p = \frac{m_j \rho_2 c_2}{i \alpha_j^2} \left( \frac{\partial v_x}{\partial x} + \frac{1}{\varepsilon} \frac{\partial v_x}{\partial \xi_1} + \frac{\partial v_y}{\partial y} + \frac{1}{\varepsilon} \frac{\partial v_y}{\partial \xi_2} \right), \quad v = \frac{1}{m_j i \rho_2 c_2} \left( \frac{\partial p}{\partial x} + \frac{1}{\varepsilon} \frac{\partial p}{\partial \xi_1}, \frac{\partial p}{\partial y} + \frac{1}{\varepsilon} \frac{\partial p}{\partial \xi_2} \right), \quad (3)$$

Substituting the velocity components given in the second equation of Eq. (3) into the first equation of Eq. (3) and doing the corresponding algebraic work, we arrive at

$$\frac{\partial^2 p}{\partial x^2} + 2\varepsilon^{-1} \frac{\partial^2 p}{\partial x \partial \xi_1} + \varepsilon^{-2} \frac{\partial^2 p}{\partial \xi_1^2} + \frac{\partial^2 p}{\partial y^2} + 2\varepsilon^{-1} \frac{\partial^2 p}{\partial x \partial \xi_2} + \varepsilon^{-2} \frac{\partial^2 p}{\partial \xi_2^2} + \alpha_j^2 p = 0. \quad (4)$$

Expanding asymptotically to pressure and velocity as in [1], we have the equalities  $p(X, \xi) = \sum_{n=0}^{\infty} \varepsilon^n p_n(X, \xi)$  and  $v(X, \xi) = \varepsilon^{-1} \sum_{n=0}^{\infty} \varepsilon^n v_n(X, \xi)$ . Substituting the pressure expansion into Eq.(4) and grouping into powers of  $\varepsilon$  results in a sum of the form  $\sum_{n=-2}^{\infty} \varepsilon^n H_n(X, X/\varepsilon) = 0$ , where the equations must be satisfied in every order in  $\varepsilon$  and the expressions of  $H_n$  are

$$H_{-2} = \frac{\partial^2 p_0}{\partial \xi_1^2} + \frac{\partial^2 p_0}{\partial \xi_2^2}, \quad (5)$$

$$H_{-1} = \frac{\partial^2 p_1}{\partial \xi_1^2} + \frac{\partial^2 p_1}{\partial \xi_2^2} + 2 \frac{\partial^2 p_0}{\partial x \partial \xi_1} + 2 \frac{\partial^2 p_0}{\partial y \partial \xi_2}, \quad (6)$$

$$H_n = \frac{\partial^2 p_{n+2}}{\partial \xi_1^2} + \frac{\partial^2 p_{n+2}}{\partial \xi_2^2} + 2 \frac{\partial^2 p_{n+1}}{\partial x \partial \xi_1} + 2 \frac{\partial^2 p_{n+1}}{\partial y \partial \xi_2} + \frac{\partial^2 p_n}{\partial x^2} + \frac{\partial^2 p_n}{\partial y^2} + \alpha_j^2 p_n, \quad (n > -1). \quad (7)$$

Following [4] we have that  $H_n = 0$  for  $n \geq -2$ . Then, the equation of order  $\varepsilon^{-2}$  is  $H_{-2} = 0$ . On the other hand,  $p$  and the  $x$  component of  $v$  must be periodic on the microscale and continuous at the  $\xi_1 = r = 1 - R/\ell$  interface and as  $\xi_1 \in (0, 1)$ , then  $p_0(X, 0) = p_0(X, 1)$ . In addition, the boundary conditions at [1], where the partial derivative of  $p_0$  with respect to  $\xi_1$  over  $\partial D_1$  is  $m$  times the value of the derivative over  $\partial D_2$  and therefore its value is 0, where  $\partial D_j$  is the limit of  $D_j$ ,  $j = 1, 2$ . Then, the solution in order  $\varepsilon^{-2}$  is  $p_0 = A(X)$ , where  $A$  is an arbitrary function of  $X$ , that is, it depends only from the macroscopic coordinates.

Since  $p_0$  is independent of  $\xi_1$  and since the pressures must be constant in the direction of  $\xi_2$  (due to domain symmetry and boundary conditions at interfaces), in particular  $p_1$  is constant in direction  $\xi_2$ . Then, from the equation of order  $\varepsilon^{-1}$  we have  $\partial^2 p_1 / \partial \xi_1^2 = 0$ , from which it follows that  $p_1 = N(\xi)(\partial p_0 / \partial x)$  and carrying out the corresponding calculations, together with the continuity of the function  $p_1$  through the interfaces, the periodicity and the boundary conditions, we get the function

$$p_1 = \begin{cases} (d_1 + b_1 \xi_1) \frac{\partial A}{\partial x}, & \xi_1 \in D_1 \\ d_1 \xi_1 \frac{\partial A}{\partial x}, & \xi_1 \in D_2 \end{cases}, \quad (8)$$

where  $b_1 = (\rho_2 - \rho_1)(r - 1) / [(1 - r)\rho_2 + \rho_1 r]$  and  $d_1 = (\rho_2 - \rho_1)r / [(1 - r)\rho_2 + \rho_1 r]$ .

The  $\varepsilon^0$  order problem leads to the effective wave equation on the macroscale. From Eq. (7) corresponding to this order and taking into account that  $\partial^2 p_0 / \partial \xi_1 \partial x = 0$  because  $p_0$  is independent of the fast variable  $\xi_1$ , then the following equation is satisfied.

$$\frac{\partial^2 p_2}{\partial \xi_1^2} + \frac{\partial^2 p_1}{\partial \xi_1 \partial x} + \frac{\partial^2 p_0}{\partial \xi_1 \partial x} = - \frac{\partial^2 p_1}{\partial \xi_1 \partial x} - \frac{\partial^2 p_0}{\partial \xi_1 \partial x} - \frac{\partial^2 p_0}{\partial x^2} - \frac{\partial^2 p_0}{\partial y^2} - \alpha_j^2 p_0.$$

Then, due to the periodicity, the continuity of  $p_2$  across the interfaces and the boundary condition

$$\left( \frac{\partial p_2}{\partial \xi_1} + \frac{\partial p_1}{\partial x} + \frac{\partial p_0}{\partial x} \right) \Big|_{\partial D_1} = m \left( \frac{\partial p_2}{\partial \xi_1} + \frac{\partial p_1}{\partial x} + \frac{\partial p_0}{\partial x} \right) \Big|_{\partial D_2}, \quad (9)$$

it is possible to integrate the expression between parentheses in Eq. (9) from 0 to  $r$ , adding  $m$  times the integral from  $r$  to 1, over  $\xi_1$ , whose sum is equal to zero. Developing the calculation and substituting functions  $p_0$  and  $p_1$  for  $A(X)$  and the expression in Eq. (8), respectively, we get the effective equation for  $A$

$$\left[ r(b_1 + 1) + m(d_1 + 1)(1 - r) \right] \frac{\partial^2 A}{\partial x^2} + \left[ r + m(1 - r) \right] \frac{\partial^2 A}{\partial y^2} + \left[ \alpha^2 r + m(1 - r) \right] A = 0, \quad (10)$$

which constitutes the effective wave equation for pressure, since  $p \approx A(X) + O(\varepsilon)$  and its values must get closer and closer to those of the function  $A$  when  $\varepsilon \rightarrow 0$ .

On the other hand, the effective speed can be obtained if we work with the homogenized variables  $\hat{p}$  and  $\hat{v}$ , which result from integrating from 0 to 1 their respective asymptotic functions with

respect to variable  $\xi_1$ . From the expression obtained for  $\hat{v}$ , the homogenized equations of motion are reached. Besides, the expression that relates  $\hat{p}$  and  $\hat{v}$  is the homogenized constitutive relationship.

### 3. EXAMPLE

If it is assumed that  $y$  takes a constant value,  $y = y_0$ , then a solution to the effective wave equation is obtained by solving the equation

$$C_1 \frac{d^2 A(x, y_0)}{dx^2} + C_2 \frac{d^2 A(x, y_0)}{dy^2} + C_3 A(x, y_0) = 0,$$

where  $C_1 = r(b_1+1)+m(d_1+1)(1-r)$ ,  $C_2 = r+m(1-r)$  and  $C_3 = \alpha^2 r+m(1-r)$ . Since  $A(x, y_0) = P(x)$ , the effective wave equation takes the form  $C_1 P''(x) + C_3 P(x) = 0$  whose general solution is  $P(x) = a_1 \cos(bx) + a_2 \sin(bx)$ ,  $b^2 = C_3/C_1$ .

Taking the data  $\ell = 0.1$  m,  $R = 0.09$  m,  $\ell - R = 0.01$  m,  $\rho_1 = 998$  kg/m<sup>3</sup>,  $\rho_2 = 790$  kg/m<sup>3</sup>,  $c_1 = 1480$  m/s and  $c_2 = 1150$  m/s from [5], then the function is

$$A(x, y_0) = y_0 \cos\left(\sqrt{\frac{C_3}{C_1}}x\right) + y_0 \left[1 - \cos\left(\sqrt{\frac{C_3}{C_1}}0.1\right)\right] \sin\left(\sqrt{\frac{C_3}{C_1}}0.1\right)^{-1} \sin\left(\sqrt{\frac{C_3}{C_1}}x\right).$$

The Fig. 2 represents the function  $A(x, y_0)$  for different values of  $y_0$ , specifically for  $y_0 = 0, 1/2, 1, 2$  and when  $y_0 = 0$  the function is the null constant. The graph shows that the wave elongation increases as the value of  $y_0$  increases.

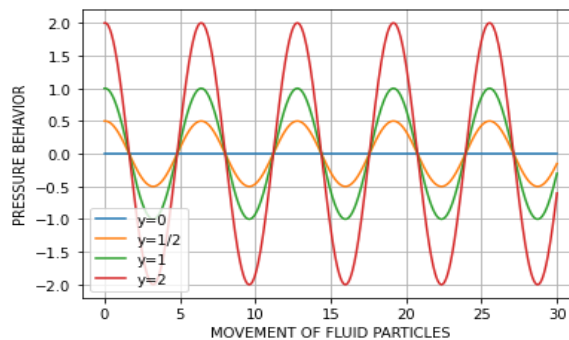


Figure 2 – Representation of the function  $A(x, y_0)$ .

### REFERENCES

- [1] J. D. Smith. *Application of the method of asymptotic homogenization to an acoustic metafluid*. Proc. R. Soc. A. (doi:10.1098/rspa.2011.0231) (2011).
- [2] H. Andrade Loarca. *Metafluido acústico: Homogeneização periódica por convergência a dos escalas*. Thesis. Autonomous University of Mexico. May. (2015).
- [3] N. Bakhvalov, G. Panasenko. *Homogenisation: Averaging Processes in Periodic Media*. (1989).
- [4] J. M. Vivar Pérez. *Dispersión de ondas en materiales compuestos provistos de estructura periódica*. Dissertation. July. (2002).
- [5] M. B. Muhlestein. *Effective acoustic metamaterial homogenization based on Hamilton's principle with a multiple scales approximation*. J. Acoust. Soc. Am. 147. May. (2020).

## ANALYSIS OF GFRP COMPOSITES REPAIRED WITH ADHESIVELY BONDED STEEL PATCH

Alex Sousa Lassé, João Marciano Laredo Dos Reis, Heraldo Silva Da Costa Mattos

Fluminense Federal University, Francisco Eduardo Mourão Saboya Graduate Program in Mechanical Engineering (PGMEC)

Rua Passo da Pátria, 156 - Sala 213 Bloco E, Niterói 24210-240, Brazil  
[alexlasse@id.uff.br](mailto:alexlasse@id.uff.br), [jreis@id.uff.br](mailto:jreis@id.uff.br), [heraldomattos@id.uff.br](mailto:heraldomattos@id.uff.br)

**Keywords:** composite repair, glass fiber composite, metallic patch, adhesive

### 1. INTRODUCTION

The use of polymeric composite materials has grown significantly in recent decades due to their excellent combination of mechanical strength and low weight [1], largely replacing metallic materials that are highly susceptible to corrosion [2]. However, similar to other materials, polymeric composites are susceptible to damage, with the majority of such damage being related to impacts [3]. Often, these damaged components need to be completely replaced, which can be costly [4]. In light of this, the study and investigation of the possibility of repairing these materials are of great importance.

Repairs of composite materials can be carried out through mechanical fastening, complete lamination around the damage, and as proposed in this study, the repair using adhesive metallic patches, where a metal plate is bonded around the damage using a polymeric adhesive, as depicted in Figure 1.

The objective of this research is to ascertain whether it is possible to restore the mechanical properties of a damaged epoxy resin matrix composite reinforced with fiberglass through this type of repair approach.



Figure 1 - GRFP repaired with bounded metallic patch



## 2. EXPERIMENTAL SETUP

To assess the repair efficiency, multiple tensile tests were conducted in accordance with the ASTM D 3039/D 3039M standard [5], which defines testing properties, specimen dimensions, and data treatment procedures. The tests were performed to ascertain property losses in damaged materials and the restoration of properties in repaired materials, as described:

- Tensile tests were conducted according to the standard [5] on an intact specimen to use it as a benchmark.
- Tests were conducted on damaged specimens, and changes in properties were compared with the intact material.
- The specimens were repaired and tested to assess the restoration of mechanical properties.
- Mechanical properties including stiffness, ultimate strength, and fracture strain were evaluated.

### 2.1. Specimens fabrication

The test specimens were fabricated from a sheet of bidirectional fiberglass laminate and epoxy resin, following the standard [5]. To simulate damages, holes of different dimensions were created in the specimens to assess the impact of hole size on the effective working area and the stress concentration associated with the damage. The hole dimensions were 3 mm, 6 mm, and 10 mm, and they were precisely placed at the center of the specimen. As for the metal patches, they were crafted from a 2 mm thick carbon steel sheet with a width matching that of the specimen and lengths of 20 mm, 40 mm, and 60 mm. These patches were adhered using Rengel® SW 404 epoxy adhesive from HUNTSMAN®. For the metallic patch a superficial treatment has been performed to improve the adhesion between adhesive and patch. No superficial treatment was performed on composite.

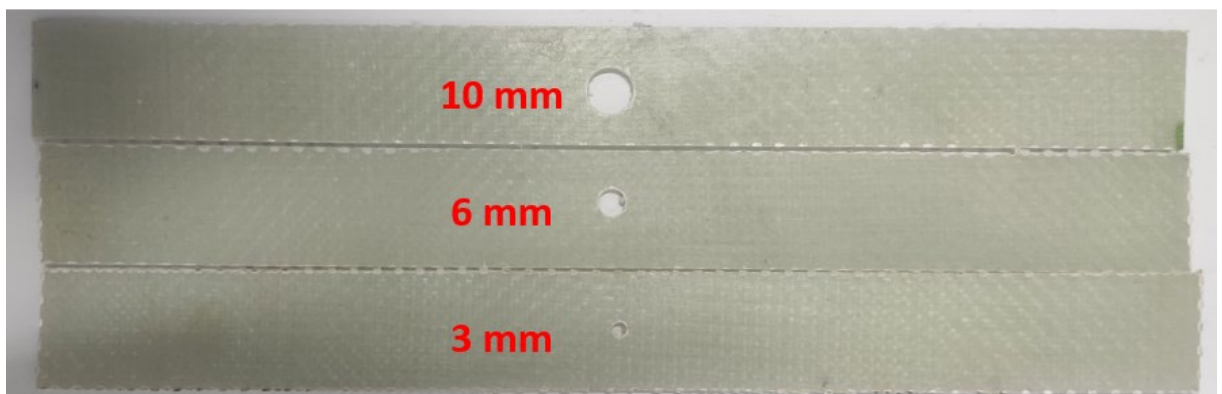


Figure 2 - Damaged test specimens

### 2.2. Tests parameters and tests matrix

Three tests were conducted for each test configuration, three tests for each hole in the damaged specimens, totaling 9 tests, and three tests for each patch length, totaling 27 tests on the repaired specimens as indicated in the Table 1. The test speed and other parameters were followed in accordance with [5], and the test setup can be seen in the Figure 3.

**Table 1 - Test matrix.**

Tests numbers	Hole diameter (mm)	Patch length (mm)
3	Intact	Intact
3	3	Damaged
3	3	20
3	3	40
3	3	60
3	6	Damaged
3	6	20
3	6	40
3	6	60
3	10	Damaged
3	10	20
3	10	40
3	10	60

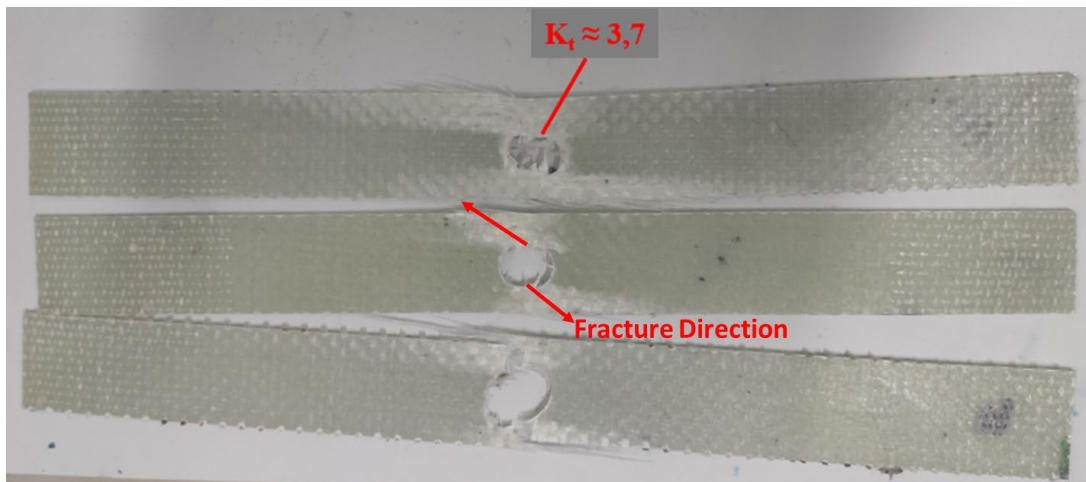


**Figure 3 - Test setup**

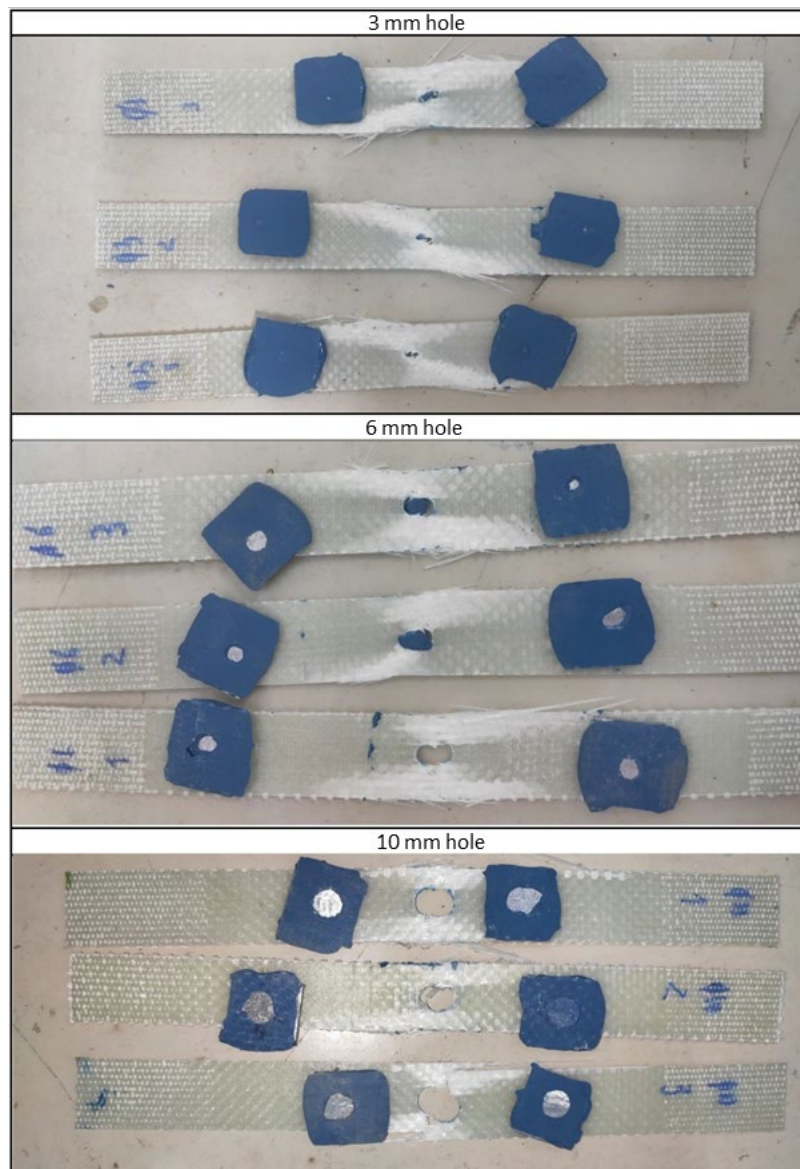
### 3. RESULTS

The results show a significant reduction in mechanical properties for the damaged cases, with a decrease of up to 60% in Ultimate Tensile Strength (UTS) for the specimen with a 10 mm hole due to the reduction in the effective area and stress concentration around the damage as seen in Figure 4.

For the repaired specimens, there was debond between the adhesive and the composite seen in Figure 5, which significantly affected the strength of the repair. It was anticipated that the length of the patch would result in a larger contact area between the adhesive and the composite, thus enhancing the repair's strength. However, due to poor adhesion, the length of the repairs had no impact on the outcomes.



**Figure 4 - Fracture direction around damage**



**Figure 5 - Debond of the adhesive.**

Figure 6 provides a concise overview of the average Ultimate Tensile Strength (UTS) across all test configurations, where the hatched bar represents the damaged cases, and the other bars represent the repaired specimens. The reduction in property for the damaged cases compared to the intact case, represented by the blue bar, is evident. Similarly, it can be confirmed that there was no significant improvement between the damaged and repaired cases. The stiffness among the intact, damaged, and repaired cases did not exhibit significant variation. However, the maximum deformation at fracture follows the same proportion as the UTS.

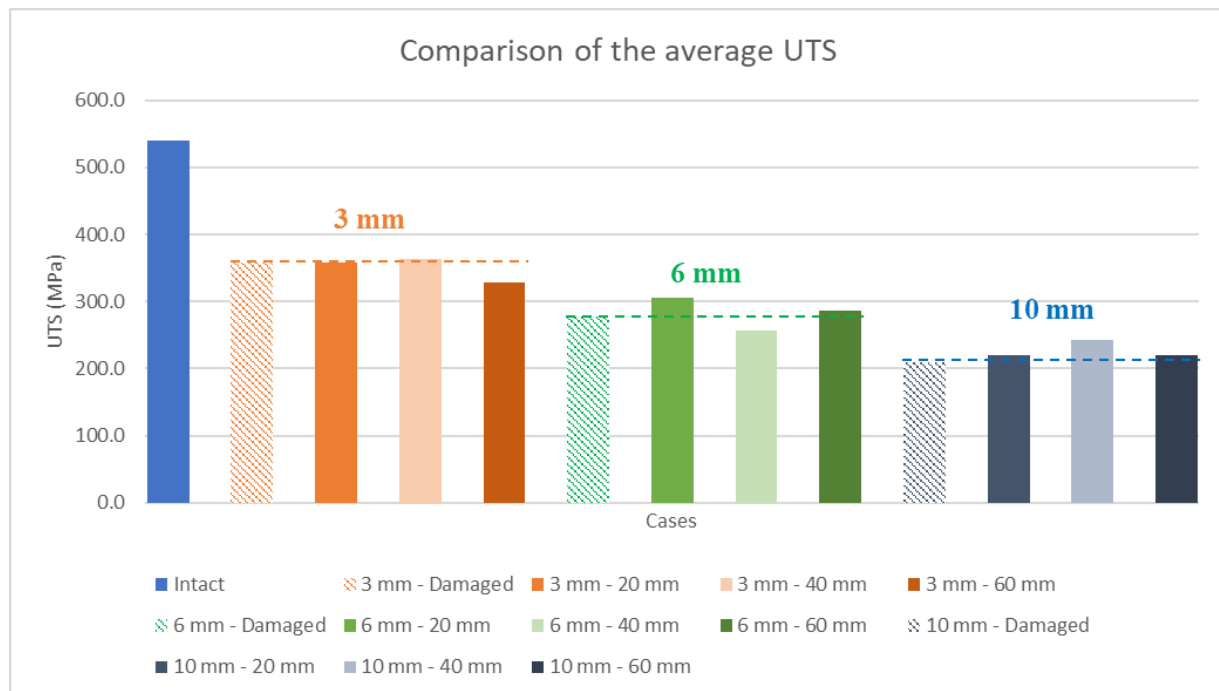


Figure 6 - Comparison of the average UTS for all cases.

#### 4. CONCLUSION

The results have made it clear that repairing the composite through this method is not feasible without strong adhesion between the adhesive and the composite. This is due to the direct relationship between adhesive efficiency and repair strength. Therefore, it is necessary to implement a procedure to enhance the adhesion between these components. This could involve adding additives to the adhesive, applying a surface treatment to the composite, or introducing some form of roughness during the lamination process.

#### REFERENCES

- [1] A. Kaw. *Mechanics of composite materials*. CRC press. (2005).
- [2] A. Gorni. *A evolução dos materiais poliméricos ao longo do tempo*. Revista plástico industrial. (2003).
- [3] K. Katnam, L. da Silva, T. Young. *Bonded repair of composite aircraft structures: A review of scientific challenges and opportunities*. Progress in Aerospace Sciences. v. 61, p. 26-42.(2013).

- [4] W. Hou, W. Zhang, Q. Tang. *Progress in patch repair of aerospace composite structures. In: Third International Conference on Smart Materials and Nanotechnology in Engineering*. SPIE. p. 884-891. (2012).
- [5] American Society for Testing and Materials – D 3039/D 3039M-08. *Standard test method for tensile properties of plastics*. EUA: 13p. (2008).

#### **RESPONSIBILITY NOTICE**

The author(s) is (are) the only responsible for the printed material included in this manuscript.

# ANALYTICAL MODEL FOR BISTABLE DEPLOYABLE COMPOSITE BOOM

Tian-Wei Liu<sup>a,b</sup>, Jiang-Bo Bai<sup>a</sup>, Nicholas Fantuzzi<sup>b</sup>

<sup>a</sup>School of Transportation Science and Engineering, Beihang University, Beijing, 100191, People's Republic of China  
[liutianwei@buaa.edu.cn](mailto:liutianwei@buaa.edu.cn)  
[baijiangbo@buaa.edu.cn](mailto:baijiangbo@buaa.edu.cn)

<sup>b</sup>DICAM Department, University of Bologna, Bologna 40136, Italy  
[nicholas.fantuzzi@unibo.it](mailto:nicholas.fantuzzi@unibo.it)

**Keywords:** Bistable deployable composite boom; Archimedes helix; Tsai-Hill criterion; Maximum stress criterion.

## 1. INTRODUCTION

With continuously evolving engineering technology, the requirement for next-generation intelligent structures and materials with novel functions has increased significantly. As a new type of intelligent composite structure, bistable composite structure has attracted more and more attention due to its advantages of light weight, excellent mechanical properties and high space utilization [1,2]. Bistable composite structures have two stable configurations that remain in their respective equilibrium positions without the continuous application of an external force [3]. Due to the above characteristic, bistable composite structures are applied in many fields, including aerospace (e.g., deployable booms and morphing skins) [4], civil engineering [5], bionic structures (e.g., flytraps) [6], energy harvesting [7], robots [8], etc.

As a bistable composite structure with promising application prospects, the bistable deployable composite boom (Bi-DCB) with antisymmetric layup is utilized as the deployment mechanism of solar array, with advantages of high storage ratio and light weight [9], as shown in Fig. 1. In 1996, after the British scholar Daton Lovett first proposed the design scheme of the bistable deployable composite boom (Bi-DCB) with antisymmetric layup [10], the University of Cambridge took the lead in carrying out relevant research on this structure. Based on the classical laminate theory and the minimum energy principle, Iqbal et al. [11] established a simple linear elastic bistable analytical model. The expressions of strain energy with respect to the longitudinal and transverse curvature and the central angle of the cross-section was obtained, and the radius of the cross-section of the folding stable state was predicted. However, this analytical model can not distinguish the behaviour of symmetric and antisymmetric laminates. Galletly and Guest [12] extended the analytical model proposed by Iqbal and presented a beam model to include all possible deformation modes, including twist and shear, and stretching-bending coupling effects. The predicted radius of the cross-section of the folding stable state is in good agreement with numerical simulation results, but there is a big difference with experimental results. Later, Galletly and Guest [13] proposed a shell model, which deletes the assumption of cross-section shape. Prediction results are basically consistent with the beam model, but differ greatly from experimental results. Galletly proposes that the result disparities are due to the fact that the polypropylene matrix had entered the plastic region, while the analytical models are based on linear-elastic material assumptions. Guest and Pellegrino [14] developed an inextensional bending model. The analytical model assumes that the deformation of the shell is uniform everywhere and the Gaussian curvature is always zero, which enables the analytical model to determine the radius of the cross-section

of the folding stable state. Prediction results of this model are in good agreement with those of the above three analytical models [11-13].

From the previous reviews, the geometric configuration of the cross-section of the Bi-DCB in the folding stable state has been comprehensively investigated. The geometric configuration of the cross-section in the folding stable state is a key index to evaluate the bistable behaviour of the Bi-DCB. Thus, in order to accurately and efficiently predict the bistable behaviour of the Bi-DCB, more accurate geometric equations describing the Bi-DCB in the folding stable state were established in this paper. Based on the energy principle, an analytical model was presented to predict the geometric configuration of the cross-section of the Bi-DCB in the folding stable state. In addition, based on the analytical model, Tsai-Hill and maximum stress criteria were utilized to analyze the failure index of the Bi-DCB in the folding stable state.

This paper is organized as follows: the geometrical model of the Bi-DCB is established in Section 2; an analytical model for predicting the geometric configuration of the cross-section of the Bi-DCB in the folding stable state is presented in Section 3; The stress analysis is conducted in Section 4; in Section 5, experiments and numerical simulation results are used to validate the analytical models presented in Sections 3 and 4; the effect of geometric parameters on the bistable behaviour of the Bi-DCB is further analyzed in Section 6; the key findings are summarized and conclusions are drawn in Section 7.

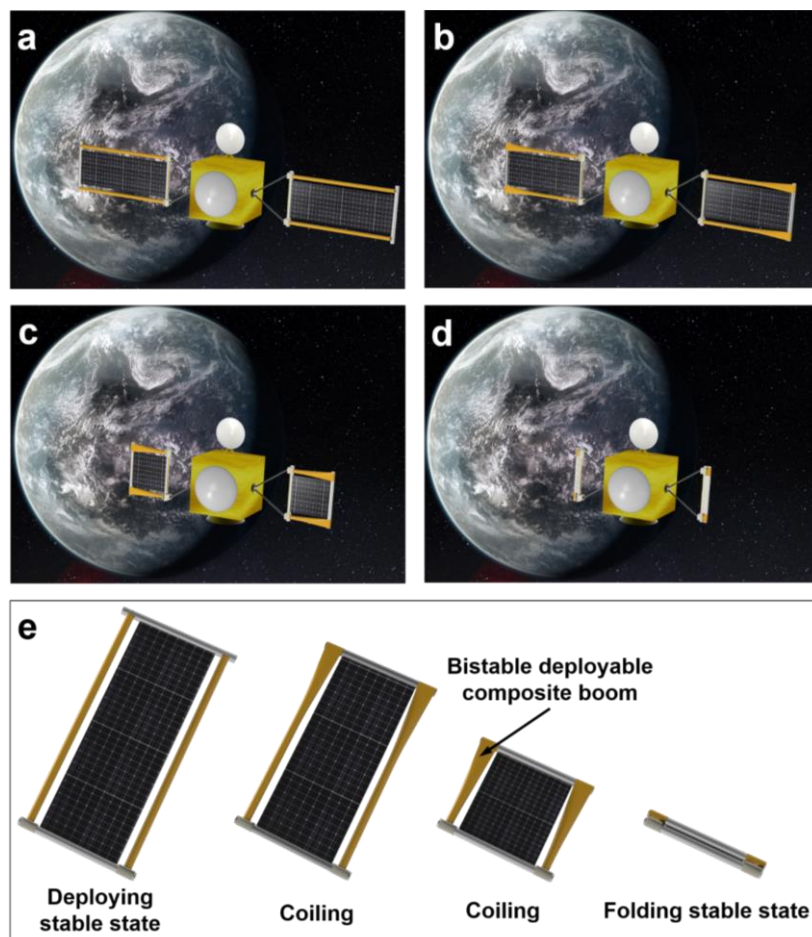


Fig. 1 - Schematic diagrams of typical application and folding deformation process (a) Deploying stable state of the deployable solar array; (b) Coiling process of the deployable solar array; (c) Coiling process of the deployable solar array; (d) Folding stable state of the deployable solar array; (e) Bistable deformation processes of the deployable solar array and the Bi-DCB.

## 2. GEOMETRICAL MODEL

The Bi-DCB can realize the conversion between the deploying stable state and the folding stable state by storing and releasing elastic strain energy, as shown in Fig. 2a. The curvature directions corresponding to the two stable states of the Bi-DCB are on the same side. A stable state is the initial deploying state, which has good bearing capacity; the other stable state is the folding state, where the Bi-DCB is closely and stably coiled together. The geometrical configuration of the Bi-DCB in the deploying stable state is determined by the length  $L$ , thickness  $t$ , radius  $R$  and central angle  $\theta$ , as shown in Fig. 2b. The central line of the longitudinal section of the Bi-DCB in the folding stable state is Archimedes helix, and any two circles are closely attached, as shown in Fig. 2c. The thickness change of the Bi-DCB shell is negligibly small in the bistable deformation process, so the overall deformation can be described with the changes of shape and curvature of the neutral surface without local extension. The curvature in the  $y$  direction of the Bi-DCB is uniform in the bistable deformation process, and the curvature in the  $y$  direction is zero in the folding stable state.

According to assumption (1) and Fig. 2c, the geometric configuration of the cross-section of the Bi-DCB in the folding stable state can be described by the multinomial shape function in a polar coordinate system of  $(\rho, \alpha)$ , that is

$$\rho = a\alpha + b, \quad (\alpha \in [\alpha_0, \alpha_1]) \quad (1)$$

where  $a$  controls the distance between two adjacent circles,  $b$  is the distance from the start-point to the origin of the polar coordinate system, and  $\alpha_0$  and  $\alpha_1$  are the polar angles at the start-point and the end-point of the Bi-DCB in the folding stable state, respectively.

According to assumption (1), when the Bi-DCB is in the folding stable state, any two circles are closely attached. It is possible to have

$$a = \frac{t}{2\pi} \quad (2)$$

According to geometric relationship, Eq. (1) should satisfy geometrical boundary condition as [15]

$$\begin{cases} a\alpha_0 + b = r_0 \\ a\alpha_1 + b = r_1 \end{cases} \quad (3)$$

where  $r_0$  and  $r_1$  are the polar radii at the start-point and the end-point of the Bi-DCB in the folding stable state, respectively.

Generally,  $\alpha_0$  is zero, (i.e.,  $\alpha_0 = 0$ ), then Eq. (3) can be written as

$$\begin{cases} b = r_0 \\ \alpha_1 = \frac{r_1 - r_0}{a} \end{cases} \quad (4)$$

Substituting Eq. (2) into Eq. (4), it is possible to obtain as



$$\begin{cases} b = r_0 \\ \alpha_1 = \frac{2\pi(r_1 - r_0)}{t} \end{cases} \quad (5)$$

According to assumption (2), it is possible to obtain as

$$\int_{\alpha_0}^{\alpha_1} \sqrt{\rho^2 + (\rho')^2} d\alpha = L \quad (6)$$

where  $L$  is the length of the Bi-DCB.

Substituting Eqs. (1) to (5) into Eq. (6) and integrating shows

$$\frac{t}{2\pi} \left[ \frac{\pi r_1}{t} \sqrt{\left(\frac{2\pi r_1}{t}\right)^2 + 1} + \frac{1}{2} \ln \left( \frac{\pi r_1}{t} + \sqrt{\left(\frac{2\pi r_1}{t}\right)^2 + 1} \right) \right] - \frac{t}{2\pi} \left[ \frac{\pi r_0}{t} \sqrt{\left(\frac{2\pi r_0}{t}\right)^2 + 1} + \frac{1}{2} \ln \left( \frac{\pi r_0}{t} + \sqrt{\left(\frac{2\pi r_0}{t}\right)^2 + 1} \right) \right] = L \quad (7)$$

Obviously, Eq. (7) is an implicit function, and the quantitative relationship between  $r_0$  and  $r_1$  can be determined by Newton iterative method. According to the definition of curvature, the curvature of the Bi-DCB in the  $x$  direction (i.e., length direction) can be deduced as

$$\kappa_x = \frac{2(\rho')^2 + \rho^2}{[(\rho')^2 + \rho^2]^{\frac{3}{2}}} = \frac{\frac{t^2}{2\pi^2} + \rho^2}{\left(\frac{t^2}{4\pi^2} + \rho^2\right)^{\frac{3}{2}}}, \quad \alpha \in \left[0, \frac{2\pi(r_1 - r_0)}{t}\right] \quad (8)$$

### 3. ANALYTICAL MODEL FOR BISTABLE BEHAVIOUR

The energy method is used to determine the geometric configuration of the Bi-DCB in the folding stable state. To establish the strain energy of the Bi-DCB in the folding stable state, the bistable deformation process is divided into two stages, as shown in Fig. 2d. Firstly, a bending moment  $M_y$  is applied at the edge to change the curvature in the  $y$  direction of the Bi-DCB from  $1/R$  to 0. In the first stage, the external work is converted into bending strain energy. Then, a bending moment  $M_x$  is applied at the edge to change the curvature in the  $x$  direction of the Bi-DCB from 0 to  $\kappa_x$ . Similarly, the external work is converted into bending strain energy in the second stage.

Utilizing an ABD matrix of the classical laminate theory, the relationship between internal forces and deformation of the Bi-DCB with antisymmetric layup in bistable deformation process can be expressed as

$$\begin{bmatrix} N_x \\ N_y \\ N_{xy} \\ M_x \\ M_y \\ M_{xy} \end{bmatrix} = \begin{bmatrix} A_{11} & A_{12} & 0 & 0 & 0 & B_{16} \\ A_{12} & A_{22} & 0 & 0 & 0 & B_{26} \\ 0 & 0 & A_{66} & B_{16} & B_{26} & 0 \\ 0 & 0 & B_{16} & D_{11} & D_{12} & 0 \\ 0 & 0 & B_{26} & D_{12} & D_{22} & 0 \\ B_{16} & B_{26} & 0 & 0 & 0 & D_{66} \end{bmatrix} \begin{bmatrix} \Delta \varepsilon_x \\ \Delta \varepsilon_y \\ \Delta \gamma_{xy} \\ \Delta \kappa_x \\ \Delta \kappa_y \\ \Delta \kappa_{xy} \end{bmatrix} \quad (9)$$

where

$$\begin{cases} N_x = 0 \\ N_y = 0 \\ N_{xy} = 0 \\ M_{xy} = 0 \\ \Delta\kappa_{xy} = 0 \end{cases} \quad (10)$$

Mansfield deduced the bending strain energy per unit area in the mid-surface of a laminated plate [16], as follows:

$$u = \frac{1}{2}(M_x \Delta\kappa_x + M_y \Delta\kappa_y + M_{xy} \Delta\kappa_{xy}) \quad (11)$$

where

$$\begin{cases} \Delta\kappa_x = \kappa_x \\ \Delta\kappa_y = \kappa_y - \frac{1}{R} \end{cases} \quad (12)$$

Substituting Eqs. (9), (10) and (12) into Eq. (11), it is possible to deduce as

$$u = \frac{1}{2}\kappa_x \left[ B_{16}\gamma_{xy} + D_{11}\kappa_x + D_{12}\left(\kappa_y - \frac{1}{R}\right) \right] + \frac{1}{2}\left(\kappa_y - \frac{1}{R}\right) \left[ B_{26}\gamma_{xy} + D_{12}\kappa_x + D_{22}\left(\kappa_y - \frac{1}{R}\right) \right] \quad (13)$$

Substituting Eq. (10) into Eq. (9) and solving Eq. (9), it is possible to determine as

$$\gamma_{xy} = B_{61}^*\kappa_x + B_{62}^*\kappa_y \quad (14)$$

where

$$B^* = -A^{-1}B \quad (15)$$

According to assumption (3),  $u$  is uniform. Substituting Eqs. (14) and (15) into Eq. (13), the expression of the strain energy for a unit longitudinal length of Bi-DCB in the folding stable state is given as

$$U = \frac{R\theta}{2} \left[ (D_{11} + B_{16}B_{61}^*)\kappa_x^2 + (2D_{12} + B_{16}B_{62}^* + B_{26}B_{61}^*)\left(\kappa_y - \frac{1}{R}\right)\kappa_x + (D_{22} + B_{26}B_{62}^*)\left(\kappa_y - \frac{1}{R}\right)^2 \right] \quad (16)$$

where  $R$  and  $\theta$  are the radius and central angle of the cross-section of the Bi-DCB, respectively.

According to assumption (3), when the Bi-DCB is in the folding stable state, the curvature in the  $y$  direction is 0 (i.e.,  $\kappa_y = 0$ ). Eq. (16) can be simplified to

$$U = \frac{R\theta}{2} \left[ (D_{11} + B_{16}B_{61}^*)\kappa_x^2 - (2D_{12} + B_{16}B_{62}^* + B_{26}B_{61}^*)\frac{\kappa_x}{R} + (D_{22} + B_{26}B_{62}^*)\frac{1}{R^2} \right] \quad (17)$$

Therefore, the total strain energy of the Bi-DCB in the folding stable state can be expressed as

$$\Pi = \int_{\alpha_0}^{\alpha_1} U(\alpha) \rho(\alpha) d\alpha \quad (18)$$

Substituting Eqs. (8) and (17) into Eq. (18), it is possible to obtain as

$$\Pi = \frac{R\theta}{2} \int_0^{\frac{2\pi(r_1-r_0)}{t}} \left\{ \begin{aligned} & (D_{11} + B_{16}B_{61}^*) \frac{\left[ \frac{t^2}{2\pi^2} + \left( \frac{t\alpha}{2\pi} + r_0 \right)^2 \right]^2}{\left[ \frac{t^2}{4\pi^2} + \left( \frac{t\alpha}{2\pi} + r_0 \right)^2 \right]^3} + (D_{22} + B_{26}B_{62}^*) \frac{1}{R^2} \\ & - (2D_{12} + B_{16}B_{62}^* + B_{26}B_{61}^*) \frac{\frac{t^2}{2\pi^2} + \left( \frac{t\alpha}{2\pi} + r_0 \right)^2}{R \left[ \frac{t^2}{4\pi^2} + \left( \frac{t\alpha}{2\pi} + r_0 \right)^2 \right]^{\frac{3}{2}}} \end{aligned} \right\} \left( \frac{t\alpha}{2\pi} + r_0 \right) d\alpha \quad (19)$$

$\alpha$  in Eq. (19) is represented by  $\rho$ , and Eq. (19) can be simplified as

$$\Pi = \frac{\pi R\theta}{t} \int_{r_0}^{r_1} \left\{ \begin{aligned} & (D_{11} + B_{16}B_{61}^*) \frac{\left( \frac{t^2}{2\pi^2} + \rho^2 \right)^2}{\left( \frac{t^2}{4\pi^2} + \rho^2 \right)^3} + (D_{22} + B_{26}B_{62}^*) \frac{1}{R^2} \\ & - (2D_{12} + B_{16}B_{62}^* + B_{26}B_{61}^*) \frac{\frac{t^2}{2\pi^2} + \rho^2}{R \left( \frac{t^2}{4\pi^2} + \rho^2 \right)^{\frac{3}{2}}} \end{aligned} \right\} \rho d\rho \quad (20)$$

It is known that the folding stable state of the Bi-DCB corresponds to an energy minimum. Therefore, the minimum energy principle can be used for Eq. (20). It is possible to have

$$\frac{d\Pi}{dr_0} = r_1 H_1 \frac{dr_1}{dr_0} - r_0 H_2 = 0 \quad (21)$$

where  $H_1$  and  $H_2$  are transformation variables.

$$H_1 = \frac{\pi R\theta}{t} \left\{ \begin{aligned} & (D_{11} + B_{16}B_{61}^*) \frac{\left( \frac{t^2}{2\pi^2} + r_1^2 \right)^2}{\left( \frac{t^2}{4\pi^2} + r_1^2 \right)^3} + (D_{22} + B_{26}B_{62}^*) \frac{1}{R^2} \\ & - (2D_{12} + B_{16}B_{62}^* + B_{26}B_{61}^*) \frac{\frac{t^2}{2\pi^2} + r_1^2}{R \left( \frac{t^2}{4\pi^2} + r_1^2 \right)^{\frac{3}{2}}} \end{aligned} \right\} \quad (22)$$

$$H_2 = \frac{\pi R \theta}{t} \left[ \begin{array}{l} (D_{11} + B_{16} B_{61}^*) \frac{(\frac{t^2}{4\pi^2} + r_0^2)^2}{2\pi^2} + (D_{22} + B_{26} B_{62}^*) \frac{1}{R^2} \\ -(2D_{12} + B_{16} B_{62}^* + B_{26} B_{61}^*) \frac{\frac{t^2}{2\pi^2} + r_0^2}{R(\frac{t^2}{4\pi^2} + r_0^2)^{\frac{3}{2}}} \end{array} \right] \quad (23)$$

It should be noted that there is a differential term  $\frac{dr_1}{dr_0}$  in Eq. (21), and the central difference algorithm is used to achieve numerical differentiation.

Obviously, Eqs. (7) and (21) contain only two unknown variables, namely  $r_0$  and  $r_1$ . The two unknown variables can be obtained by combining Eqs. (7) and (21) and solving them numerically. Substituting the obtained  $r_0$  and  $r_1$  into Eq. (5), it is possible to obtain the polar angle  $\alpha_1$ .

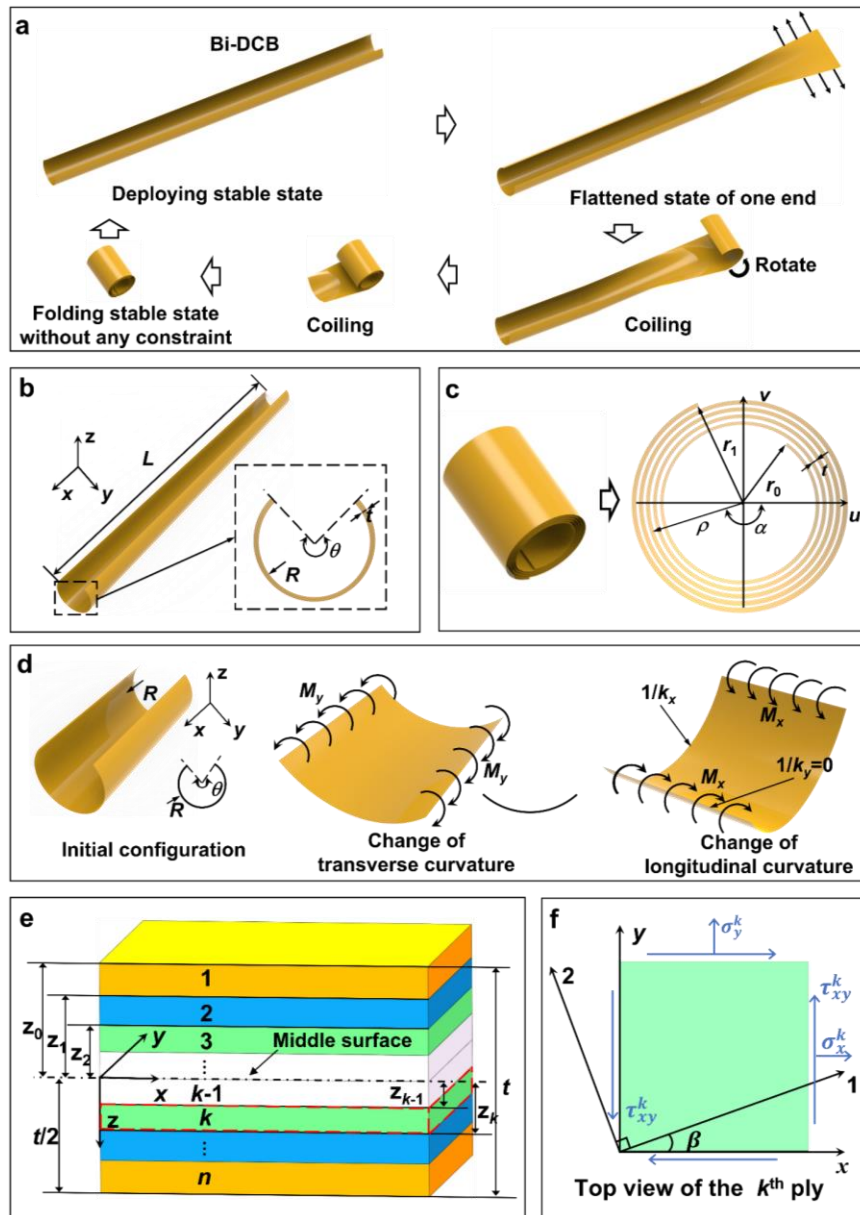


Fig. 2 - Analytical model for the Bi-DCB (a) Bistable deformation process; (b) Deploying stable state; (c) Folding stable state; (d) Force analysis and deformation; (e) Schematic diagram of the laminate ply; (f) Stress analysis.

#### 4. STRESS ANALYSIS

According to assumption (1), the Bi-DCB has the maximum strain and stress in the  $x$  direction at the start-point when it is in the folding stable state. The maximum value of the change of curvature in the  $x$  direction is

$$\Delta\kappa_x|_{\alpha=0} = \frac{\frac{t^2}{2\pi^2} + r_0^2}{\left(\frac{t^2}{4\pi^2} + r_0^2\right)^{\frac{3}{2}}} \quad (24)$$

The maximum value of the change of curvature in the y direction is

$$\Delta\kappa_y \Big|_{\alpha=0} = -\frac{1}{R} \quad (25)$$

Fig. 2e is the schematic diagram of a laminate. The stress-strain relationship of the  $k^{\text{th}}$  ply ( $k=1, 2, 3, \dots, n$ ) at the dangerous point is

$$\begin{bmatrix} \sigma_x \\ \sigma_y \\ \tau_{xy} \end{bmatrix}_k = \begin{bmatrix} \bar{Q}_{11} & \bar{Q}_{12} & \bar{Q}_{16} \\ \bar{Q}_{12} & \bar{Q}_{22} & \bar{Q}_{26} \\ \bar{Q}_{16} & \bar{Q}_{26} & \bar{Q}_{66} \end{bmatrix}_k \begin{bmatrix} z\Delta\kappa_x \\ z\Delta\kappa_y \\ z\Delta\kappa_{xy} \end{bmatrix} \quad (26)$$

Substituting Eqs. (24) and (25) into Eq. (26), it is possible to determine as

$$\sigma_x^k = z\bar{Q}_{11}^k\Delta\kappa_x + z\bar{Q}_{12}^k\Delta\kappa_y \quad (27)$$

$$\sigma_y^k = z\bar{Q}_{12}^k\Delta\kappa_x + z\bar{Q}_{22}^k\Delta\kappa_y \quad (28)$$

$$\tau_{xy}^k = z\bar{Q}_{16}^k\Delta\kappa_x + z\bar{Q}_{26}^k\Delta\kappa_y \quad (29)$$

According to the coordinate transformation equation of stress components of the  $k^{\text{th}}$  ply in the laminate (shown in Fig. 2f), the maximum principal stresses of the  $k^{\text{th}}$  ply in the laminate can be expressed as

$$\begin{bmatrix} \sigma_1 \\ \sigma_2 \\ \tau_{12} \end{bmatrix}_k = \begin{bmatrix} \cos^2 \beta & \sin^2 \beta & 2\sin \beta \cos \beta \\ \sin^2 \beta & \cos^2 \beta & -2\sin \beta \cos \beta \\ -\sin \beta \cos \beta & \sin \beta \cos \beta & \cos^2 \beta - \sin^2 \beta \end{bmatrix}_k \begin{bmatrix} \sigma_x \\ \sigma_y \\ \tau_{xy} \end{bmatrix}_k \quad (30)$$

Substituting Eqs. (27) to (29) into Eq. (30), it is possible to deduce as

$$\begin{aligned} \sigma_1^k &= z\cos^2 \beta(\bar{Q}_{11}^k\Delta\kappa_x + \bar{Q}_{12}^k\Delta\kappa_y) + z\sin^2 \beta(\bar{Q}_{12}^k\Delta\kappa_x + \bar{Q}_{22}^k\Delta\kappa_y) \\ &\quad + 2z\sin \beta \cos \beta(\bar{Q}_{16}^k\Delta\kappa_x + \bar{Q}_{26}^k\Delta\kappa_y) \end{aligned} \quad (31)$$

$$\begin{aligned} \sigma_2^k &= \sin^2 \beta(\bar{Q}_{11}^k\Delta\kappa_x + \bar{Q}_{12}^k\Delta\kappa_y) + \cos^2 \beta(\bar{Q}_{12}^k\Delta\kappa_x + \bar{Q}_{22}^k\Delta\kappa_y) \\ &\quad - 2\sin \beta \cos \beta(\bar{Q}_{16}^k\Delta\kappa_x + \bar{Q}_{26}^k\Delta\kappa_y) \end{aligned} \quad (32)$$

$$\begin{aligned} \tau_{12}^k &= -z\sin \beta \cos \beta(\bar{Q}_{11}^k\Delta\kappa_x + \bar{Q}_{12}^k\Delta\kappa_y) + z\sin \beta \cos \beta(\bar{Q}_{12}^k\Delta\kappa_x + \bar{Q}_{22}^k\Delta\kappa_y) \\ &\quad + z(\cos^2 \beta - \sin^2 \beta)(\bar{Q}_{16}^k\Delta\kappa_x + \bar{Q}_{26}^k\Delta\kappa_y) \end{aligned} \quad (33)$$

The failure criteria of laminate can be divided into limit theories and interaction theories. In limit theories, such as the maximum stress criterion, the local stress components are compared with their

corresponding strength, while the interaction between components is ignored. In interaction theories, such as Tsai-Hill criterion, the interaction between stress components is considered, and the contribution of each component to the total strain energy within structures is usually considered. Based on the above two failure criteria, the failure index is calculated to analyze the stress level of the Bi-DCB in the folding stable state. When the failure index reaches or exceeds 1, the Bi-DCB fails; otherwise, it does not fail.

The Tsai-Hill failure index  $I_{f,1}$  can be calculated as

$$I_{f,1}^2 = \frac{(\sigma_1^k)^2}{X_1^2} - \frac{\sigma_1^k \sigma_2^k}{X_2^2} + \frac{(\sigma_2^k)^2}{Y^2} + \frac{(\tau_{12}^k)^2}{S_{12}^2} \quad (34)$$

where

$$X_1 = \begin{cases} X_t & \text{if } \sigma_1^k > 0 \\ X_c & \text{if } \sigma_1^k < 0 \end{cases} \quad (35)$$

$$X_2 = \begin{cases} X_t & \text{if } \sigma_2^k > 0 \\ X_c & \text{if } \sigma_2^k < 0 \end{cases} \quad (36)$$

$$Y = \begin{cases} Y_t & \text{if } \sigma_2^k > 0 \\ Y_c & \text{if } \sigma_2^k < 0 \end{cases} \quad (37)$$

where  $\sigma_1^k$  and  $\sigma_2^k$  are the stresses of the  $k^{\text{th}}$  ply in longitudinal and transverse direction respectively,  $\tau_{12}^k$  is the shear stress of the  $k^{\text{th}}$  ply in longitudinal and transverse direction,  $X_1$  and  $X_2$  are the longitudinal strength of composite ply,  $X_t$  and  $X_c$  are longitudinal tensile and compressive strength of composite ply,  $Y$  is the transverse strength of composite ply,  $Y_t$  and  $Y_c$  are transverse tensile and compressive strength of composite ply, and  $S_{12}$  is the in-plane shear strength of composite ply.

The maximum stress failure index  $I_{f,2}$  can be calculated as

$$I_{f,2} = \max \left\{ \left| \frac{\sigma_1^k}{X_1} \right|, \left| \frac{\sigma_2^k}{Y} \right|, \left| \frac{\tau_{12}^k}{S_{12}} \right| \right\} \quad (38)$$

## 5. ANALYTICAL MODEL VALIDATION

Based on the analytical model for predicting the bistable behaviour of the Bi-DCB established in Sections 2 to 4, the solution procedure was designed with MATLAB software. To validate the analytical model proposed in this research, the prediction results are compared with experimental results and FEM results in literature [17]. A total of six Bi-DCB specimens were prepared. Table 1 lists basic properties of T700/epoxy ply, and Table 2 lists geometric parameters and stacking sequence of six Bi-DCB specimens. Fig. 3 shows total strain energy versus start-point polar radius curves of the six Bi-DCBs. It is shown that the bistable behaviour of the Bi-DCB is related to the existence of the local minimum of total strain energy.

Fig. 6 illustrates the geometric configuration of the Bi-DCB in the folding stable state determined by experiments, two FEMs and analytical model, and the four are in good agreement. Archimedes helix was used to linearly fit the data points of the cross-section of the folding stable state determined by experiments, two FEMs and analytical model. The fitted Archimedes helix is shown in Fig. 5, and the polar radii  $r_0$  and  $r_1$  at the start-point and the end-point as well as the polar angle  $\alpha_1$  of

Archimedes helix are listed in Table 3. It is clear that the geometric configuration of the folding stable state, the polar radii  $r_0$  and  $r_1$  at the start-point and the end-point as well as the polar angle  $\alpha_1$  of Archimedes helix are in good agreement. For the six Bi-DCBs, the maximum errors between the polar radii  $r_0$  and  $r_1$  at the start-point and the end-point as well as the polar angle  $\alpha_1$  of Archimedes helix predicted by the analytical model and experiments are 9.42%, 8.82% and 10.08% respectively; the maximum errors between the polar radii at the start-point and the end-point as well as the polar angle of Archimedes helix predicted by the analytical model and the FEM 1 results are 7.21%, 7.67% and 6.93% respectively; the maximum errors between the polar radii at the start-point and the end-point as well as the polar angle of Archimedes helix predicted by the analytical model and the FEM 2 results are 6.85%, 7.48% and 6.69% respectively.

The two failure criteria in Section 4 (namely, Tsai-Hill criterion and maximum stress criterion) are applied to calculate the maximum failure index of each layer of six Bi-DCBs in the folding stable state, and the maximum failure indices are listed in Fig. 6 and Table 4. According to Fig. 6 and Table 4, among all the failure indices, the maximum values of FEM 1 and FEM 2 are 0.3694 and 0.3705 respectively, and the maximum value of the analytical model is 0.3445. It means that the six Bi-DCBs can realize the bistable function without failure, which is consistent with experimental results. In conclusion, the analytical model proposed in this research shows good prediction accuracy for evaluating the bistable behaviour of the Bi-DCB, which proves the validity of the analytical model.

For the six Bi-DCBs, the polar radii at the start-point and the end-point of Archimedes helix predicted by the analytical model are higher than experimental results, while the polar angles of Archimedes helix predicted by the analytical model are lower than experimental results. There are three possible reasons for the difference between prediction results of the analytical model and experimental results: (1) In the analytical model, it is assumed that the transverse curvature is uniformly distributed; (2) The epoxy matrix material has nonlinear behavior, because the epoxy matrix material will be viscoelastic when it involves high strain changes. However, it is assumed that the epoxy matrix material is always linear-elastic in the analytical model; (3) Another reason is that residual thermal stress will inevitably occur in the composite monolayer during the manufacturing process of the Bi-DCB specimen. Quantitatively research on the above three reasons will be carried out in the future.

Table 1 Specifications and properties of T700/epoxy composite ply [17].

Specifications and properties	Values
Longitudinal elastic modulus $E_1$ (GPa)	128.61
Transverse elastic modulus $E_2$ (GPa)	7.52
In-plane shear modulus $G_{12}$ (GPa)	4.82
Inter-laminar shear modulus $G_{13}$ (GPa)	4.50
Inter-laminar shear modulus $G_{23}$ (GPa)	4.50
Poisson's ratio $\nu_{12}$	0.314
Poisson's ratio $\nu_{21}$	0.018
Longitudinal tensile strength $X_t$ (MPa)	2103.44
Transverse tensile strength $Y_t$ (MPa)	75.97
Longitudinal compressive strength $X_c$ (MPa)	1233.65
Transverse compressive strength $Y_c$ (MPa)	181.46
In-plane shear strength $S_{12}$ (MPa)	216.36
Density ( $\text{g}/\text{mm}^3$ )	$1.60 \times 10^{-3}$
Ply thickness (mm)	0.03



Table 2 Specifications of the six Bi-DCB specimens.

No.	Radius (mm)	Arc length (mm)	Center angle (deg)	Length (mm)	Stacking Configuration
1	20	80	229	620	[45/-45/45/-45/45/90/-45/45/-45/45/-45]
2	20	80	229	400	[45/-45/45/-45/0/45/-45/45/-45]
3	20	80	229	200	[45/-45/45/-45/90/45/-45/45/-45]
4	27.5	80	167	650	[45/-45/45/-45/0/90/45/-45/45/-45]
5	27.5	80	167	650	[45/-45/45/-45/45/-45/45/-45/45/-45]
6	30	100	191	620	[45/-45/45/-45/45/90/-45/45/-45/45/-45]

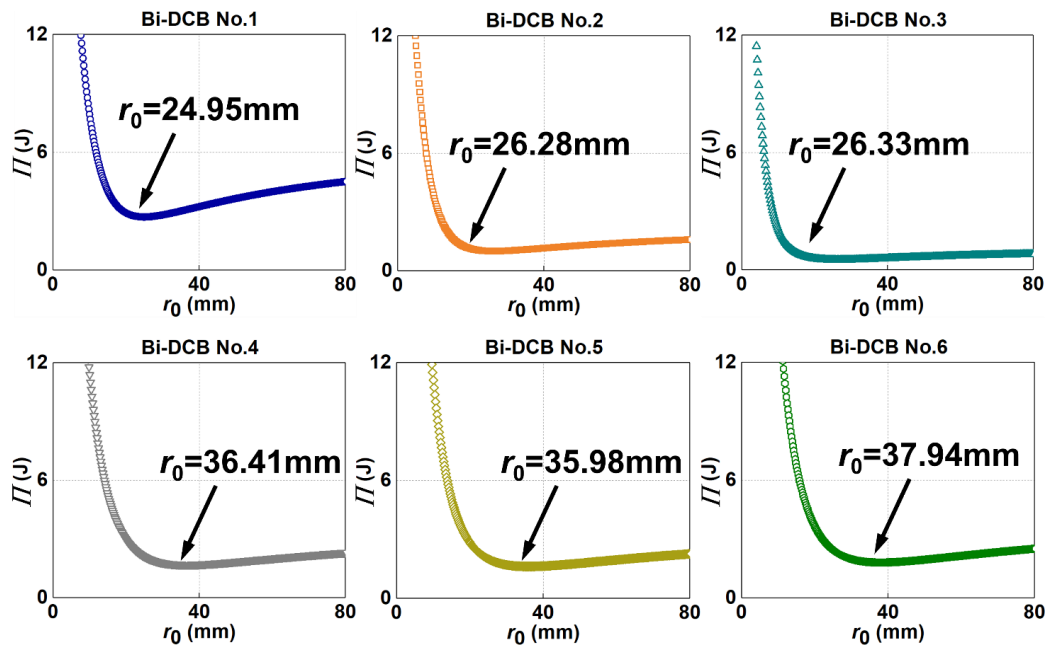


Fig. 3 - Total strain energy versus polar radius at the start-point curves of six Bi-DCBs.


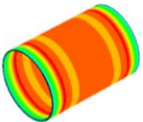
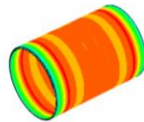

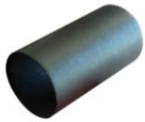

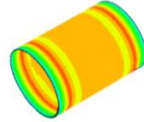

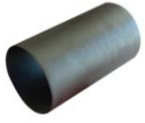
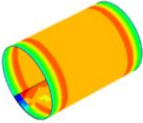
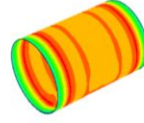

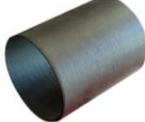
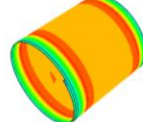


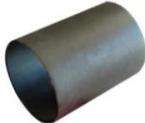
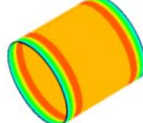
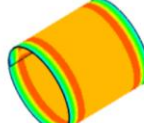

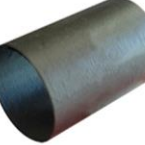
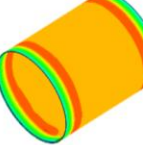
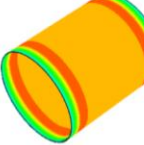

No.	Experiment	FEM 1	FEM 2	Analytical model
1		 <p>Tsai-Hill            +3.69e-01            +3.55e-01            +3.41e-01            +3.26e-01            +3.12e-01            +2.98e-01            +2.83e-01            +2.69e-01            +2.55e-01            +2.40e-01            +2.26e-01            +2.12e-01            +1.97e-01</p>	 <p>Tsai-Hill            +3.70e-01            +3.55e-01            +3.41e-01            +3.26e-01            +3.12e-01            +2.98e-01            +2.83e-01            +2.69e-01            +2.55e-01            +2.40e-01            +2.26e-01            +1.97e-01</p>	
2		 <p>Tsai-Hill            +2.98e-01            +2.86e-01            +2.74e-01            +2.63e-01            +2.51e-01            +2.39e-01            +2.27e-01            +2.15e-01            +2.04e-01            +1.92e-01            +1.80e-01            +1.68e-01            +1.56e-01</p>	 <p>Tsai-Hill            +2.77e-01            +2.67e-01            +2.56e-01            +2.46e-01            +2.36e-01            +2.25e-01            +2.15e-01            +2.05e-01            +1.95e-01            +1.84e-01            +1.74e-01            +1.64e-01            +1.53e-01</p>	
3		 <p>Tsai-Hill            +3.08e-01            +2.96e-01            +2.84e-01            +2.72e-01            +2.60e-01            +2.48e-01            +2.36e-01            +2.24e-01            +2.12e-01            +2.00e-01            +1.88e-01            +1.76e-01            +1.65e-01</p>	 <p>Tsai-Hill            +3.02e-01            +2.91e-01            +2.79e-01            +2.68e-01            +2.57e-01            +2.45e-01            +2.34e-01            +2.23e-01            +2.11e-01            +1.99e-01            +1.88e-01            +1.76e-01            +1.65e-01</p>	
4		 <p>Tsai-Hill            +2.27e-01            +2.17e-01            +2.06e-01            +1.95e-01            +1.90e-01            +1.80e-01            +1.71e-01            +1.62e-01            +1.52e-01            +1.43e-01            +1.34e-01            +1.25e-01            +1.15e-01</p>	 <p>Tsai-Hill            +2.27e-01            +2.18e-01            +2.08e-01            +1.98e-01            +1.90e-01            +1.80e-01            +1.71e-01            +1.62e-01            +1.53e-01            +1.43e-01            +1.34e-01            +1.25e-01            +1.15e-01</p>	
5		 <p>Tsai-Hill            +2.51e-01            +2.40e-01            +2.30e-01            +2.19e-01            +2.09e-01            +1.98e-01            +1.88e-01            +1.77e-01            +1.67e-01            +1.57e-01            +1.46e-01            +1.36e-01            +1.25e-01</p>	 <p>Tsai-Hill            +2.51e-01            +2.40e-01            +2.30e-01            +2.19e-01            +2.09e-01            +1.98e-01            +1.88e-01            +1.77e-01            +1.67e-01            +1.56e-01            +1.45e-01            +1.35e-01            +1.24e-01</p>	
6		 <p>Tsai-Hill            +2.52e-01            +2.41e-01            +2.30e-01            +2.19e-01            +2.08e-01            +1.97e-01            +1.86e-01            +1.75e-01            +1.64e-01            +1.53e-01            +1.42e-01            +1.31e-01            +1.20e-01</p>	 <p>Tsai-Hill            +2.51e-01            +2.40e-01            +2.29e-01            +2.19e-01            +2.08e-01            +1.97e-01            +1.86e-01            +1.75e-01            +1.65e-01            +1.54e-01            +1.43e-01            +1.32e-01            +1.22e-01</p>	

Fig. 4 - Geometric configuration of six Bi-DCBs in the folding stable state.

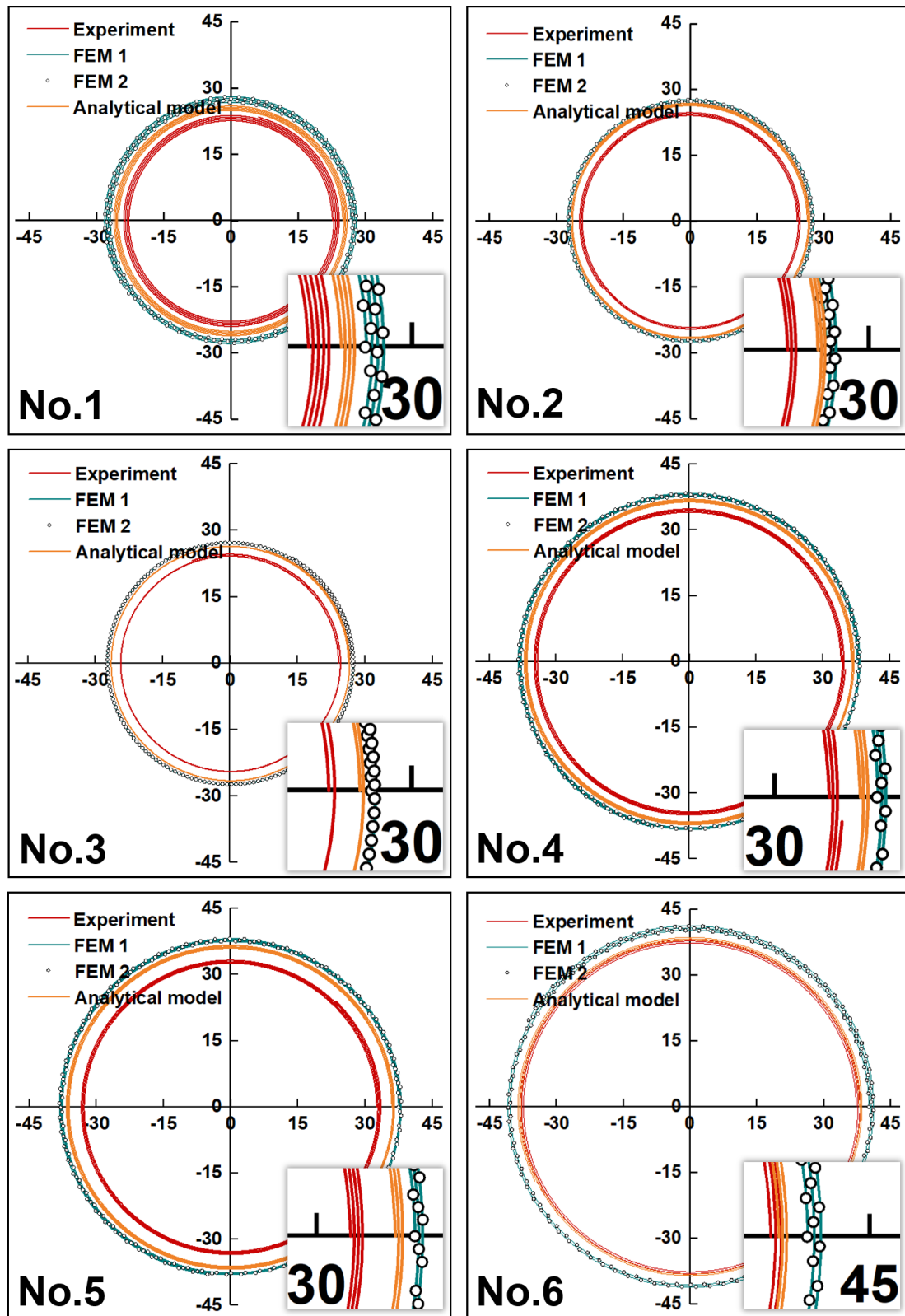


Fig. 5 - Geometric configuration of the cross-section of six Bi-DCBs in the folding stable state.

Table 3 Polar radii at the start-point and the end-point as well as polar angle of six Bi-DCBs in the folding stable state.

Geometrical parameter		No.1	No.2	No.3	No.4	No.5	No.6		
$r_0$ (mm)	Analytical model	24.95	26.28	26.33	36.41	35.98	37.94		
	Experiment	Value	22.63	24.04	24.13	34.08	32.59	37.31	
		Error	9.30%	8.52%	8.36%	6.40%	9.42%	1.66%	
	FEM 1	Value	26.75	26.89	27.16	37.75	37.49	40.21	
		Error	7.21%	2.32%	3.15%	3.68%	4.20%	5.98%	
	FEM 2	Value	26.66	26.85	27.15	37.68	37.47	40.15	
		Error	6.85%	2.17%	3.11%	3.49%	4.14%	5.82%	
	$r_1$ (mm)	Analytical model	26.22	26.93	26.65	37.25	36.83	38.79	
		Experiment	Value	24.23	24.87	24.66	35.08	33.58	38.41
			Error	7.59%	7.65%	7.47%	5.82%	8.82%	0.98%
FEM 1		Value	28.23	27.75	27.52	38.57	38.32	41.47	
		Error	7.67%	3.04%	3.26%	3.54%	4.04%	6.91%	
FEM 2		Value	28.18	27.67	27.44	38.55	38.31	41.35	
		Error	7.48%	2.75%	2.94%	3.49%	4.02%	6.60%	
$\alpha_1$ (rad)		Analytical model	24.23	15.04	7.55	17.65	17.85	16.16	
		Experiment	Value	26.46	16.36	8.20	18.80	19.65	16.38
			Error	9.20%	8.78%	8.61%	6.52%	10.08%	1.36%
	FEM 1	Value	22.55	14.64	7.32	17.03	17.15	15.07	
		Error	6.93%	2.66%	3.05%	3.51%	3.92%	6.75%	
	FEM 2	Value	22.61	14.67	7.33	17.05	17.15	15.11	
		Error	6.69%	2.46%	2.91%	3.40%	3.92%	6.50%	

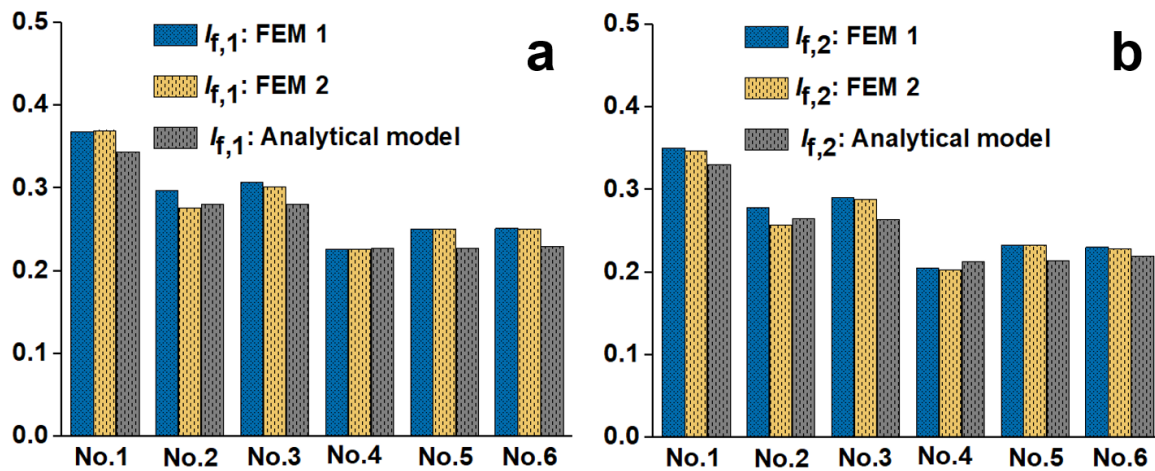


Fig. 6 - Comparison of the failure indices of six Bi-DCBs in the folding stable state (a) Tsai-Hill failure index; (b) Maximum stress failure index.

Table 4 Failure indices of six Bi-DCBs in the folding stable state.

Failure index		No.1	No.2	No.3	No.4	No.5	No.6	
$I_{f,1}$	Analytical model	0.3445	0.2810	0.2810	0.2270	0.2271	0.2294	
	FEM 1	Value	0.3694	0.2981	0.3079	0.2266	0.2505	0.2520
		Error	7.23%	6.09%	9.57%	0.18%	10.30%	9.85%
	FEM 2	Value	0.3705	0.2769	0.3024	0.2270	0.2509	0.2509
		Error	7.55%	1.46%	7.62%	0%	10.48%	9.37%
	$I_{f,2}$	Analytical model	0.3311	0.2648	0.2646	0.2133	0.2144	0.2194
FEM 1		Value	0.3514	0.2786	0.2907	0.2058	0.2333	0.2304
		Error	6.13%	5.21%	9.86%	3.52%	8.81%	5.01%
FEM 2		Value	0.3477	0.2577	0.2880	0.2034	0.2328	0.2284
		Error	5.01%	2.68%	8.84%	4.64%	8.58%	4.10%

## 6. PARAMETRIC STUDY

According to the analytical model, it is known that geometric parameters of the Bi-DCB in deploying stable state can significantly affect the bistable behaviour of the Bi-DCB, such as the radius of the cross-section, thickness and length. According to Fig. 6 and Table 3, the analytical model proposed in this paper and the two FEMs can accurately predict the bistable behaviour of the Bi-DCB, but compared with the two FEMs, the analytical model can save a lot of time. Therefore, the analytical model is used to explore the effect of the radius of the cross-section, thickness and length on the bistable behaviour of the Bi-DCB. The material properties and remaining geometric parameters are consistent with the Bi-DCB No.4.

### 6.1 EFFECT OF RADIUS OF CROSS-SECTION ON THE BISTABLE BEHAVIOUR

The analytical model proposed in this research is applied to predict the effect of the radius of the cross-section on the bistable behaviour of the Bi-DCB, as shown in Figs. 7a to 7c. It is clear from Figs. 7a to 7c that the local minimum of total strain energy exists in the Bi-DCBs with different radii of the cross-section. With the increase of the radius of the cross-section, the polar radii  $r_0$  and  $r_1$  at the start-point and the end-point of Archimedes helix increase, while the polar angle  $\alpha_1$  of Archimedes helix decreases. In addition, the failure indices of the Bi-DCBs with different radii of the cross-section do not reach 1 when they are in the folding stable state, indicating that the Bi-DCBs can achieve the bistable function without failure. With the increase of the radius of the cross-section, the Tsai-Hill failure index and the maximum stress failure index decrease significantly. The reason is that the change of curvature in the  $y$  direction in Eq. (25) decreases, resulting in the decrease of the Tsai-Hill failure index and the maximum stress failure index.

### 6.2 EFFECT OF THICKNESS ON THE BISTABLE BEHAVIOUR

The analytical model proposed in this research is applied to predict the effect of the thickness on the bistable behaviour of the Bi-DCB, as shown in Figs. 7d to 7f. It is clear from Figs. 7d to 7f that the local minimum of total strain energy exists in the Bi-DCBs with different thicknesses. With the increase of the thickness, the polar radii  $r_0$  and  $r_1$  at the start-point and the end-point of Archimedes helix increase, while the polar angle  $\alpha_1$  of Archimedes helix decreases. In addition, the failure indices of the Bi-DCBs with different thicknesses do not reach 1 when they are in the folding stable state, indicating that the Bi-DCBs can achieve the bistable function without failure. With the increase of the thickness, the Tsai-Hill failure index and the maximum stress failure index increase. The reason is that the values

of  $z$  in Eqs. (26) to (33) increase, resulting in the Tsai-Hill failure index and the maximum stress failure index increase.

### 6.3 EFFECT OF LENGTH ON THE BISTABLE BEHAVIOUR

The analytical model proposed in this research is applied to predict the effect of the length on the bistable behaviour of the Bi-DCB, as shown in Figs. 7g to 7i. It is clear from Figs. 7g to 7i that the local minimum of total strain energy exists in the Bi-DCBs with different lengths. With the increase of the length, the polar radii  $r_0$  and  $r_1$  at the start-point and the end-point of Archimedes helix gradually decrease and increase, respectively, while the polar angle  $\alpha_1$  of Archimedes helix increases significantly. In addition, the failure indices of the Bi-DCBs with different lengths do not reach 1 when they are in the folding stable state, indicating that the Bi-DCBs can achieve the bistable function without failure. With the increase of the length, the Tsai-Hill failure index and the maximum stress failure index almost do not change.

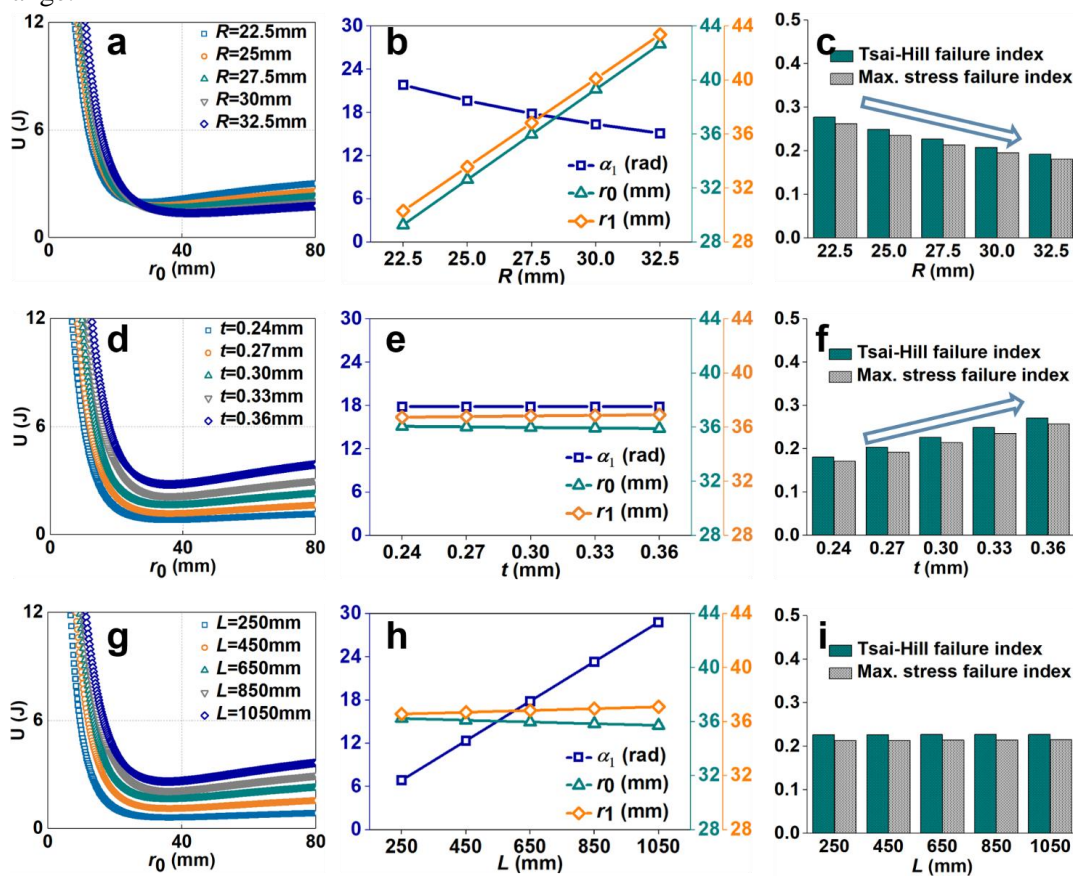


Fig. 7 - Effect of geometric parameters on the bistable behaviour of the Bi-DCB (a) Total strain energy versus polar radius at the start-point curves with different radii of the cross-section; (b) Geometric configuration with different radii of the cross-section; (c) Failure indices with different radii of the cross-section; (d) Total strain energy versus polar radius at the start-point curves with different thicknesses; (e) Geometric configuration with different thicknesses; (f) Failure indices with different thicknesses; (g) Total strain energy versus polar radius at the start-point curves with different lengths; (h) Geometric configuration with different lengths; (i) Failure indices with different lengths.

## 7. CONCLUSIONS

This paper established an analytical model for predicting the bistable behaviour of the Bi-DCB, revealing functional mechanisms of the Bi-DCB. Based on Archimedes helix equation, the geometric

behaviour of the Bi-DCB in the folding stable state was established. Using the energy principle, an analytical model for predicting the bistable behaviour of the Bi-DCB was derived. The maximum failure indices of the Bi-DCB in the folding stable state were analyzed by utilizing the Tsai-Hill criterion and the maximum stress criterion. To validate the analytical model proposed in this paper, the prediction results of the analytical model were compared with experimental results and the results of the two FEMs. The results obtained from the four methods are in good agreement with each other. With the aid of the analytical model presented in this paper, the influence of geometric parameters (i.e., the radius of the cross-section, thickness and length) on the bistable behaviour of the Bi-DCB was analyzed.

## ACKNOWLEDGEMENTS

This project was supported by the National Natural Science Foundation of China (Grant No. 52275231 and Grant No. 51875026) and the National Defense Basic Scientific Research Program of China (Grant No. JCKY2019205C002). The first author acknowledges the China Scholarship Council (Grant No. 202106020152).

## REFERENCES

- [1] M.V.B. Santana, L.I.W. Arnouts, T.J. Massart, et al. Corotational 3D joint finite element tailored for the simulation of bistable deployable structures. *Engineering Structures*, v.227, 111387. (2021).
- [2] F.H. Dai, H. Li, S.Y. Du. A multi-stable lattice structure and its snap-through behavior among multiple states. *Composite Structures*, v.97, p.56-63. (2013).
- [3] S. Daynes, P.M. Weaver, K.D. Potter. Aeroelastic study of bistable composite airfoils. *Journal of Aircraft*, v.46, p.2169-2174. (2009).
- [4] A.J. Lee, J.M. Fernandez. Inducing bistability in collapsible tubular mast booms with thin-ply composite shells. *Composite Structures*, v.225, 111166. (2019).
- [5] M.V.B. Santana, M. Hjiiaj, P.Z. Berke. Modal analysis of a bistable deployable module with a refined joint model. *Engineering Structures*, v.269, 114798. (2022).
- [6] Winkelmann C, Kim SS, La Saponara V. Design and development of hybrid composite bistable structures for energy absorption under quasi-static tensile loading. *Composite Structures*, v.93, p.171-178. (2010).
- [7] R.L. Harne, K.W. Wang . A review of the recent research on vibration energy harvesting via bistable systems. *Smart Materials and Structures*, v.22, 023001. (20113).
- [8] S.P. Jung, G. Jung, J.S. Koh et al. Fabrication of composite and sheet metal laminated bistable jumping mechanism. *Journal of Mechanisms and Robotics*, v.7, 021010. (2015).
- [9] A.J. Lee, J.M. Fernandez. Mechanics of bistable two-shelled composite booms. *AIAA Spacecraft Structures Conference*. (2018).
- [10] L.Y. Yang, H.F. Tan, Z.S. Cao. Modeling and analysis of the ploy region of bistable composite cylindrical shells. *Composite Structures*, v.192, p.347-354. (2018).
- [11] K. Iqbal, S. Pellegrino, A. Daton-Lovett. Bistable composite slit tubes. *IUTAM-IASS Symposium on Deployable Structures*. (1998).
- [12] D.A. Galletly, S.D. Guest. Bistable composite slit tubes. I. A beam model. *International Journal of Solids and Structures*, v.41, p.4517-4533. (2004).
- [13] Galletly DA, Guest SD. Bistable composite slit tubes. II. A shell model. *International Journal of Solids and Structures*, v.41, p.4503-4516. (2004).
- [14] S.D. Guest, S. Pellegrino. Analytical models for bistable cylindrical shells. *Proceedings of the Royal Society A: Mathematical, Physical and Engineering Sciences*, v.462, p. 839-854. (2006).
- [15] J.B. Bai, J.J. Xiong, J.P. Gao et al. Analytical solutions for predicting in-plane strain and interlaminar shear stress of ultra-thin-walled lenticular collapsible composite tube in fold deformation. *Composite Structures*, v.97, p.64-75. (2013).
- [16] E.H. Mansfield. The bending and stretching of plates. (2005).

[17] T.W. Liu, J.B. Bai, N. Fantuzzi et al. Bistable behaviour of deployable composite boom. (Submitted to the Composite Structures)

**RESPONSIBILITY NOTICE**

The author(s) is (are) the only responsible for the printed material included in this manuscript.



# ARBITRARILY SHAPED LAMINATED THIN PLATES IN GRADIENT ELASTICITY: A FINITE ELEMENT SOLUTION

Michele Bacciocchi<sup>a</sup>, Nicholas Fantuzzi<sup>b</sup>, Ana M.A. Neves<sup>c</sup>, Antonio J.M. Ferreira<sup>c</sup>

<sup>a</sup>DESD Department, University of the Republic of San Marino  
Via Consiglio dei Sessanta 99, 47891 Dogana, San Marino  
michele.bacciocchi@unirms.sm

<sup>b</sup>DICAM Department, University of Bologna  
Viale del Risorgimento 2, 40126 Bologna, Italy  
nicholas.fantuzzi@unibo.it

<sup>c</sup>Faculty of Engineering, University of Porto  
Rua Dr. Roberto Frias, s/n 4200-465 Porto, Portugal  
ananeves@fe.up.pt; ferreira@fe.up.pt

**Keywords:** numerical analysis, composite materials, laminated plates, mapping procedure, strain gradient theory

## 1. INTRODUCTION

The research aims to investigate laminated composite plates with arbitrary domains in gradient elasticity by means of a finite element methodology. For this purpose, a nonlocal theory is employed to characterize the stress components in a specific point of the domain in terms of both local strains and the divergence of the gradient of the strains. This approach is known as strain gradient [1-3]. In this context, the size effect is controlled by only one length-scale parameter as suggested by Altan and Aifantis as a simplification of Mindlin model [4,5].

This approach is becoming more and more popular in the study of nanoplates but is mostly used for isotropic configurations [6-10]. Some attempts have been proposed recently to deal with laminated composites in terms of both analytical [11-14] and numerical approaches [15,16].

As far as the numerical methods for thin plates based on strain gradient are concerned, it should be recalled that the approximated solutions require Hermite interpolating functions [15-17]. Therefore, conforming (C) and nonconforming (NC) formulations must be developed [17], which are able to guarantee  $C^1$  and  $C^2$  continuity for the membrane and bending degrees of freedom, respectively. This difficulty has limited the study of these structures only to regular domains.

In the current research, this limitation is overcome, and a new higher-order mapping procedure based on Hermite polynomials is proposed for the coordinate change. As a result, this study opens the possibility to investigate the mechanical behavior of composites plates with distorted domains [18]. Some numerical tests are developed to prove the accuracy of the finite element solution within the theoretical framework of Kirchhoff model embedded with the strain gradient approach.

## 2. SUMMARY OF THE NUMERICAL MODEL

Since a thin plate model in gradient elasticity is considered, the primary variables to be interpolated are both displacements and their higher-order derivatives. The degrees of freedom assume a different meaning depending on the formulation, which can be conforming (C) or nonconforming (NC). This interpolation is carried out within a 4-noded quadrilateral element; therefore, these parameters are defined only in its four corners. As far as the bending state is concerned, it should be

noted that 36 nodal quantities are required by the element within the C formulation, whereas the corresponding NC approach is characterized by 24 nodal terms. Likewise, the membrane state needs 12 and 16 nodal variables, respectively for the NC and C formulations. As a result, the continuity requirements are  $C^1$  and  $C^2$  for the membrane and bending approximation. Further details about this finite element model can be found in [15-18].

### 3. HIGHER-ORDER HERMITE MAPPING

It is well-known that in finite elements the fundamental operators are conveniently computed in the master element (or parent space), which is described by natural coordinates. Therefore, the proper coordinate change is required to move from the physical domain to the corresponding master element as shown in Figure 1.

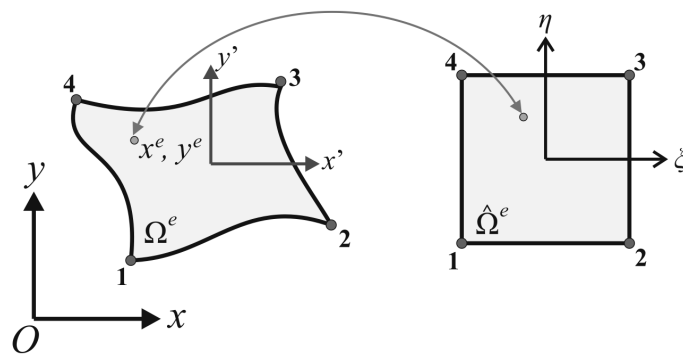


Figure 1 – Physical ( $\Omega^e$ ) and master ( $\hat{\Omega}^e$ ) elements: coordinate change. The image is taken from [18].

In this research, an isoparametric mapping is developed. This means that the same Hermite functions used for the interpolation of the degrees of freedom are employed to characterize the geometric distortions. Very few papers are available in the literature concerning this topic, only for classic elasticity [18]. This fact is justified by the higher level of complexity needed by the strain gradient approach, which required the mapping of derivatives up to the third order. The explicit definition of this coordinate change is presented by the authors in [18].

### 4. NUMERICAL RESULTS

The convergence and accuracy of the proposed approach are investigated taking into account three different meshes (Figure 2).

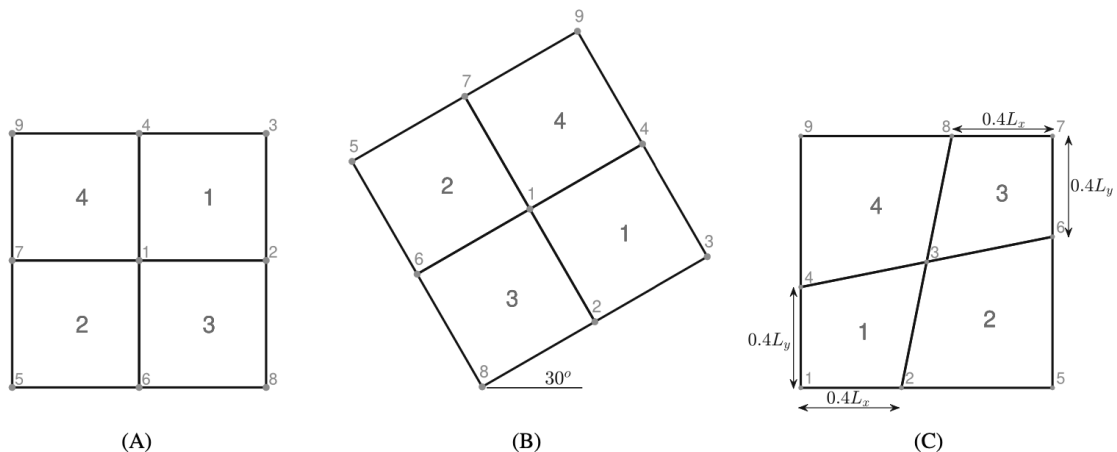


Figure 2 – Definition of the domains: (A) mesh1; (B) mesh2; (C) mesh3. The image is taken from [18].

It can be observed that “mesh1” is regular and structured; “mesh2”, instead, is structured but distorted; finally, “mesh3” is distorted and unstructured. Therefore, these meshes cover various situations that can be encountered. The results are presented in Figure 3 in terms of relative error computed with respect to the analytical solutions provided by the Navier method. The outcome is given in terms of the first natural frequency.

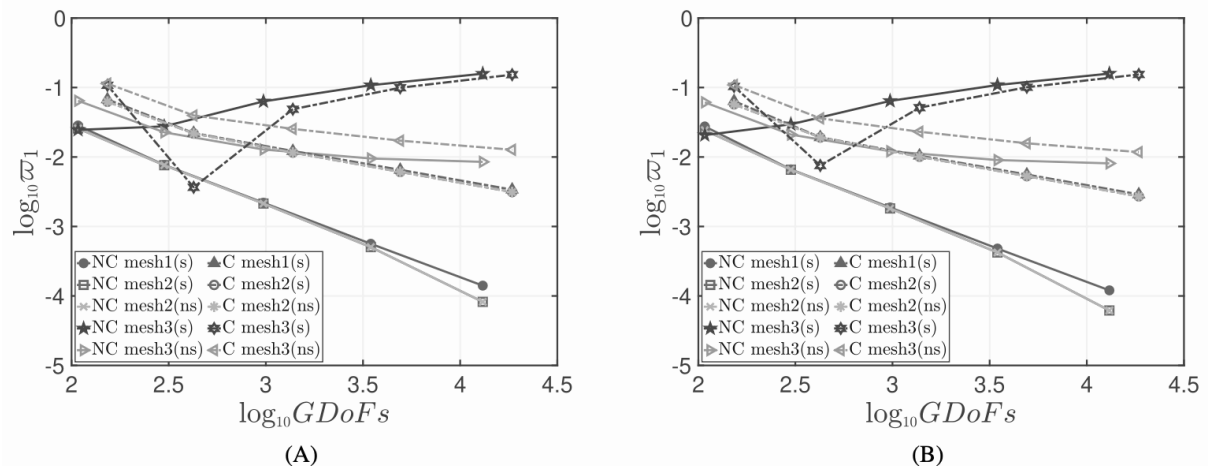


Figure 3 – Converge of the first frequency (relative error vs degrees of freedom) in gradient elasticity: (A) single isotropic layer; (B) four-layered symmetric laminate. A smoothness procedure is applied when the notation (s) is used; on the contrary, this procedure is neglected when the notation (ns) is added. The image is taken from [18].

## 5. CONCLUSIONS

A good convergent and monotonic behavior is observed independently from the lamination scheme for the structured meshes, both regular and distorted. On the other hand, if a smoothness procedure is applied, the solution loses its convergence features due to the introduction of some inconsistencies in the formulation [18]. This error is reduced if the smoothness procedure is not applied, even if the continuity requirement is only partially satisfied.

Examples of structured distorted domains that could be investigated by means of this approach are given by skew, rhomboidal, or trapezoidal plates, as well as domains with curved edges, such as parabolic, circular, sectorial, or annular plates. Future developments will be focused on these geometries. The current results prove that this approach is a good candidate to deal with this kind of problems.

## ACKNOWLEDGEMENTS

The first author gratefully acknowledges the University of the Republic of San Marino for the financial support in the framework of the Research Project PRIU2022: “*Principi generali di accertamento e caratterizzazione di terre e rocce da scavo e dei materiali da demolizione per un riutilizzo economicamente e ambientalmente sostenibile nelle strutture ed infrastrutture del territorio sammarinese*”.

## REFERENCES

- [1] C.Q. Ru, E.C. Aifantis. A simple approach to solve boundary-value problems in gradient elasticity. *Acta Mechanica*, v.101, p.59-68. (1993).
- [2] E.C. Aifantis. Update on a class of gradient theories. *Mechanics of Materials*, v.35, p.259-280. (2003).
- [3] H. Askes, E.C. Aifantis. Gradient elasticity in statics and dynamics: an overview of formulations, length scale identification procedures, finite element implementations and new results. *International Journal of Solids and Structures*, v.48, p.1962-1990. (2011).

- [4] S. Altan, E.C. Aifantis. On the structure of the mode III crack-tip in gradient elasticity. *Scripta Metallurgica et Materialia*, v.26, p.319-324. (1992).
- [5] S. Altan, E.C. Aifantis. On some aspects in the special theory of gradient elasticity. *Journal of the Mechanical Behavior of Materials*, v.8, p.231-282. (1997).
- [6] S. Hosseini, J. Niiranen. 3D strain gradient elasticity: variational formulations, isogeometric analysis and model peculiarities. *Computer Methods in Applied Mechanics and Engineering*, v.389, p.114324. (2022).
- [7] K. Lazopoulos. On the gradient strain elasticity theory of plates. *European Journal of Mechanics-A/Solids*, v.23, p.843-852. (2004).
- [8] B. Babu, B. Patel. Analytical solution for strain gradient elastic Kirchhoff rectangular plates under transverse static loading. *European Journal of Mechanics-A/Solids*, v.73, p-101-111. (2019).
- [9] B. Babu, B. Patel. A new computationally efficient finite element formulation for nanoplates using second-order strain gradient Kirchhoff's plate theory. *Composites Part B: Engineering*, v.168, p.302-311. (2019).
- [10] J. Niiranen, A.H. Niemi. Variational formulations and general boundary conditions for sixth-order boundary value problems of boundary value problems of gradient-elastic Kirchhoff plates. *European Journal of Mechanics-A/Solids*, v.61, p.164-179. (2017).
- [11] F. Cornacchia, N. Fantuzzi, R. Luciano, R. Penna. Solution for cross-and angle-ply laminated Kirchhoff nano plates in bending using strain gradient theory. *Composites Part B: Engineering*, v.173, p. 107006. (2019).
- [12] F. Cornacchia, F. Fabbrocino, N. Fantuzzi, R. Luciano, R. Penna. Analytical solution of cross- and angle-ply nano plates with strain gradient theory for linear vibrations and buckling. *Mechanics of Advanced Materials and Structures*, v.28, p.1201-1215. (2019).
- [13] G. Tocci Monaco, N. Fantuzzi, F. Fabbrocino, R. Luciano. Semi-analytical static analysis of nonlocal strain gradient laminated composite nanoplates in hygrothermal environment. *Journal of the Brazilian Society of Mechanical Sciences and Engineering*, v.43, p.1-20. (2021).
- [14] M. Baccocchi, A.M. Tarantino. Analytical solutions for vibrations and buckling analysis of laminated composite nanoplates based on third-order theory and strain gradient approach. *Composite Structures*, v.272, p. 114083. (2021).
- [15] M. Baccocchi, N. Fantuzzi, A.J.M. Ferreira. Static finite element analysis of thin laminated strain gradient nanoplates in hygro-thermal environment. *Continuum Mechanics and Thermodynamics*, v.33, p.969-992. (2020).
- [16] M. Baccocchi, N. Fantuzzi, R. Luciano, A.M. Tarantino. Linear eigenvalue analysis of laminated thin plates including the strain gradient effect by means of conforming and nonconforming rectangular finite elements. *Computers & Structures*, v.257, p. 106676. (2021).
- [17] M. Baccocchi, N. Fantuzzi, A.J.M. Ferreira. Conforming and nonconforming laminated finite element Kirchhoff nanoplates in bending using strain gradient theory. *Computers & Structures*, v.239, p. 106322. (2020).
- [18] M. Baccocchi, N. Fantuzzi. On the mapping procedure based on higher-order Hermite polynomials for laminated thin plates with arbitrary domains in gradient elasticity. *International Journal for Numerical Methods in Engineering*. In press. (2023).

## RESPONSIBILITY NOTICE

The authors are the only responsible for the printed material included in this manuscript.

## A BRIEF OUTLINE ON PREVIOUS RESULTS OF FLEXURAL MODULUS ESTIMATION FOR ASYMMETRIC SANDWICH STRUCTURES

Rodrigo José da Silva<sup>a,1</sup>, Túlio Hallak Panzera<sup>a,2</sup>, Fabrizio Scarpa<sup>b,3</sup>  
 Júlio Cesar dos Santos<sup>a,4</sup>, Fabiano Bianchini Batista<sup>a,5</sup>, André Luis Christoforo<sup>c,6</sup>

<sup>a</sup> Centre for Innovation and Technology in Composite Materials  
 Federal University of São João del-Rei (UFSJ), São João del-Rei, 36307-352, Brazil  
[r.j.silva\\_msc@outlook.com](mailto:r.j.silva_msc@outlook.com), [panzera@ufsj.edu.br](mailto:panzera@ufsj.edu.br), [dsantosjcs@gmail.com](mailto:dsantosjcs@gmail.com), [fabianchini@ufsj.edu.br](mailto:fabianchini@ufsj.edu.br)

<sup>b</sup> Bristol Composites Institute  
 University of Bristol, Bristol, BS8 1TR, United Kingdom  
[f.scarpa@bristol.ac.uk](mailto:f.scarpa@bristol.ac.uk)

<sup>c</sup> Centre for Innovation and Technology in Composite Materials  
 Federal University of São Carlos (UFSCar), São Carlos, 13565-905, Brazil  
[alchristoforo@ufscar.br](mailto:alchristoforo@ufscar.br)

<sup>1</sup> [ID 0000-0001-8016-3165](https://orcid.org/0000-0001-8016-3165), <sup>2</sup> [ID 0000-0001-7091-456X](https://orcid.org/0000-0001-7091-456X), <sup>3</sup> [ID 0000-0002-5470-4834](https://orcid.org/0000-0002-5470-4834)  
<sup>4</sup> [ID 0000-0002-7485-491X](https://orcid.org/0000-0002-7485-491X), <sup>5</sup> [ID 0000-0002-2402-4918](https://orcid.org/0000-0002-2402-4918), <sup>6</sup> [ID 0000-0002-4066-080X](https://orcid.org/0000-0002-4066-080X)

**Keywords:** sandwich structures, flexural modulus, pure bending

### 1. INTRODUCTION

From a macro-mechanical standpoint, a sandwich panel can be assumed as a solid and homogenised structure with equivalent dimensions and global elastic properties under bending in each direction of the plane [1]. The same can be considered for the phases of the panel, i.e., its faces and core (see Fig. 1).

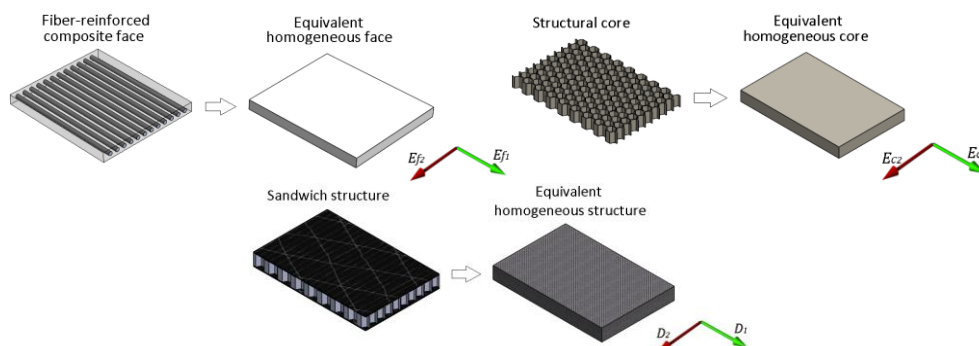


Figure 1 – Interpretation of a sandwich panel and its phases as solid and homogenised structures with equivalent dimensions and global elastic properties under bending. R.J. da Silva *et al.* [1].

As discussed by R.J. da Silva *et al.* [1], the concept of homogenisation is an appropriate approach to estimate the global flexural modulus of sandwich structures by the constitutive relation  $D = E_s \cdot I$ . Core structures with complex geometries, such as lattices or honeycombs, have varying

moments of inertia for different cross-sections. Considering homogenisation, the moment of inertia of the panel ( $I$ ) is constant and is described by the total thickness and width of the panel. As a result, the global flexural modulus ( $E_s$ ) can be calculated by dividing the panel stiffness ( $D$ ) by the homogenised moment of inertia ( $I$ ), stiffness being typically measured according to ASTM D7250 [2].

The authors [1] discussed in detail how the flexural modulus of sandwich panels can be obtained experimentally through three-point bending tests, as well as the influence of the geometric parameters of the specimen (width and span) on the measured response. The proposed method is called RJS Method. In general, it is pointed out that the global flexural modulus calculated through a theoretical approach can only be equally measured during an experimental approach if pure bending occurs (quasi-absence of shear deformations). The experimental approach considers the normalisation of force-displacement curves to mean stress-strain curves assuming the concept of homogenisation – see [3]. If pure bending does not occur, then the experimental flexural modulus is less than the theoretical one, being smaller as more shear deformation occurs. Pure bending can be achieved for larger specimen dimensions (width and span) relative to total thickness. The lower the core rigidity relative to rigidity of the faces, the greater the increase in specimen dimensions is required to promote pure bending.

The theoretical approach to estimate the flexural modulus is based on the calculation of the panel stiffness considering the contribution of each panel phase in relation to the panel neutral axis. R.J. da Silva *et al.* [1] have considered, at first, only symmetric structures, i.e., those with faces of the same thickness and composition. Moreover, the possible contribution of the rigidity of the face-core adhesives was not discussed. In this work, an enhanced approach is proposed, in which a fully asymmetrical structure is considered, i.e., panels with different faces or adhesives. The equations are presented, and numerical results obtained via ABAQUS<sup>TM</sup> are briefly discussed.

## 2. ENHANCED APPROACH: EQUATIONS FOR ASSYMETRIC STRUCTURES

Figure 2 shows the cross-sectional dimensions of a rectangular panel under bending, in which  $b$  is the sandwich width,  $t_1$  and  $t_2$  are the facing thicknesses,  $a_1$  and  $a_2$  are the adhesives thicknesses,  $c$  is the core thickness, and  $h = t_1 + t_2 + a_1 + a_2 + c$  is the panel thickness.  $E_i$  indicates the global elastic modulus under the bending of each homogenised phase. The neutral axis of the structure is at a distance of  $\bar{y}$  from its bottom surface and can be estimated by the transformed-section method – Eq. (1). Using the parallel axis theorem, also known as Huygens–Steiner theorem, the panel stiffness ( $D$ ) is calculated using Eq. (2). It is considered  $D = \sum D_i$  and  $D_i = E_i \cdot I_i = E_i \cdot (b \cdot x_i^3 / 12 + b \cdot x_i \cdot d_i^2)$ , where  $D_i$  is the stiffness of the phase  $i$  with the moment of inertia  $I_i$ , thickness  $x_i$ , and  $d_i$  is the distance between the centroidal axis of phase and the neutral axis of the sandwich structure. Finally, assuming the concept of homogenisation, the panel flexural modulus ( $E_s$ ) can be calculated by dividing Eq. (2) by the homogenised moment of inertia of the panel along its neutral axis – Eq. (3). The homogenised moment of inertia of the panel about its neutral axis is  $I = [b \cdot h^3 / 12 + b \cdot h \cdot (\bar{y} - h/2)^2]$ .

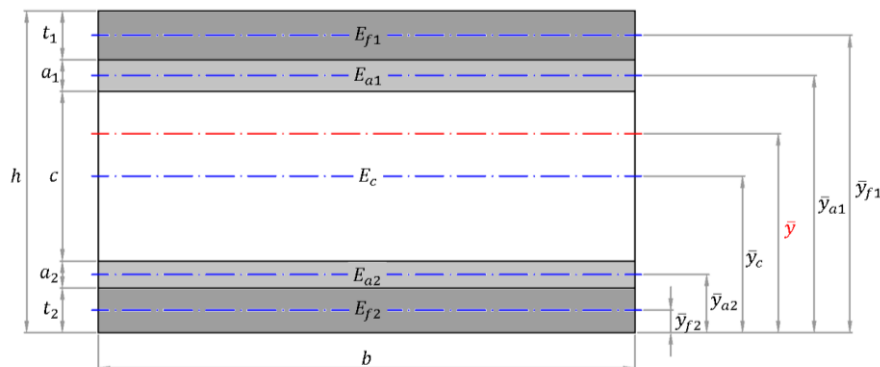


Figure 2 – Dimensions of the rectangular cross-section of a panel with different faces and adhesives. The centroidal axes of the phases are marked by the blue reference lines and the panel neutral axis under bending by the red one.

$$\bar{y} = \frac{n_{f1} \cdot t_1 \cdot \left(h - \frac{t_1}{2}\right) + n_{a1} \cdot a_1 \cdot \left(h - t_1 - \frac{a_1}{2}\right) + n_{f2} \cdot t_2 \cdot \left(\frac{t_2}{2}\right) + n_{a2} \cdot a_2 \cdot \left(t_2 + \frac{a_2}{2}\right) + n_c \cdot c \cdot \left(t_2 + a_2 + \frac{c}{2}\right)}{n_{f1} \cdot t_1 + n_{a1} \cdot a_1 + n_{f2} \cdot t_2 + n_{a2} \cdot a_2 + n_c \cdot c} \quad (1)$$

$$D = E_{f1} \cdot \left[ \frac{b \cdot t_1^3}{12} + b \cdot t_1 \cdot \left(h - \frac{t_1}{2} - \bar{y}\right)^2 \right] + E_{a1} \cdot \left[ \frac{b \cdot a_1^3}{12} + b \cdot a_1 \cdot \left(h - t_1 - \frac{a_1}{2} - \bar{y}\right)^2 \right] + E_{f2} \cdot \left[ \frac{b \cdot t_2^3}{12} + b \cdot t_2 \cdot \left(\bar{y} - \frac{t_2}{2}\right)^2 \right] + E_{a2} \cdot \left[ \frac{b \cdot a_2^3}{12} + b \cdot a_2 \cdot \left(\bar{y} - \left(t_2 + \frac{a_2}{2}\right)\right)^2 \right] + E_c \cdot \left[ \frac{b \cdot c^3}{12} + b \cdot c \cdot \left(\bar{y} - \left(t_2 + a_2 + \frac{c}{2}\right)\right)^2 \right] \quad (2)$$

$$\left\{ \begin{array}{l} E_s = \underbrace{\frac{E_{f1}}{k} \cdot \left[ t_1^3 + 12t_1 \cdot \left(h - \frac{t_1}{2} - \bar{y}\right)^2 \right]}_{\text{Top face contribution}} + \underbrace{\frac{E_{a1}}{k} \cdot \left[ a_1^3 + 12a_1 \cdot \left(h - t_1 - \frac{a_1}{2} - \bar{y}\right)^2 \right]}_{\text{Top adhesive contribution}} + \underbrace{\frac{E_{f2}}{k} \cdot \left[ t_2^3 + 12t_2 \cdot \left(\bar{y} - \frac{t_2}{2}\right)^2 \right]}_{\text{Bottom face contribution}} \\ \quad + \underbrace{\frac{E_{a2}}{k} \cdot \left[ a_2^3 + 12a_2 \cdot \left(\bar{y} - \left(t_2 + \frac{a_2}{2}\right)\right)^2 \right]}_{\text{Bottom adhesive contribution}} + \underbrace{\frac{E_c}{k} \cdot \left[ c^3 + 12c \cdot \left(\bar{y} - \left(t_2 + a_2 + \frac{c}{2}\right)\right)^2 \right]}_{\text{Core contribution}} \end{array} \right. \quad (3)$$

$$k = 4h \cdot (h^2 - 3h \cdot \bar{y} + 3\bar{y}^2)$$

### 3. NUMERICAL RESULTS AND CONCLUSIONS

A fully asymmetrical panel (Table 1) is considered for a numerical simulation under three-point bending. Two specimen geometry configurations are investigated: (i) 72 mm in width and 144 mm in support span, and (ii) 72 mm in width and 2500 mm in support span – see Fig. 3 (a) and (b), respectively. Simulations are performed considering a sectioned 3D extruded body for each phase of the panel. Continuum Shell S4R elements are used for faces and adhesives, and 3D Stress elements for the core. The mesh size is 5 and the indenters are defined as Analytical Rigid Surfaces. The load point displacement is defined as 1% of the support span.

Table 1 – Sandwich structure configuration.

Panel phase	Material	Thickness	Elastic modulus	Poisson's ratio
Top face	S2-Glass/Epoxy	2 mm	48 GPa	0.14
Top adhesive	Polymer based I	0.6 mm	2.5 GPa	0.35
Core	Low density foam	20 mm	0.4 GPa	0.25
Bottom adhesive	Polymer based II	0.4 mm	1.5 GPa	0.35
Bottom face	Kevlar/Epoxy	1 mm	65 GPa	0.00

Facing properties adapted from T. Bitzer [5, Appendix H]. Adhesives and core properties are hypothetical.

The investigated panel has a total thickness of 24 mm, and the neutral axis is at a distance of 13.82 mm from the bottom surface of the panel – Eq. (1). The flexural modulus considering the theoretical approach proposed in this work (RJS equation) is 16.37 GPa – Eq. (3). Figure 3 (a) and (b) show the slope of the mean stress-strain curves obtained by normalising the force-displacement data obtained in the ABAQUS™ simulation. The predicted slope considering the RJS equation is also evidenced. Small specimens (relative to panel thickness) under bending return underestimated values for the slope of the straight-line portion of a mean stress-strain curve, since shear deformations are predominant (3.84 GPa << 16.37 GPa) – Fig. 3 (a). On the other hand, for a long-span configuration with the quasi-absence of shear deformations (pure bending), the panel flexural modulus tends to converge to the theoretical value (16.25 GPa ≈ 16.37 GPa) – Fig. 3 (b). These findings corroborate the assertions of the RJS Method [1].

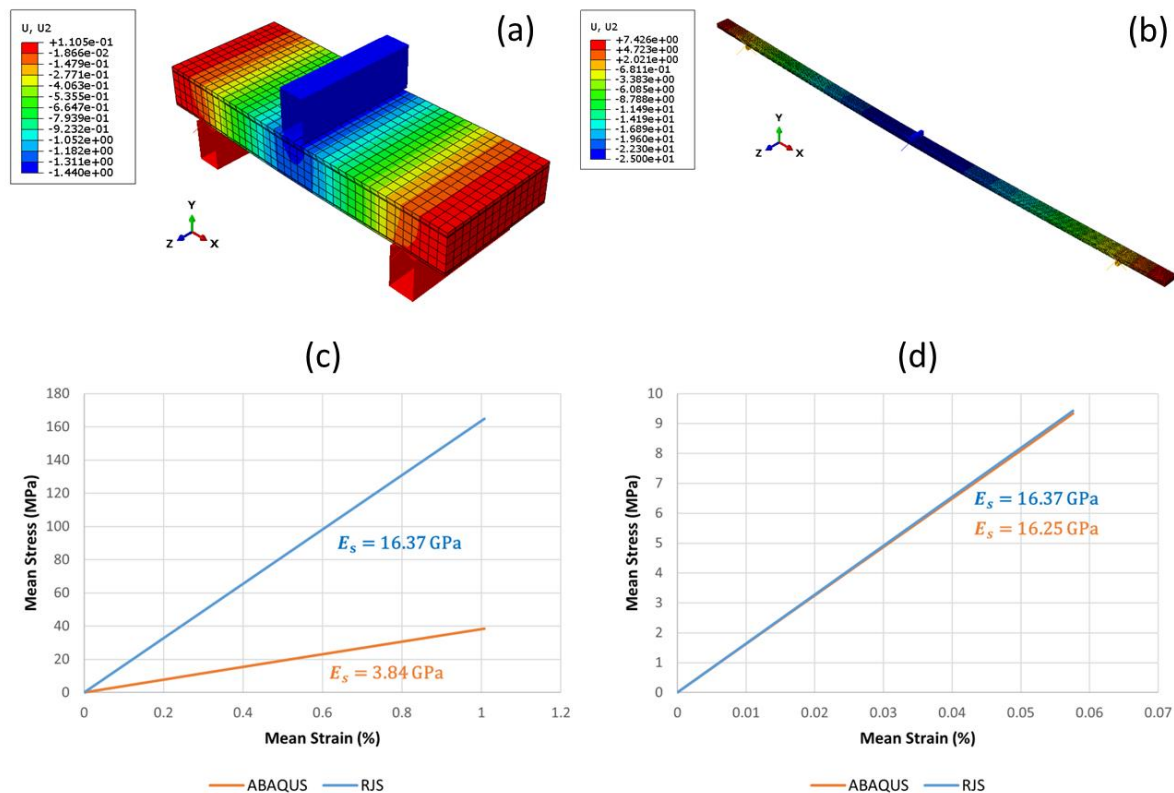


Figure 3 – Numerical results for (a) short span and (b) long span, and respective comparison of theoretical flexural modulus (RJS) with numerical (ABAQUS).

## ACKNOWLEDGEMENTS

The authors would like to thank the Brazilian Research Agencies, CAPES and CNPq for the financial support provided.

## REFERENCES

- [1] R. J. da Silva et al., “A core rigidity classifier method and a novel approach to account for geometric effects on the elastic properties of sandwich structures,” *Composite Structures*, vol. 282, p. 115075, Feb. 2022, doi: <https://doi.org/10.1016/j.compstruct.2021.115075>.
- [2] ASTM D7250 / D7250M-20, Standard Practice for Determining Sandwich Beam Flexural and Shear Stiffness, ASTM International, West Conshohocken, PA, 2020, [www.astm.org](http://www.astm.org).
- [3] Rodrigo José da Silva. (2022, November 7). Equations for flexural tests: three- and four-point bending. Zenodo. <https://doi.org/10.5281/zenodo.7301896>.
- [4] ABAQUS™ CAE (2017). [Computer software]. San Diego, CA: Dassault Systèmes, Simulia Corp. ([www.3ds.com](http://www.3ds.com)).
- [5] T. Bitzer, Honeycomb Technology. Dordrecht: Springer Netherlands, 1997. doi: <https://doi.org/10.1007/978-94-011-5856-5>.

## RESPONSIBILITY NOTICE

The authors are the only responsible for the printed material included in this manuscript.



# CARACTERIZAÇÃO DO TALO DA CARNAÚBA E A INFLUÊNCIA DA SUA INCORPORAÇÃO EM COMPÓSITOS DE PEAD

Laura Nunes de Menezes<sup>a</sup>, José Roberto Moraes d’Almeida<sup>a</sup>

<sup>a</sup>Pontifícia Universidade Católica do Rio de Janeiro  
Departamento de Engenharia Química e de Materiais, Rua Marquês de São Vicente 124, Rio de Janeiro, RJ, Brasil  
[laura.nunes@aluno.puc-rio.br](mailto:laura.nunes@aluno.puc-rio.br) [dalmeida@puc-rio.br](mailto:dalmeida@puc-rio.br)

**Palavras-chave:** *Copernicia Prunifera*, Polietileno de Alta Densidade, Biocompósitos, Propriedades Mecânicas

## 1. INTRODUÇÃO

Atualmente, a demanda por novos materiais a partir de recursos renováveis tem despertado o interesse da comunidade científica, principalmente no desenvolvimento de materiais compósitos mais acessíveis e sustentáveis, utilizando resíduos orgânicos como material de reforço [1]. O emprego de fibras naturais lignocelulósicas em compósitos apresenta vantagens como: baixo custo, biodegradabilidade, boas propriedades, fácil processamento e menor desgaste dos equipamentos durante o processamento e reciclagem [2].

A carnaúba (*Copernicia prunifera*) é uma espécie de palmeira abundante na região Nordeste do Brasil e possui grande importância econômica para a região devido à produção de cera a partir das folhas [3]. As outras partes da palmeira também são utilizadas, só que em menor escala, na produção de artesanatos, telhados, cercas, móveis, etc. Durante o processo de produção da cera o talo e as folhas são retirados da palmeira e apenas as folhas contêm o pó cerífero, sendo completamente beneficiadas enquanto talos, em sua maioria, se tornam resíduos orgânicos.

Considerando o panorama citado, este estudo visa avaliar o potencial do uso dos talos de carnaúba como reforço em uma matriz de polietileno de alta densidade (PEAD), buscando desenvolver um compósito sustentável e eficiente mecanicamente. Três composições de PEAD/resíduo foram utilizadas para a fabricação dos corpos de prova dos compósitos: 5, 10 e 15% em peso de resíduo, a fim de avaliar o efeito da incorporação do mesmo sobre as propriedades da matriz.

Com esse fim, foi realizada a análise térmica do material buscando avaliar se o reforço suporta as temperaturas de processamento do polímero sem sofrer processos degradativos. Os compósitos também foram avaliados termicamente e comparados ao PEAD puro a fim de verificar se a adição do reforço acarreta mudanças na estabilidade térmica da matriz. Os espécimes dos compósitos e do PEAD puro são submetidos ao ensaio uniaxial de tração para compreender as alterações nas propriedades mecânicas dos compósitos provocadas pela inserção do reforço. Todos os testes realizados buscam compreender os efeitos do reforço na matriz, qual a melhor proporção a ser utilizada e as possibilidades de aplicações futuras para o compósito.

## 2. PROCEDIMENTO EXPERIMENTAL

### 2.1. Material

Os talos de carnaúba utilizados nesse estudo foram obtidos de um produtor rural, em agosto de 2022, em um carnaúbal do município de Limoeiro do Norte, Ceará, Brasil. Após os talos serem extraídos da palmeira, eles foram cortados em pedaços de aproximadamente 20 cm e os espinhos removidos, a fim de facilitar o manuseio e o transporte.

## 2.2. Processamento do talo

Os talos ainda verdes foram postos em uma estufa de secagem e esterilização a 80°C por 5 dias, em um equipamento da marca FANEM modelo 315 SE. Após a retirada da umidade e com a finalidade de obter o resíduo na forma de pó, os talos secos foram submetidos a moagem em um moinho de facas da marca Solab modelo SL-30. O pó obtido não foi passado por nenhum tipo de processamento ou peneiramento. A Fig. 1 mostra os talos antes e após a secagem, a estufa e moinho utilizados e os talos após a moagem.

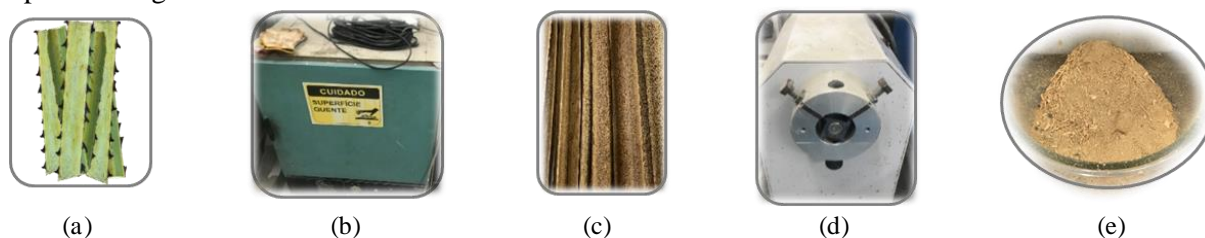


Figura 1 – O material e os equipamentos utilizados para o processamento do reforço: (a) talos verdes; (b) estufa; (c) talos secos; (d) moinho de facas; (e) pó do talo.

## 2.3. Preparação do compósito

Os compósitos foram feitos em três composições seguindo as seguintes proporções: 85% em peso de PEAD e 15% em peso de pó do talo, 90% em peso de PEAD e 10% em peso de pó do talo e 95% em peso de PEAD e 5% em peso de pó do talo. O pó do talo e os pellets de PEAD foram pesados, separadamente e misturados manualmente. A Fig. 2 abaixo mostra o pó do talo, os pellets do polímero utilizado e um exemplo da mistura dos dois.

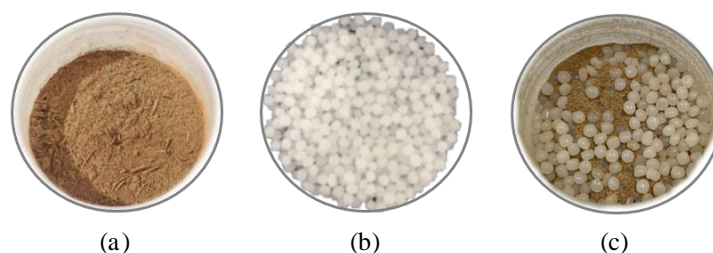


Figura 2 – Materiais utilizados para fabricar os compósitos (a) pó do talo; (b) pellets de PEAD; (c) uma amostra da mistura.

Para realizar a homogeneização das misturas foi utilizada uma mini extrusora dupla rosca paralela (DSM Xplore 5cc). As misturas foram adicionadas através do alimentador e as zonas de aquecimento tiveram as seguintes temperaturas de entrada, homogeneização e saída: 180 °C, 190 °C e 200 °C. A mistura foi realizada sob fluxo constante de nitrogênio, garantindo uma atmosfera inerte. Após a extrusão, os corpos de prova foram injetados utilizando uma mini injetora também da marca Xplore (modelo DSM Xplore 5,5cc) em um molde com cavidade para um corpo de prova do tipo V, de

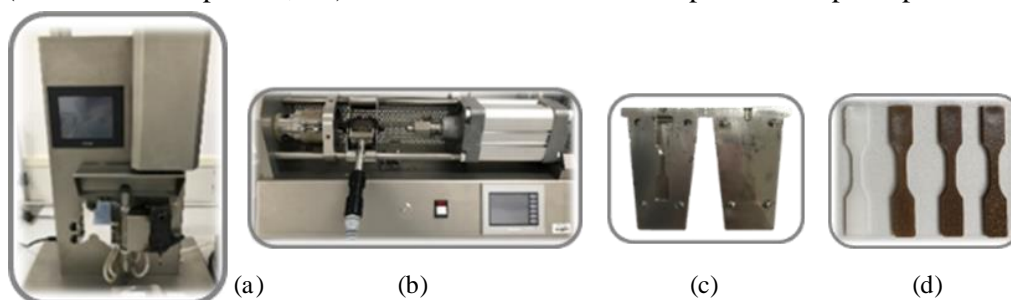


Figura 3 – Equipamentos utilizados na fabricação dos corpos de prova: (a) Mini extrusora; (b) mini injetora; (c) molde; (d) corpos de provas fabricados.

acordo com a norma ASTM D 638. A temperatura do molde foi de 80 °C. As imagens da mini extrusora, mini injetora, molde e corpos de prova prontos são mostrados na Fig. 3.

## 2.4. Caracterizações

Após a moagem e sem nenhum processo de separação de tamanho de partículas, 19 mm<sup>3</sup> de pó foram colocados no analisador de partículas Morphologi 4-ID da marca Malvern. As partículas foram pulverizadas e dispersas em uma lâmina e posteriormente analisadas a fim de obter dados da morfologia do material particulado, caracterizando a forma e tamanho das partículas. Na Fig. 4 pode ser observado o equipamento utilizado para análise de partículas e o pó do talo disperso na lâmina de vidro do porta amostra.

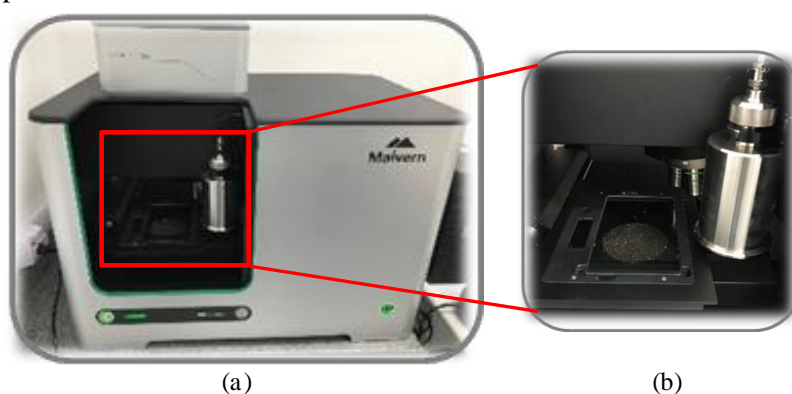


Figura 4 – Equipamento utilizado na análise de partículas (a) Morphologi 4-ID; (b) porta amostra.

Para obtenção das propriedades térmicas do talo e dos compósitos foi utilizado o equipamento da marca PerkinElmer modelo Pyris 1 TGA. A faixa de temperatura utilizada na caracterização do talo foi de 30 °C a 600 °C e a faixa de temperatura utilizada na análise dos compósitos e do PEAD puro foi 40 °C a 660 °C. A taxa de aquecimento foi fixada em 10 °C/min em todas as análises. A atmosfera inerte utilizada durante a caracterização foi de nitrogênio, com uma vazão de 20 ml/min.

Para obter as propriedades mecânicas dos espécimes dos compósitos, 5 corpos de provas de cada composição e do PEAD puro testados em tração uniaxial utilizando um equipamento da marca Oswaldo Filizola, modelo AME-2kN. Os ensaios foram feitos a uma velocidade de 10 mm/min, com a distância entre garras ( $L_0$ ) de 25,47 mm e com área da seção da transversal ( $S_0$ ) de 10,49 mm<sup>2</sup>. Todos os ensaios foram feitos a temperatura ambiente. Os dados do ensaio foram obtidos através do software DynaView e processados no Excel para obtenção das propriedades dos materiais. A Fig. 5 mostra os equipamentos utilizados na análise térmica da fase dispersa, dos compósitos e do PEAD puro e também o equipamento em que foram realizados os ensaios de tração.

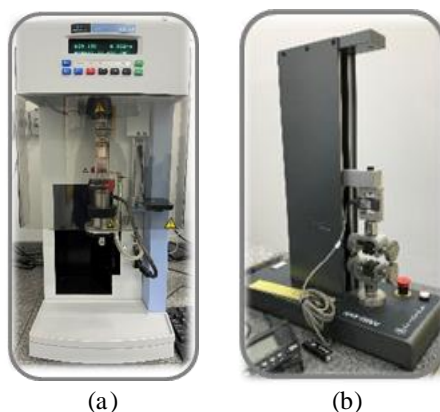


Figura 5 – Equipamentos utilizados nas análises térmicas e mecânicas: (a) Analisador Termogravimétrico (TGA); (b) equipamento de tração.

### 3. RESULTADOS E DISCURSSÃO

Após a moagem e sem nenhum processo de separação de tamanho de partículas, 19 mm<sup>3</sup> de resíduo foram colocados no analisador de partículas. Nesse volume, foram detectadas 401.594 partículas. A morfologia de cada uma delas foi observada, resultando em gráficos de distribuição de frequência e valores da área, diâmetro equivalente, circularidade e razão de aspecto como mostrado na Tab. 1.

O valor tão distinto da mínima e da máxima área das partículas e o desvio padrão alto mostra que há uma grande dispersão de área das partículas, sendo que as partículas muito grandes podem gerar pontos concentradores de tensão no compósito. O gráfico de distribuição de área das partículas, Fig. 6, mostra que há outliers e que a maior população tem em média 25000 μm<sup>2</sup>. A presença de duas populações com valores muito distintos faz com que o desvio padrão seja alto. Através dos valores de circularidade e razão de aspecto é possível concluir que as partículas são levemente arredondadas.

Tabela 1 – Análise de parâmetros das partículas do talo da carnauba.

Parâmetros	Área (μm <sup>2</sup> )	Diâmetro equivalente do círculo (μm)	Circularidade	Razão de aspecto
Média	25214,06	145,63	0,86	0,64
Desvio Padrão	32177,00	104,58	0,11	0,17
Mínimo	3,22	2,01	0,44	0,20
Máximo	162126,09	452,77	1,00	1,00

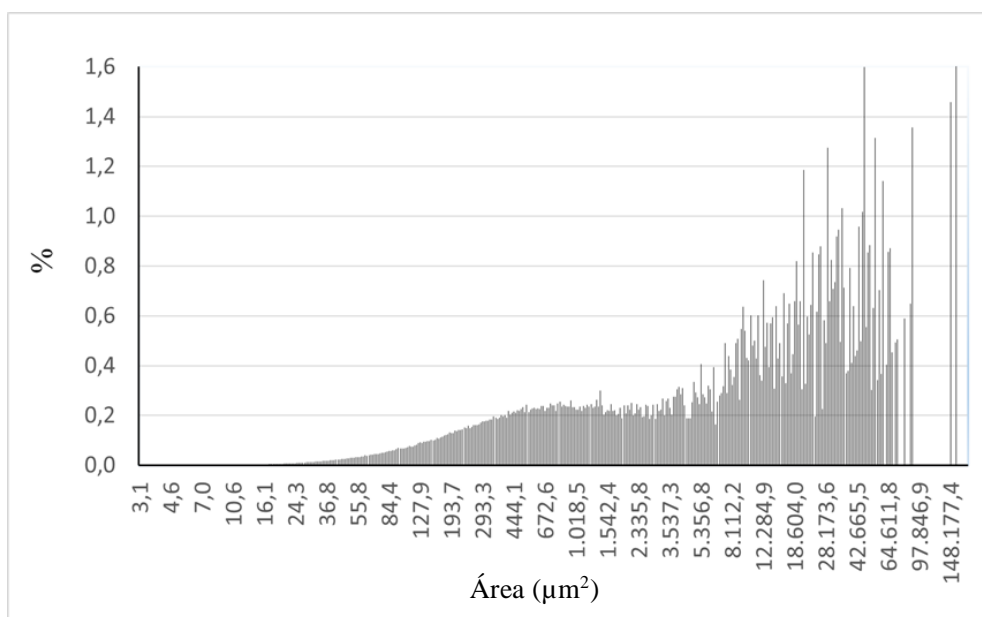


Figura 6 – Gráfico de distribuição de área das partículas.

A Figura 7 mostra o resultado da análise termogravimétrica do talo de carnaúba e dos espécimes de compósito e do PEAD. A partir da termogravimetria é possível observar que a primeira perda de massa ocorre devido à evaporação de umidade, a segunda e terceira etapas referem-se à degradação da hemicelulose e celulose [4]. A degradação se inicia em aproximadamente 220 °C e conforme a curva da derivada, a temperatura de degradação máxima foi de 340 °C. Os resultados da TGA confirmam que o talo da carnaúba pode ser utilizado como reforço em termoplásticos, pois confere estabilidade térmica de até 220 °C [5] e a máxima temperatura utilizada durante o processamento do compósito foi de 200 °C.

As curvas referentes a degradação dos compósitos das três composições e do PEAD, utilizado como referência para analisar se a adição de fibra gera alterações significativas na temperatura de degradação térmica, mostram que quanto maior a porcentagem em peso de fibras, maior é a temperatura de degradação térmica. Conforme a derivada de cada uma das curvas obtidas, os picos de degradação térmica do PEAD puro, PEAD + 5%, PEAD + 10% e PEAD + 15% foram, respectivamente, 483, 491, 498 e 506 °C. É possível concluir que as curvas seguiram um comportamento padrão e o compósito com maior quantidade de reforço preservou mais massa mesmo após a degradação máxima.

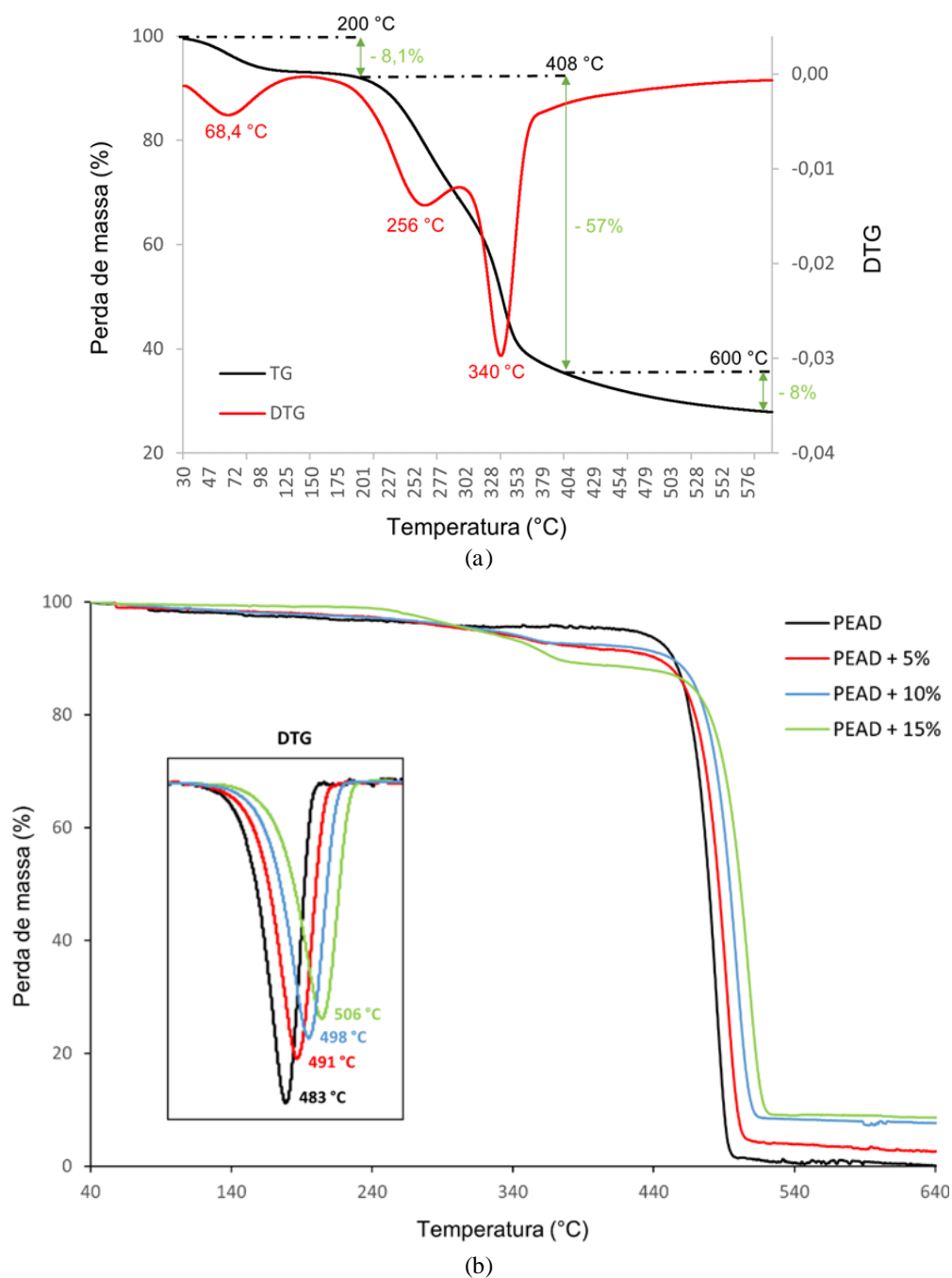


Figura 7 – Curvas termogravimétricas obtidas (a) TG/DTG do talo da carnaúba; (b) TG/DTG dos espécimes de compósitos e do PEAD.

A Fig. 8 mostra as curvas tensão-deformação típicas do PEAD e dos compósitos PEAD-carnaúba. É possível observar uma perda de ductilidade e de tenacidade consoante o aumento da quantidade de reforço, como previsto na literatura. Normalmente o aumento da resistência mecânica pela incorporação de reforços em termoplásticos acarreta uma perda de ductilidade, pois o reforço reduz a mobilidade das cadeias [6].

Os valores médios das propriedades obtidas de cada composição estão listados na Tab. 2. O módulo de elasticidade dos compósitos PEAD + 5%, PEAD + 10% e PEAD + 15% sofreram um aumento de aproximadamente 15, 12 e 18%, respectivamente, quando comparados ao módulo de elasticidade do PEAD. De maneira geral, o limite de escoamento não sofreu grandes alterações, apenas no compósito com 5% em peso de fibra foi possível perceber um leve aumento e uma menor perda de ductilidade.

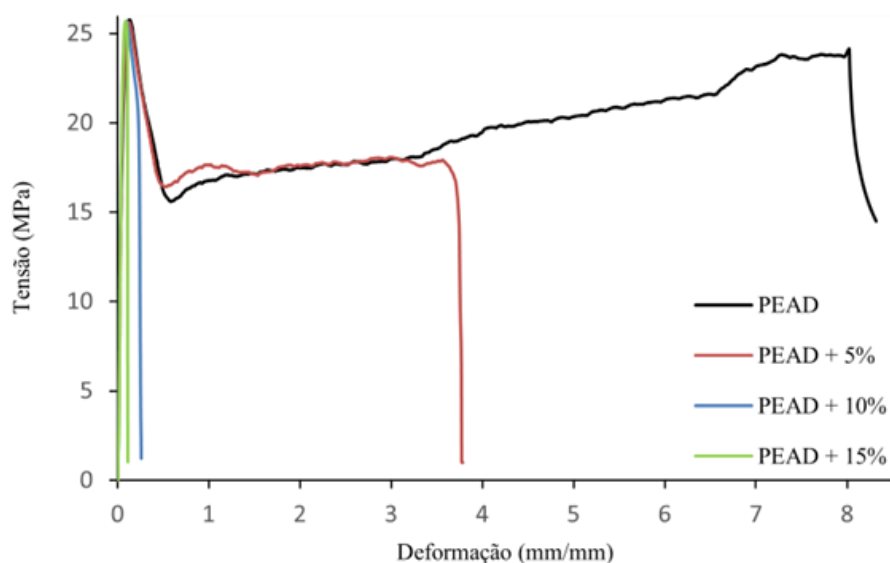


Figura 8 – Curvas tensão-deformação de um espécime representativo de cada material.

Tabela 2 – Valores médios das propriedades mecânicas obtidas a partir do ensaio de tração.

Composição	Limite de escoamento (MPa)	Tensão de ruptura (MPa)	Deformação na ruptura (mm/mm)
PEAD	25,63 ± 0,23	23,35 ± 0,73	7,95 ± 0,14
PEAD + 5%	26,36 ± 0,70	17,90 ± 1,37	3,84 ± 1,77
PEAD + 10%	25,70 ± 0,47	21,59 ± 2,38	1,01 ± 0,07
PEAD + 15%	25,60 ± 0,50	23,61 ± 1,25	0,11 ± 0,03

## AGRADECIMENTOS

Os autores agradecem o apoio financeiro da CAPES e do CNPq.

## REFERÊNCIAS

- [1] S. Candiotti et al. Assessment of the mechanical properties of peruvian *Stipa Obtusa* fibers for their use as reinforcement in composite materials. *Composites Part A: Applied Science and Manufacturing*, v. 135, p. 105950. (2020).

- [2] S.N. Monteiro, F.P.D. Lopes, A.P. Barbosa et al. Natural lignocellulosic fibers as engineering materials - An overview. *Metallurgical and Materials Transactions*. v. 42, p. 2963–2974. (2011).
- [3] J.V. STEINLE. CARNAUBA WAX an expedition to its source. *Industrial & Engineering Chemistry*. v. 28, n. 9, p. 1004–1008. (1936).
- [4] S. Kumar et al. Thermogravimetric analysis of lignocellulosic leaf-based fiber-reinforced thermosets polymer composites: an overview. *Composite Structures Biomass Conversion and Biorefinery*, p. 1–26. (2022).
- [5] M. Rokbi et al. Effect of processing parameters on tensile properties of recycled polypropylene based composites reinforced with jute fabrics. *International Journal of Lightweight Materials and Manufacture*, v. 3, p. 144–149. (2020).
- [6] A.K. Mehrjerdi, A. Kalantar, T. Bashir, M. Skrifvars. Melt rheology and extrudate swell properties of talc filled polyethylene compounds. *Heliyon*, v. 6, p. e04060, (2020).

### AVISO DE RESPONSABILIDADE

O(s) autor(es) é(são) o(s) único(s) responsável(is) pelo material impresso incluído neste manuscrito.

# COMPUTATIONAL ANALYSIS OF 2D-DCB BONDED COMPOSITE JOINTS USING TRAPEZOIDAL TRACTION SEPARATION LAW

Jailto A.P. da Silva<sup>a</sup>, Rafael Beck<sup>b</sup>, Lucas F.M. da Silva<sup>c</sup>  
Volnei Tita<sup>a,c</sup>, and Ricardo de Medeiros<sup>b</sup>

[japrado12@alumni.usp.br](mailto:japrado12@alumni.usp.br), [r.beck@udesc.br](mailto:r.beck@udesc.br), [lucas@fe.up.pt](mailto:lucas@fe.up.pt), [voltita@sc.usp.br](mailto:voltita@sc.usp.br),  
[ricardo.medeiros@udesc.br](mailto:ricardo.medeiros@udesc.br)

<sup>a</sup>Department of Aeronautical Engineering, São Carlos School of Engineering, University of São Paulo  
Av. João Dagnone, 1100, 13573-120, São Carlos, Brazil.

<sup>b</sup>Department of Mechanical Engineering, Santa Catarina State University, Rua Paulo Malschitzki, 200,  
89.219-710, Joinville, Brazil.

<sup>c</sup>Department of Mechanical Engineering, Faculty of Engineering of University of Porto, Rua Dr.  
Roberto Frias, s/n, 4200-465, Porto, Portugal.

**Keywords:** Composite bonded joint, Double Cantilever Beam, Cohesive Zone Model.

## 1. INTRODUCTION

Finite Element Analysis (FEA) simulations have proven to be a valuable tool for evaluating the mechanical behaviour of bonded joints. In particular, cohesive models have enabled the simulation of adhesive degradation, making it possible to simulate failure mechanisms such as ductile, adhesive, and mixed adhesive-adherent failure [1]. Although FEA analyses can provide advantages and disadvantages, intrinsic and epistemic uncertainties that can affect experimental analysis are often not taken into account [2]. Studies involving the failure mechanisms of laminates and their failure mechanisms, such as failure with Cohesive Zone Model (CZM) in bonded composite joints, have shown interesting results [3-6]. Trapezoidal traction separation law (TSL) has been found to be a useful tool in such studies and can be applied to simulate brittle and ductile behaviour, depending on the failure type (*e.g.*, hybrid failure adhesive-laminate).

This work presents a contribution that applies trapezoidal traction separation law in two-dimensional models of Double Cantilever Beam specimens made of different carbon/epoxy laminates and adhesives. The numerical results are compared with experimental results of force x displacement, obtained using finite element models created using Abaqus® software [7]. The models employed a quadrilateral four-node plane strain element (CPE4R) to represent the composite adherents and a quadrilateral two-dimensional cohesive element (COH2D4) for the adhesive layer. Python™ scripts were used to generate all numerical models, which were then linked with Abaqus® software.

## 2. MATERIALS AND METHOD

To conduct this study, several steps were taken to obtain numerical simulations of DCB bonded composite joints. The traction separation laws were used to generate the simulations.

### 2.1. Numerical analysis

The numerical model used in this study is based on [8] and utilizes a Double Cantilever Beam (DCB) specimen made of carbon/epoxy with a pre-crack length ( $a_0$ ) of 58 mm, an adherent length ( $L$ ) of 120 mm, an adherent width ( $B$ ) of 21.5 mm, an adherent thickness ( $h$ ) of 1.82 mm, and an adhesive thickness ( $t_A$ ) of 0.2 mm. The geometric properties of the DCB specimen and boundary conditions are shown in Figure 1.



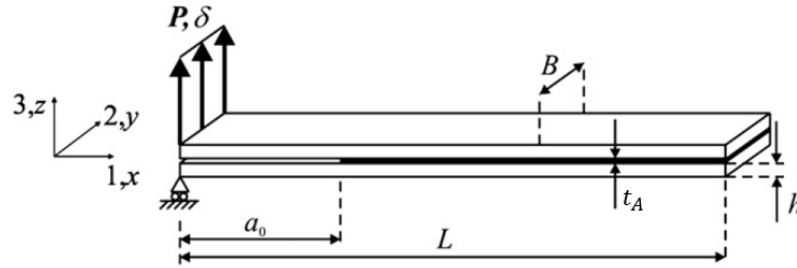


Figure 1 – DCB modelling containing its geometric dimensions:  $h$  – adherent thickness,  $a_0$  – pre-crack length,  $L$  – Adherent length,  $t_A$  – Adhesive thickness, and  $B$  – adherent width. (Adapted from [8]).

The DCB model used in this study employs a two-dimensional approach, which was implemented using Abaqus® software. To account for the large displacement/rotation fields that occur under increasing loadings, geometric non-linearity was considered. The DCB joint is modelled using two types of elements: a quadrilateral four-node plane strain element (CPE4R) to represent the composite adherent and a quadrilateral two-dimensional cohesive element (COH2D4) to represent the adhesive layer. A viscosity parameter of  $10^{-5}$  was applied to the COH2D4 element to improve its convergence. The use of this meshing size methodology ensured accurate numerical results. To generate all numerical models, macro-Python™ scripts were employed and linked with Abaqus® software.

## 2.2. Damage model

To model the damage degradation of the adhesive layer, this study utilized a traction separation law based on the Cohesive Zone Model [7] that takes into account the mechanical properties of the adhesive. Equation (1) was used to apply the damage variable ( $D$ ), and the relationship between traction and displacement was defined as follows:

$$t = (I - D)K\varepsilon, \quad (1)$$

where  $\mathbf{t}$  and  $\boldsymbol{\varepsilon}$  are the tensile and strain vectors,  $\mathbf{K}$  is the stiffness matrix, and  $I$  is the identity matrix.

Uncoupled behaviour ( $K_{ns} = K_{sn} = 0$ ) was taken into consideration in this study. Following the methodology described by Campilho *et al.* [8], normal stiffness was defined as  $K_{nn} = E$  and shear stiffness as  $K_{ss} = G$  for small adhesive thickness. The trapezoidal traction separation law was defined as tabular softening using Abaqus® [7] and based on [6].

Independent mode was employed in all simulations due to the loading, which was only in a single direction (pure mode I). The damage initiation was the quadratic damage stress (QUADS). This damage model becomes active when it reaches or exceeds a value of one, and is defined as follows:

$$f = \left\{ \frac{\langle t_n \rangle}{t_n^0} \right\}^2 + \left\{ \frac{t_s}{t_s^0} \right\}^2, \quad (2)$$

where  $t_n$  is the component normal to the cracked surface and  $t_s$  is the shear component of the cracked surface,  $t_n^0$  and  $t_s^0$  are the peak values of the nominal stresses.

### 3. RESULTS AND DISCUSSION

The numerical and experimental results are presented in Figure 2. In all cases, when  $r = 0.0$ , the TSL takes on a linear shape. Each set of numerical results with varying  $r$  values from 0.0 to 0.40 represents a different behaviour of the trapezoidal TSL, with notable differences between them. It was observed that as the  $r$  values increase, the peak values of force ( $P$ ) also increase, but not significantly.

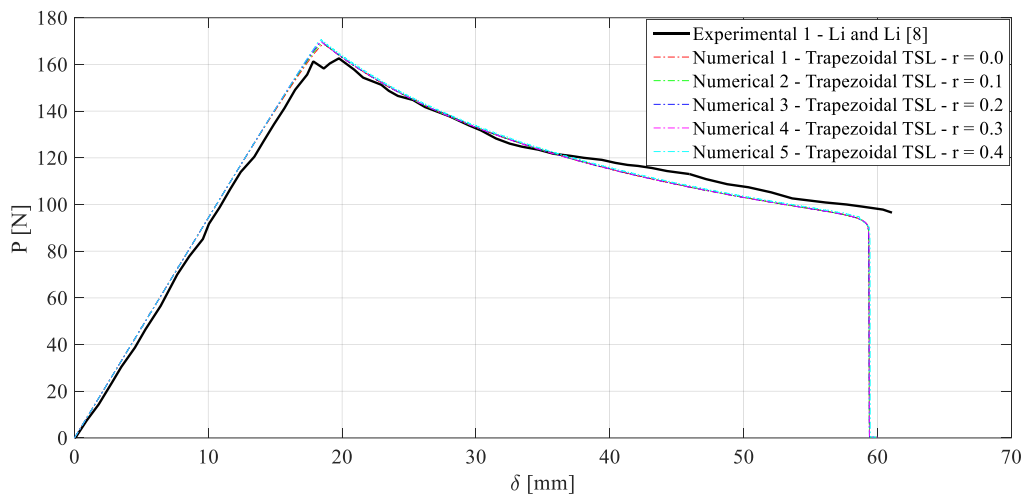


Figure 2 – Experimental and numerical results of DCB based on traction separation laws.

Although some discrepancies between numerical and experimental results were observed, the numerical models employed in this study offer several advantages. Specifically, the meshing size approach used in the simulations resulted in good agreement with experimental data. However, it is worth noting that there may have been modelling errors that could have impacted the numerical results [9]. To gain a deeper understanding of the relationship between various mechanical and geometric factors and fracture strength, the incorporation of statistical methods may be beneficial. Furthermore, employing other approaches could also help to refine both numerical and experimental investigations of mechanical failure in bonded composite joints subjected to pure mode I loading.

### 4. CONCLUSIONS

This study presents an interesting approach for evaluating the trapezoidal traction separation law [6] in Double Cantilever Beam bonded composite joints using two-dimensional Finite Element models based on experimental results [8]. The numerical approach used in the simulations showed good agreement with the experimental results, indicating the effectiveness of this methodology. However, it is important to consider possible modelling errors that could have influenced the numerical results. Future studies could incorporate statistical analysis to better understand the influence of mechanical and geometric variables on the force-displacement relationship in DCB bonded composite joints.

### ACKNOWLEDGEMENTS

The authors acknowledge the financial support of the Santa Catarina State Research and Innovation Foundation (FAPESC number: 2017TR1747, 2019TR779, and 2021TR843). As well as, Coordination for the Improvement of Higher-Level Personnel (CAPES Finance Code 001), PROMOP (Programa de Bolsas de Monitoria de Pós-Graduação) of the Santa Catarina State University. Ricardo de Medeiros acknowledges the financial support of the National Council for Scientific and Technological Development (CNPq process number: 304795/2022-4), and Volnei Tita acknowledges the National Council for Scientific and Technological Development (CNPq process number: 202491/2018-8).

## REFERENCES

- [1] L.F.M. Silva, A. Öchsner, R.D. Adams (Editors). *Handbook of Adhesion Technology*: Second Edition. Springer International Publishing, 1805 pages. (2018).
- [2] S. Omairey, N. Jayasree, M. Kazilas. Defect and uncertainties of adhesively bonded composite joints. *SN Applied Science*. 3:769. (2021).
- [3] I. Adarraga, N. Insausti, J. De Gracia, U. Osés. Applicability of and experimental procedure applied to DCB in adhesive joints. *International Journal of Adhesion & Adhesives*, v. 107, 102843. (2021).
- [4] J.P. Reis, M.F.S.F. Moura, R.D.F. Moreira, F.G.A. Silva. Pure mode I and II interlaminar fracture characterization of carbon-fibre reinforced polyamide composite. *Composites Part B*, v. 169, p. 126-132. (2019).
- [5] R.D.S.G. Campilho, M.F.S.F. Moura, D.A. Ramantani, J.P.M. Gonçalves. Obtaining the cohesive laws of a trapezoidal mixed-mode damage model using an inverse method. *Ciência e Tecnologia dos Materiais*, vol. 20, no 1-2. (2008).
- [6] M.S. Islam, K.S. Alfredsson. Peeling of metal foil from a compliant substrate. *The Journal of Adhesion*, vol. 97, no. 7, 672-703. (2021).
- [7] Dassault Systèmes. 2020. *Abaqus 6.20 documentation*. Analysis User's Manual.
- [8] G. Li, C. Li. An analytical analysis of energy release rate in bonded composite joints in a mode I condition. *Composites: Part B*, vol. 44, p. 704-713. (2013).
- [9] R.E. Melchers, A.T. Beck. *Structural Reliability Analysis and Prediction*. 3rd Edition. John Wiley & Sons. 506 pages. (2018).

## RESPONSIBILITY NOTICE

The authors are the only responsible for the printed material included in this manuscript.

# CRACK PROPAGATION DUE TO ANISOTROPIC DAMAGE IN ORTHOTROPIC MATERIALS

Carlos L. C. S. Esteves<sup>a</sup>, Jose L. Boldrini<sup>a</sup>, Marco L. Bittencourt<sup>a</sup>

<sup>a</sup>Universidade Estadual de Campinas, Department of Integrated Systems, School of Mechanical Engineering, 13083-970, SP, Brazil  
 c212012@dac.unicamp.br  
 josephbold@gmail.com  
 mlb@fem.unicamp.br

**Keywords:** Phase-field, Fracture, Orthotropy.

## 1. INTRODUCTION

One of the most important aspects in the design of mechanical components is the prediction of failure in materials. Identifying the places where cracks start, how they propagate and if they branch while evolving is a crucial aspect to be considered during the project phase. It is even more challenging when the material behaves differently depending on the loading directions and material anisotropy.

A crack is naturally described as an emerging surface, the result of accumulated energy, that splits the material into two separate regions. Several models have been developed over the last decades to predict cracking behavior, the majority of them using the finite element model (FEM). Numerically, a crack introduces discontinuities in the displacement field which are not easily implemented in a continuum mechanics (CM) framework.

One recent alternative is the use of phase-field models (PF) which introduces a continuous variable that represents the damage in the material [1-8]. The damage variable not only make easier the direct use of CM, but also overcomes most of the difficulties previously described due to the energetic description of the phenomenon.

Another complication when predicting complex crack paths is the consideration of local anisotropy induced by the fracture. The local degradation may introduce anisotropy in initially isotropic materials or change the original anisotropy of materials. This change in the material properties as a result of crack propagation is called local damage anisotropy.

Inspired by the previous seminal works [9-11], an anisotropic damage phase-field model was developed in a thermodynamically consistent framework based on [12]. In the present work, the degradation of the material properties is not given by the composition of a damage variable with any arbitrary degradation function. Instead, the degradation is defined by a fourth-order degradation tensor which is introduced as an internal variable and governed by an evolution law based on thermodynamic considerations. Further details can be found in [13].

## 2. PHASE-FIELD FORMULATION

Based on considerations from [12], the following governing equations are obtained:

$$\rho \ddot{\mathbf{u}} = \text{div} \mathbf{T} + \mathbf{f}, \quad (1)$$

$$\mathbf{T} = (\mathbb{G} : \mathbb{C}^0 : \mathbb{G}) : \mathbf{E} - \text{sym}(g_c l \nabla \mathbb{G} :: \nabla \mathbb{G}) + \hat{b} \mathbf{D}, \quad (2)$$

$$\dot{\mathbb{G}} = -\hat{F} [\mathbf{E} \otimes (\mathbb{C}^0 : \mathbb{G} : \mathbf{E})]^{\hat{s}} - \hat{F} \frac{g_c}{l} \kappa (\mathbb{G} - \mathbb{I}_s) + \hat{F} g_c l \text{div}(\nabla \mathbb{G}), \quad (3)$$

where  $\rho$  is the material density,  $\mathbf{u}$  is the displacement vector,  $\mathbf{T}$  is the Cauchy stress tensor,  $\mathbf{f}$  is the body force vector,  $\mathbb{C}^0$  is the virgin fourth-order elasticity tensor,  $\mathbb{G}$  is the fourth-order degradation tensor,  $\mathbf{E}$  is the linear strain tensor,  $\mathbf{D}$  is the symmetric part of the velocity gradient,  $g_c$  is the Griffith energy fracture,  $l$  is the length-scale parameter,  $\kappa$  is a material parameter that controls crack propagation,  $\hat{F}$  and  $\hat{b}$  are

positive constants,  $\mathbb{I}_s$  is the fourth-order symmetric identity tensor and  $\mathbb{G}$  is the fourth-order degradation tensor.

The presented equations were derived under the assumptions of small strains, isothermal conditions and plane strain state. The term  $\mathbb{G} : \mathbb{C}^0 : \mathbb{G}$  is responsible for the anisotropic degradation of the material and represents the degraded elasticity tensor ( $\mathbb{C}$ ). The minor and major symmetries of  $\mathbb{G}$  are necessary to ensure the symmetry of the stress tensor. For plane strain state, the original 81 components of  $\mathbb{G}$  are reduced to 6 independent components.

Unlike the scalar damage variable, which associates value zero as corresponding to the virgin state, the approach using the degradation tensor associates the tensor-value  $\mathbb{I}_s$  to the virgin state. From the evolution equation. (3), the change in the degradation tensor is driven by the current strain state of the material; the first term in Eq. (3) is the main contribution to the evolution rate  $\dot{\mathbb{G}}$  and is dictated by the relevant strains components.

After obtaining the weak form, the equations are discretized and solved separately for the displacement field and then for the degradation tensor field. The standard implicit Newmark method is used to solve for the displacement field and a backward Euler method is used to solve for the degradation field with the updated displacement field.

## 2.1. Material model

The fourth-order elasticity tensor  $\mathbb{C}^0$  can represent an anisotropic or an initially isotropic elastic state of the material. From the derivative of the elastic energy, we have the general expression for the stress

$$\mathbf{T} = \mathbb{G} : \mathbb{C}^0 : \mathbb{G} : \mathbf{E}. \quad (4)$$

A generic orthotropic material has 9 independent components and are necessary to obtain the reduced  $3 \times 3$  matrix to represent the degraded elasticity tensor. Before applying this transformation, the original material directions can be rotated by an arbitrary angle  $\alpha$  for orthotropic materials not aligned with the global system of coordinates [15].

From Eq. (4), it can be seen that the components of the elasticity tensor are multiplied by a squared term of the degradation tensor, which is the tensor analogy to the quadratic degradation function in traditional phase-field models. As the degradation progresses, the norm of  $\mathbb{C}$  decreases and the stress decreases as well to the point where larger strains result in almost no stress (very soft or lack of material).

## 2.2. Damage criterion

As the phase-field variable used here is a fourth-order tensor, it is initially difficult to assess how much the material has degraded by just looking at each of the six independent components of the degradation tensor. It is necessary to establish a parameter that summarizes the nodal degradation based on these tensor components.

For this, we introduce a scalar variable  $\zeta_r$  to represent the local relative damage resulting from a given degradation tensor  $\mathbb{G}$ . Defining  $\zeta_n$  as the geometric mean of the eigenvalues of the degraded elasticity tensor at time  $n$ , then we have:

$$\zeta_r = \frac{\zeta_n}{\zeta_0}. \quad (5)$$

This scalar variable is the relative measurement of the degradation applied for a given node. These eigenvalues can be understood as the energy density for the material considering an unitary strain in the direction of its normalized eigenvector. If it is close to zero, then the material is softer in that respective direction and is closer to failure [15]. Since more than one eigenvalue can be degraded for given a degradation state, the geometric mean is a reliable measure to uniformly track the effect of the degradation on the material node.

Initially,  $\zeta_r = 1$  and as the degradation progresses,  $\zeta_r \rightarrow 0$  at failure. This behavior is similar to the standard scalar phase-field methods except we also have the possibility of analyzing the degradation components and understand failure mechanisms behind the scalar variable. Additionally,

we can guarantee damage irreversibility by enforcing the condition that  $\zeta_r$  does not increase at each time-step.

### 3. RESULTS

In terms of crack prediction and propagation, an interesting example is the case of “guided fractures”, where the crack is forced to follow a specific path in order to protect other regions where a more valuable component or material is located.

Adapting the examples from [16,17], three configurations were adopted and simulated using an orthotropic generic brittle material. Isothermal and plane strain conditions are considered. The geometry and boundary conditions of the domain are given in Fig. 1. A vertical tractive displacement is imposed on both top and bottom boundary lines with rate 0.005 m/s. The shape of the initial holes are isosceles triangles and  $\frac{h_2}{h_1} = 2$ . Height  $H=0.3$  m and width  $W=0.5$  m.

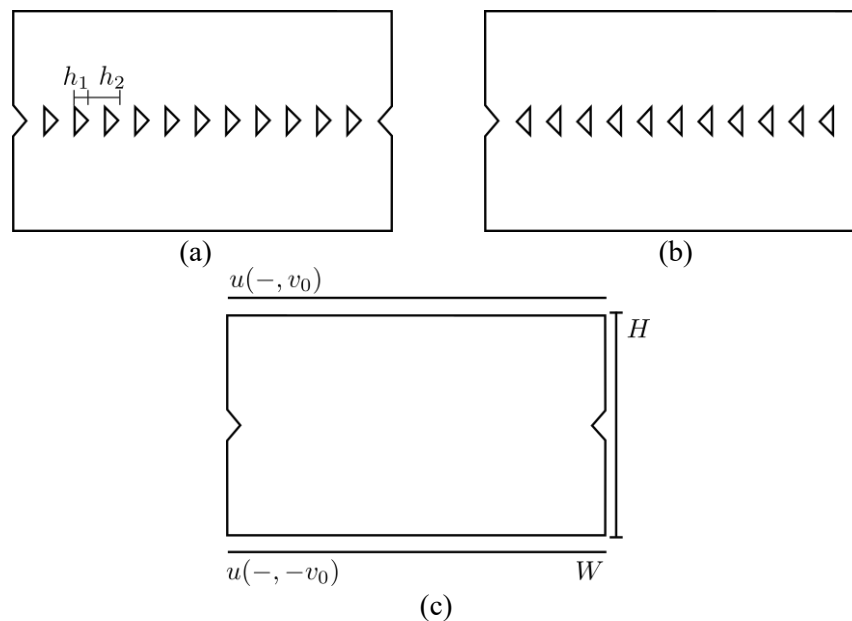


Figure 1 - Configurations for the guided fractures: forward (a), backward (b), and bi-notched with no holes.

The results are illustrated in terms of the  $\zeta_r$  field where the blue region means crack. All images have the same scale from 0 to 1. The first configuration is the plate with no holes in each side. Since we have a dynamic model, the total time is 2.0 s and 200 time-steps were used. Figure 2 shows the results for the case with no holes. A mesh of 44984 four node quadrilateral elements was used for Fig. 2(a) and 164218 four node quadrilateral elements was used for Fig. 2(b).

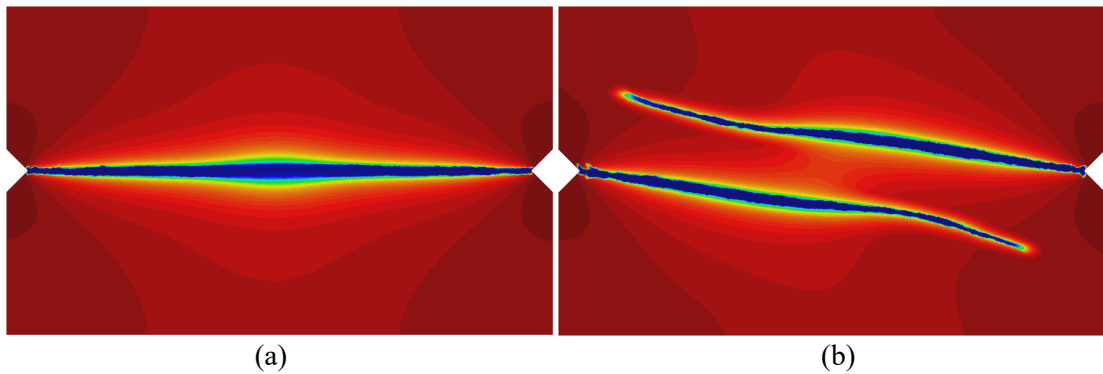


Figure 2 - Crack propagation for the bi-notched specimen with no holes. Two material directions are considered (a) 0° and (b) 10°.

As this is an orthotropic material, the material directions can be rotated around the out-of-plane axis. Figure 2(b) shows the crack propagation when 10° rotation is considered. The first result is expected given the boundary conditions, while the second shows an interesting path influenced by the change in the direction of highest stiffness.

The next example is the forward configuration. For this case, the total time is 0.5 s and 200 time-steps were used. The mesh has 41779 four node quadrilateral elements. Figure 3 shows the evolution of the crack with no rotation of the material directions.

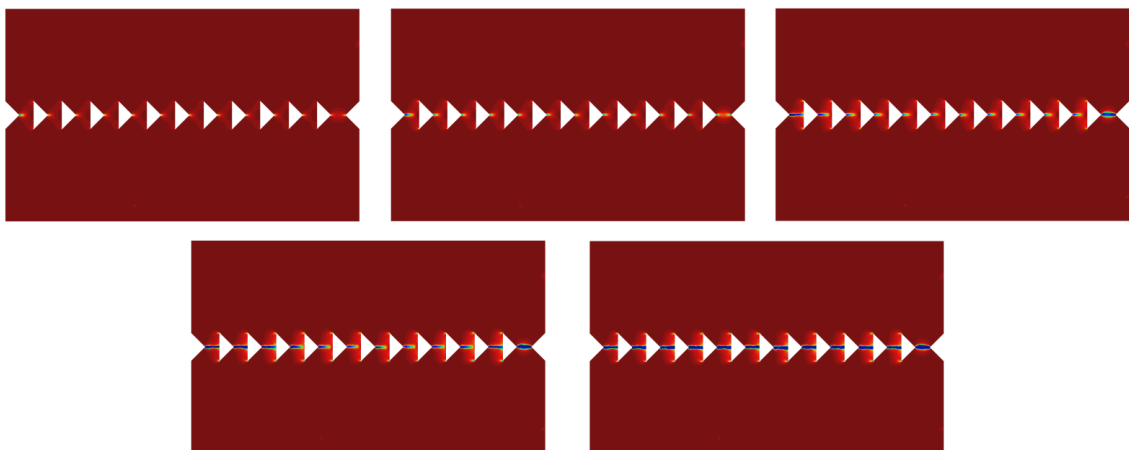


Figure 3 - Crack evolution for the forward configuration.

Due to the phase-field model considered in this work, the material is taken as initially virgin and homogeneous everywhere. Because of this, the crack initiates at the tip of nearly every triangular hole at the same time, but the propagation proceeds from left to right. Unlike [16], before crack propagation appears on the entire domain, failure happens at the right-most side of the plate where the tips of two triangular holes face each other.

Figure 4 shows the crack pattern for the forward scheme when a 45° rotation is considered. Unlike the previous result, every crack starts at the same time from the tips and reaches the next hole at the same time.

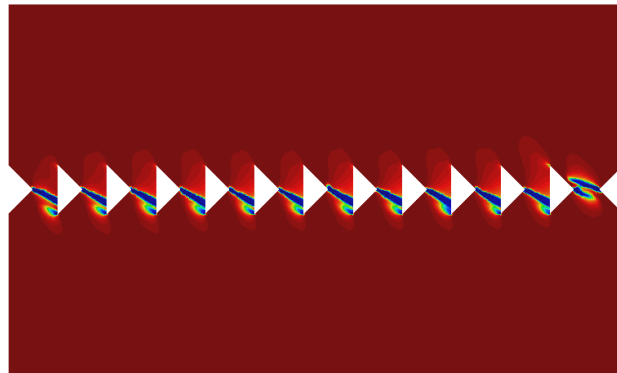


Figure 4 - Crack propagation for the forward scheme specimen when rotation of 45° is considered.

The final example is the backward configuration. For this case, the total time is 0.7 s and 140 time-steps were used. This mesh has 41940 four node quadrilateral elements. Figure 5 shows the crack evolution when no rotation of the material directions is considered.

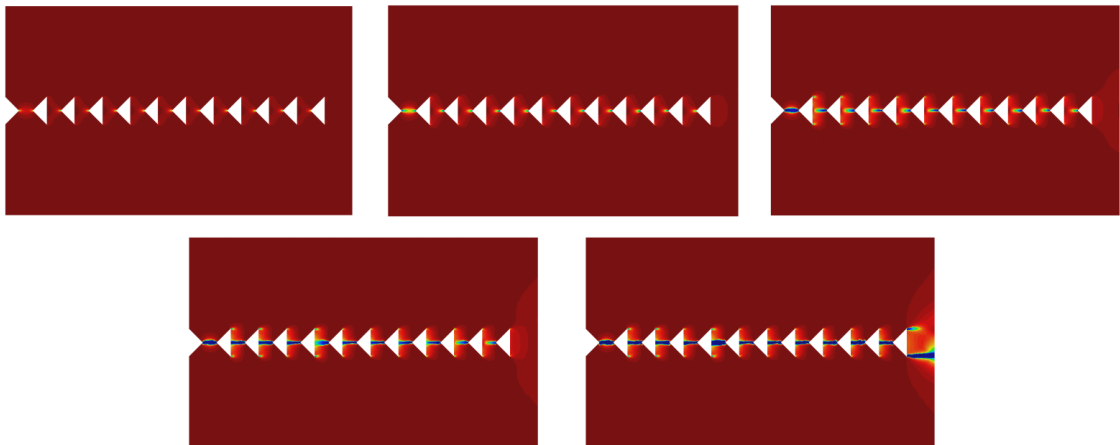


Figure 5 - Crack evolution for the backward scheme configuration.

Figure 5 shows an interesting result regarding the crack propagation. As with Fig. 3, the crack initiates simultaneously at the tip of the triangular holes, but now it propagates from right to left until the next hole. However, the left-most cracks complete the propagation first and right-most holes finish the propagation later. Therefore, while each individual crack goes from right to left, the whole specimen fractures (domain separation) from left to right. The same behavior was experimentally observed in [17].

Lastly, Fig. 6 shows the crack pattern for the backward scheme when a rotation of 30° is considered for the material direction. The same crack propagation behavior is observed and nearly all individual cracks propagate at the same time. Once again, the rotation of the material directions influences the slope of the exit crack.



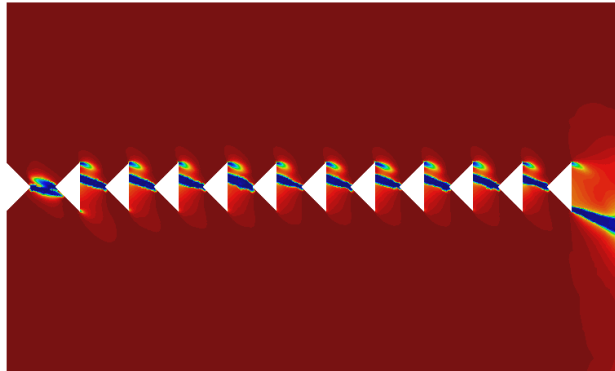


Figure 6 - Crack propagation for the backward specimen when a rotation of  $30^\circ$  is considered.

#### 4. CONCLUSIONS

The previously developed phase-field model with a fourth-order degradation tensor was used to predict crack nucleation and propagation in orthotropic material. Crack patterns were analyzed for different configurations and fiber directions of the material.

Each configuration had “guiding” holes in triangular shape across the middle of the plate. The model was capable of tracking failure according to the presence and to the position of the holes in the plates. It was also able of dealing with the change in the material directions where the coupling between the normal and shear components has more influence in the material behavior.

Overall, the results are in good agreement with the literature in both crack propagation and nucleation. Experimental results are still needed to validate the propagation in plates where the material directions are not aligned with the global system.

#### ACKNOWLEDGEMENTS

This work was supported by the Conselho Nacional de Pesquisa Científica e Tecnológica under grand number 140214/2022-4.

#### REFERENCES

- [1] S. Goswami, C. Anitescu, T. Rabczuk, *Adaptive fourth-order phase field analysis for brittle fracture*, Computer Methods in Applied Mechanics and Engineering 361 (2020).
- [2] J. Jaric, D. Kuzmanovic, D. Sumarac, *On anisotropic elasticity damage mechanics*, International Journal of Damage Mechanics 22 (2013) 1023– 1038.
- [3] S. Wulfinghoff, M. Fassin, S. Reese, *A damage growth criterion for anisotropic damage models motivated from micromechanics*, International Journal of Solids and Structures 121 (2017) 21– 32.
- [4] R. Ma, W. Sun, *FFT-based solver for higher-order and multi-phase-field fracture models applied to strongly anisotropic brittle materials*, Computer Methods in Applied Mechanics and Engineering 362 (2020).
- [5] L. Svoulos, H. M. Mourad, G. Manzini, K. Garikipati, *A fourth-order phase-field fracture model: Formulation and numerical solution using a continuous/discontinuous Galerkin method*, Journal of the Mechanics and Physics of Solids 165 (2022).
- [6] R. Alessi, F. Freddi, *Phase-field modelling of failure in hybrid laminates*, Composite Structures 181 (2017) 9–25.
- [7] T. T. Nguyen, J. Réthoré, J. Yvonnet, M. C. Baietto, *Multi-phase-field modeling of anisotropic crack propagation for polycrystalline materials*, Computational Mechanics 60 (2017) 289–314.
- [8] V. Ziaei-Rad, M. Mollaali, T. Nagel, O. Kolditz, K. Yoshioka, *Orthogonal decomposition of anisotropic constitutive models for the phase field approach to fracture*, Journal of the Mechanics and Physics of Solids 171 (2023).

- [9] G. A. Francfort, J. J. Marigo, *Revisiting brittle fracture as an energy minimization problem*, Journal of the Mechanics and Physics of Solids 46 (1998) 1319–1342.
- [10] B. Bourdin, G. A. Francfort, J. J. Marigo, *Numerical experiments in revisited brittle fracture*, Journal of the Mechanics and Physics of Solids 48 (2000) 797–826.
- [11] C. Miehe, F. Welschinger, M. Hofacker, *Thermodynamically consistent phase-field models of fracture: Variational principles and multi-field FE implementations*, International Journal for Numerical Methods in Engineering (2010).
- [12] J. L. Boldrini, E. A. B. D. Moraes, L. R. Chiarelli, F. G. Fumes, M. L. Bittencourt, *A non-isothermal thermodynamically consistent phase field framework for structural damage and fatigue*, Computer Methods in Applied Mechanics and Engineering 312 (2016) 395–427.
- [13] A.L.E.R. Petrini, C.L.C.S. Esteves, J.L. Boldrini, M.L. Bittencourt, *A fourth-order degradation tensor for an anisotropic damage phase-field model*, Forces in Mechanics, 12 (2023).
- [14] B. Li, C. Maurini, *Crack kinking in a variational phase-field model of brittle fracture with strongly anisotropic surface energy*, Journal of the Mechanics and Physics of Solids 125 (2019) 502–522.
- [15] A. G. Neeman, R. Brannon, B. Jeremic, A. V. Gelder and A. Pang. *Decomposition and visualization of fourth-order elastic-plastic tensors*. IEEE/EG Symposium on Volume and Point-Based Graphics, 2008.
- [16] L. C. Felix, D. S. Galvão, *Guided fractures in graphene mechanical diode-like structures*, Phys. Chem. Chem. Phys. (2002).
- [17] N. R. Brodnik, S. Brach, C. M. Long, G. Ravichandran, B. Bourdin, K. T. Faber, K. Bhattacharya. *Fracture Diodes: Directional Asymmetry of Fracture Toughness*. Phys. Rev. Lett. (2021).

#### RESPONSIBILITY NOTICE

The authors are the only responsible for the printed material included in this manuscript.

## DISPERSION PROBLEMS FOR A ONE-DIMENSIONAL PERIODIC MEDIUM USING THE THREE-SCALE HOMOGENIZATION METHOD

Carlos Núñez Almaguer<sup>a</sup>, Laura Saez Lombira<sup>a</sup>, Reinaldo Rodríguez-Ramos<sup>a,b</sup>,  
 Raúl Guinovart-Díaz<sup>a</sup>, Humberto Brito Santana<sup>c</sup>

<sup>a</sup>Faculty of Mathematics and Computing Science, University of Havana  
 San Lázaro and L, Vedado, La Habana, CP 10400, Cuba  
[charles.almaguer4501@gmail.com](mailto:charles.almaguer4501@gmail.com), [laura.lombira@gmail.com](mailto:laura.lombira@gmail.com), [guino@matcom.uh.cu](mailto:guino@matcom.uh.cu)

<sup>b</sup>Universidade Federal Fluminense  
 Av. Dos Trabalhadores 420, Vila Sta, Cecília, CP 27255-125 Volta Rodonda, RJ, Brasil  
[reinaldorr@id.uff.br](mailto:reinaldorr@id.uff.br), [reinaldo@matcom.uh.cu](mailto:reinaldo@matcom.uh.cu)

<sup>c</sup>Departamento de Matemática, Universidad Tecnológica Metropolitana,  
 Las Palmeras 3360, Ñuñoa, Santiago de Chile, Chile  
[h.britos@utem.cl](mailto:h.britos@utem.cl)

**Keywords:** Asymptotic Homogenization, Local Problem, Effective Coefficients.

### 1. INTRODUCTION

The homogenization process is a mathematical tool that allows the study of heterogeneous materials based on the macro-micro properties and characteristics of the constituents. In the present work, the Asymptotic Homogenization Method will be applied to 1-dimensional hyperbolic problems, with periodic and rapidly oscillating coefficients. The proposed model is an extension of the results obtained in [1] but in this case using three-scale expansion. A numerical algorithm is also proposed to perform the corresponding calculations, based on examples from [2]. They are observed limit cases considering a static model, validating the results of [3].

### 2. METHOD OF THREE SCALE DYNAMIC HOMOGENIZATION

As the problem that is studied is one-dimensional, it is considered a non-homogeneous bar composed of  $n$  small bars of length  $l \ll L$  and composed each one by different homogeneous elastic materials with Young Module  $E_i$  and density  $\rho_i$ . The bar of length  $L$  is also under a force action.

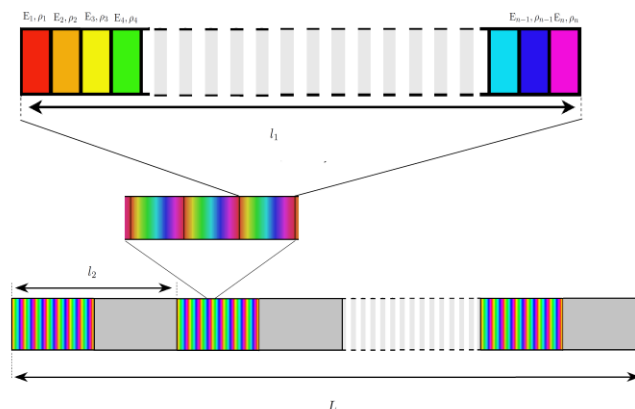


Figure 1: One-dimensional periodic bar composed of  $n$  materials arranged periodically, with cells of periodicity size  $l_1$  and  $l_2$  at each structural level respectively.

The bar is assumed with Young's module  $E(y, z)$  is a differentiable, positive, bounded and one-periodic function that depends on the rapid variables  $y = x / \varepsilon_1$  and  $z = y = x / \varepsilon_2$ , where  $\varepsilon_1$  y  $\varepsilon_2$  are small parameters relative to each variable,  $\varepsilon_2 < \varepsilon_1$ . The problem consists on find the solution of the 1-periodic function  $u(x, y, z, t)$ , regarding the variables  $y$  and  $z$  which satisfies the equation that describes the problem. The conditions at the edges are  $u|_{z=0} = g_1$  and  $u|_{z=L} = g_2$ ,  $g_1$  and  $g_2$  are initial and final displacement.

The equation of the dynamic process in one dimensional can be written as

$$\frac{d}{dx} \left( E(y, z) \frac{d}{dx} u(x, y, z, t) \right) - \rho(y, z) \frac{\partial^2}{\partial t^2} u(x, y, z, t) = 0. \quad (1)$$

The solution of the problem can be found by an asymptotic expansion in terms of  $\varepsilon_1$  and  $\varepsilon_2$ , and a convenient truncation will be carried out

$$u^{\varepsilon_1 \varepsilon_2}(x, y, z, t) = u_0(x, y, z, t) + \varepsilon_1 u_1(x, y, z, t) + \varepsilon_1^2 u_2(x, y, z, t) + \varepsilon_2 u_3(x, y, z, t) + \varepsilon_1 \varepsilon_2 u_4(x, y, z, t) + O(\varepsilon_2). \quad (2)$$

Expressions for each  $u_i(x, y, z, t)$  of the “Eq. (2)” are found in [3] and [4].

Substituting “Eq.(2)” in “Eq.(1)” a system of differential equation is derived, can be solved originating the First and Second Local Problem used to obtain the Homogenization Problem.  
 The First Local Problem

$$\begin{cases} \frac{d}{dz} \left( E(y, z) \frac{dM}{dz} + E(y, z) \right) = 0, \\ M(y, z) = 0, \quad z \in \partial Z, \end{cases} \quad (3)$$

where  $M^{(i)}(y, z) = M^{(i+1)}(y, z)$  and  $E^{(i)}(y, z) \frac{d}{dy} M^{(i)}(y, z) + E^{(i)}(y) = E^{(i+1)}(y, z) \frac{d}{dy} M^{(i+1)}(y, z) + E^{(i+1)}(y, z)$ ,

where the superscripts are the references phases in the composite material.

The Second Local Problem

$$\begin{cases} \frac{d}{dy} \left( \hat{E}(y) \frac{d}{dy} N(y) + \hat{E}(y) \right) = 0, \\ N(y) = 0, \quad y \in \partial Y, \end{cases} \quad (4)$$

where  $N^{(i)}(y) = N^{(i+1)}(y)$  and  $\hat{E}^{(i)}(y) \frac{d}{dy} N^{(i)}(y) + \hat{E}^{(i)}(y) = \hat{E}^{(i+1)}(y) \frac{d}{dy} N^{(i+1)}(y) + \hat{E}^{(i+1)}(y)$ ,

where the superscripts are the references phases in the composite material.

The functions  $M(y, z) = \hat{E}(y) \int_0^z E^{-1}(y, z) dz - z$  and  $N(y) = \tilde{E} \int_0^y (\hat{E}(y))^{-1} dy - y$  are the solution of the First and Second Local Problem respectively where  $\hat{E}(y) = \left( \int_0^1 E^{-1}(y, z) dz \right)^{-1}$  and  $\tilde{E} = \left( \int_0^1 \int_0^1 E^{-1}(y, z) dz dy \right)^{-1}$  are the intermediate and global effective coefficient respectively used to find the homogenized problem

$$\tilde{E} v_{xx} = \tilde{\rho} v_u \quad , \quad \tilde{\rho} = \int_0^1 \int_0^1 \rho(y, z) dz dy. \quad (5)$$

The homogenized problem (“Eq.(5)”) can be solved using the variable separable method.

### 3. NUMERICAL RESULTS

#### 3.1 Static Case

The following problem has been extracted from [2]. The exact solution of the dispersion relation is  $u^e(x) = x$  and was determined in [2].

Applying the homogenization method,

$$\hat{E}(y) = \left( \int_0^1 (1 + 0.25 \sin(2\pi y) \cos(2\pi z)) dz \right)^{-1} = 1, \quad (6)$$

$$\tilde{E} = \left( \int_0^1 \int_0^1 (1 + 0.25 \sin(2\pi y) \cos(2\pi z)) dz dy \right)^{-1} = 1. \quad (7)$$

Since it is a static case  $\rho(y, z) \frac{\partial^2}{\partial t^2} u(x, y, z, t) = 0$ .

As a result, the homogenized problem is

$$\{v_{xx} = 0, \quad v(0) = 0, \quad v(1) = 1, \quad (8)$$

which when solved gives the expression  $v(x) = x$ ,

$$M(y, z) = \hat{E}(y) \int_0^z E^{-1}(y, z) dz - z = \frac{0.125}{\pi} \sin(2\pi y) \sin(2\pi z), \quad (9)$$

$$N(y) = \tilde{E} \int_0^y \hat{E}(y) dy - y = 1 \int_0^y 1 dy - y = y - y = 0. \quad (10)$$

$$u^{\varepsilon_1 \varepsilon_2} \left( x, \frac{x}{\varepsilon_1}, \frac{x}{\varepsilon_2} \right) = x + \varepsilon_2 \frac{0.125}{\pi} \sin \left( \frac{2\pi x}{\varepsilon_1} \right) \sin \left( \frac{2\pi x}{\varepsilon_2} \right). \quad (11)$$

The graph “Fig. 2.a” shows the similarity of the exact solution and the solution obtained from the homogenization method for values of  $\varepsilon_1$  and  $\varepsilon_2$ .

#### 3.2 Dynamical Case

The next problem is extracted from [2] section 8A, a problem, which consists of a dynamic case in which it has composed with periodicity cell formed by two homogeneous materials.

Applying the homogenization method

$$\hat{E}(y) = \left( \int_0^1 E^{-1}(y) dz \right)^{-1} = E(y), \quad (12)$$

$$\tilde{E} = \left( \int_0^1 \int_0^1 E^{-1}(y) dz dy \right)^{-1} = 11,43 \text{ GPa} \quad , \quad \tilde{\rho} = \int_0^{1/2} \rho_1 dy + \int_{1/2}^1 \rho_2 dy = 5500 \text{ kg/m}^3. \quad (13)$$

The homogenized problem is  $2077922, 25v_{xx} = v_n$ , applying the method of variables separation,

$$v(x, t) = \sum_{n=1}^{\infty} \sin \left( \frac{(2n-1)\pi}{L} x \right) C_n \cos \left( \frac{(2n-1)a\pi}{L} t \right). \quad (14)$$

where

$$\text{for } \delta = 0.6: C_n = \frac{2}{L} \int_{19,4}^{20,6} 59.537(x - 20.6)^4(x - 19.4)^4 \sin\left(\frac{(2n-1)\pi}{L}x\right), \quad (15)$$

$$\text{for } \delta = 1.4: C_n = \frac{2}{L} \int_{18,6}^{21,4} 0.06776(x - 21.4)^4(x - 18.6)^4 \sin\left(\frac{(2n-1)\pi}{L}x\right). \quad (16)$$

Now, it proceeds to the computational calculation to find  $v(x, t)$ .

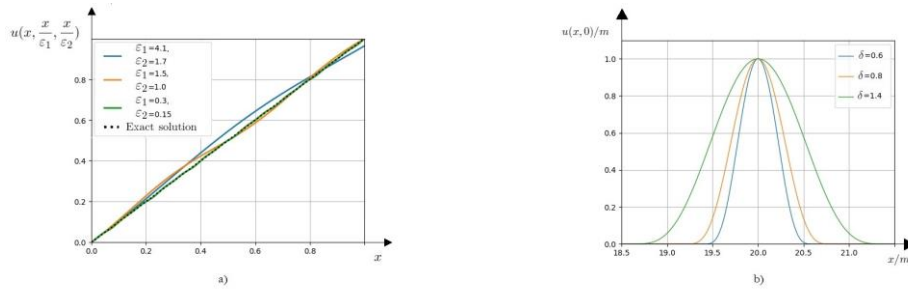


Figure 2: figure a) Similarity of the homogenization obtained solution with the exact solution, static case, figure b) Shape and position of the initial pulses used for numerical illustration, dynamic case.

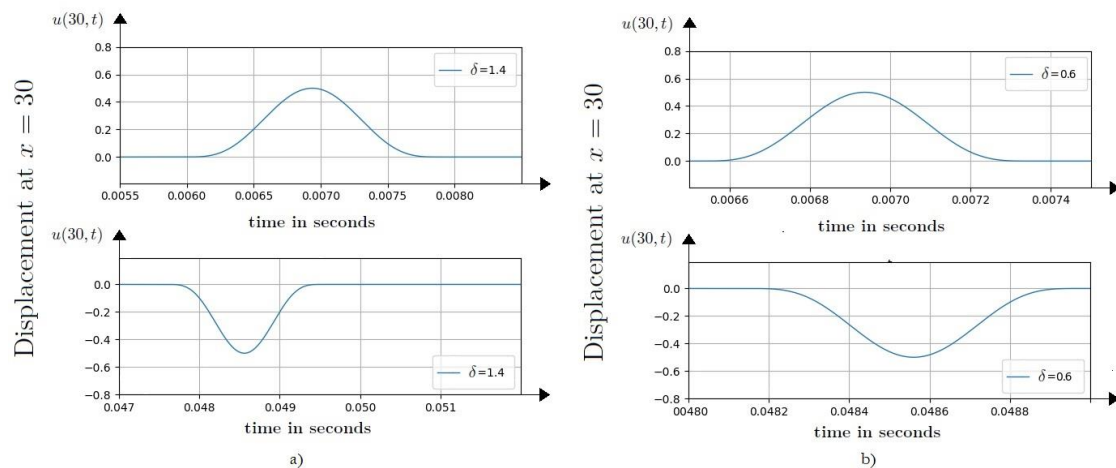


Figure 3: Value of the solution at  $x = 30$  m as a function of time: figure a) for  $\delta = 1.4$ , figure b) for  $\delta = 0.6$ .

## REFERENCES

- [1] J. Vivar Pérez. *Dispersión de ondas en materiales compuestos provistos de estructura periódica*. Tesis de Licenciatura en Matemática. Universidad de La Habana. (2002)
- [2] J. Vivar Pérez, U. Gabbert, H. Berger, R. Rodríguez-Ramos, J. Bravo-Castillero, R. Guinovart-Díaz, F. Sabina, J. A. *A dispersive nonlocal model for wave propagation in periodic composites*. Journal of Mechanics of Materials and Structures Vol 4, No.5. (2009)
- [3] Álvarez Borges. *Homogeneización reiterada de problemas elípticos unidimensionales*. Tesis de Licenciatura en Matemática. Universidad de La Habana. (2015)
- [4] G. Xiaofei, L. Xian, J. Xin, Y. Yong, C. Junzhi, M. Herbert. *A stochastic multiscale model for predicting mechanical properties of fiber reinforced concrete*. International Journal of Solids and Structures, p. 56-57. (2015)
- [5] Y. Zihao, Z. Yang, D. Hao, C. Junzhi, G. Xiaofei, Y. Zhiqiang. *High-order three-scale method for mechanical behavior analysis of composite structures with multiple periodic configurations*. Composites Science and Technology 152. (2017).

# DYNAMIC ASYMPTOTIC HOMOGENIZATION FOR MAGNETO-ELECTRO-ELASTIC PERIODIC LAYERED COMPOSITE WITH IMPERFECT INTERFACE

Mriganka Shekhar Chaki<sup>a</sup>, Julián Bravo-Castillero<sup>a</sup>

<sup>a</sup>Unidad Académica, Instituto de Investigaciones en Matemáticas Aplicadas y Sistemas (IIMAS), Universidad Nacional Autónoma de México (UNAM), Parque Científico y Tecnológico de Yucatán, CP 97302, Yucatán, México

E-mail: [mriganka.shekhar@iimas.unam.mx](mailto:mriganka.shekhar@iimas.unam.mx) (Mriganka Shekhar Chaki)  
[julian@mym.iimas.unam.mx](mailto:julian@mym.iimas.unam.mx) (Julián Bravo-Castillero)

**Keywords:** Dynamic asymptotic homogenization; Magneto-electro-elastic media; Laminated composite; Anti-plane wave; Imperfect bonding

## 1. INTRODUCTION

The Magneto-Electro-Elastic (MEE) materials exhibit coupling effect and transform energy between elastic, electric and magnetic fields due to which such materials have numerous applications in ultrasonic imaging devices, detectors, energy harvesters, smart sensors. In particular, multi-laminated or multilayered magneto-electro-elastic structures have been the subject of interest in recent studies. Several homogenization techniques have been applied to investigate the effective properties of magneto-electro-elastic composites for static case [1]. The Asymptotic Homogenization Method (AHM) is proven to be a powerful tool for the prediction of global or effective properties for composites with small-scale heterogeneities and it is well documented in the book of Bakhvalov and Panasenko [2]. Bravo-Castillero et al. [3] gave a unified general formula for effective properties by applying AHM to magneto-electro-elastic multilaminated materials. Recently, Caballero-Perez et al. [4] calculated effective thermo-magneto-electro-elastic properties of laminates with non-uniform imperfect contact.

In dynamic problems, the physical role of the scale effects is more significant. For example, in elastodynamics, if the traveling wavelength is comparable to the size of the material's heterogeneities, then successive wave dispersion phenomena can be observed. Craster et al. [5] suggested a high-frequency asymptotic homogenization method for periodic media. Later, Brito-Santana et al. [6] studied a dispersive nonlocal model for shear wave propagation in laminated triclinic composites with periodic structures. Later, Brito-Santana et al. [6] studied the similar laminated structure with imperfect interface. Consideration of imperfect interface resembles realistic scenario in case of laminated structure. To the best of authors' knowledge, dynamic asymptotic homogenization has not yet been applied to study dispersive phenomena for the MEE laminated composite periodic structure with imperfect interface.

## 2. ANTI-PLANE WAVE PROBLEM

In the present study, we consider a Magneto-Electro-Elastic (MEE) laminate occupying a region  $\Omega = (0,1)^3 \subset \mathbb{R}^3$  with Lipschitz boundary  $\partial\Omega$ . The region  $\Omega$  is made up by  $N$  identical sets of  $p$  laminae that are stacked along  $x_1$ -direction (direction may also be taken arbitrarily) (see Figure 1). A

small positive parameter  $\varepsilon = \frac{1}{N} \ll 1$  is assumed that characterizes the periodicity of the composite. The local cell  $Y$  is chosen as a set of  $p$  laminae that constructs the laminate by repeating itself.

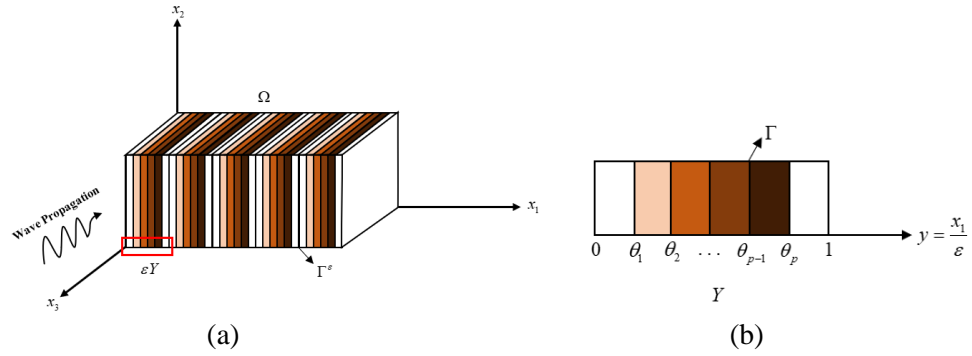


Figure 1 – (a) MEE laminate stacked periodically in the  $x_1$ -direction; (b) unit local cell.

The anti-plane problem is formulated in a bounded subset  $\Omega^\varepsilon$  of  $\mathbb{R}^2$ , i.e. a boundary-value problem within a two-dimensional domain in  $x_1x_2$ -plane, where

$$Y = \left\{ \mathbf{y} = (y_1, y_2) \in \mathbb{R}^2 \mid 0 < y_i < 1, i = 1, 2 \right\}, \quad \Omega^\varepsilon = \varepsilon Y = \left\{ \mathbf{x} = (x_1, x_2) \in \mathbb{R}^2 \mid \frac{x_i}{\varepsilon} \in Y, i = 1, 2 \right\}$$

where  $\mathbf{y} = \frac{\mathbf{x}}{\varepsilon}$ . The equation of motion along with boundary conditions for anti-plane problem can be written as:

$$\frac{\partial}{\partial x_j} \left( M_{jl}^\varepsilon \frac{\partial U^\varepsilon}{\partial x_l} \right) = \mathcal{P}^\varepsilon \frac{\partial U^\varepsilon}{\partial t^2}, \quad \mathbf{x} \in \Omega^\varepsilon \setminus \Gamma^\varepsilon \quad (1)$$

along with imperfect interface condition:

$$\Sigma_j^\varepsilon n_j \equiv M_{jl}^\varepsilon \frac{\partial U^\varepsilon(\mathbf{x})}{\partial x_l} n_j = K^\varepsilon \left[ U^\varepsilon(\mathbf{x}) \right] = 0, \quad \text{and} \quad \left[ \Sigma_j^\varepsilon \right] n_j = 0, \quad \mathbf{x} \in \Gamma^\varepsilon$$

and at the boundary  $U^\varepsilon = \tilde{U}$ ,  $\mathbf{x} \in \partial\Omega_1^\varepsilon$  and  $\Sigma_j^\varepsilon n_j = \tilde{S}$ ,  $\mathbf{x} \in \partial\Omega_2^\varepsilon$ , where  $n_j$  is the unit vector in the outward normal direction and

$$M_{jl}^\varepsilon = M_{jl}(y_1, y_2) = \begin{pmatrix} c_{3j3l}^\varepsilon & e_{j3l}^\varepsilon & q_{j3l}^\varepsilon \\ e_{j3l}^\varepsilon & -\kappa_{jl}^\varepsilon & -\alpha_{jl}^\varepsilon \\ q_{j3l}^\varepsilon & -\alpha_{jl}^\varepsilon & -\mu_{jl}^\varepsilon \end{pmatrix}, \quad \Sigma_j^\varepsilon = \begin{pmatrix} \sigma_{3j}^\varepsilon \\ D_j^\varepsilon \\ B_j^\varepsilon \end{pmatrix}, \quad U^\varepsilon = \begin{pmatrix} u_3^\varepsilon \\ \phi^\varepsilon \\ \psi^\varepsilon \end{pmatrix}, \quad \mathcal{P}^\varepsilon = \begin{pmatrix} \rho^\varepsilon & 0 & 0 \\ 0 & 0 & 0 \\ 0 & 0 & 0 \end{pmatrix},$$

$$K = \begin{pmatrix} K_1 & 0 & 0 & 0 & 0 \\ 0 & K_2 & 0 & 0 & 0 \\ 0 & 0 & K_3 & 0 & 0 \\ 0 & 0 & 0 & -E & 0 \\ 0 & 0 & 0 & 0 & -M \end{pmatrix},$$

along with  $K^\varepsilon = \varepsilon^{-1}K$ , where  $K_i, E, M$  are mechanical, electric and magnetic imperfect proportionality constant.

Here,  $M_{jl}^\varepsilon$  is coefficient matrix which comprises of the components:  $c_{ijkl}^\varepsilon$  for stiffness,  $e_{ij}^\varepsilon$  for piezoelectric coefficient,  $\kappa_{jl}^\varepsilon$  for dielectric permittivity,  $q_{ij}^\varepsilon$  for piezomagnetic coefficient,  $\mu_{jl}^\varepsilon$  for magnetic permeability,  $\alpha_{jl}^\varepsilon$  for magnetoelectric coefficient;  $\Sigma_j^\varepsilon$  is having  $\sigma_{ij}^\varepsilon$  for stress field,  $D_j^\varepsilon$  for electric displacement,  $B_j^\varepsilon$  for magnetic induction; and  $U^\varepsilon$  is having  $u_k^\varepsilon$  for deformation vector,  $\phi^\varepsilon$



electric potential and  $\psi^\varepsilon$  for magnetic potential. The material density is  $\rho^\varepsilon$ . Here,  $c_{ijkl}^\varepsilon(\mathbf{x}) = c_{ijkl} \left( \frac{x_1}{\varepsilon} \right)$  and so on.

## 2.1. Asymptotic homogenization

Now, considering the regular asymptotic expansion, we obtain the following expansions:

$$\omega = \sum_{n \geq 0} \varepsilon^n \cdot \omega_n, U(\mathbf{x}, \mathbf{y}) = \sum_{n \geq 0} \varepsilon^n \cdot U^{(n)}(\mathbf{x}, \mathbf{y}) \text{ and } \omega^2 = \sum_{n \geq 0} \varepsilon^n \cdot \bar{\omega}_n$$

where  $\bar{\omega}_0 = \omega_0^2$ ,  $\bar{\omega}_1 = 2\omega_1\omega_0$ ,  $\bar{\omega}_2 = 2\omega_2\omega_0 + \omega_1^2, \dots, \bar{\omega}_n = \sum_{k=0}^n \omega_k \omega_{n-k}$ . On using the above

expansions and the chain rule due to  $\mathbf{y}$  (fast variables), we obtain expressions for  $O(\varepsilon^n), n \geq -1$ , from which we derive local problems. A generalization of the local problem of infinite order are also derived satisfying the necessary and sufficient condition for the existence of 1-periodic solutions. Further, the explicit solutions of first and second local problems have been obtained through rigorous calculation.

## 2.2. Dispersion relation

The dispersion equation for the homogenized system for  $O(\varepsilon^2)$  is derived as

$$\text{Det} \left[ \left( I - \varepsilon^2 \eta \omega^2 \right) \left( \hat{M}_{11} k^2 \sin^2 \theta + \hat{M}_{12} k^2 \sin 2\theta + \hat{M}_{22} k^2 \cos^2 \theta \right) - \mathcal{P} \omega^2 \right] = 0. \quad (2)$$

Here,  $\theta$  is wave incident angle and  $k$  being the wave number.

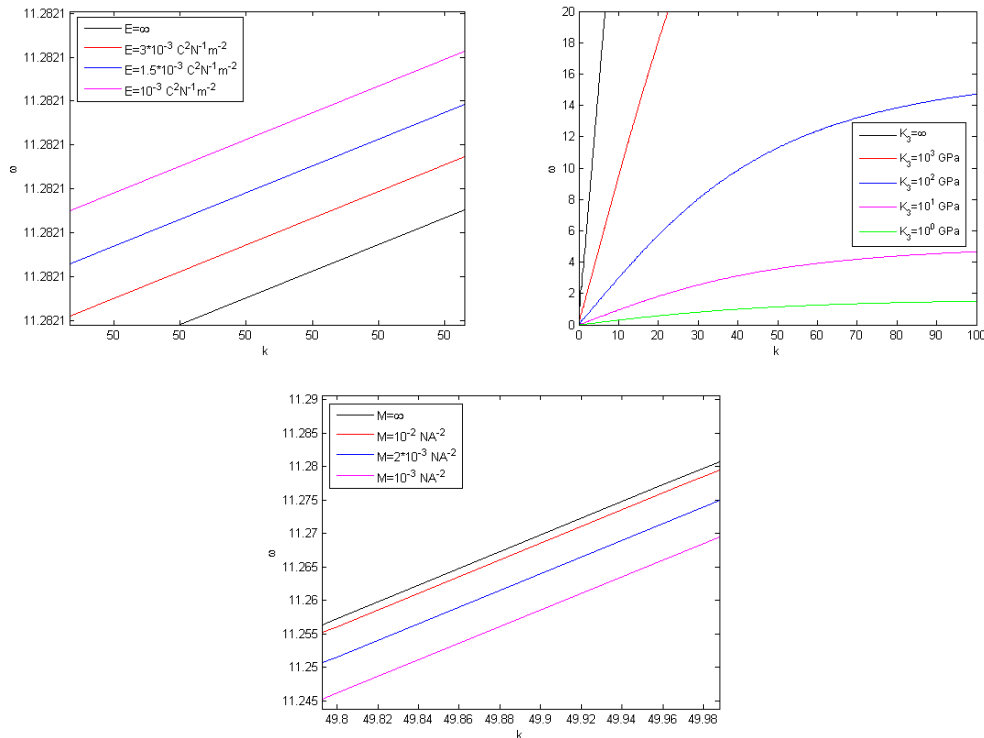


Figure 2 – The effect of mechanical, electrical and magnetic imperfect interface on dispersion curve.

### 3. NUMERICAL RESULTS

A 3-layered  $(0,1) = (0, \theta_1) \cup (\theta_1, \theta_2) \cup (\theta_2, 1)$  composite distributed perpendicular to  $x_1$ -axis with harmonic waves traveling at an angle  $\theta$  to the layer is considered. Numerical data for BaTiO<sub>3</sub> is considered for the piezoelectric phase and CoFe<sub>2</sub>O<sub>4</sub> is considered for piezomagnetic phase. Figure 2 shows the effect of mechanical, electrical and magnetic imperfect contact on the dispersion curves for BaTiO<sub>3</sub>/CoFe<sub>2</sub>O<sub>4</sub>/BaTiO<sub>3</sub> MEE laminated composite. It is reported that mechanical imperfect bonding dominates over electric and magnetic one making the system more dispersive.

### 4. CONCLUSION

In the present work, in order to describe the anti-plane wave propagation in MEE periodic composite with imperfect interface, a more general dynamic asymptotic homogenization model is developed. The local problems, dispersion equation and solutions of the first and second local problems are derived explicitly. Mathematical models are validated with those reported for the purely elastic case of Brito-Santana et al. [7]. As for the numerical results, the dispersion curve of the perfect contact has been found to be higher than imperfect case. In particular, the mechanical imperfect bonding has dominating effect on the dispersion curve as compared to electric or magnetic one.

### ACKNOWLEDGEMENTS

MSC would like to thanks CTIC for providing UNAM Postdoctoral Fellowship. The authors would also like to thanks IIMAS Computing Unit (LUCAR) for providing parallel computing processors. PAPIIT DGAPA UNAM (IN101822) project is also acknowledged.

### REFERENCES

- [1] J. Y. Li and M. L. Dunn. Micromechanics of magneto-electro-elastic composite materials: average fields and effective behavior. *Journal of Intelligent Material Systems and Structures*, v. 9(6), p. 404-416. (1998).
- [2] N. S. Bakhvalov and G. Panasenko. Homogenisation: averaging processes in periodic media: mathematical problems in the mechanics of composite materials. v 36, Dordrecht, London: Kluwer Academic. (1989).
- [3] J. Bravo-Castillero, R. Rodríguez-Ramos, H. Mechkour, J. A. Otero, and F. J. Sabina. Homogenization of magneto-electro-elastic multilaminated materials. *The Quarterly Journal of Mechanics & Applied Mathematics*, v. 61(3), p. 311-332. (2008).
- [4] R. O. Caballero-Pérez, J. Bravo-Castillero, and L. F. López-Ríos. Effective thermo-magneto-electro-elastic properties of laminates with non-uniform imperfect contact: delamination and product properties. *Acta Mechanica*, v. 233(1), p. 137-155. (2022).
- [5] R. V. Craster, J. Kaplunov and A. V. Pichugin. High-frequency homogenization for periodic media. *Proceedings of the Royal Society A: Mathematical, Physical and Engineering Sciences*, v. 466(2120), p. 2341-2362. (2010).
- [6] H. Brito-Santana, Y. S. Wang, R. Rodríguez-Ramos, J. Bravo-Castillero, R. Guinovart-Díaz and V. Tita. A dispersive nonlocal model for shear wave propagation in laminated composites with periodic structures. *European Journal of Mechanics-A/Solids*, v. 49, p. 35-48. (2015).
- [7] H. Brito-Santana, Y. S. Wang, R. Rodríguez-Ramos, J. Bravo-Castillero, and R. Guinovart-Díaz. Dispersive shear-wave propagation in a periodic layered composite with imperfect interfaces. *International Journal of Automotive Composites*, v. 1(2-3), p. 184-204. (2015).

### RESPONSIBILITY NOTICE

The authors are the only responsible for the printed material included in this manuscript.

## EFFECTS OF THERMAL ACTIVATION ON GEOPOLYMERIZATION OF SLAG-BASED PURE GEOPOLYMER

Lais Alves <sup>a</sup>, Nordine Leclou <sup>b</sup>, João dos Santos <sup>c</sup>, Fábio de Souza <sup>d</sup>, Silvio de Barros <sup>e</sup>

<sup>a</sup> Federal Center of Technological Education (CEFET/RJ),  
Rio De Janeiro, 20271-110, Brazil  
E-mail: lais.alves@cefet-rj.br

<sup>b</sup> Nantes Université, École Centrale Nantes, CNRS, GeM, UMR 6183,  
F- 44600 Saint-Nazaire, France  
E-mail: nordine.leclou@univ-nantes.fr

<sup>c</sup> Federal Center of Technological Education (CEFET/RJ),  
Rio De Janeiro, 20271-110, Brazil  
E-mail: joao.santos@cefet-rj.br

<sup>d</sup> Federal Center of Technological Education (CEFET/RJ),  
Rio De Janeiro, 20271-110, Brazil  
E-mail: fabio.souza@cefet-rj.br

<sup>e</sup> CESI LINEACT,  
Saint-Nazaire, 44600, France  
E-mail: silvio.debarros@gmail.com

**Keywords:** Blast furnace slag, Sodium silicate, Thermal activation, Geopolymerization, Mechanical properties

### 1. INTRODUCTION

During the initial period of the geopolymerization reaction, some factors, such as different Al<sub>2</sub>O<sub>3</sub>/SiO<sub>2</sub> ratio, alkali concentration, curing temperature with curing time, water/solid ratio, and pH, have significant influence on the formation and properties of the hardened mixtures [1]. Geopolymerization is a reaction that chemically integrates materials such as precursors (source of silica and alumina) dissolved in activator (alkaline) solution [2-5]. With an increase in temperature, accelerated setting and hardening have been shown [6,7], improving early age strength in geopolymer [8]. Thus, heat curing is recommended for geopolymer [9].

Many research deals with geopolymer mortars and binders, especially metakaolin and fly ash matrix [2, 10-16]. Few studies have been found on geopolymerization of pure geopolymer matrix and ground blast furnace slag (GBFS) as precursor material. This work seeks to study the effect of curing on the properties of hardened geopolymer, based on a pure GBFS matrix. The specimens were cured at curing temperatures of 20°C, 40°C, 60°C and 80°C with adaptations from the theoretical cycle, to simulate the accelerated curing treatment adopted by some precast industries [9, 17]. The paper aims to examine the differences caused by different curing conditions in the specimens and to assess the curing conditions that results on the best performance for the mixture. The findings should lay a good foundation for future research on the shrinkage of slag-based geopolymer pastes and their utilization.

## 2. MATERIALS AND METHODS

Ground blast furnace slag (GBFS) was obtained by ECOCEM from France. Median particle size for the as-received GBFS is  $D_{50} = 11.8 \mu\text{m}$ , with 95% of particles passing through  $32 \mu\text{m}$  and a Blaine fineness of  $4450 \pm 250 \text{ cm}^2/\text{g}$ . The apparent density of the GBFS is  $0,8 \pm 0,1 \text{ g/cm}^3$  and the loss on ignition 0.7wt%.

Alkaline activators employed in the mixtures were sodium silicate ( $\text{Na}_2\text{SiO}_3$ ) solution with 8 wt%  $\text{Na}_2\text{O}$ , 27 wt%  $\text{SiO}_2$ , and 65 wt% water and 10 M sodium hydroxide ( $\text{NaOH}$ ).  $\text{Na}_2\text{SiO}_3$  was purchased from VWR in liquid form, of pH between 11-11.5 and density  $1.35 \text{ g/cm}^3$  at  $20^\circ\text{C}$ .  $\text{NaOH}$  was purchased from ALFA-AESAR prepared in pellet form, white colored, with 98% purity.

Sodium silicate activator (Na-Si) was prepared by mixing 10M sodium hydroxide solution ( $\text{NaOH}$ ) and sodium silicate ( $\text{Na}_2\text{SiO}_3$ ) solution with a mass ratio of 2  $\text{Na}_2\text{SiO}_3/\text{NaOH}$ . The produced Na-Si activator contained 66.7% water with 0.7  $\text{Na}_2\text{O}/\text{SiO}_2$  molar ratio. After preparation, the solution was kept for 24 hours in ambient conditions. All specimens were made with a solid to liquid ration of 2.0 and formulation of  $335.3 \text{ kg/m}^3$  of Na-Si,  $1,458.3 \text{ kg/m}^3$  of GBFS and  $208.3 \text{ kg/m}^3$  of water. This mixture is supported by previous study [18] that indicate that the solid-to-liquid ratio of 2.0 gives the highest compressive strength amongst the studied compositions.

For ambient curing temperature, specimens were cured inside a chamber with an average temperature and humidity of  $20^\circ\text{C} \pm 3^\circ\text{C}$  and  $50\% \pm 5\%$ , respectively. The control specimens were demolded after 24h. For curing temperatures of  $40^\circ\text{C}$ ,  $60^\circ\text{C}$  and  $80^\circ\text{C}$ , the procedure was adapted from theoretical cycles proposed by Leklou et. al [33], where initially there is a pre-cure at  $20^\circ\text{C}$  for 1h. Then, the temperature rises at a constant rate for 3h until it reaches the proposed temperature. Afterwards, it maintains constant temperature for 10h. And finally, decreases to ambient temperature ( $20^\circ\text{C}$ ) at a constant rate over 10h. After cooling the specimens were demolded and stored inside a chamber with an average temperature and humidity of  $20^\circ\text{C} \pm 3^\circ\text{C}$  and  $50\% \pm 5\%$ , respectively, until testing date.

## 3. RESULTS AND DISCUSSION

Bing-hui et. al [12] stated that the polycondensation processes, polymerization rate of precursors and dehydration of water in the early stage geopolymerization reaction were accelerated by raising the curing temperature of the geopolymer paste. To verify the theory on GBFS geopolymer, the specimens were cut after one day to observe the geopolymerization rate. The observations can be seen in Figure 1 for the different curing temperatures of  $80^\circ\text{C}$ ,  $60^\circ\text{C}$ ,  $40^\circ\text{C}$  and  $20^\circ\text{C}$  (Figure 1a, Figure 1b, Figure 1c, Figure 1d, respectively), where the lighter portions of the specimen are the places where the geopolymerization has already occurred. The geopolymerization process for  $40^\circ\text{C}$  curing can be observed at Figure 2 for different curing ages: at day two (Figure 2a), day three (Figure 2b), day four (Figure 2c) and day five (Figure 2d).

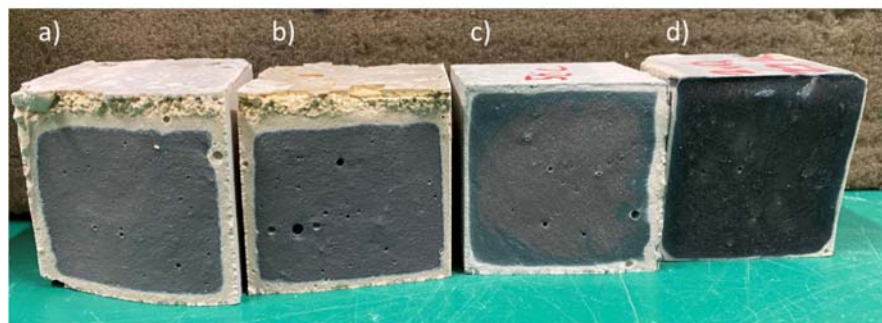


Figure 1 - Geopolymerization process at day one after mixing, and thermal curing at a)  $80^\circ\text{C}$ , b)  $60^\circ\text{C}$  and c)  $40^\circ\text{C}$  and curing at d)  $20^\circ\text{C}$ .

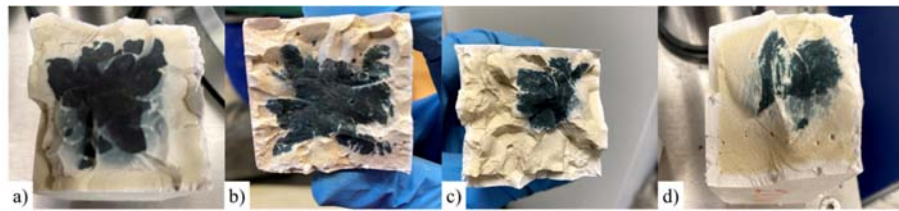


Figure 2 - Geopolymerization process for 40°C curing at a) day two, b) day three, c) day four and d) day five.

It can be observed that the higher the temperature, the more advanced the geopolymerization on the specimen. It can also be noted that for 60°C and 80°C, the top surface of the specimen suffered from drying shrinkage causing a more fragile material. X-ray fluorescence (XRF) was also done to assess the chemical compositions of the geopolymer paste cured at 20°C and 40°C one day after mixing. Results can be observed in Table 2.

Table 2 - Chemical composition (wt%) of geopolymer paste at day three

Temperature	B2O3	Na2O	Al2O3	SiO2	CaO	MnO
20°C	33	6.6	-	24.5	35.7	0.22
40°C	33	6.6	7.3	23.7	29.2	0.16

From these results, it can be noted that condensation process has already begun for sample cured at 40°C due to the presence of aluminum in the composition. While for sample cured at 20°C, it is probable that the process of synthesis of the geopolymer is still in the dissolution of the solid aluminosilicate in the activator solution [12,19].

#### 4. CONCLUSIONS

The study consisted of assessing the effects of curing temperatures of 20°C, 40°C, 60°C and 80°C on setting time and compressive strength. For thermal curing, theoretical cycles were adopted, consisting in four phases. First a pre-cure at 20°C for 1h. Second, a constant rate for 3h until rising temperature reaches 40°C. Third, maintenance of 40°C for 10h. And fourth, decreases to 20°C, over 10h. The geopolymerization of GBFS is considered a silicate and calcium system and the process occurs with the contact of air. The results show that the elevation of the curing temperature accelerates the geopolymerization reaction of the GBFS geopolymer paste studied. This statement is consistent with the results of the variations of setting time, and macro and micro-structure observations. Elevating curing temperature up to 40°C improved the hardening process and the physical properties of the mixture. Specimens cured at 60°C and 80°C started to show a decrease on compressive strength. Rapid setting time for these specimens suggest a limitation on dissolution of amorphous phases affecting the hardened geopolymer.

#### ACKNOWLEDGEMENTS

The authors acknowledge the Brazilian institutions CAPES (Coordenação de Aperfeiçoamento de pessoal de nível superior - Coordination of Improvement of senior staff), CNPq (Conselho Nacional de Desenvolvimento Científico e Tecnológico - National Council for Scientific and Technological Development), FAPERJ (Fundação de Amparo à Pesquisa do Estado do Rio de Janeiro - Research Support Foundation of the State of Rio de Janeiro) and Institut de Recherche en Génie Civil et Mécanique – Research Institute on Civil and Mechanical Engineering for their support in conducting the study.

## REFERENCES

- [1] D Khale, R Chaudhary. *Mechanism of geopolymerization and factors influencing its development: a review*. In: J Mater Sci 42:729–746 (2007)
- [2] JGS van Jaarsveld, JSJ van Deventer, GC Lukey. *The Effect of Composition and Temperature on the Properties of Fly Ash- and Kaolinite-Based Geopolymers*. In: Chem. Eng. J. 89, 63-73 (2002)
- [3] H Xu, JSJ van Deventer. *The Geopolymerisation of Alumino-Silicate Minerals*. In: Int. J. Miner. Process., 59, 247-266 (2000)
- [4] CJ Xiong, CH Ban, X Pei, Z Fang. *A study on complex alkali-slag environmental Concrete*. In: International workshop on sustainable development and concrete technology. Beijing, p 299:308 (2004)
- [5] E Hermann, C Kunze, R Gatzweiler, G Kiebig, J Davitovits. *Solidification of various radioactive residues by geopolymers with special emphasis on long term stability*. In: Proceedings of Geopolymers, p 211-225 (1999)
- [6] D Bondar, CJ Lynsdale, NB Milestone, N Hassani, AA Ramezaniapour. *Effect of type, form, and dosage of activators on strength of alkali-activated natural pozzolans*. In: Cem. Concr. Compos. 33, 251–260 (2011)
- [7] F Pacheco-Torgal, J Castro-Gomes, S Jalali. *Alkali-activated binders: a review. Part 2. About materials and binders manufacture*. In: Constr. Build. Mater. 22, 1315–1322 (2008)
- [8] P Rovnanik. *Effect of curing temperature on the development of hard structure of metakaolin-based geopolymer*. In: Constr. Build. Mater. 24, 1176–1183 (2010)
- [9] K Neupane, R Sriravindrarajah, D Baweja, D Chalmers. *Effect of curing on the compressive strength development in structural grades of geocement concrete*. In: Constr. Build. Mater. 94, 241–248 (2015)
- [10] C Ridtirud, P Chindapasirt, K Pimraksa. *Factors affecting the shrinkage of fly ash geopolymers*. Int. J. Miner. Metall., 18(1): 100-105 (2011) <http://dx.doi.org/10.1007/s12613-011-0407-z>
- [11] A Buchwald, M Vicent, R Kriegel, C Kaps, M Monzó, A Barba. *Geopolymeric binders with different fine fillers—phase transformations at high temperatures*. In: Appl. Clay Sci., 46, 190-196 (2009) <http://dx.doi.org/10.1016/j.clay.2009.08.002>
- [12] M Bing-hui, H Zhu, C Xue-min, H Yan, G Si-yu. *Effect of curing temperature on geopolymerization of metakaolin-based geopolymers*. In: Appl. Clay Sci. 99, 144–148 (2014)
- [13] P Chindapasirt, T Chareerat, V Sirivivatnanon. *Workability and strength of coarse high calcium fly ash geopolymer*. In: Cem. Concr. Compos., 29, 224-229 (2008)
- [14] DLY Kong, JG Sanjayan, K Sagoe-Crentsil. *Comparative Performance of Geopolymers Made with Metakaolin and Fly Ash After Exposure to Elevated Temperatures*. In: Cem. Concr. Res. 37, 1583-1589 (2007)
- [15] A Sathonsaowaphak, P Chindapasirt, K Pimraksa. *Workability and strength of lignite bottom ash geopolymer mortar*. In: J. Hazard. Mater. 168, 44-50 (2009)
- [16] S Detphan, P Chindapasirt. *Preparation of fly ash and rice husk as geopolymer*. In: Int. J. Miner. Metall. Mater., 16, 720-726 (2009)
- [17] N Leklou, J-E Aubert, G Escadeillas. *Microscopic observations of samples affected by the delayed ettringite formation (DEF)*. In: Mater. Struct. 42(10), 1369-1378 (2009)
- [18] L Alves, N Leklou, S de Barros. *A comparative study on the effect of different activating solutions and formulations on the early stage geopolymerization process*. In: MATEC Web of Conferences. 322, 01039 (2020)
- [19] K Sagoe-Crentsil, L Weng. *Dissolution processes, hydrolysis and condensation reactions during geopolymer synthesis: Part II. High Si/Al ratio systems*. In: J. Mater. Sci. 42(9), 3007-3014 (2007)



## RESPONSIBILITY NOTICE

The author(s) is (are) the only responsible for the printed material included in this manuscript.

## FATIGUE LIFE PREDICTIONS UNDER VARIABLE AMPLITUDE LOADING FOR COMPOSITE MATERIALS

Jorge Alberto Rodriguez Duran <sup>a</sup>, Panters Rodriguez Bermudez <sup>a</sup>  
Reinaldo Rodriguez Ramos<sup>a</sup>

<sup>a</sup> Escola de Engenharia Industrial Metalúrgica de Volta Redonda  
Universidade Federal Fluminense, Av. dos Trabalhadores 420, 27255-125  
Volta Redonda RJ, Brasil, e-mail: jorgeduran@id.uff.br

**Keywords:** constant life diagrams, variable amplitude loading, fatigue life predictions

### ABSTRACT

Under the safe-life design concept for fatigue assessment in laminate composites, the cyclic stresses or strains are directly associated with their corresponding fatigue strength curves. In the present work, the multiple  $R$ -ratios form of the constant life diagrams  $CLD$  (fatigue resistance) is used for computing the fatigue life under a given combination of amplitude and mean stress (fatigue actions). These last two quantities define the sector of the  $CLD$  where the load point is located and hence geometrical safety factors in stress and life can be easily computed. For load processes of varying amplitude, the approach is repeated for all *rainflow* cycles identified during the count. The fatigue damage can then be accumulated using a well-known linear rule until a critical value is reached. The number of spectra passes thus obtained can be related to a specific parameter in the load history, say, its maximum value. The procedure is demonstrated here by performing a fatigue life assessment in a unidirectional laminate with known uniaxial fatigue properties. The loads are represented by a uniaxial normalized load process which is scaled to different maximum stress values. The results are compatible with those previously reported using similar load spectra in fiber reinforced laminates.

### 1. INTRODUCTION

The fatigue approaches can be broadly divided into two groups or categories [1]. The first group is characterized by some kind of damage measurement during fatigue process, as stiffness or residual strength degradation, e.g., while the second group relies on the traditional concept of similitude, i.e., the behavior measured in small specimens and under well controlled laboratory conditions should be the same as that expected in components or structures made of the same material as the specimens. In this category, no attention is paid to probable damage mechanisms during the fatigue process and the failure criterion is macroscopic, usually including total fracture of the specimen. The present investigation belongs to the second group of fatigue approaches.

To perform fatigue life predictions under stress cycles of constant or variable amplitude, a graphical or analytical procedure can be followed. In the first situation, the equivalent stress parameter can be compared to the strength curve and safety factors are then computed from simple geometrical considerations. The aim of this work is to develop a geometrical based approach which uses the multiple  $R$ -ratio fatigue strength curve  $FSC$  for estimating the maximum stress *versus* the number of block repetitions (or spectra passes) for a given load process of variable amplitude  $VA$  loading. The method is completely based on experimental results and their fatigue life predictions should be better as the number of available experimental  $FSC$  for different  $R$ -ratios increases. The failure criterion is directly applied in the constant life diagrams  $CLD$  which are, in turn, derived from the experimental  $SN$  (strength *versus* number of cycles) curves. Since the  $CLD$  is composed of linear *isolife* curves, it is called piece wise



linear *PWL*. No attempts are made in this first version of the approach for including the multiaxial stress effects.

## 2. AN OVERVIEW OF THE FATIGUE LIFE PREDICTION METHODOLOGY

In the classic fatigue life prediction methodology, several sub-problems should be solved, sometimes in parallel, sometimes sequentially [2]. This is what some authors call the fatigue damage prediction chain [3]. It is didactic interesting to first separate these sub-problems into those related to the material behavior and those related to the applied loads. The first group (material's group) includes tasks such as modeling the fatigue strength curves and the assessment of the mean stress effects on these curves, the last one normally completed with the aid of the constant life diagrams *CLD*. This step can also be alternatively done in the load's related group through the concept of completely reverse stress amplitude [4]. On the other hand, the treatment of the applied loads includes tasks as stress or strain analysis, reduction of the multiaxiality effects, reduction of the mean stress effects (which can be alternatively performed in the material's group) and cycle counting, usually executed by the two-parameter *rainflow* counting technique.

Common to both groups are the following sub-problems: I) Adoption of the fatigue failure criterion and II) Damage summation. The first can be performed, in turn, by two different alternatives: a) equating the completely reverse stress amplitude to the material strength for a given *R-ratio* or, b) use the piece-wise linear *PWL* constant life diagram *CLD* for computing the safety factors in stress and then in life for each point  $\sigma_a \times \sigma_m$  of the *rainflow* matrix (also called the frequency matrix). The approach developed in the current research is based on the second alternative. The second task, i.e., the damage summation, is usually done by the well-known Palmgren-Miner cumulative damage rule. Various of the afore-mentioned sub-problems will be addressed in the following sections aiming to exemplify the graphical approach for fatigue life prediction under *VA* loading presented in this paper.

## 3. METHODOLOGY

To exemplify the procedure proposed in the present paper, a structural integrity assessment process in the unidirectional laminate designed as UNI-PPG1200 EP1 in [5], was simulated. This material has an epoxy resin matrix and is composed of standard E-glass type glass fibers, 92% of which are in the *0-degree* position. This information together with the material's properties were taken from the SNL/MSU/DOE database [5]. The mean values for ultimate tensile *UTS* and compressive strength *UCS* are 974 MPa and -635 MPa, respectively. The block of *VA* loading used in the simulation consisted of a normalized (between zero and one) strain time history measured under real service conditions in a structural component. The signal was discretized to a reasonable number of levels and then its constant amplitude cycles were extracted by the *rainflow* cycle counting method [6]. The bin centers of the resultant *rainflow* histogram were then scaled to a range of maximum stresses between 140 and 300 MPa ( $0,14 \leq \sigma_{max}/UTS \leq 0,3$ ). The procedure is totally implemented in the MatLab® software and thus can be immediately used for other materials and load spectra. Its main drawback is that relies completely on the existence of experimental fatigue life data under various *R-ratios*. Since there are no available fatigue test results for the same material and under the same block of loading, it was not possible, at this stage, to perform the experimental verification of the approach. The authors reinforce the fact that both stress history and strength data refer to the fiber direction in the laminated.

## 4. FATIGUE STRENGTH CURVES *FSC* AND CONSTANT LIFE DIAGRAMS *CLD*

As mentioned earlier, the experiments for measuring the fatigue strength curves *FSC* are normally performed under constant amplitude loading. Any two of the six parameters that represent a constant amplitude load pattern can be used to carry out the tests. From an operational point of view, the fatigue machines are set up to load control in this type of test. The most common graphical representation of the *FSC* is made in amplitude stress  $S_a$  versus number of cycles to complete fracture  $N_f$  coordinates. But since fatigue is a process dependent on two parameters, there will be an experimental

*SN* curve for each value of mean stress  $\sigma_m$  or stress ratio  $R = \sigma_{min}/\sigma_{max}$  used during the tests. For example, Fig. 1 (a) shows a set of experimentally measured fatigue life under a combination of stress amplitude and load ratio for the unidirectional fiber-reinforced laminate UNI-PPG1200 EP1 [5]. For obtaining the *CLD* from these curves it is first necessary to fit an equation to experimental data. The most common *SN* formulation is based on the following power law equation:

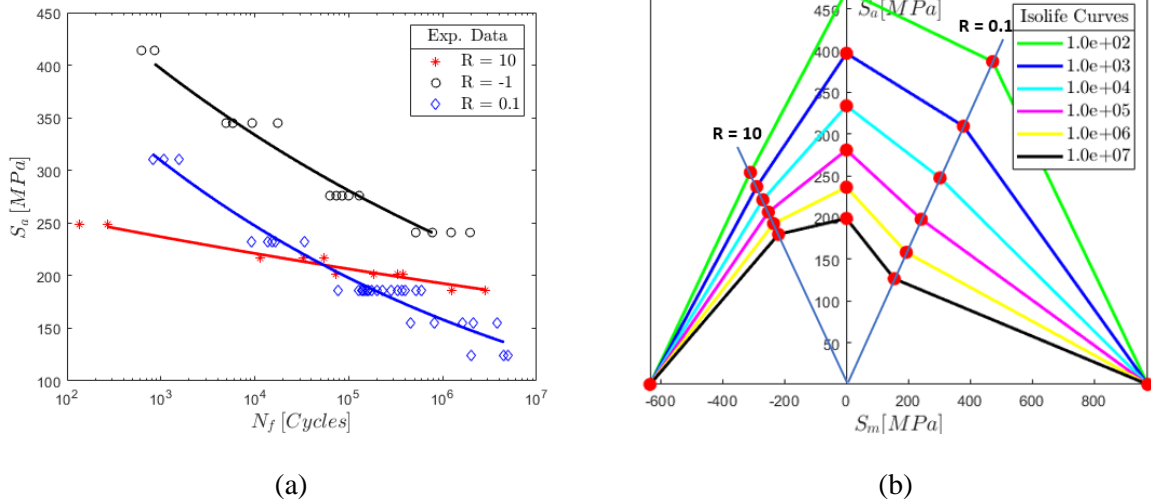


Figure 1 – Experimentally measured *SN* data (*FSC*) for the unidirectional fiber-reinforced laminate UNI-PPG1200 EP1 under various load ratios (a) [5] and the piece wise linear *PWL* constant life diagram *CLD* for the same material (b).

$$S_a = a N_f^b \tag{1}$$

where  $a$  and  $b$  are the fitting constant or material’s properties. Fatigue tests are normally performed under stress control and the dependent variable  $N_f$  is Gaussian distributed [7]. Consequently, the material’s properties must indicate the percent of failure probability, which is here assumed, in the absence of sufficient tests, as being 50%. Specifically, for the set of experimental results shown in Fig. 1(a), the material’s parameters for each *SN*( $R$ ) curve are listed in Tab. 1.

Table 1 – Material’s parameters obtained by linear regression of the experimental data shown in Fig. 1(a).

R	a MPa	b
10	292	-0.03
-1	666	-0.075
0.1	605	-0.097

For constant amplitude stress cycles, the amplitude and mean strength are related to the load ratio through the following expression:

$$\frac{S_a}{S_m} = \frac{1 - R}{1 + R} \tag{2}$$

For  $R$  constant, the *SN* data of Fig. 1(a) Figure forms radial lines in  $S_m \times S_a$  coordinates. The *isolife* curves in the *CLD* are then obtained by choosing discrete values for fatigue life ( $1e2, 1e3 \dots$

1e7 cycles, e.g.), then computing the  $S_a$  in Eq. (1) and finally  $S_m$  in Eq. (2). This procedure allows the obtention of the lines between  $R = 10$  and  $R = 0.1$ . For load ratios outside this range i.e., for  $S_a \rightarrow 0$ , the *isolife* curves should converge in the left direction to the ultimate compression strength  $UCS$  (-635 MPa) and in the right direction to the ultimate tension strength (974 MPa). The resultant constant life diagram *CLD* for the unidirectional glass/epoxy composite UNI-PPG1200 EP1 is shown in Fig. 1(b).

## 5. VARIABLE AMPLITUDE STRESS SEQUENCE AND RAINFLOW MATRIX

The block of loading consists of a normalized time series with  $N_x = 62 \times 10^4$  strain values  $\bar{x}$  (see Fig. 2(a) that were recorded using strain gages in the surface of an engineering component. After an initial filtering for eliminating all points in the signal except the peaks and valleys, the number of components reduces to  $7 \times 10^4$  reversals. The signal is then discretized to a fixed number of levels and finally cycles of known minimum and maximum are extracted according to the *rainflow* cycle counting methodology. Figure 2 (b) is a graphical representation of the *rainflow* matrix obtained for the VA loading spectrum. A discretization to 32 levels of the total strain range is enough to obtain a precise representation of the applied load. The color bar attached to Fig. 2(b) indicates the frequency  $n_{ij}$  of each *rainflow* pair, here depicted by its minimum and maximum values. Since the original strain time series is related to a point of uniaxial stress state, the *rainflow* matrix can also be considered as a matrix of stress values. The transformation to amplitudes and mean stress values from the max-min matrix of Fig. 2(b) can be done by simple transformations as  $\sigma_a = 1/2 (\sigma_{max} - \sigma_{min})$  and  $\sigma_m = \sigma_{max} - \sigma_a$ . Note in Fig. 2(b) that the more frequent combinations have low stress ranges, which implies low fatigue damage.

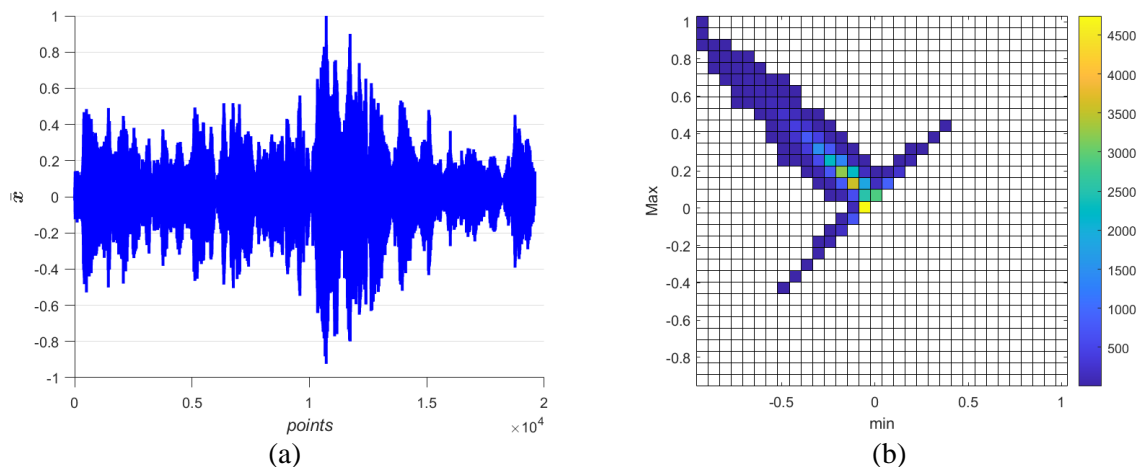


Figure 2 – A small sample of the normalized VA loading spectrum used in this paper for simulating the applied loads in the unidirectional composite (a) and its 32 levels squared *rainflow* matrix (b).

## 6. ADOPTION OF THE FATIGUE FAILURE CRITERION

The fatigue failure criterion used in this paper is based on the experimental derived *PWL* form of the *CLD*. First note that the *CLD* in Fig. 1(b) is divided into sectors, depending on the load ratio values. The equations for each *isolife* curve in each sector can be easily obtained from its extreme points. The numerical ratio between each *rainflow* pair  $\sigma_{aij}/\sigma_{mij} = r_{ij}$  is like the left-hand side of Eq. (2) but in terms of stresses and not of strengths. This point is immediately located in its respective *CLD* sector. Furthermore, the intersection between the radial line  $\sigma_{aij} = r_{ij} \sigma_{mij}$  (load line) and its most near *isolife* curve ( $N_{f2}$ , e.g.) in the corresponding *CLD* sector, represents the combination of load necessary for fatigue failure (point B in Fig. 3(a)), i.e., it defines the safety factor in stress as follows:

$$X_S = \frac{\overline{OB}}{\overline{OA}} \quad (3)$$

Safety factors in stress and in life are quite different, since the elevated nonlinearity of the *SN* data, but they can be easily related each to other as follows [4]:

$$X_N = X_S^{-1/b} \quad (4)$$

In Eq. (4) the exponent *b* corresponds, again, to the most near radial curve in each sector of the *CLD*. Finally, the *isolife* curve that passes through the point of loading (point A in Fig. 3(a)), i.e., the number of fatigue cycles  $N_{fi}$  that the component lasts under that *rainflow* pair, can be geometrically calculated as:

$$N_{fij} = X_N N_{f2} \quad (5)$$

The elementary damage done by each *rainflow* pair is  $d_{ij} = n_{ij}/N_{fij}$  while the total damage done by the whole *rainflow* matrix is  $D = \sum d_{ij}$ . It is worth remembering that  $n_{ij}$  is the frequency of each *rainflow* pair, i.e., the contents of that matrix. Finally, the number of VA blocks or spectrum passes, considering that fatigue failure occurs when the accumulated damage reaches 100 % (which means  $D = 1$ ) is simply  $1/D$ . The procedure is applied for each stress history that results from the multiplication of the normalized VA block of loading for a range of maximum stress  $140 \leq \sigma_{max} \leq 300$  MPa or  $0,14 \leq \sigma_{max}/UTS \leq 0,3$  at increments of 20 MPa, and the results are presented in Fig. 3(b).

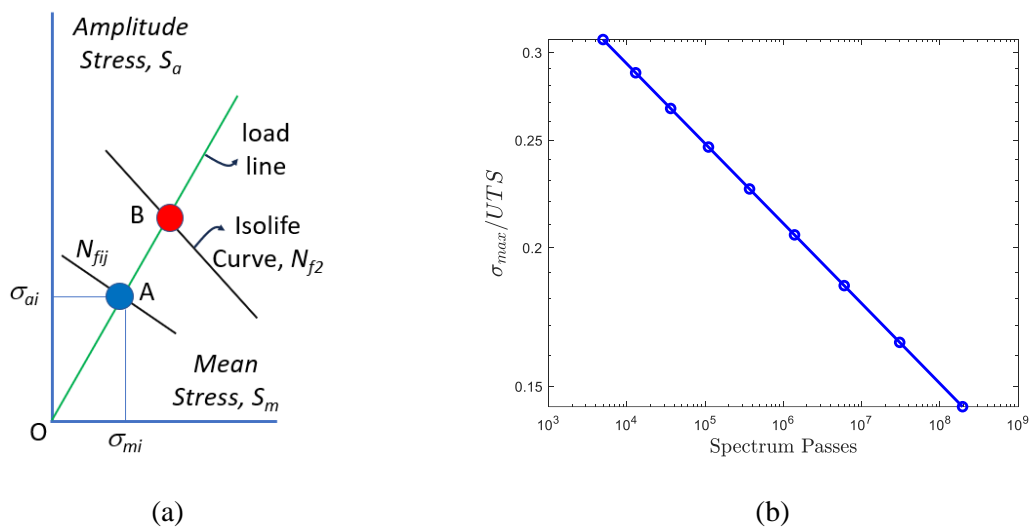


Figure 3 – Schematic procedure for computing the *isolife* curve passing through the point A (a) and the number of spectra passes for different  $\sigma_{max}/UTS$  values predicted by the approach based on the *PWL* form of the *CLD* (b).

## DISCUSSION

The paper deals with the process of fatigue analysis using the available experimental data of a unidirectional fiber-reinforced laminate. It should be noted that, in the hypothetical task of the structural integrity assessment used for exemplifying the procedure, no attention is paid to the stress transfer function, i.e., the relation between loads and stresses. It is understood that the same uniaxial stress state of the coupons, which is simply based on its transverse section, also exists in the critical point of the

structure. This clarification is considered important because otherwise, the use of coupons experimental data for fatigue assessment purposes might become useless.

Unlike metallic materials, especially ductile metals, the composites fatigue behavior is different under tensile and compressive stresses. This is one of the most important justifications for the use of the *CLD* in fatigue analysis and can be easily verified in Fig. 1(b). Furthermore, the multiple *R-values* formulation of the *CLD* is considered the most reliable both for *CA* and *VA* fatigue life predictions [8]. Among its drawbacks one can mention the fact that the information about the scatter of the *FSC* is lost in the process of data manipulation. It is worth remembering that the failure probability of the *SN* data used in the current paper is only 50 %.

## CONCLUSIONS

This work has presented a method for estimating the curve  $\sigma_{max}$  vs. spectrum passes for a given composite structure under variable amplitude stresses. The use of the method is exemplified with experimental data for a fiber reinforced composite. The experimental data consisted of an *SN* curve for three *R-ratios* and its derived piece-wise linear *CLD*. The loading was composed by a real stress load sequence of *VA*. Even though no experimental verification was performed, previous reports [8] indicate that the use of a *PWL* form of the *CLD*, i.e., with multiple *R-values*, gives the most reliable results.

## ACKNOWLEDGEMENTS

The authors would like to thank the Federal Fluminense University for the financial support for this work.

## REFERENCES

- [1] Sendeckyj, George P. Chapter 10 - Life Prediction for Resin-Matrix Composite Materials. [book auth.] K.L. Reifsnider. *Fatigue of Composite Materials*. Elsevier, 1991, pp. 431-483.
- [2] Vassilopoulos, Anastasios. *Fatigue Life Prediction of Composites and Composite Structures*. Woodhead Publishing, Elsevier Ltd., 2020.
- [3] Meggiolaro, Jaime T. P. de Castro and Marco A. *Fatigue Design Techniques*. Createspace Independent Publishing Platform, 2016.
- [4] Dowling, Norman E. *Mechanical Behavior of Materials*. Pearson Education Limited, 2013.
- [5] John F. Mandell, Daniel D. Samborsky, David A. Miller, Pancasatya Agastra and Aaron Thomas. *Analysis of SNL/MSU/DOE Fatigue Database Trends for Wind Turbine Blade Materials 2010-2015*. Albuquerque, New Mexico: Sandia National Laboratories, 2016.
- [6] Johannesson, Par. *Rainflow Analysis of Switching Markov Loads*. Ph.D. Thesis, 1999.
- [7] JL, González-Velazquez. *Mechanical Behavior and Fracture of Engineering Materials*. Springer-Nature, 2020.
- [8] Nijssen, RPL. *Fatigue life prediction and strength degradation of wind turbine rotor blade composites*. Delft: Ph.D. thesis, 2006.

## RESPONSIBILITY NOTICE

The authors are the only ones responsible for the printed material included in this manuscript.

## FIBER-MATRIX INTERFACE INFLUENCE FOR IN-PLANE SHEAR LOAD – A NOVEL MICROMECHANICAL APPROACH

Lucas L. Vignoli <sup>a</sup>, Marcelo A. Savi <sup>b</sup>, Pedro M.C.L. Pacheco <sup>c</sup>, Alexander L. Kalamkarov <sup>d</sup>

<sup>a</sup>Center for Technology and Applications of Composite Materials  
Department of Mechanical Engineering, Federal University of Rio de Janeiro  
Macaé, RJ, Brazil.  
ll.vignoli@mecanica.coppe.ufrj.br

<sup>b</sup>Center for Nonlinear Mechanics, COPPE, Department of Mechanical Engineering, Federal University of Rio de Janeiro  
Rio de Janeiro, RJ, Brazil  
savi@mecanica.coppe.ufrj.br

<sup>c</sup>Department of Mechanical Engineering, Centro Federal de Educação Tecnológica Celso Suckow da Fonseca CEFET/RJ  
Rio de Janeiro, RJ, Brazil  
pedro.pacheco@cefet-rj.br

<sup>d</sup>Department of Mechanical Engineering, Dalhousie University  
Halifax, Nova Scotia, Canada, B3H 4R2  
alex.kalamkarov@dal.ca

**Keywords:** micromechanics of composites, in-plane shear, fiber-matrix interface, VSPKc model

### 1. INTRODUCTION

The present paper aims to present an analytical micromechanical formulation to estimate the in-plane shear behavior of unidirectional laminae taking into account the influence of fiber-matrix interface in the composite nonlinear behavior. The present investigation is contributing to the research effort developed by the authors to derive the VSPKc micromechanical model [1-4]. For these previous studies, the composite is assumed linear-elastic until the rupture. For most load conditions, this brittle assumption is not an issue, but this hypothesis is too strong for in-plane shear loads [5,6]. Additionally, the interface can influence the material stiffness during the elastic range [7].

The interface modeling can be found in the literature using asymptotic homogenization technique [8], concentric cylinder model [9], and imperfect bonding conditions [10]. However, these approaches are not able to evaluate the mechanism responsible for debonding damage.

The fiber-matrix interface has a finite dimension, being characterized by a core zone and two transition zones, one close to the fiber (fiber-transition) and the other one close to the matrix (matrix-transition). Based on these assumptions, the micromechanical analytical model is presented in Section 2 and the results are compared with experimental data and numerical simulations using the finite element method in Section 3.

### 2. VSPKc MICROMECHANICAL MODEL

The VSPKc micromechanical model is proposed by Vignoli *et al.* [4] without taking into account the interface effect. Now, an extension is proposed including the interface effect. A finite

interface is considered as a transition between fiber and matrix. Figure 1 shows the unit cell considered for the analytical model. The fiber distribution is assumed to present square symmetry, resulting in a square unit cell with length  $L$  along the directions  $x_2$  and  $x_3$ . Additionally, the fiber diameter is  $d$ , the interface has internal and external diameters  $d$  and  $D$ , respectively.

Considering that the composite volume is given by a sum of fiber, interface and matrix volume fractions,  $V_f + V_i + V_m = 1$ , fiber and interface volume fractions are  $V_f = \pi d^2 / 4L^2$  and  $V_i = \pi(D^2 - d^2) / 4L^2$ , respectively. Hence, the geometrical relations  $d/L = 2\sqrt{V_f/\pi}$  and  $D/L = 2\sqrt{(V_i + V_f)/\pi}$  can be established.

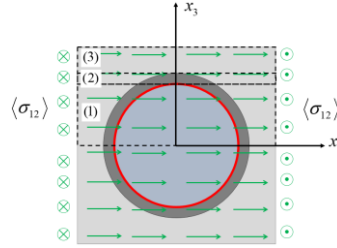


Figure 1: Unit cell for the VSPKc micromechanical model.

The key point of the proposed model is that unit cell can be split in three parts. In part (1), fiber, interface and matrix are associated in series. In part (2), only interface and matrix are associated in series. In part (3), there is just matrix. Additionally, parts (1), (2) and (3) are in parallel association concerning the whole unit cell.

Assuming these mechanical associations, the following relations are derived for the composite in-plane shear modulus

$$G_{12} = G^m \left( 1 + 2\sqrt{\frac{V_f}{\pi}} [I(a_{12}^{(1)}, \pi/2)] + 2\sqrt{\frac{V_i + V_f}{\pi}} [I(a_{12}^{(2)}, \pi/2) - I(a_{12}^{(2)}, \theta_i) - 1] \right) \quad (1)$$

where  $G_{12}^f$ ,  $G^i = \lambda G^m$  and  $G^m$  are the phase shear moduli. Note that  $\lambda$  is the ratio of interface and matrix shear moduli. Additionally,  $a_{12}^{(1)} = 2\{[(1/\lambda) - 1]\sqrt{(V_i + V_f)/\pi} + [(G^m/G_{12}^f) - (1/\lambda)]\sqrt{V_f/\pi}\}$ ,  $a_{12}^{(2)} = 2[(1/\lambda) - 1]\sqrt{(V_i + V_f)/\pi}$ ,  $\theta_i = a \sin(d/D) = a \sin[\sqrt{V_f/(V_i + V_f)}]$  and

$$I(a, \theta) = \int \left( \frac{\cos \theta}{1 + a \cos \theta} \right) d\theta = \begin{cases} -\sin \theta + K & \text{if } a = 0 \\ \frac{\theta}{a} - \frac{1}{a\sqrt{a^2 - 1}} \ln \left( \frac{a + \cos \theta + \sin \theta \sqrt{a^2 - 1}}{a \cos \theta + 1} \right) + K & \text{otherwise} \end{cases} \quad (2)$$

where  $K$  is a generic integral constant.

The damage of unidirectional laminae under in-plane shear is complex phenomenon since both matrix and interface may be damaged. For simplicity, the matrix is assumed to be linear elastic and just the damage in the transition zone between fiber and interface is considered, being induced by the radial component of the shear stress in this interface,  $\tau_{rz}$ .

From micromechanics, damage onset is defined by  $\tau_{rz} = S_s^i$ . Alternatively, the macromechanical damage condition is defined by  $\langle \sigma_{12} \rangle = S_{12}^{s,o}$ .  $S_s^i$  and  $S_{12}^{s,o}$  are the interface shear

strength and the lamina onset in-plane shear strength, respectively. Due to the load sharing, the following relation is obtained

$$S_{12}^{s,o} = (1 + a_{12}^{(1)}) \frac{G_{12}}{G^m} S_s^i \quad (3)$$

The damage propagation can be considered as stable for in-plane shear load [ASTM]. Hence, the damage initiates in an angle  $\theta = 0^\circ$  in relation to  $x_2$  and it can propagate for any angle  $0^\circ \leq \theta \leq 90^\circ$ , where  $\tau_{zx} = S_s^i$  for  $\theta \leq \theta_d$  and the material has a linear-elastic response for  $\theta > \theta_d$ . Considering a strain-driven load, i.e. the in-plane shear strain  $\langle \varepsilon_{12} \rangle$  is an input, the macromechanical effective stress in the inelastic regime is computed by

$$\langle \sigma_{12} \rangle = 2 \sqrt{\frac{V_f}{\pi}} \theta_d S_s^i + 2 G_{12}^T \langle \varepsilon_{12} \rangle \quad (4)$$

where  $G_{12}^T$  is the lamina in-plane shear tangent modulus and  $\theta_d$  is the damage angle defined by

$$G_{12}^T = G^m \left( 1 + 2 \sqrt{\frac{V_f}{\pi}} [I(a_{12}^{(1)}, \pi/2) - I(a_{12}^{(1)}, \theta_d)] + 2 \sqrt{\frac{V_i + V_f}{\pi}} [I(a_{12}^{(2)}, \pi/2) - I(a_{12}^{(2)}, \theta_i) - 1] \right) \quad (5)$$

$$\theta_d = a \cos \left( \frac{S_s^i}{2 G^m \langle \varepsilon_{12} \rangle - a_{12}^{(1)} S_s^i} \right) \quad (6)$$

### 3. RESULTS AND DISCUSSION

The estimations of proposed model developed on the previous section is compared with experimental data from unidirectional CFRP made by IM7 fiber and 8552 epoxy matrix [11]. A finite element simulation is also carried out using the commercial software Ansys.

Initially, the micromechanical properties  $\lambda$ ,  $V_i$  and  $S_s^i$  of the lamina is obtained and Figure 2 shows the calibration of these parameters. In Fig. 2a, the combinations of  $\lambda$  and  $V_i$  to fit the analytical estimation of  $G_{12}$  are presented. Considering three different combinations of  $\lambda$  and  $V_i$ , the average error between the analytical results and the experimental shear stress-strain curve is presented in Fig. 2b according to  $S_s^i$ . It should be pointed out that all combinations of  $\lambda$  and  $V_i$  results in an average error equal to 2.1% for  $S_s^i = 82\text{MPa}$ .

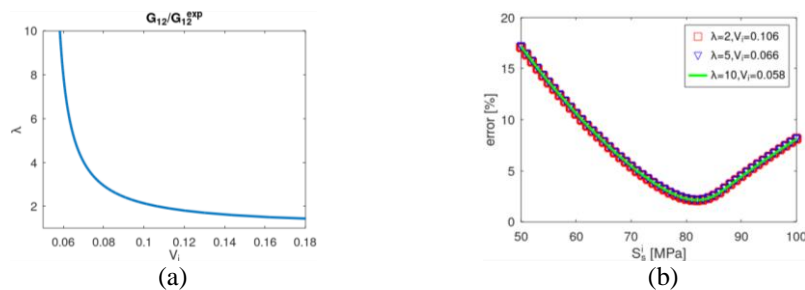


Figure 2 – Influence of micromechanical properties: (a) elastic response; (b) inelastic response.

After the calibration of these properties, a finite element analysis is developed and the shear stress-strain diagram is built from analytical, numerical and experimental approaches, being presented



in Fig. 3. Results indicate a good agreement between the analytical model and the experimental data, as well as the physical consistence compared with the numerical simulation.

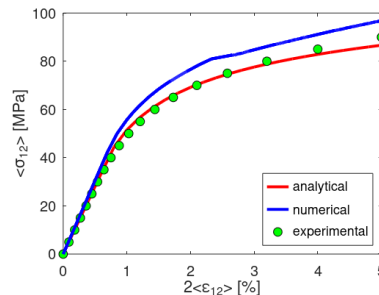


Figure 3 – Comparison between shear stress-strain curves: analytical model, numerical simulation and experimental data.

## ACKNOWLEDGEMENTS

The authors would like to acknowledge the support of the Brazilian Research Agencies CNPq, CAPES, FAPERJ and the Natural Sciences and Engineering Research Council of Canada (NSERC).

## REFERENCES

The list of references must be introduced as a new section, located at the end of the manuscript. The first line of each reference must be aligned at left. All the other lines must be indented by 1.25 cm from the left margin. All references included in the reference list must have been mentioned in the text.

- [1] L.L. Vignoli, M.A. Savi, P.M.C.L. Pacheco, A.L. Kalamkarov. Comparative analysis of micromechanical models for the elastic composite laminae. *Composites Part B: Engineering*, 174, 106961. (2019).
- [2] L.L. Vignoli, M.A. Savi, P.M.C.L. Pacheco, A.L. Kalamkarov. Micromechanical analysis of transversal strength of composite laminae. *Composite Structures*, 250, 112546. (2020).
- [3] L.L. Vignoli, M.A. Savi, P.M.C.L. Pacheco, A.L. Kalamkarov. Micromechanical analysis of longitudinal and shear strength of composite laminae. *Journal of Composite Materials*, 54, 4853-4873. (2020).
- [4] L.L. Vignoli, M.A. Savi, P.M.C.L. Pacheco, A.L. Kalamkarov. A Novel Micromechanical Model Based on the Rule of Mixtures to Estimate Effective Elastic Properties of Circular Fiber Composites. *Applied Composite Materials*, 29, 1715–1731. (2022).
- [5] C.N. O’Brien, A.E. Zoghi. Modelling the nonlinear shear stress-strain response of composites with metal and non-metal reinforcement. *Composites Part B*, 221, 109009. (2021).
- [6] A. Sabik. In-plane shear nonlinearity in failure behavior of angle-ply laminated shells. *Composite Structures*, 225, 111164. (2019).
- [7] L. Riaño, L. Belec, J.F. Chailan, Y. Joliff. Effect of interphase region on the elastic behavior of unidirectional glass fiber/epoxy composites. *Composite Structures*, 198, 109–116. (2018).
- [8] I.V. Andrianov, V.I. Bolshakov, V.V. Danishevs’kyy, W. Weichert. Asymptotic simulation of imperfect bonding in periodic fibre-reinforced composite materials under axial shear. *International Journal of Mechanical Sciences*, 49, 1344-1354. (2007).
- [9] D. Zhang, A.M. Waas. A micromechanics based multiscale model for nonlinear composites. *Acta Mech*, 225, 1391–1417. (2014).
- [10] I. Sevostianov, R. Rodriguez-Ramos, R. Guinovart-Diaz, J. Bravo-Castillero, F.J. Sabina. Connections between different models describing imperfect interfaces in periodic fiber-reinforced composites. *International Journal of Solids and Structures*, 49, 1518–1525. (2012).

- [11] A.S. Kaddour, M.J. Hinton, P.A. Smith, S. Li. Mechanical properties and details of composite laminates for the test cases used in the third world-wide failure exercise. *J Compos Mater*, 47, 2427–2442. (2013).

### **RESPONSIBILITY NOTICE**

The authors are the only responsible for the printed material included in this manuscript.

# GENERATION OF IRREGULAR COMPOSITE MICROSTRUCTURES THROUGH OPTIMIZATION

Matheus Urzedo Quirino<sup>a</sup>, Volnei Tita<sup>a</sup>, Marcelo Leite Ribeiro<sup>a</sup>

<sup>a</sup>São Carlos School of Engineering, University of São Paulo  
Av. João Dagnone, 1100 – Jardim Santa Angelina, São Carlos, SP, Brazil – 13563-120  
matheus.quirino@usp.br, voltita@sc.usp.br, malribei@usp.br

**Keywords:** composites materials, random microstructures, point process statistics, optimization.

## 1. INTRODUCTION

Composite materials are of general use nowadays, which may be justified by their resistances to corrosion and fatigue, as well as their specific stiffness and strength [1]. However, their structural integrity depends on failure mechanisms initiating at the material microstructure, which, in turn, lead to macrostructural effects [2], that is, effects at the coupon or component levels [3], therefore supporting the use of multiscale simulations.

These simulations require a microstructural model, regarded as a representative volume element (RVE), whose size must be sufficiently large to appropriately represent the microstructure, yet sufficiently small to represent a point at the macrostructure [4]. Said RVE can be regular, as the one shown in Fig. 1a, or not (Fig. 1b) – both figures present bidimensional microstructures, as cross-sections with a plane perpendicular to the fiber length.

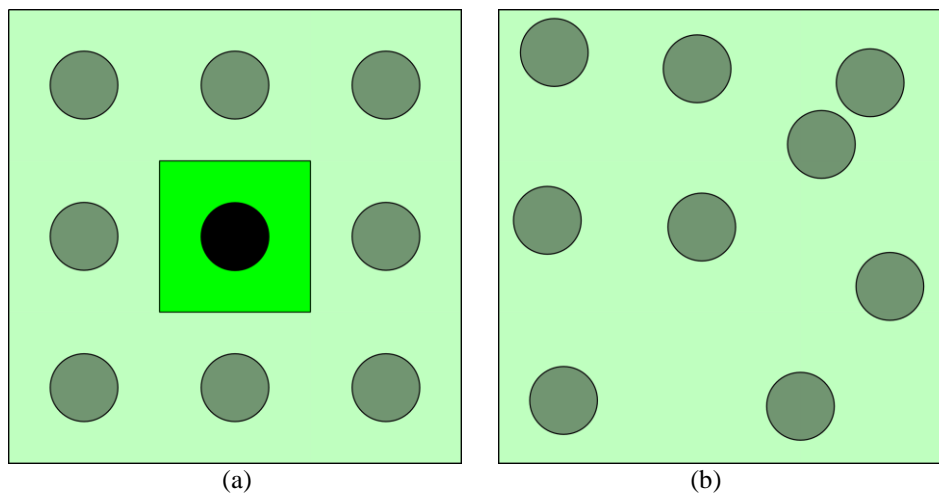


Figure 1 – Composite microstructural models: (a) regular; (b) irregular.

Regular microstructures (Fig. 1a) tend to be less computationally expensive, because they can be reduced to much simpler fiber–matrix arrangements. However, real microstructures are normally irregular, being also influenced by the manufacturing process [6]. As local stress concentrations depend on the fiber arrangement [7], the necessity of analyzing irregular microstructures is clear.

Such microstructures may be interpreted as point patterns (random distributions of objects throughout specified areas called windows), which may be described through Point Process Statistics techniques, as done in [7], for example; this effectively considers the fiber centers as said randomly distributed points. These spatial distributions, although not regular, also fail to exhibit complete spatial

randomness (CSR) [8,9], in which a given point can be in any location within the window with equal probability and independently from all the other points [7]; furthermore, the simple imposition of constraints on fiber centers to ensure fiber impenetrability in random arrangements (simple hard-core model) is also unsuitable for real microstructures [10].

As CSR and simple hard-core models are ruled out as possible models for irregular microstructures, many procedures have been proposed in the literature for the generation of those fiber arrangements. Said procedures may be grouped in two broad categories: numerical generation or image processing [5]. The first category involves fully computational methods [6,10-12], whereas the second necessarily employs experimental images of the real microstructure and image processing techniques [8,9], even if the final microstructure is to be computationally generated; this is especially true if the final algorithm performs pattern reconstruction, i.e., generation of a pattern whose statistical summary characteristics are as close as possible to those of the real pattern [13].

The optimization algorithm for pattern reconstruction presented in [13] is employed here, having been implemented in R [14] with package “spatstat” [15], with adaptations for generating fiber arrangements. The following sections outline the final algorithm and preliminary verification results.

## 2. METHODOLOGY

### 2.1. Theory

Prior to presenting the employed algorithm, it is important to define the Point Process Statistics tools employed herein for pattern characterization and reconstruction; as these tools are functions, parametrized in coordinate  $r$ , they are denoted functional statistics. The ones employed in this work are defined below, according to [13], with  $\mathcal{P}$  denoting probability,  $\mathcal{E}$  representing an expected value,  $N$  being the number of points in a given set,  $\mu$  being the point density (number of points per unit area, commonly denoted pattern intensity), and  $\mathcal{B}(\mathbf{o}, r)$  representing a circle of radius  $r$  centered at a position of coordinates  $\mathbf{o}$ . Also, the subscript  $\mathbf{o}$  denotes that a probability or expected value is calculated given that there is a point pattern at coordinates  $\mathbf{o}$ , whereas the symbol  $\{\mathbf{o}\}$  represents a set containing only said point.

- Spherical contact distribution function,  $H(r)$ : cumulative probability distribution of the minimum required radius  $r$  for a circumference centered at the origin to touch a point of the pattern, according to Eq. 1.

$$H(r) = 1 - \mathcal{P}\{N[\mathcal{B}(\mathbf{o}, r) = 0]\} \quad (1)$$

- Nearest neighbor distance distribution function  $D(r)$ : cumulative probability distribution of the distance between a typical point and its nearest neighbor, according to Eq. 2. In the case of fibers in a matrix, this distance is taken between fiber centers.

$$D(r) = \mathcal{P}_{\mathbf{o}}\{N[\mathcal{B}(\mathbf{o}, r) \setminus \{\mathbf{o}\}] > 0\} \quad (2)$$

- Ripley’s K-function  $K(r)$  and Besag’s L-function,  $L(r)$ : the former is related to the mean number of points inside a circle of radius  $r$  centered at a typical point (which, in turn, is not counted), according to Eq. 3, whereas the latter is closely related to Ripley’s K-function through Eq. 4.

$$K(r) = \frac{1}{\mu} \mathcal{E}_{\mathbf{o}}\{N[\mathcal{B}(\mathbf{o}, r) \setminus \{\mathbf{o}\}]\} \quad (3)$$

$$L(r) = \sqrt{\frac{K(r)}{\pi}} \quad (4)$$

- Pair correlation function  $g(r)$ : contains the same statistical information as Ripley’s K-function and Besag’s L-function, according to Eq. 5, being related to the probability of a point existing between two infinitesimally close circles of radius  $r$  centered at a typical point.

$$g(r) = \frac{1}{2\pi r} \frac{dK(r)}{dr} \quad (5)$$

Functions  $H(r)$ ,  $D(r)$ ,  $K(r)$  and  $g(r)$  are illustrated in Figures 2a through 2d below.

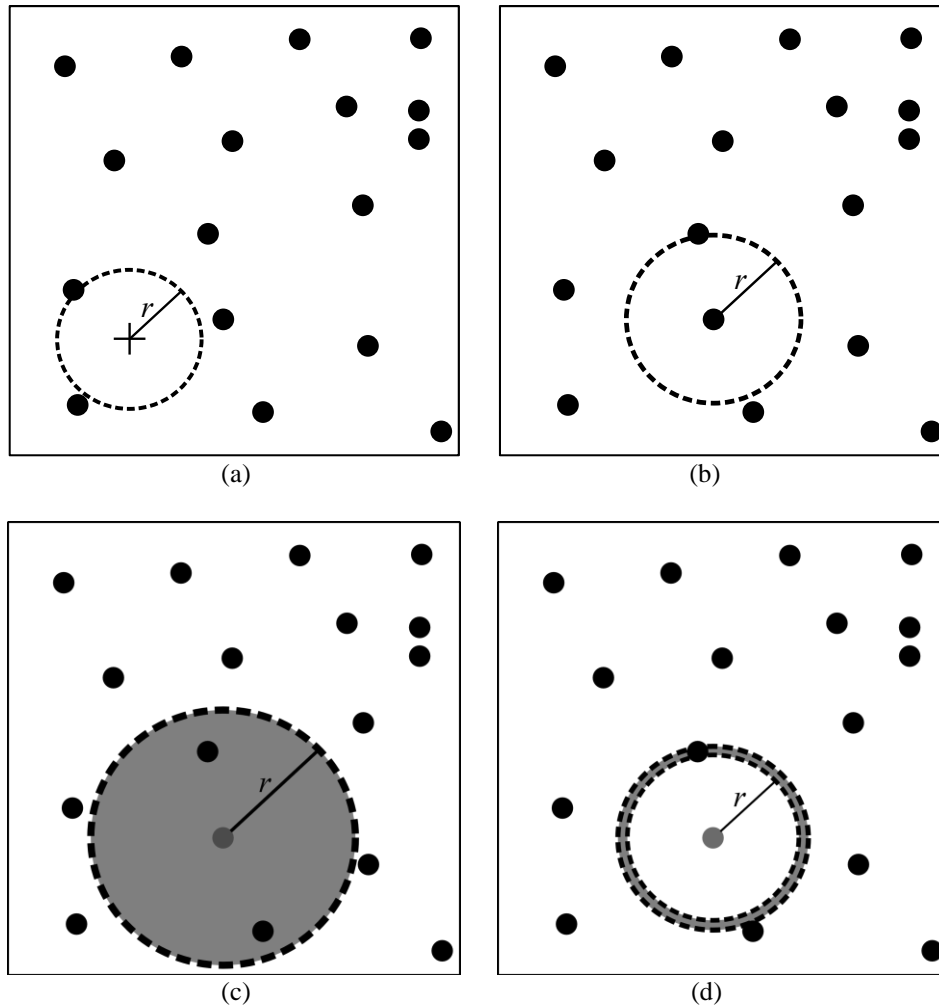


Figure 2 – Functional statistics for pattern characterization and reconstruction: (a)  $H(r)$ ; (b)  $D(r)$ ; (c)  $K(r)$ ; (d)  $g(r)$

## 2.2. Pattern reconstruction algorithm

The algorithm presented in [13] starts from a first trial pattern having already the final number of fibers with distances between one another no greater than the minimum one measured from the reference pattern. This first trial pattern, in contrast to the final one, can be a simple hard-core one, and is, indeed, generated as such by spatstat through a simple procedure.

Afterwards, the statistics of the trial pattern are compared to those from a reference pattern, providing a value for some cost functional. Following that, the trial pattern is optimized by randomly

moving its fiber centers, in order to minimize the cost functional, i.e., to make the trial pattern statistics as close as possible to those of the reference pattern. This reference pattern is preferably obtained from experiments, but, in the verification results presented here, pattern “cells” [16], already present in spatstat, was employed.

The algorithm follows the flowchart in Fig. 3. As hypotheses, the pattern is assumed to continue far beyond the RVE while keeping its statistical characteristics; also, the arrangement is assumed statistically homogeneous (translation-invariant), isotropic (rotation-invariant, which implies a transversely isotropic composite), and periodic.

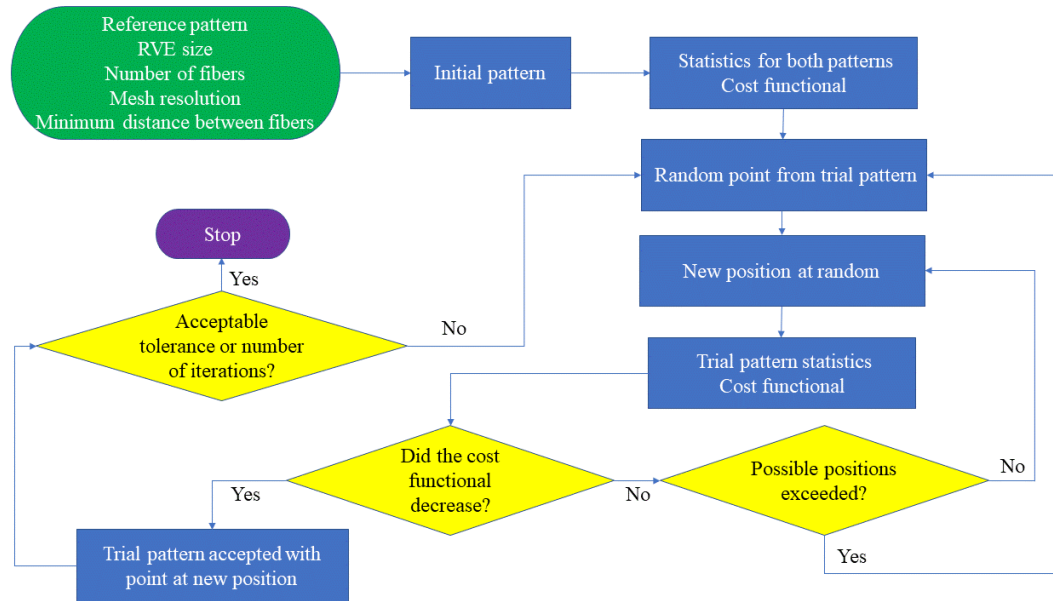


Figure 3 – Microstructure generation algorithm flowchart.

In each iteration, a random point (fiber center) is selected and moved to a random position within a mesh, whose resolution is given before the run. Moreover, uniform random noise (up to 40% of the spacing between mesh locations) is added to this trial position to prevent point superposition.

Four characteristics are employed as optimization criteria:  $D(r)$  – as it affects the material stresses [7];  $L(r)$  – as it describes longer-range interactions between points and is more tractable than Ripley’s K-function [13];  $H(r)$  – as it complements the information provided by the other two functions [13]; and the minimum distance between fibers ( $r_{min}$ ) – penalizes patterns not respecting its admissible value, given before the run. Nevertheless, for the optimization procedure,  $L(r)$  is normalized so that its maximum is 1,0, which is already true for the other two functions. The three functional statistics, collectively referred to as  $f_k$ , are calculated with appropriate edge corrections (because of the finite RVE size):  $H(r)$  and  $D(r)$  are calculated in reduced windows, whereas  $L(r)$  takes periodicity into account. Thus, the cost functional,  $\mathcal{F}$  is written Eq. 6, adapted from [13]:

$$\mathcal{F} = \sum_{k=1}^3 \sum_{i=0}^{N_k} [f_k(r_{ik}) - f_k^0(r_{ik})]^2 + \frac{1}{r_{min}^0} \langle r_{min} - r_{min}^0 \rangle \quad (6)$$

Above,  $N_k$  represents the number of values  $r_{ik}$  in which each  $f_k$  is calculated. Quantities calculated for the reference pattern are marked with a “0” superscript, whereas their values for the trial pattern are left with no superscript; in particular,  $r_{min}^0$  is the minimum admissible distance between fibers, which can come from the reference pattern or be given arbitrarily. In addition, the symbol “ $\langle \rangle$ ”

represents adapted Macaulay brackets, shown in Eq. (7). Furthermore, to ensure periodicity (fiber impenetrability at the RVE edges), the distance  $r_{min}$  was calculated with the torus metric [13]: said metric,  $\delta$ , measures the distance between two points  $A = (x_1^A, x_2^A)$  and  $B = (x_1^B, x_2^B)$  according to Eq. (8) [13], considering a rectangular RVE with sides of lengths  $l_1$  and  $l_2$ .

$$\langle y \rangle = \frac{1}{2}(|y| - y) = \begin{cases} 0, & y \geq 0 \\ -y, & y < 0 \end{cases} \quad (7)$$

$$\delta = \sqrt{(\min\{|x_1^A - x_1^B|, l_1 - |x_1^A - x_1^B|\})^2 + (\min\{|x_2^A - x_2^B|, l_2 - |x_2^A - x_2^B|\})^2} \quad (8)$$

### 3. RESULTS

The algorithm was employed for reconstruction of the pattern cells [16], having 42 points (considered as fiber centers), with a clear minimum distance between them, in a unit rectangle window. Here, the minimum admissible distance between fibers,  $r_{min}^0$ , was set to be 0.06 for convenience, which is smaller than the minimum distance between points in the reference pattern, whether measured through the Euclidean metric (0.084) or the torus metric (0.063). In other words, this means that the fibers represented by the pattern could have a diameter (when supposed uniform) of up to  $r_{min}^0$ , in which case they would be allowed to at most contact one another through a single point.

The final pattern and the reference one are presented in Fig. 4.

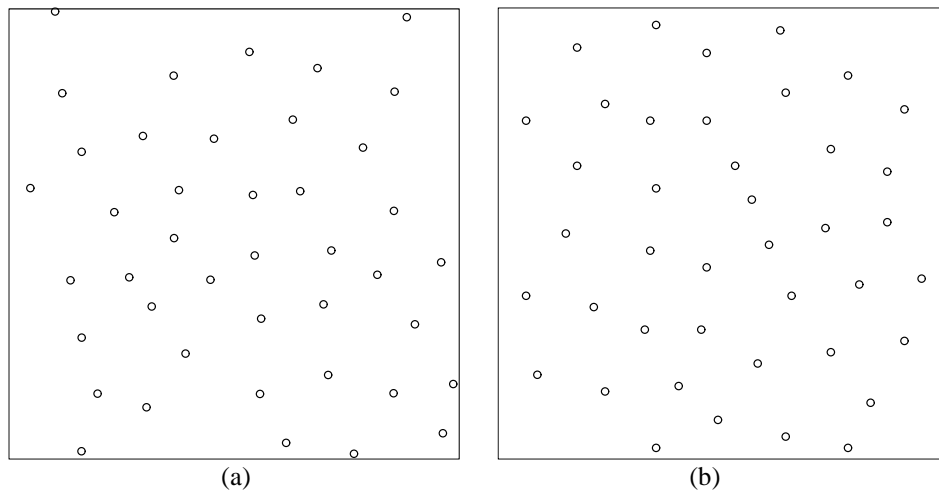


Figure 4 – Point patterns for algorithm verification: (a) reconstructed; (b) reference.

The total runtime was 1.12 hours, and the final cost functional was 0.204; the respective cost contributions are given in Tab. 1: as it can be seen from said table,  $r_{min}$  had no contribution to the final cost, meaning that the minimum distance between fibers in the final pattern was satisfactory, considering the chosen value for  $r_{min}^0$ .

Table 1 – Optimization cost contributions

Cost contribution	$H(r)$	$D(r)$	$L(r)$	$r_{min}$
Absolute	0.007	0.123	0.074	0.0
Relative (%)	3.43	60.29	36.27	0.0

Figures 5 through 8, produced in R [14], compare  $H(r)$ ,  $D(r)$ ,  $L(r)$  and  $g(r)$  for the reference and the reconstructed patterns; in the former three figures, the cost contributions presented in Tab. 1 can be seen graphically.

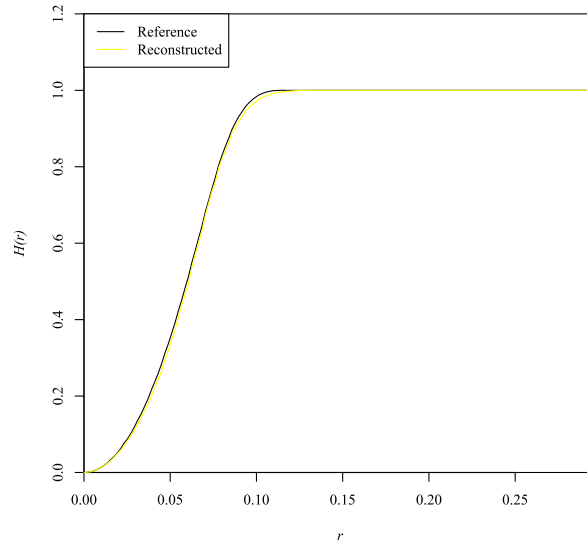


Figure 5 –  $H(r)$  for the reference and reconstructed patterns.

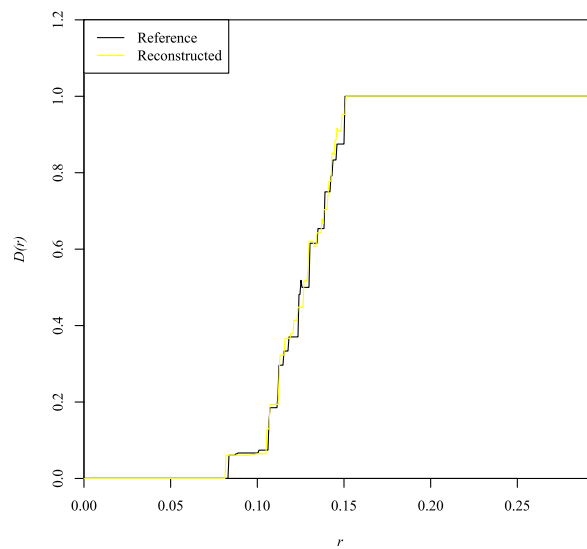


Figure 6 –  $D(r)$  for the reference and reconstructed patterns.



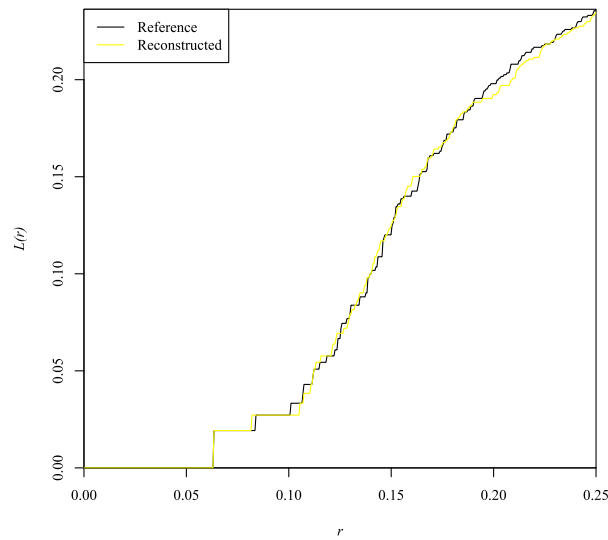


Figure 7 –  $L(r)$  for the reference and reconstructed patterns.

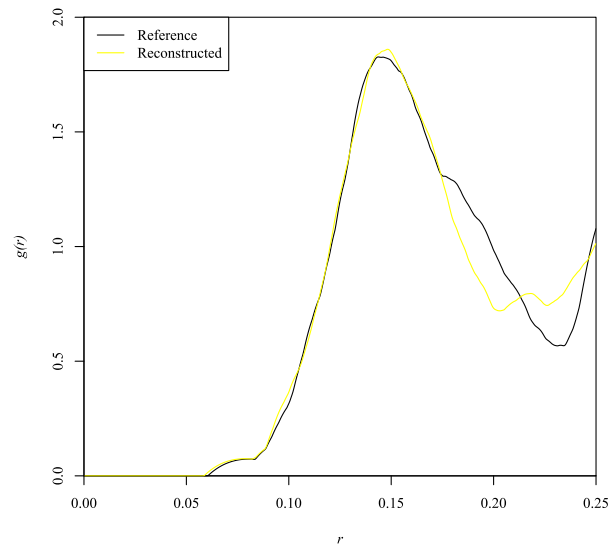


Figure 8 –  $g(r)$  for the reference and reconstructed patterns.

From the figures, the final produced pattern presented functional characteristics arguably close to those of the reference point pattern.

#### 4. CONCLUSION

The proposed algorithm has been capable of satisfactorily reconstructing a given point pattern, although further tests are necessary to verify its performance when applied to fiber distributions with greater fiber volumetric fractions. In addition, the isotropy hypothesis is currently being studied, to verify more rigorously if it holds for both the reference and the reconstructed patterns.

Future works include extending the procedure to the generation of microstructures with voids, effectively reconstructing patterns with more features.

## ACKNOWLEDGEMENTS

Volnei Tita would like to thank the National Council for Scientific and Technological Development (CNPq process number: 310159/2022-9).

## REFERENCES

- [1] W. Tan, B.G. Falzon, L.N.S. Chiu et al. Predicting low-velocity impact damage and compression after impact (CAI) behaviour of composite laminates. *Composites Part A: Applied Science and Manufacturing*, v. 71, p. 212–226. (2015).
- [2] R. Talreja. Assessment of the fundamentals of failure theories for composite materials. *Composites Science and Technology*, v. 105, p. 190-201. (2014).
- [3] M.J. Bogdanor, C. Oskay, S.B. Clay. Multiscale modeling of failure in composites under model parameter uncertainty. *Computational Mechanics*, v. 56, p. 389-404. (2015).
- [4] G. Chatzigeorgiou, F. Meraghni, N. Charalambakis. *Multiscale modeling approaches for composites*. Elsevier Inc. Amsterdam; Oxford; Cambridge, Massachusetts. (2022).
- [5] H. Ghayoor, S.V. Hoa, C.C. Marsden. A micromechanical study of stress concentrations in composites. *Composites Part B: Engineering*, v. 132, p. 115-124. (2018).
- [6] A.R Melro, P.P. Camanho, S.T. Pinho. Generation of random distribution of fibres in long-fibre reinforced composites. *Composites Science and Technology*, v. 68, p. 2092-2102. (2008).
- [7] R. Pyrz. Correlation of microstructure variability and local stress field in two-phase materials. *Materials Science and Engineering: A*, v. 177, p. 253-259. (1994).
- [8] V.N. Bulsara, R. Talreja, J. Qu. Damage initiation under transverse loading of unidirectional composites with arbitrarily distributed fibers. *Composites Science and Technology*, v. 59, p. 673-682. (1999).
- [9] T.J. Vaughan, C.T. McCarthy. A combined experimental-numerical approach for generating statistically equivalent fibre distributions for high strength laminated composite materials. *Composites Science and Technology*, v. 70, p. 291-297. (2010).
- [10] A. Sudhir, R. Talreja. Simulation of manufacturing induced fiber clustering and matrix voids and their effect on transverse crack formation in unidirectional composites. *Composites Part A: Applied Science and Manufacturing*, v. 127, p. 105620. (2017).
- [11] S.A. Elnekhaily, R. Talreja. Damage initiation in unidirectional fiber composites with different degrees of nonuniform fiber distribution. *Composites Science and Technology*, v. 155, p. 22-32. (2018).
- [12] G. Li, F. Sharifpour, A. Bahmani et al. A new approach to rapidly generate random periodic representative volume elements for microstructural assessment of high volume fraction composites. *Materials and Design*, v. 150, p. 124-138. (2018).
- [13] J. Illian, A. Penttinen, H. Stoyan et al. *Statistical analysis and modelling of spatial point patterns*. John Wiley & Sons, Ltd. Chichester, UK. (2008).
- [14] R Core Team. *R: a language and environment for statistical computing*. Vienna, Austria. (2008).
- [15] A. Baddeley, E. Rubak, R. Turner. *Spatial point patterns: Methodology and applications with R*. Chapman and Hall/CRC Press. London, UK. (2015).
- [16] B. D. Ripley. Modelling spatial patterns. *Journal of the Royal Statistical Society: Series B (Methodological)*, v. 39, n. 2, p. 172-192. (1977).

## RESPONSIBILITY NOTICE

The author(s) is (are) the only responsible for the printed material included in this manuscript.

# MECHANICAL BEHAVIOR OF CFRP STRENGTHENED TUBULAR STEEL STRUCTURES

Bárbara Thaís Jacques Minosso<sup>a</sup>, Rogério José Marczak<sup>a</sup>

<sup>a</sup>PROMEC, Federal University of Rio Grande do Sul  
Rua Sarmiento Leite, 425, Porto Alegre, RS CEP 90050-170, Brasil  
[barbara.minosso@ufrgs.br](mailto:barbara.minosso@ufrgs.br), [rato@mecanica.ufrgs.br](mailto:rato@mecanica.ufrgs.br)

**Keywords:** Finite element analysis, Composite tube, Filament winding, Composite materials.

## 1. INTRODUCTION

Steel structures used in buildings intended for housing, commerce or industry, as well as structures for pedestrian walkways and equipment supports, must follow the requirements established by NBR 8800/08. Among the design limitations to be followed is the maximum displacement of the structure components [1].

Carbon fiber-reinforced epoxy composites have numerous applications being commonly used in applications with high structural demand, such as aeronautical, aerospace, automotive, construction, and marine sectors [2]. Among the manufacturing processes available for composites, filament winding (FW) stands out, being the most suitable automated manufacturing technique for producing cylindrical composites with continuous fiber reinforcement, which are accurately placed onto a rotating mandrel. The high fiber content, high precision in angle deposition, low void content and good automation capability along with the use of continuous reinforcement are the main features of FW [3].

With the advance in the use of prefabricated metallic structures, added to the reduction of costs and quantity of material, several projects do not consider the need for future expansions. Due to this, in some installations when there is a need to increase the load supported by the metallic structure, it does not meet the required standards, mainly in relation to displacement. An alternative besides replacing the structure is reinforcing the damaged parts.

Concerning reticulated structures, a good number of them are built using beams of circular cross-sections. Aiming the reusability and life extensibility of these structures, FW techniques can be used to strengthen these structures and raise their load bearing capability to a higher level. Evidently, the calculations of such structures become one of layered beams, and besides the original material, a new layer of FR composite is added to the individual bars. Thus, the objective of this work is to evaluate the mechanical behavior of steel tubes reinforced with carbon fiber/epoxy through FW, compare their mechanical behavior with the original structure, quantify to increase in load capacity and investigate changes in the dynamic behavior.

## 2. MATERIALS

In this study, steel structures are analyzed before and after reinforcement with composite material. According to NBR 8800/08, for steel structure projects, the values of mechanical properties presented in Table 1 must be adopted.

Carbon fiber/epoxy prepreg tow (towpreg) from TCR Composites, with Toray T700-12K-50C carbon fiber and UF3369 epoxy resin system, was used in this work. The material properties of unidirectional carbon/epoxy laminate with a fiber volume fraction of  $\approx 72\%$  has been used in the computational analyses (Table 2) [3]. The fiber density is  $\rho = 1800 \text{ kg/m}^3$ , and the resin density is  $\rho = 1180 \text{ kg/m}^3$  [5,6]. With these data, it is possible to calculate the density of the carbon fiber/epoxy composite using the mixture rule, corresponding  $\rho = 1626 \text{ kg/m}^3$ .

Table 1 – Mechanical properties of structural steel [1].

Description	Symbol	Value
Elastic modulus	$E = E_a$ (GPa)	200
Transversal elastic modulus	$G$ (GPa)	77
Poisson's ratio	$\nu_a$	0.3
Density	$\rho_a$ (kg/m <sup>3</sup> )	7850

Table 2 – Material properties used as input in the numerical models [3,4].

Description	Symbol	Value
Longitudinal elastic modulus	$E_1$ (GPa)	129.3
Transversal elastic modulus	$E_2 = E_3$ (GPa)	9.11
Poisson's ratio in plane 1-2	$\nu_{12} = \nu_{13}$	0.32
Poisson's ratio in plane 2-3	$\nu_{23}$	0.35
In-plane shear modulus	$G_{12} = G_{13}$ (GPa)	5.44
Transverse shear modulus in plane 2-3	$G_{23}$ (GPa)	2.10
Longitudinal tensile strength	$X_t$ (MPa)	1409.9
Transversal tensile strength	$Y_t$ (MPa)	42.5
Longitudinal compressive strength	$X_c$ (MPa)	-740.0
Transversal compressive strength	$Y_c$ (MPa)	-140.3
In-plane shear strength	$S_{12}$ (MPa)	68.9

## 2.1. Determination of engineering elastic properties of composite material

When using beam elements in the numerical simulation, it is not possible to enter the data of the properties of the unidirectional layer composite directly in ANSYS because the calculation of the properties of the laminate is only done in the use of shell elements [7]. The properties of the total laminate are then obtained from script in MATLAB following the classical theory of laminates, considering each layer FW is orthotropic [8]. The flowchart shown in the Figure 1 show the layout of the script for determining the engineering elastic properties of the reinforcement FW. Several stacking sequences had their properties calculated, in order to choose the one that best suits the application. The resulting properties of the chosen stacking sequence were used as input data in ANSYS software.

The stacking sequence was chosen based on the parameters critical to the application: tension, bending, and torsion. The optimal angles for these parameters are  $0^\circ$  and  $\pm 45^\circ$ , however the  $\pm 25^\circ$  layers were selected instead  $0^\circ$ , while respecting the limitations of the considered FW setup [4]. The lamina thickness is  $t_l \approx 0.5$  mm, corresponding  $\pm\theta$  winding plies. The considered FW reinforcement is composed of two layers, with configurations  $[\pm 25^\circ]_2$ ,  $[\pm 45^\circ]_2$ , and  $[\pm 25^\circ/\pm 45^\circ]$  evaluated in this study.

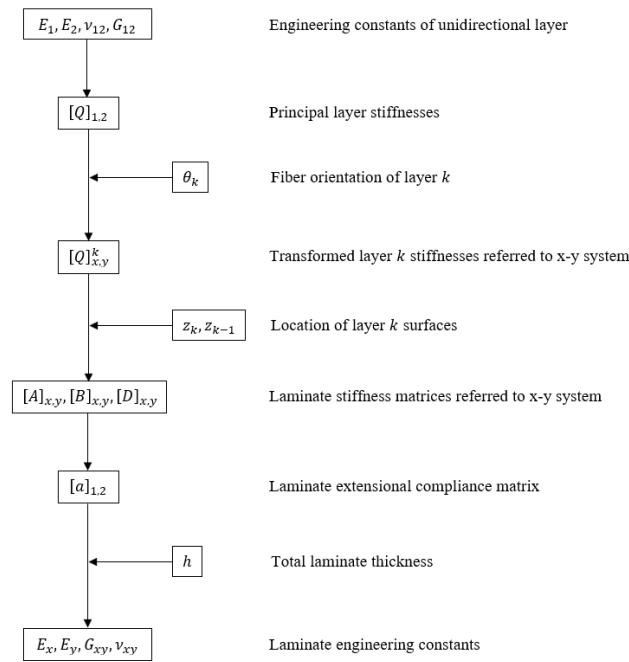


Figure 1 – Flowchart of the determination of engineering elastic properties of composite laminate.

### 3. NUMERICAL MODEL VALIDATION

A steel tube of circular section (Figure 2) with length,  $L$ , 1 m, external diameter,  $D_e$ , equal to 33.4 mm and thickness,  $t$ , 3.2 mm was used as the original structure in this step. This structure is analyzed under 3 different load conditions: 1) bi-supported beam under flexion, with central loading,  $F = -1$  kN; 2) cantilever beam under traction, with loading at the free end,  $F = 100$  kN; and 3) cantilever beam under torsion, with torque of 450 N.m at the free end. After analysis of the original structure, it is analyzed under the effect of the FW reinforcement, with the three different configurations previously defined.

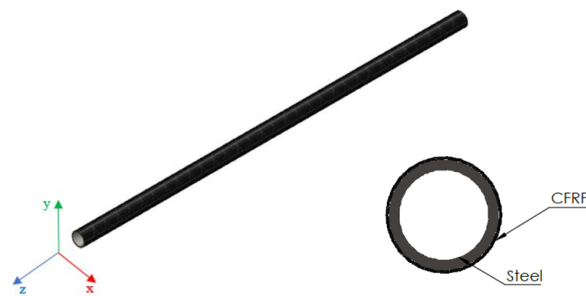


Figure 2 – Steel tube reinforcement with CFRP.

Computational models were developed on ANSYS software. Static and modal analysis were performed in order to evaluate the behavior of the structure. The evaluation of the stiffness of the structure is carried out through the analysis of the resulting displacement. Numerically, this analysis is performed through the principle of virtual displacements (for undamped systems) [9]:

$$[M]\{\ddot{u}\} + [K]\{u\} = \{F\} \quad (1)$$

where  $[M]$  is the mass matrix,  $[K]$  is the stiffness matrix,  $\{F\}$  is the applied forces vector, and  $\{u\}$  is the displacements vector and  $\{\ddot{u}\}$  is the accelerations vector.

### 3.1. Static analysis

Considering a static analysis, Eq. (1) is reduced to:

$$[K]\{u\} = \{F\} \quad (2)$$

where  $\{u\}$  are the unknown displacements of the problem.

In general, for the loading conditions under study, the resulting displacements can be obtained by the following equations:

$$u_y = -\frac{FL^3}{48EI} \quad (3)$$

$$u_z = -\frac{FL}{EA} \quad (4)$$

$$\phi = \frac{TL}{GJ} \quad (5)$$

where  $u_y$  is the displacement in the direction of the y-axis,  $u_z$  is the displacement in the direction of the z-axis,  $\phi$  is the angle of rotation,  $F$  is the applied force,  $T$  is the applied torque,  $L$  is the length of the beam,  $E$  is the longitudinal elastic modulus,  $G$  is the shear modulus,  $I$  is the moment of inertia of area,  $A$  is the area of section, and  $J$  is the polar moment of inertia.

### 3.2. Modal analysis

Modal analysis is used to obtain the vibration modes and their respective frequencies. Starting from the principle of virtual displacements and considering that the natural frequency has no relation to the applied load, i.e,  $F = 0$ , we can rearrange Equation (1) in such a way that the frequency is obtained through the relationship between the matrices of stiffness and mass, so that the determinant of the eigensystem vanishes and the roots  $\omega_n$  [rad/s], match the frequencies in the  $n$  vibration modes:

$$[[K] - \omega^2[M]] = 0 \quad (6)$$

In general, the natural frequency,  $f$  [Hz], of a beam is obtained through:

$$f = \frac{1}{2\pi} \sqrt{\frac{k}{m}} \quad (7)$$

where  $k$  is the stiffness and  $m$  the mass of the beam.

For the cases of bi-supported beam under bending and cantilever beam under traction and under torsion, the natural frequency can be calculated analytically according to:

$$f_{bending} = \frac{n^2\pi}{2} \sqrt{\frac{E_x I}{mL^4}}, \quad n = 1,2,3, \dots \quad (8)$$

$$f_{traction} = \frac{(2n-1)}{4} \sqrt{\frac{E_x A}{mL^2}}, \quad n = 1,2,3, \dots \quad (9)$$

$$f_{torsion} = \frac{(2n-1)}{4} \sqrt{\frac{G_{xy}}{\rho L^2}}, \quad n = 1, 2, 3, \dots \quad (10)$$

#### 4. RESULTS AND DISCUSSION

Results are shown evaluating the mechanical properties resulting from the combination between steel and carbon fiber/epoxy for beam and trusses, showing the variation of the mechanical behavior of the original structure compared to the reinforced one.

The static analysis of the first two loading conditions was performed using beam and shell finite elements, comparing the results with the objective of validating or not the use of beam elements for analysis of steel structures reinforced with composite material.

The beam element used was the BEAM189, with which it was possible to generate a mesh for the original beam with 154 nodes and 51 elements of size 20 mm and for the reinforced beam of 205 nodes and 102 elements. For the shell element, SHELL281 was used, whose mesh was generated using quadratic elements of size 20 mm, defined from convergence analysis, having 5100 nodes and 1692 elements. Figure 3 shows the mesh generated with the different finite elements used.

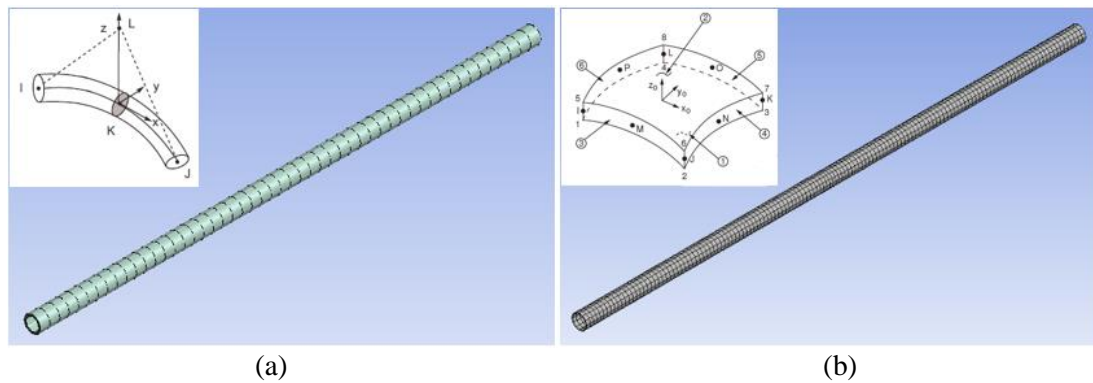


Figure 3 – Mesh used with (a) beam finite element; (b) shell finite element.

The displacements resulting from the static analysis of the beam under the three different loading conditions are presented in Tables 3 to 5, for the beam under bending, traction and torsion, respectively. Comparing the results between the different elements, it is possible to identify that the maximum difference between values occurs for the Steel+[±25°/±45°] configuration and corresponds to 4.12%, a considerably small value that makes it feasible to use beam elements for the analysis of reinforced steel structures later. In addition, it is possible to identify that the configuration that presented the greatest stiffness gain and consecutively that greatest displacement reduction was Steel+[±25°]<sub>2</sub>, with 13.12% for the flexion condition and 10.55% for the traction condition. For the torsion condition, as expected, the Steel+[±45°]<sub>2</sub> configuration obtained the highest torsional stiffness gain, 16.56%.

Table 3 – Resultant displacements for the simply supported beam under bending.

Configuration	Displacements (mm)		Difference (%)
	Beam Element	Shell Element	
Steel	3.0033	3.0022	0.04
Steel+[±25°] <sub>2</sub>	2.6092	2.5313	3.08
Steel+[±45°] <sub>2</sub>	2.8769	2.8281	1.72
Steel+[±25°/±45°]	2.7906	2.6778	4.12

Table 4 – Resultant displacements for the cantilever beam under traction.

Configuration	Displacements (mm)		Difference (%)
	Beam Element	Shell Element	
Steel	1.6482	1.7048	3.32
Steel+[±25°] <sub>2</sub>	1.4743	1.4929	1.24
Steel+[±45°] <sub>2</sub>	1.5945	1.6272	2.01
Steel+[±25°/±45°]	1.5562	1.5581	0.12

Table 5 – Resultant displacements for the cantilever beam under torsion.

Configuration	Angle of rotation (°)	Displacement reduction (%)
Steel	4.7981	-
Steel+[±25°] <sub>2</sub>	4.2469	11.49
Steel+[±45°] <sub>2</sub>	4.0037	16.56
Steel+[±25°/±45°]	4.1409	13.70

The modal analysis for the same loading conditions was performed in order to identify the variation of the frequencies in the first four vibration modes of the structure with the FW reinforcement. Tables 6 to 8 present the values obtained numerically as well as the value of the natural frequency, which corresponds to the first vibration mode, obtained analytically. Comparing the results, it can be identified that the values of the frequencies suffered small variations, since in addition to the increase in stiffness there is an increase in the mass of the structure, balancing the value of the frequency.

Table 6 – Vibration modes of simply supported beam.

Configuration	Analytical results	Mode I	Mode II	Mode III	Mode IV
Steel	85.190Hz	84.782Hz	335.69Hz	743.00Hz	1292.3Hz
Steel+[±25°] <sub>2</sub>	89.232Hz	87.783Hz	347.42Hz	768.46Hz	1335.4Hz
Steel+[±45°] <sub>2</sub>	81.190Hz	83.592Hz	331.23Hz	734.01Hz	744.43Hz
Steel+[±25°/±45°]	85.250Hz	84.878Hz	336.17Hz	1278.6Hz	1295.6Hz

Table 7 – Vibration modes of cantilever beam.

Configuration	Analytical results	Mode I	Mode II	Mode III	Mode IV
Steel	1262.8Hz	1262.9Hz	3788.8Hz	6314.6Hz	8840.5Hz
Steel+[±25°] <sub>2</sub>	1275.9Hz	1288.5Hz	3865.6Hz	6442.7Hz	9019.8Hz
Steel+[±45°] <sub>2</sub>	1161.0Hz	1239.1Hz	3717.4Hz	6195.6Hz	8673.8Hz
Steel+[±25°/±45°]	1219.0Hz	1254.2Hz	3762.7Hz	6271.2Hz	8779.7Hz



Table 8 – Vibration modes of torsion of cantilever beam.

Configuration	Analytical results	Mode I	Mode II	Mode III	Mode IV
Steel	782.98Hz	782.59Hz	2347.8Hz	3912.9Hz	5478.1Hz
Steel+[±25°] <sub>2</sub>	795.22Hz	785.03Hz	2385.1Hz	3975.2Hz	5565.2Hz
Steel+[±45°] <sub>2</sub>	798.38Hz	818.82Hz	2456.5Hz	4094.1Hz	5731.8Hz
Steel+[±25°/±45°]	784.06Hz	805.15Hz	2415.4Hz	4025.7Hz	5636.0Hz

A cantilever truss resulting from optimization work performed in [11] was also evaluated. Its geometry is shown in Figure 4 along with the illustration of the loading condition. The truss is set at one end and loaded with a charge  $F_1 = 120$  kN at the free end. The same FW reinforcement configurations were analyzed for this case. Table 9 presents the result of the static analysis of the structure while Table 10 present the frequencies of the first three modes of vibration of the truss. Comparing the results obtained, it can be identified that among the analyzed configurations, the Steel+[±25°]<sub>2</sub> has a greater gain in stiffness, being possible to reduce the displacement by 3.98%. As for the frequencies obtained by the modal analysis of the structure, it is possible to identify a small change in values, being the configuration Steel+[±25°]<sub>2</sub> the one with the greatest increase in value.

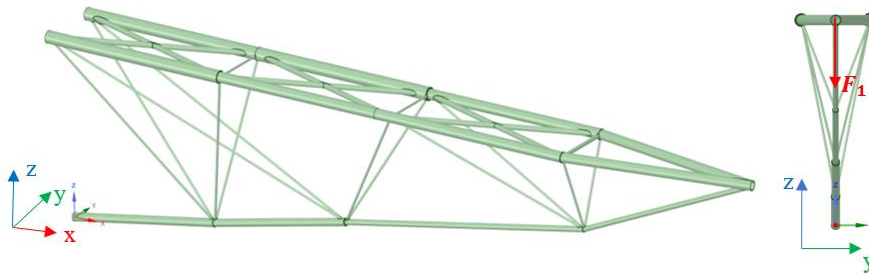


Figure 4 – Cantilever truss structure.

Table 9 – Resultant displacements for the cantilever truss reticulated.

Configuration	Displacement (mm)	Displacement reduction (%)
Steel	45.649	-
Steel+[±25°] <sub>2</sub>	43.833	3.98
Steel+[±45°] <sub>2</sub>	45.19	1.00
Steel+[±25°/±45°]	44.792	1.92

Table 10 – Vibration modes of cantilever truss reticulated.

Configuration	Mode I	Mode II	Mode III
Steel	4.7713Hz	8.6911Hz	10.167Hz
Steel+[±25°] <sub>2</sub>	4.8146Hz	8.8278Hz	10.376Hz
Steel+[±45°] <sub>2</sub>	4.7393Hz	8.6466Hz	10.127Hz
Steel+[±25°/±45°]	4.7621Hz	8.7036Hz	10.202Hz

An estimate of raw material costs was made, with an average value of R\$9.00/kg for steel and R\$300.00/kg (\$61.50/kg) for towpreg. The original structure of truss reticulated, in steel, has 4430 kg, without considering the connections. When reinforced with two FW layers, there is an increase of approximately 120 kg, which causes a cost of R\$36000.00 with raw material. To identify the feasibility of using FW as an alternative to replacing the steel structure, it is necessary, in addition to estimation the costs with material, labor, disassembly and assembly of the structure, transportation to the place where the reinforcement will be carried out and return to the installation site, FW machine and inputs. In addition, perform a thorough analysis of the steel structure in order to identify the possibility of replacement or FW reinforcement of only a few bars of the truss. Assuming that it is necessary to replace the entire truss with a more robust one, the amount spent on steel for a reticulated truss of 4600 kg is R\$41400.00 plus labor for manufacturing, inputs and connecting elements, costs with manufacturing, transportation and assembly, as well as disassembly of the truss to be replaced. Finally, the feasibility or not of the FW reinforcement is defined according to the comparison of these values.

## 5. CONCLUSIONS

In this work we presented a study of the stiffness and natural frequency changes when existing tubular structures are reinforced by FR using FW. The following considerations can be made:

1. Beam finite elements can be used to analyze the reinforced structures without the need of shell elements, reducing computational costs.
2. The composite reinforcement proved to increase significantly the overall load bearing capacity of the structure.
3. The best angle of reinforcement was found to be  $\pm 25^\circ$ , for the configurations here analyzed.
4. Natural frequencies barely changed, showing that the increase in stiffness is balanced by the increase in mass.
5. The present study showed that FW reinforcement can be a viable alternative to increase the load capacity of existing structures, pending a cost analysis.

## ACKNOWLEDGEMENTS

We thank the CAPES for the financial support to present this paper. RJ Marczak acknowledges CNPq grant 317140/2021-3 and Capes PROBRAL 88887.701013/2022-00.

## REFERENCES

- [1] ABNT (Associação Brasileira de Normas Técnicas). NBR 8800:2008, *Projeto de estruturas de aço e de estruturas mistas de aço e concreto de edifícios*. (2008).
- [2] M.A. Masuelli, *Introduction of Fibre-Reinforced Polymers – Polymers and Composites: Concepts, Properties and Processes*. In: *Fiber Reinforced Polymers – The Technology Applied for Concrete Repair*. 1ed. [online]. (2013).
- [3] J.H.S. Almeida Jr, S.D.B. Souza, E.C. Botelho, S.C. Amico. Carbon fiber-reinforced epoxy filament-wound composite laminates exposed to hygrothermal conditioning. *J Mater Sci*. v.51, p. 4697-4708. (2016).
- [4] P. Stedile Filho, J.H.S. Almeida Jr, S.C. Amico. Carbon/epoxy filament wound composite drive shafts under torsion and compression. *Journal of Composite Materials*. v.52, n.8, p. 1103-1111. (2018).
- [5] TORAY. *T700S Standard Modulus Carbon Fiber*. Technical Data Sheet. 2 p.
- [6] TCR. *UF3369 TCR Resin System*. Technical Data Sheet. 3 p.
- [7] ANSYS. *Workbench User's Guide*. Ansys Inc. (2023).
- [8] H. Hernández-Moreno, B. Douchin, F. Collombet et al. Influence of winding pattern on the mechanical behavior of filament wound composite cylinders under external pressure. *Composite Science and Technology*. v.68, p. 1015-1024. (2008).
- [9] K.J. Bathe. *Finite Element Procedures*, Klaus-Jürgen Bathe. (2007).

- [10] M.P. Paz, Y.H. Kim, *Structural Dynamics*, 6ed. Springer. (2019).  
[11] P.S. Santos. *Layout and topology optimization of three-dimensional tubular gantries with semi-rigid connections including mixed variables and reduction of complexity*. Master's thesis. State University of Santa Catarina. (2023).

### **RESPONSIBILITY NOTICE**

The author(s) is (are) the only responsible for the printed material included in this manuscript.

# MECHANICAL CHARACTERIZATION OF JUTE/CARBON HYBRID EPOXY COMPOSITES

**Henrique Queiroz<sup>a</sup>, Vitor Pastor<sup>a</sup>, Anna Mendonça<sup>a</sup>, Jorge Neto<sup>a</sup>, Daniel Cavalcanti<sup>a</sup>, Mariana Banea<sup>a</sup>**

<sup>a</sup>CEFET/RJ, Federal Center of Technological Education in Rio de Janeiro, R. Gen. Canabarro, 485 - Maracanã, Rio de Janeiro - RJ, 20271-204, Brazil

[henriquefmq@gmail.com](mailto:henriquefmq@gmail.com), [vitorpastor91@gmail.com](mailto:vitorpastor91@gmail.com), [annacarolina.mendonca2014@gmail.com](mailto:annacarolina.mendonca2014@gmail.com), [jorgesouzanetto@gmail.com](mailto:jorgesouzanetto@gmail.com), [danielkkc@gmail.com](mailto:danielkkc@gmail.com), [doina.banea@cefet-rj.br](mailto:doina.banea@cefet-rj.br)

**Keywords:** Composite materials, hybrid composites, natural fibres, synthetic fibres, bonded joints

## 1. INTRODUCTION

Composite materials are a type of structure that possess a wide variety of applications. From non-structural to structural applications in an ever-increasing envelope of industrial areas. Due to its inherent wide range of variables that can be fine-tuned for each specific application, even within the same fibre type, several different materials can be fabricated [1]. The main benefits of composite structures when compared to more common structural industrial materials (e.g., steel and aluminum), are the strength to weight ratio, which means that the design specifications of material properties can be maintained, or even exceeded, while lowering the overall weight. On the other hand, nowadays, almost every single industry is concerned with the overall decrease of the carbon footprint of their structures.

In this context, the hybridization of synthetic fibres with natural fibres offers a cost-effective way of reducing the carbon footprint of a composite structure without such a detrimental effect to the material properties, due to the inherent lower properties of natural fibres. As such, natural fibre reinforced composites (NFRCs) have come to the forefront as a promising alternative for future structural and non-structural applications. Another salient concern of any material that is to be part of a larger structure is the joining mechanism. It has been well documented that structural adhesion is the optimum joining technique for composite structures, due to the better stress distribution, non-destructive nature, vibration absorbing capabilities and ability to bond different materials. The effect of natural/synthetic hybridization in the composite material properties and bonding efficiency has been previously investigated [2].

The objective of this research is the analysis of a novel composite material that uses jute and carbon bidirectional fabrics as a synthetic hybridization on the outer layers, as well as the effect of the symmetry in the mechanical properties.

## 2. MATERIALS AND METHODS

Neat jute composites (JFRP) and interlaminar hybrid jute/carbon fibre composites were fabricated using bidirectional jute and carbon fibres. The jute fibres used were supplied by the Sisalsul (São Paulo, Brazil), while the carbon fabrics (RC203P) were supplied by Barracuda Advanced Composites (Rio de Janeiro, Brazil). A bi-component epoxy resin HEX 135 SLOW, supplied by Barracuda Advanced Composites (Rio de Janeiro, Brazil), was used as matrix. The material properties of the resin used can be seen in Table 1.

Table 1 - Material properties of the resin used [3].

Polymer	Tensile strength (MPa)	Young's modulus (GPa)	Tensile strain (%)
HEX 135 SLOW	60.92 ± 1.42	3.25 ± 0.008	3.20 ± 0.20

## 2.1. Specimen manufacture

The composites were fabricated using the compression molding technique using a steel mould and a hydraulic press, Solab SL 20 (São Paulo, Brazil). All the composites were fabricated with a core of 5 layers of jute bidirectional fabrics and the carbon fibre layers were placed on the outer surfaces, symmetrically and asymmetrically. For the interlaminar hybrid composites 1 to 2 layers of carbon were used on either side for the asymmetric and symmetric specimens and a nomenclature based on fibre hybridization and architecture was chosen (i.e., JFRP, AC1, AC2, C1, C2 and CFRP, respectively). For example, the asymmetric specimens with one layer of carbon on one side is called AC1, while the symmetric counterpart with one layer on both sides is C1. For the CFRP specimens, 11 layers of bidirectional carbon fibre fabric was used. The composite plate thickness was controlled via steel tabs. The specimens were cut from the composite plates with the aid of a tungsten carbide blade.

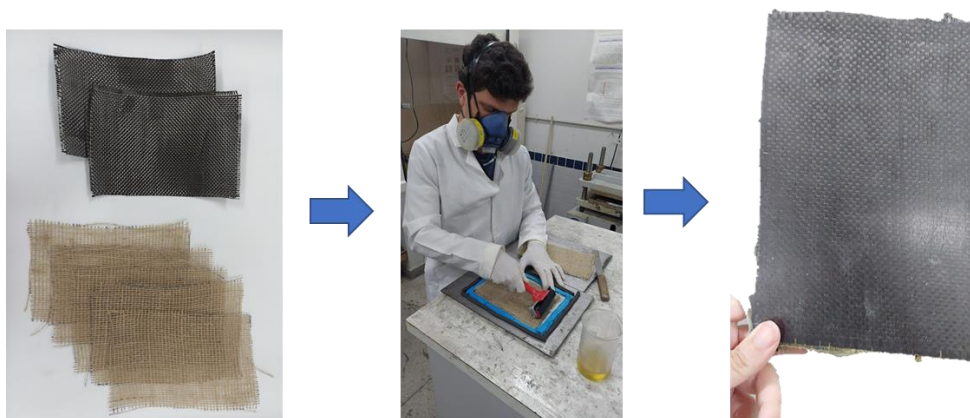


Figure 1 – Example of the composite lamination process (C1 specimens).

## 2.2. Measurements and characterization

The specimens were tested with the aid of an Instron<sup>®</sup>5966 universal testing machine (Norwood, Massachusetts, USA). For the tensile tests a 10 kN load cell and a crosshead speed of 1 mm/min was used, while for the flexural tests a 1 kN load cell and a crosshead speed 1 mm/min was used. A 120 mm three-point bending rig was used for the flexural tests. The impact tests were conducted using a WPM PS 30 Leipzig impact tester (error of 0.0075 kgf). The tests were conducted based on ASTM international standards. At least four specimens were tested for each condition.

## 3. RESULTS AND DISCUSSION

### 3.1. Tensile properties

Figure 2 presents the quantitative tensile strength as a function of hybridization architecture. The tensile strength values varied as a function of layers of the reinforcement material and architecture. All hybrid composites presented significant improvements when compared to the neat JFRP, as expected. The trend for the hybrid composites as a function of architecture was quasi-linear. For example, the C1 specimens presented an enhancement in tensile strength of approx. 99% when

compared to the AC1, while the C2 presented an improvement of approx. 104% when compared to the AC2. A higher variation was observed for the C2 specimens, with an improvement in tensile strength of approx. 53%, when compared to the C1 case. These enhancements are expected due to the higher resistance of the carbon fibre.

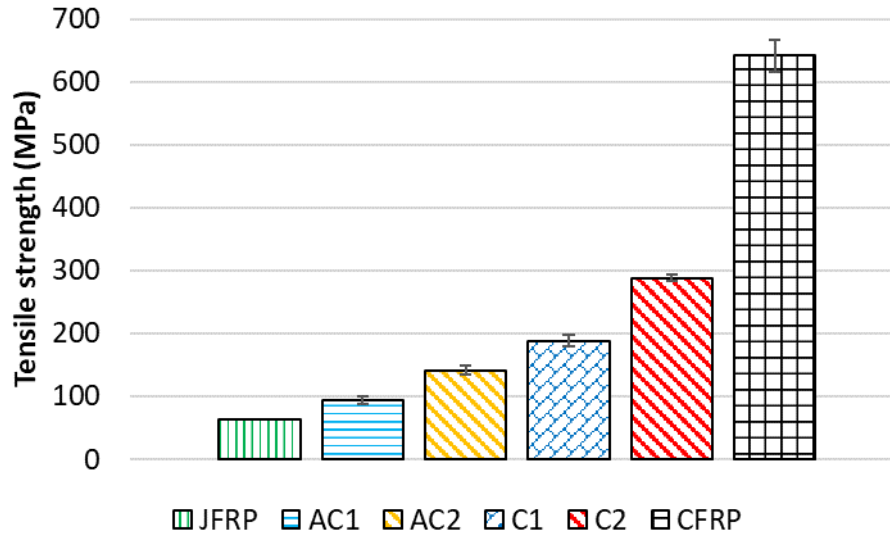


Figure 2 - Tensile strength as a function of hybridization architecture.

### 3.2. Flexural properties

Table 2 presents the quantitative flexural strength as a function of hybridization architecture. All cases presented enhancements when compared to the neat JFRP, similar to the tensile strength. It is important to note that for the asymmetric specimens, the face of the composite reinforced with carbon was under traction during flexural loading, while the jute fibre face was under compression. Little variation was observed for all cases, except CFRP, in flexural strength when compared to the neat JFRP, (i.e., approx. 95% and 138%, when compared to the AC1 and C2 specimens, respectively). Therefore, the AC2 or C2 specimens already present an optimum point depending on application.

Table 2 – Flexural strength of the tested specimens.

Composite	Flexural strength (MPa)	Standard deviation (MPa)
JFRP	97.27	8.83
AC1	189.34	9.81
AC2	201.96	21.01
C1	204.12	9.26
C2	231.92	11.32
CFRP	603.25	11.86

### 3.3. Impact properties

Figure 3 presents the impact properties as a function of hybridization architecture. Similar to the flexural tests, the carbon reinforced face was facing the punch of the machine for the asymmetric specimens. Compared to the neat JFRP specimens, the AC2 and AC2 specimens presented a significant

improvement in impact energy, approx. 22% and 32%, respectively as well as a plateau tendency as a function of number of layers. On the other hand, for the symmetrically reinforced composites, a tendency of linear increase when compared to the neat CFRP was observed as well as a highly significant enhancement when compared to both the asymmetric specimens and the neat JFRP. For example, the C2 and C1 specimens presented improvements in energy absorption of approx. 287% and 351%, when compared to the AC2 and AC1 specimens, respectively. This more significant difference suggests that under impact conditions, it is advantageous for the specimen to be symmetrically reinforced given the traction loads that the back of the specimen is under during impact.

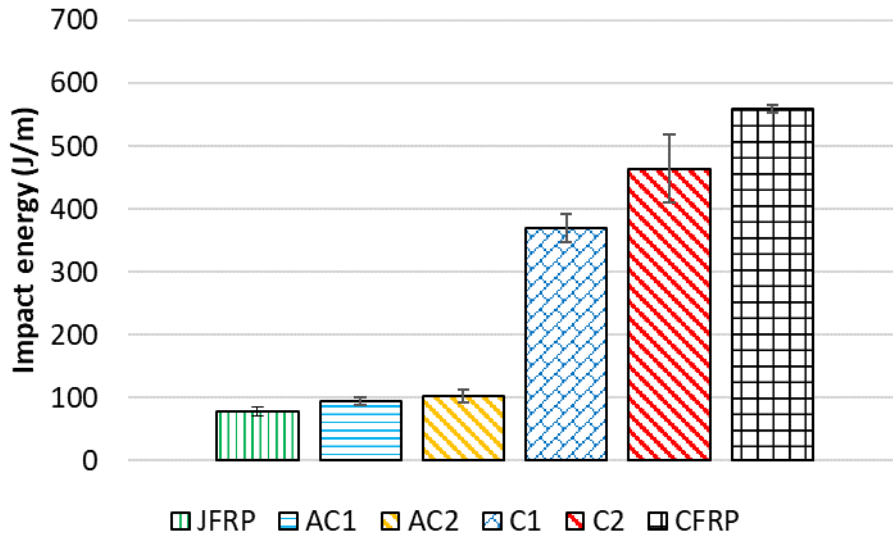


Figure 3 – Impact material properties as a function of hybridization architecture.

#### 4. CONCLUSIONS

It was found that all the mechanical properties benefitted from the hybridization technique. Nearly exponential improvements in tensile and impact properties were observed. The flexural strength was shown to present a more plateau-like tendency as a function of hybridization architecture. The impact results strongly suggest that symmetry is highly significant for maximum energy absorption.

#### REFERENCES

- [1] Banea, M.D. and L.F.M. da Silva, Adhesively bonded joints in composite materials: An overview. *Proceedings of the Institution of Mechanical Engineers, Part L: Journal of Materials: Design and Applications*, v. 223, p. 1-18. (2009).
- [2] de Queiroz, H.F.M. and Banea, M.D., Methods to increase the mechanical performance of composite adhesive joints: An overview with focus on joints with natural fibre composite adherends. *Journal of Composite Materials*, v. 56. p. 3993-4010. (2022).
- [3] de Queiroz, H.F.M., Banea, M.D., Cavalcanti, D.K.K., Adhesively bonded joints of jute, glass and hybrid jute/glass fibre-reinforced polymer composites for automotive industry. *Applied Adhesion Science*, v. 9. (2021).

#### RESPONSIBILITY NOTICE

The author(s) is (are) the only responsible for the printed material included in this manuscript.

## MECHANICAL PROPERTIES CHARACTERIZATION OF POLYURETHANE BASED BIO-BASED ADHESIVES IN ZERO- THICKNESS BONDS

**Shahin Jalali<sup>a</sup>, Catarina da Silva Pereira Borges<sup>a</sup>, Eduardo André de Sousa Marques<sup>b</sup>,  
Ricardo João Camilo Carbas Carbas<sup>a</sup>, L.F.M. da Silva<sup>b</sup>**

<sup>a</sup>Institute of Science and Innovation in Mechanical and Industrial Engineering (INEGI), Rua Dr.  
Roberto Frias, 4200-465 Porto, Portugal

[Sh.jalali.94@gmail.com](mailto:Sh.jalali.94@gmail.com), [Cspborges@fe.up.pt](mailto:Cspborges@fe.up.pt), [rcarbas@fe.up.pt](mailto:rcarbas@fe.up.pt)

<sup>b</sup>Departamento de Engenharia Mecânica, Faculdade de Engenharia, Universidade do  
Porto, Rua Dr. Roberto Frias, 4200-465 Porto, Portugal

[emarques@fe.up.pt](mailto:emarques@fe.up.pt), [lucas@fe.up.pt](mailto:lucas@fe.up.pt)

### ABSTRACT

The increased awareness of environmental concerns and the need for sustainable products has led to a significant shift towards using natural, renewable, and eco-friendly materials in various fields. In particular, the use of bio-adhesives made from natural resources has been gaining attention due to their potential for different applications, including industries such as the automotive.

However, synthetic adhesives made from petroleum-based products continue to be widely used in various structural applications due to their high strength, durability, and energy damping properties. Nevertheless, these adhesives have some significant drawbacks, such as high production costs, environmental pollution, and health hazards associated to their production and disposal. Therefore, there is a growing need for alternative bio-adhesives that offer similar or better properties while being more sustainable and eco-friendlier.

In this work, a polyurethane-based bio-adhesive that uses 70% natural resources, and was formulated to provide excellent adhesion to wood and cork was characterized. The curing procedure for the adhesive requires a zero-thickness bond, which means that the adhesive only cures between wood or cork substrates in direct contact. The strength properties of the adhesive were comprehensively characterized using butt joints. The mode I fracture properties were determined through double cantilever beam (DCB) tests, while mode II was assessed through end-loaded split (ELS) tests. A novel technique was developed to assess the bio-adhesive, applied as a zero-thickness layer. The results from this technique indicate promising mechanical properties, suggesting the bio-adhesive's potential as a sustainable alternative to synthetic adhesives in the wood industry.

**Keywords:** bio-adhesive, mechanical properties, zero thickness adhesive, polyurethane adhesive.



## REFERENCES

- [1] C. S. P. Borges, S. Jalali, P. Tsokanas, E. A. S. Marques, R. J. C. Carbas, and L. F. M. da Silva, “Sustainable Development Approaches through Wooden Adhesive Joints Design,” *Polymers (Basel)*, vol. 15, no. 1, p. 89, 2022.
- [2] L. M. R. M. Corte-Real, S. Jalali, C. S. P. Borges, E. A. S. Marques, R. J. C. Carbas, and L. F. M. da Silva, “Development and Characterisation of Joints with Novel Densified and Wood/Cork Composite Substrates,” *Materials (Basel)*, vol. 15, no. 20, 2022, doi: 10.3390/ma15207163.
- [3] M. N. Islam, F. Rahman, A. K. Das, and S. Hiziroglu, “An overview of different types and potential of bio-based adhesives used for wood products,” *Int. J. Adhes. Adhes.*, vol. 112, p. 102992, 2022, doi: <https://doi.org/10.1016/j.ijadhadh.2021.102992>.
- [4] C. Yuan, M. Chen, J. Luo, X. Li, Q. Gao, and J. Li, “A novel water-based process produces eco-friendly bio-adhesive made from green cross-linked soybean soluble polysaccharide and soy protein,” *Carbohydr. Polym.*, vol. 169, pp. 417–425, 2017, doi: <https://doi.org/10.1016/j.carbpol.2017.04.058>.
- [5] C. Wang, J. Wu, and G. M. Bernard, “Preparation and characterization of canola protein isolate–poly(glycidyl methacrylate) conjugates: A bio-based adhesive,” *Ind. Crops Prod.*, vol. 57, pp. 124–131, 2014, doi: <https://doi.org/10.1016/j.indcrop.2014.03.024>.

# MECHANICAL RESPONSE OF COMPOSITE LAMINATES CONTAINING ELASTOMERIC LAYERS

Amanda Pereira Peres<sup>a</sup>, Rogerio José Marczak<sup>b</sup>

<sup>a</sup> Mechanical Engineer Department, Federal University of Rio Grande do Sul  
Rua Sarmento Leite, 425, Porto Alegre – 90040-001, Brazil  
Amandaperes09@hotmail.com

<sup>b</sup> Mechanical Engineer Department, Federal University of Rio Grande do Sul  
Rua Sarmento Leite, 425, Porto Alegre – 90040-001, Brazil  
rato@mecanica.ufrgs.br

**Keywords:** Composite material, Hyperelasticity, Stiffness, Finite element Analysis

## 1. INTRODUCTION

For years, development in composite materials seek to improve properties such as specific strength. The behavior of sandwich panels containing composite and elastomeric materials using different methods of vibration calculation has been studied since the 1980s [2]. There are also studies on the influence of viscoelastic materials in sandwich panels on damping properties and how it affects their vibration [5]. Some recent studies even analyze the tensile and bending properties using a sandwich panel containing natural fibers layers and a natural rubber and cork core [3].

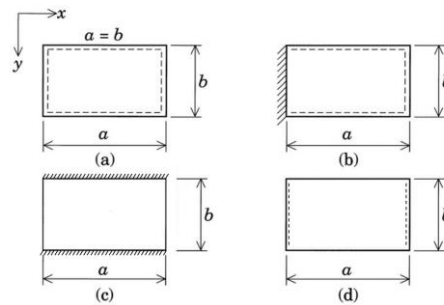
There is analysis on the variation of dynamic stiffness when combining 3 plies of silicon and metal rubber composite material [6], however, little study has been done on the impact on stiffness when adding elastomeric material between Carbon Fiber Reinforced Polymer (CFRP) layers.

This work presents a comparative analysis of the influence of replacing plies in a rectangular CFRP plate with natural rubber. The purpose is to evaluate the variation in stiffness in comparison to the original laminate. The analysis compares the results of plates with different aspect ratios and boundary conditions using classic hyperelastic invariant-based potentials to model the elastomeric material and orthotropic material properties to model the CFRP. The study is done using ABAQUS, with a static analysis performed to obtain the stiffness properties.

## 2. MODELING

The laminate is composed of 16 layers with a stacking sequence of  $[0^\circ/90^\circ]_{8s}$ . To form the composite and elastomeric laminate, two composite plies were replaced by rubber plies with the same thickness, forming a laminate with the following stacking sequence  $[0^\circ/90^\circ/0^\circ/90^\circ/0^\circ/90^\circ/\text{rubber}/90^\circ]_s$ . Each ply has a thickness of 0,3mm that combined forms a laminate with a total thickness of 4,8mm.

The two panels were submitted to 4 different boundary conditions: SSSS, SSSC, CFCF, and FSFS, with S, meaning simply supported, C clamped, and F free edge. Figure 1 shows the boundary conditions arrangements. Three aspect ratios of  $b/a = 1, 1/2, \text{ and } 1/3$  were analyzed in both types of panels as well.



**Figure 1** - Boundary conditions (a) SSSS; (b) SSSC; (c) FCFC; (d) FSFS.

## 2.1. Materials

The CFRP was used in the composite plies, the values are presented in Table 1 [4].

Table 1 - Composite material mechanical properties [4].

Description	Symbol	Value
Elastic modulus	$E_1$ (GPa)	127,6
Elastic modulus	$E_2 = E_3$ (GPa)	11,3
Transversal elastic modulus	$G_{12} = G_{13}$ (GPa)	6
Transversal elastic modulus	$G_{23}$ (GPa)	1,8
Poisson's ratio	$\nu_{12} = \nu_{13}$	0,3
Poisson's ratio	$\nu_{23}$	0,36
Density	$\rho$ (kg/m <sup>3</sup> )	1633,1

For the elastomeric material, the PCR master natural rubber was used. Hyperfit software used the experimental data to make the curve fit and showed how well different hyperelastic models fit the data curves. The model that best adjusted the curves was the three-term Yeoh. Table 2 presents its coefficients.

Table 2 - PCR Master mechanical properties.

Description	Symbol	Value
First coefficient	$C_{10}$	$2,83e^{-1}$
Second coefficient	$C_{20}$	$-9,48e^{-3}$
Third coefficient	$C_{30}$	$8,26e^{-4}$
Density	$\rho$ (kg/m <sup>3</sup> )	1130

## 2.2. Finite element model

The Abaqus software was used to run the static analysis. First, a model based on the classical laminate theory using shell elements was run in the SSSS boundary condition and  $b/a = 1$  aspect ratio laminate composed only of composite material. This case was used to validate the other analyses that modeled the laminate as a solid. The other cases in this study were all modeled as a solid with large deformations considered, since to fully model the nonlinear hyperelastic material behavior, solid elements are required.

For the shell model S4R elements are used, which are four-node shell elements with reduced integration. For the solid model, CFRP layers use C3D8R elements, which are eight-node brick elements with reduced integration and the PCR Master plies use C3D8RH, which are eight-node brick hybrid elements [1].

The final mesh is presented in Table 3, for all the laminates.

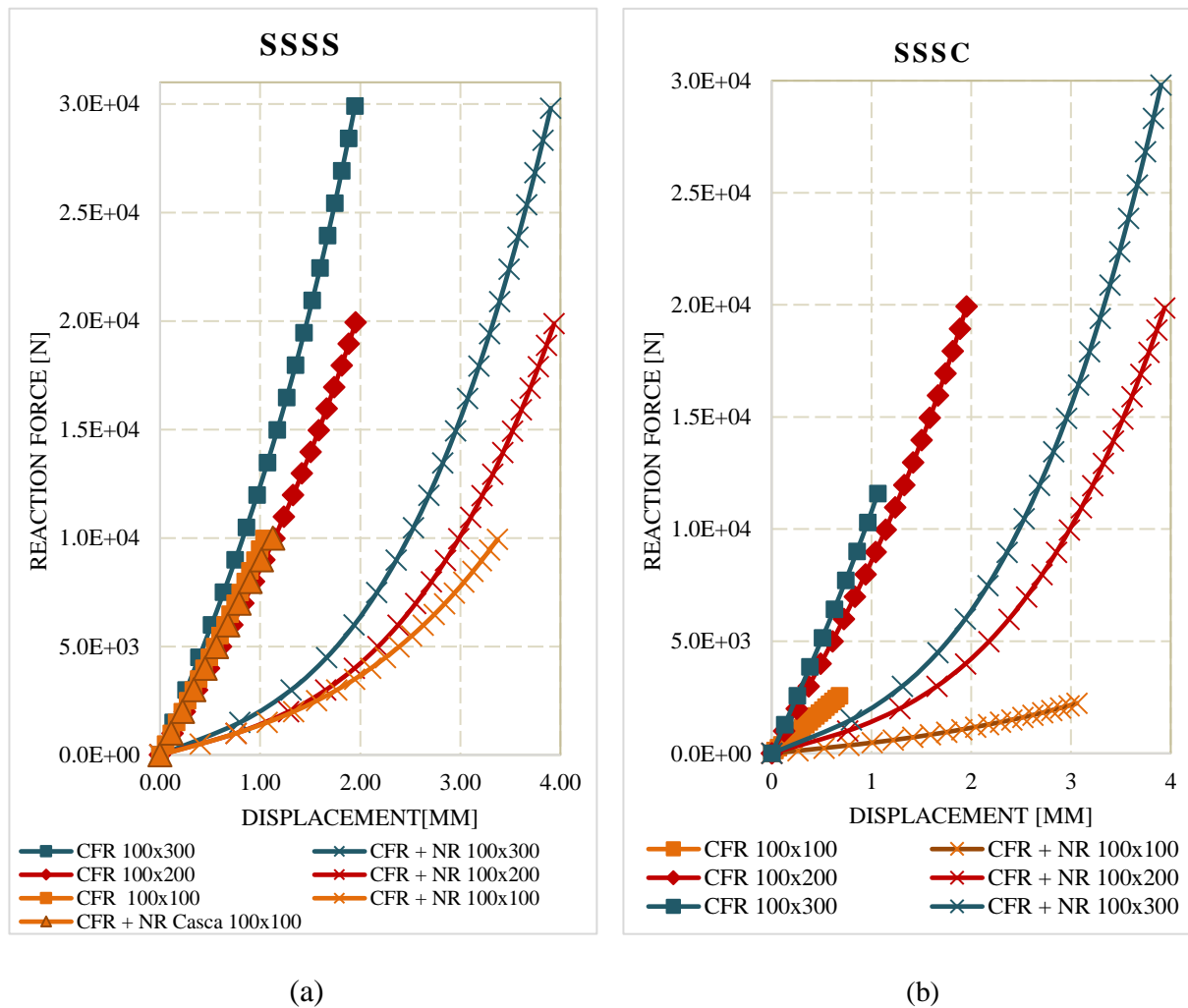
Table 3 - Number of elements of the mesh for each model analyzed.

Model	Dimension [mm]	Number of elements
Shell	100x100	1.600
Solid	100x100	80.000
Solid	100x200	160.000
Solid	100x300	240.000

### 3. RESULTS

The results present a comparison between the stiffness of the composite laminate and composite and rubber laminate for all the cases. They show a decrease in stiffness when adding elastomeric layers. The nonlinearity in the behavior of the composite plates becomes more noticeable in the plates with lower aspect ratios.

Figure 2 3presents the displacements of the central node in  $z$  directions and the sum of the forces in the boundary conditions.



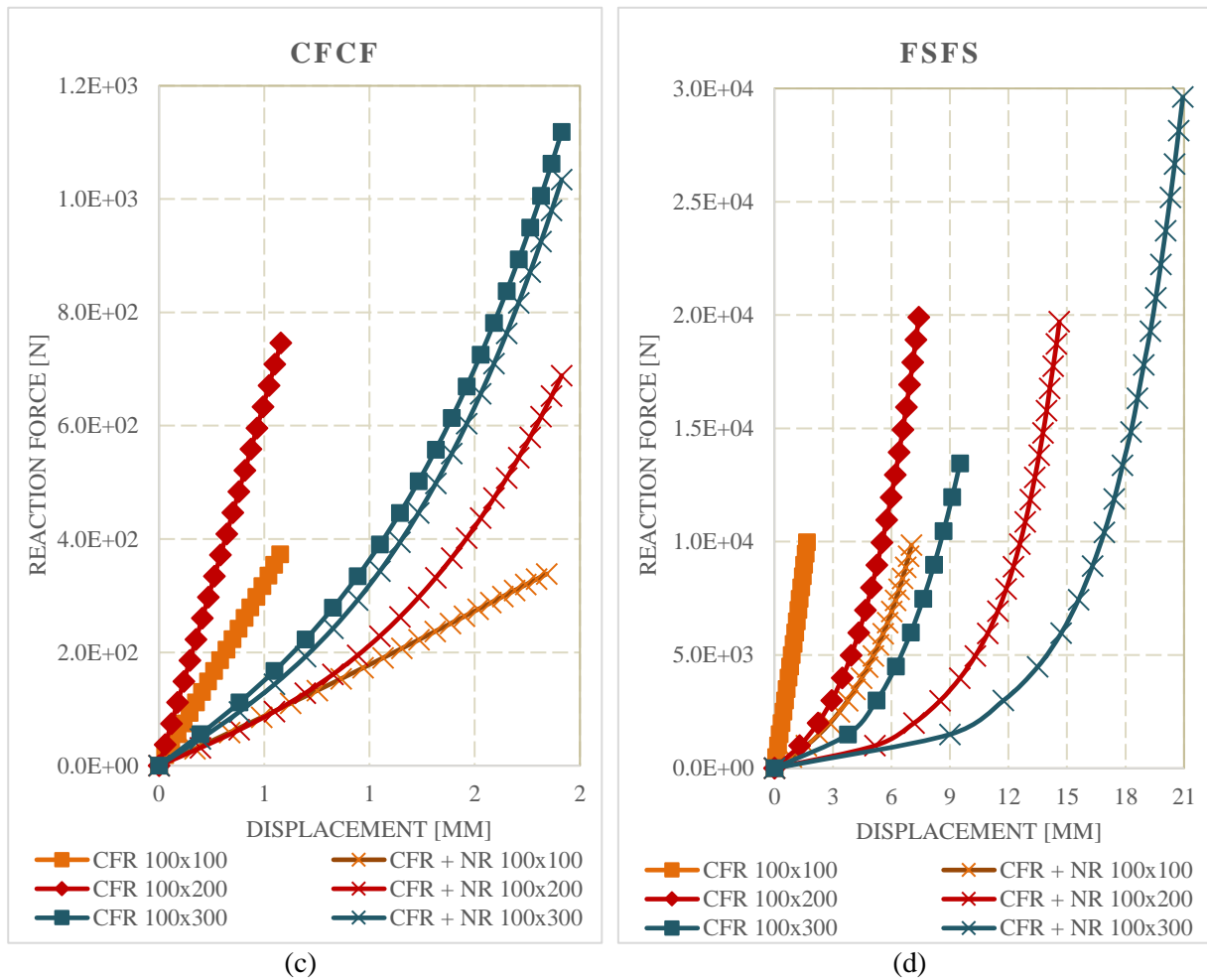


Figure 2 - Displacements versus force reactions charts for (a) SSS BC; (b) SSSC BC (c) CFCF BC; (d) FCFC BC.

The first thing to highlight is that the behavior of the shell and solid CFR laminates are similar, therefore we can expect similar responses. It is also possible to notice that the non-linearity increases when the NR plies are added and with the aspect ratio. For the 100x200mm and 100x300mm, there is also a non-linearity in the CFR laminate behavior, that is because the plates have bigger dimensions and the boundary conditions allow large displacements.

The stiffness is obtained in three different points of the displacement vs. reaction force curve, beginning, middle, and end. present the stiffness for all the BC in these positions.

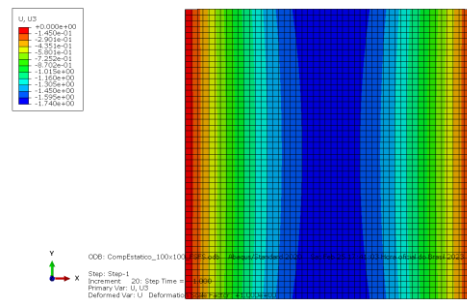
Table 4 - Stiffness for all the BC and aspect ratios laminates.

CC	Dimensão [mm]	CFR			CFRP + NR		
		K <sub>início</sub> [N/mm]	K <sub>central</sub> [N/mm]	K <sub>fim</sub> [N/mm]	K <sub>início</sub> [N/mm]	K <sub>central</sub> [N/mm]	K <sub>fim</sub> [N/mm]
	100x100 (Casca)	8862,4	8862,4	8862,9	-	-	-
SSSS	100x100	8983,4	9348,7	10720,6	1248,9	3676,9	6288,6
	100x200	8014,9	8753,7	14479,5	1313,5	4972,5	12879,1
	100x300	11407,6	12010,3	23148,2	1878,8	5446,9	19360,9

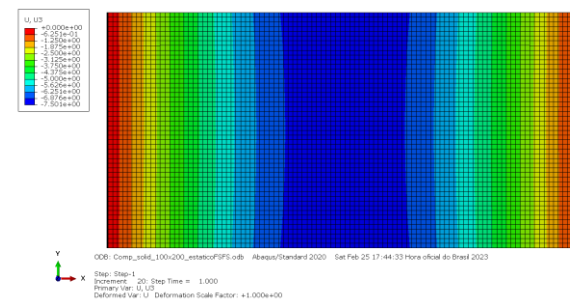
SSSC	100x100	3764,2	3790,2	3875,3	443,5	850,2	1289,6
	100x200	8014,8	8753,7	14479,5	1313,4	4972,4	12879,0
	100x300	9942,2	10432,9	12561,5	1878,8	5446,9	19360,8
CFCF	100x100	636,9	646,5	669,1	174,2	189,9	190,6
	100x200	1266,6	1272,0	1330,7	159,9	285,9	756,6
	100x300	282,8	377,5	633,0	240,1	332,3	1136,7
FSFS	100x100	5429,5	5924,2	6928,7	571,9	1865,1	3396,7
	100x200	769,5	2555,8	6545,3	193,3	1552,4	6543,4
	100x300	397,4	1949,5	3697,5	166,3	1233,0	7174,6

As expected, with the addition of the NR plies the stiffness reduces, it is also noticeable the influence of the boundary conditions in the stiffness, some BC like FSFS presents less support to the laminates when compared to other BC. The laminate dimensions also influence the responses, the larger aspect ratio plates have smaller stiffness.

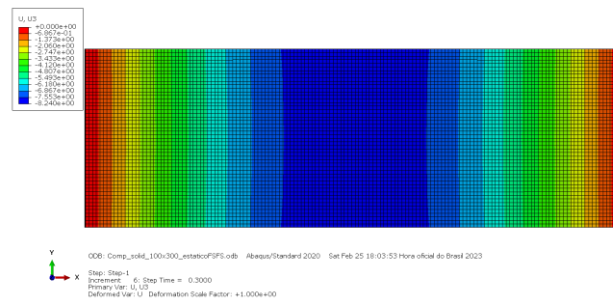
Figure 3 presents the deformed plate for the FSFS boundary condition.



(a)



(b)



(c)

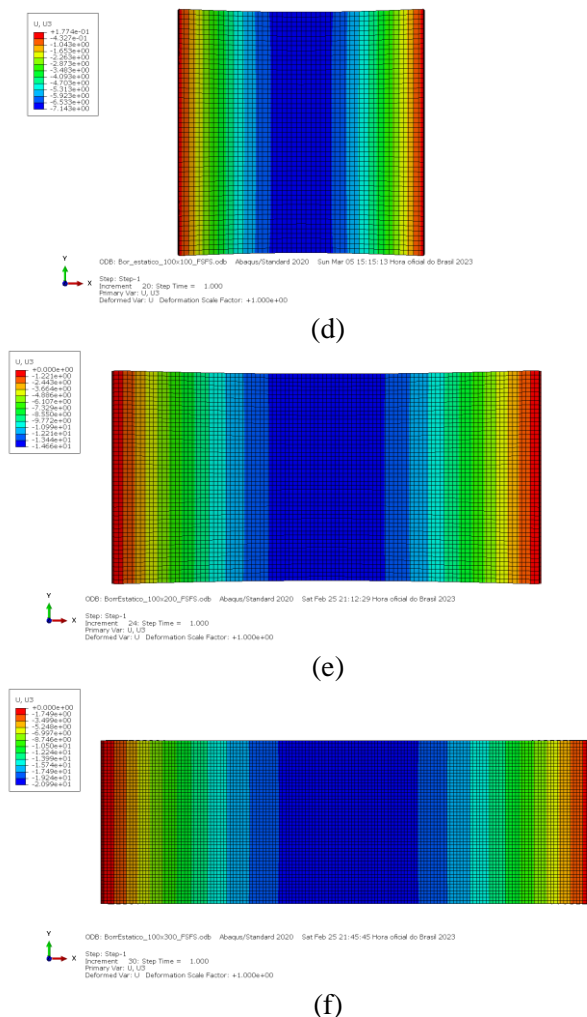


Figure 3 - Deformed plate for the FSFS BC for (a) 100x100 mm CFR laminate; (b) 100x200 mm CFR laminate; (c) 100x300 mm CFR laminate; (d) 100x100 mm CFR + NR laminate; (e) 100x200 mm CFR + NR laminate; (f) 100x300 mm CFR + NR laminate;

#### 4. CONCLUSION

This work presented the analysis of laminated plates containing elastomeric layers. The classical laminate theory could not be used because of the non-linear behavior that these layers add to the plates.

The results of the combination of the NR and CFR plies show the reduction in the stiffness of the laminates and the increase in displacement when compared to the composite-only laminates. The shear resistance between layers seems to be the main factor for these larger displacements of the plies.

The boundary conditions were another factor that influenced the results and affected the behavior of the plates. Some of the boundary conditions offered less support to the laminate. Therefore, it is an important variable to be considered when using this material in a project.

## ACKNOWLEDGMENTS

The authors acknowledge CNPq grant 317140/2021-3 and Capes PROBRAL 88887.701013/2022-00.

## REFERENCES

- [1] Abaqus, Inc. *Analysis User's Manual*. (2006)
- [2] D. J. Kienholz, C. Johnson. Finite element prediction of damping in structures with constrained viscoelastic layers. *Structural Dynamics and Materials Conference*, p. 8, (1981).
- [3] R. Selvaraj, A. Maneengam, M. Sathiyamoorthy. Characterization of mechanical and dynamic properties of natural fiber reinforced laminated composite multiple-core sandwich plates. *Composite Structures*, p. 115141, (2022).
- [4] S. Valvano, E. Carrera. A variable ESL/LW kinematic plate formulation for free-vibration thermoelastic analysis of laminated structures. *Journal of Thermal Stresses*, p. 24, (2018).
- [5] H. Wan, Y. Li, L. Zheng. Vibration and Damping Analysis of a Multilayered Composite Plate with a Viscoelastic Midlayer. *Shock and Vibration*, p.10, (2016).
- [6] X. Zheng, Z. Ren, L. Shen, et al. Dynamic Performance of Laminated High-Damping and High-Stiffness Composite Structure Composed of Metal Rubber and Silicone Rubber. *Materials*, p. 187, (2021)

## RESPONSIBILITY NOTICE

The author(s) is (are) the only one responsible for the printed material included in this manuscript.



# NUMERICAL ANALYSIS OF A MULTI-MATERIAL DAM VIA IGABEM AND THE SUBREGIONS TECHNIQUE

Deborah C. Nardi<sup>a</sup>, Edson Denner Leonel<sup>a</sup>

<sup>a</sup>São Carlos School of Engineering, Department of Structural Engineering, University of São Paulo  
Av. Trabalhador São Carlense, 400, 13566-590, São Carlos, Brazil  
deborahnardi@usp.br  
edleonel@sc.usp.br

**Keywords:** BEM, IGABEM, Multi-Material Dam, Geotechnical numerical analysis.

## 1. INTRODUCTION

The Boundary Element Method (BEM) is a widely used numerical technique that involves boundary discretization and solving boundary integral equations. Traditionally, Lagrangian polynomials are used to discretize both the geometry and fields under analysis. However, recent research has shown that non-uniform rational B-splines (NURBS) can provide a more precise description of complex geometries, giving rise to a new method known as Isogeometric Boundary Element Method (IGABEM). With IGABEM, the boundary is discretized using the same basis functions as the geometry, resulting in a more accurate representation of the geometry, providing then a more precise analysis [1].

Thus, the BEM has a wide range of applications in several engineering areas, and great advances have been developed in the geotechnics field [2, 3]. It is known that dams are one of the most impressive geotechnical constructions. Many modern dams are constructed using a combination of materials to take advantage of the beneficial properties of each one [4]. In this context, as the BEM provides a very good precision of the stress field evaluation [5, 6], the use of this method allows an adequate estimative of the adopted constitutive model, predicting more accurately the real behavior of the structures. For this, there are techniques such as the sub-regions approach, that easily allow the consideration of non-homogenous materials [7].

This study uses the Isogeometric Boundary Element Method (IGABEM) with the sub-regions technique to conduct an elastic analysis of a multi-material dam. The dam design is inspired by the Itaipu Dam [8] in Foz do Iguaçu, Paraná, Brazil, and includes clay, a transition material, and rockfill for reinforcement. The parameters and dimensions that are of public knowledge are used for numerical modeling. Overall, this study serves as an important application of the BEM and sub-regions technique in the analysis of multi-material dams.

## 2. THE BOUNDARY ELEMENT METHOD

The integral formulation of the elasticity problem can be obtained through Betti's reciprocity theorem. For sake of simplicity, more details of the mathematical development are presented in [7, 9]. By applying the strain-displacement relations in Betti's reciprocity theorem, by integrating it by parts, and by considering the fundamental problem, the Somigliana Identity is obtained after integrating the Dirac Delta function. Equation 1 shows the integral equation of the elasticity problem, already considering the limit analysis to take the inner point to the contour to solve the boundary value problem, as follows:

$$\frac{1}{2} \mathbf{C}\mathbf{u}(\mathbf{s}) + \int_{\Gamma} \mathbf{P}^*(\mathbf{s}, \mathbf{f}) \mathbf{u}(\mathbf{f}) d\Gamma = \int_{\Gamma} \mathbf{U}^*(\mathbf{s}, \mathbf{f}) \mathbf{p}(\mathbf{f}) d\Gamma + \int_{\Omega} \mathbf{U}^*(\mathbf{s}, \mathbf{f}) \mathbf{b}(\mathbf{f}) d\Omega \quad (1)$$

where  $\mathbf{C}$  is the free-term;  $\mathbf{P}^*(\mathbf{s},\mathbf{f})$  and  $\mathbf{U}^*(\mathbf{s},\mathbf{f})$  are the traction and the displacement fundamental solution, respectively;  $\mathbf{u}(\mathbf{s})$  and  $\mathbf{p}(\mathbf{f})$  are the displacement and traction boundary solutions of the real problem, respectively; and  $\mathbf{b}(\mathbf{f})$  refers to the domain term [10]. Thus, a set of matrices can be assembled relating all displacement and all the tractions components:

$$\mathbf{H}\mathbf{u} = \mathbf{G}\mathbf{t} + \mathbf{b} \quad (2)$$

where the square matrix  $\mathbf{H}$  contains all the integrals of the  $\mathbf{P}^*(\mathbf{s},\mathbf{f})$  kernel and  $\mathbf{G}$  of the  $\mathbf{U}^*(\mathbf{s},\mathbf{f})$  one;  $\mathbf{u}$ ,  $\mathbf{t}$  and  $\mathbf{b}$  are the vectors that contain the nodal displacements, the tractions and the independent vector of the domain forces obtained through the Galerkin vector [7], respectively. After prescribing the boundary conditions, Eq. (2) is rearranged according to the following system:

$$\mathbf{A}\mathbf{x} = \mathbf{f} \quad (3)$$

where  $\mathbf{x}$  corresponds to the vector of unknown degrees of freedom and  $\mathbf{A}$  is a full and non-symmetric matrix.

## 2.2 Subregion Technique

Non-homogenous problems are problems where more than one region must be considered. Hence, consider a region  $V$  assembled by two different materials, where  $V_1$  and  $V_2$  are two different subregions which have boundaries  $S_1$  and  $S_2$  and are connected by an interface  $S_I$  [7]. The nodal displacements and tractions at the external boundary  $S_1$  is defined by  $\mathbf{U}^1$  and  $\mathbf{T}^1$ , respectively; similarly,  $\mathbf{U}^2$  and  $\mathbf{T}^2$  are defined for boundary  $S_2$  and  $\mathbf{U}_I^1$ ,  $\mathbf{U}_I^2$ ,  $\mathbf{T}_I^1$  and  $\mathbf{T}_I^2$  are displacements and tractions at the interface  $S_I$ . Thus, according to [7], the system of equations for the subregion  $V_1$  can be written as:

$$[\mathbf{H}^1 \quad \mathbf{H}_I^1] \begin{Bmatrix} \mathbf{U}^1 \\ \mathbf{U}_I^1 \end{Bmatrix} = [\mathbf{G}^1 \quad \mathbf{G}_I^1] \begin{Bmatrix} \mathbf{T}^1 \\ \mathbf{T}_I^1 \end{Bmatrix} \quad (4)$$

A similar equation is written for  $V_2$ . The compatibility and the equilibrium conditions at the interface  $S_I$  are:

$$\begin{aligned} \mathbf{U}_I^1 &= +\mathbf{U}_I^2 \equiv \mathbf{U}_I \\ \mathbf{T}_I^1 &= -\mathbf{T}_I^2 \equiv \mathbf{T}_I \end{aligned} \quad (5)$$

Applying the relations shown in Eq. (4), the following expression is obtained:

$$\begin{bmatrix} \mathbf{H}^1 & \mathbf{H}_I^1 & 0 & 0 \\ 0 & 0 & \mathbf{H}^2 & \mathbf{H}_I^2 \\ 0 & 1 & 0 & -1 \\ 0 & 0 & 0 & 0 \end{bmatrix} \begin{Bmatrix} \mathbf{U}^1 \\ \mathbf{U}_I^1 \\ \mathbf{U}^2 \\ \mathbf{U}_I^2 \end{Bmatrix} = \begin{bmatrix} \mathbf{G}^1 & \mathbf{G}_I^1 & 0 & 0 \\ 0 & 0 & \mathbf{G}^2 & \mathbf{G}_I^2 \\ 0 & 0 & 0 & 0 \\ 0 & 1 & 0 & 1 \end{bmatrix} \begin{Bmatrix} \mathbf{T}^1 \\ \mathbf{T}_I^1 \\ \mathbf{T}^2 \\ \mathbf{T}_I^2 \end{Bmatrix} \quad (6)$$

## 3. NUMERICAL EXAMPLE

The dam illustrated in Fig. 1 is based on section K of the Itaipu Binational Dam [8] and is composed of three materials: clay, transition, and rockfill. The dam's dimensions, including a height of 70m and a

crest weight of 12m, are the same as those of Itaipu's section K. However, the other dimensions are adopted due to the unavailability of public information.

To discretize the model, 18 linear NURBS are used, with additional control points inserted via knot insertion technique [10], without modifying the order of each NURB. Hence, a total of 545 control points is used for the analysis. A plane strain state is considered.

The adopted materials characteristics are: transition -  $E=250\text{MPa}$ ,  $\nu = 0,375$  and  $\gamma=18\text{kN/m}^3$ ; clay -  $E=50\text{MPa}$ ,  $\nu=0,35$  and  $\gamma=15\text{kN/m}^3$ ; and rockfill -  $E=35\text{GPa}$ ,  $\nu=0,2$  and  $\gamma=20\text{kN/m}^3$ . Note that the body force of each domain is herein considered via the Galerkin vector approach [7].

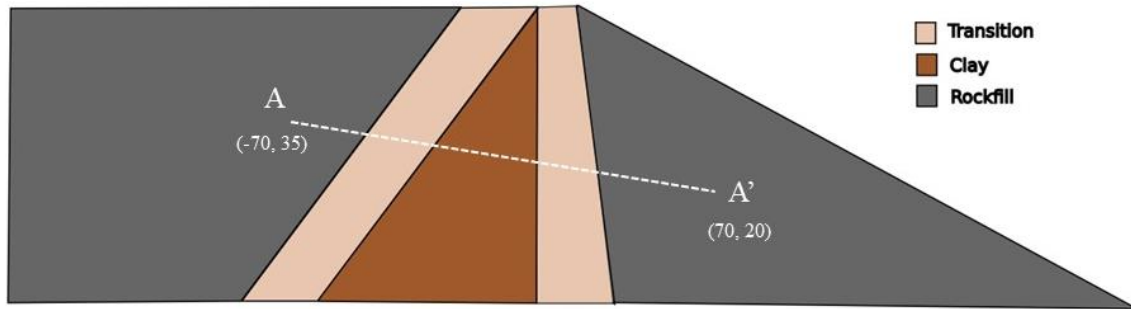


Figure 1 - Dam composed of three different materials: transition, clay, and rockfill.

Figure 2 presents the obtained deformation section via IGABEM and the subregions technique. A comparison with the Finite Element software ANSYS is also carried out. The results show agreement between the two numerical approaches. Furthermore, the internal path A-A' shown in Fig. 1 is chosen for the internal stress evaluation. A coordinate  $s$  that represents the path length is introduced, assuming the value  $s=0\text{m}$  at the beginning and  $s=140,8\text{m}$  at its end. The comparative results are presented in Fig. 3.

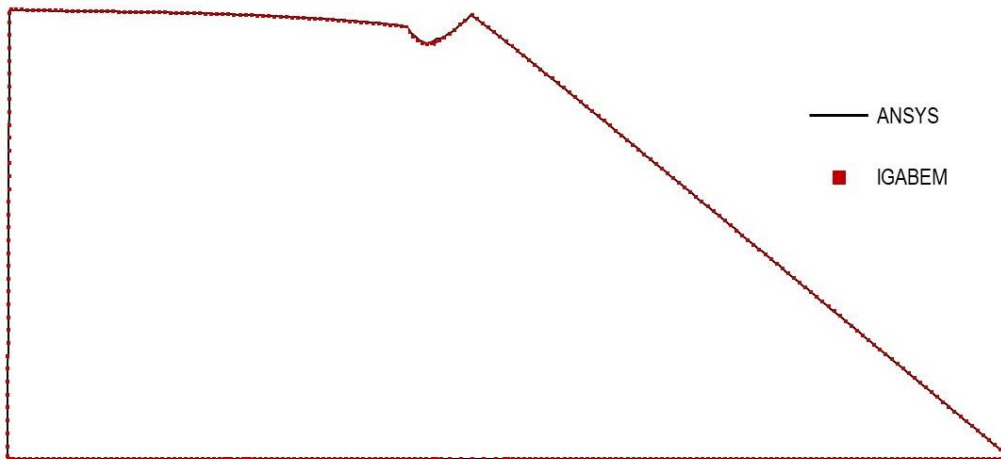


Figure 2 – Deformed Configuration via FEM versus IGABEM.

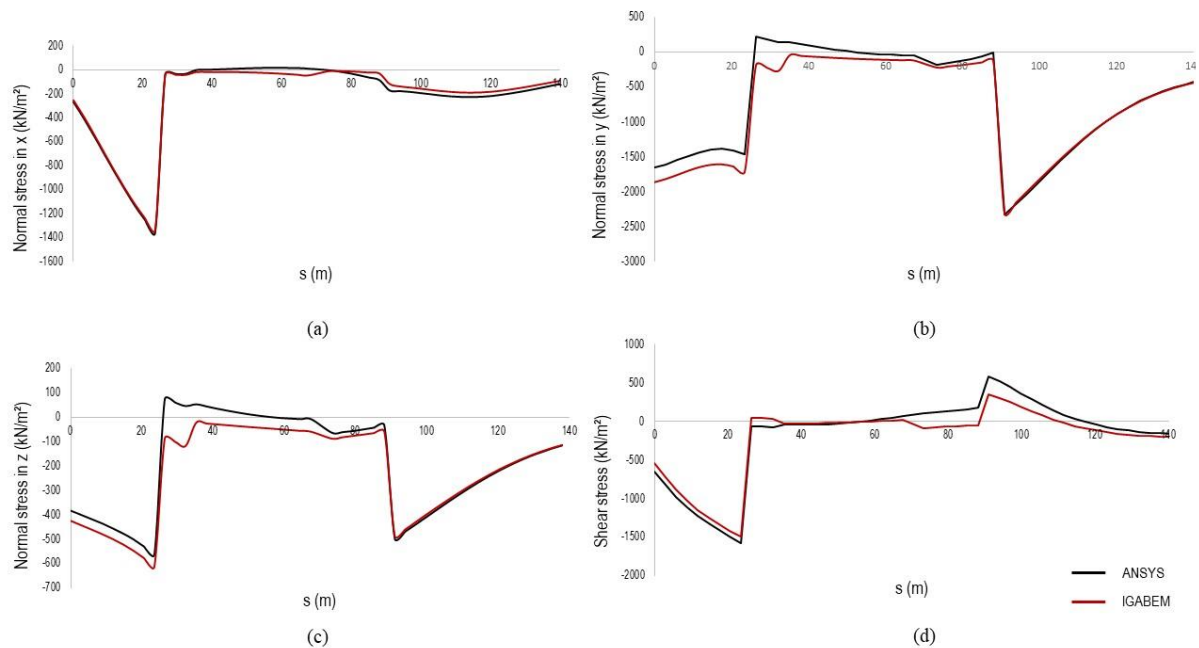


Figure 3 – (a) Normal stresses in x (b) Normal stresses in y (c) Normal stresses in z and (d) Shear stresses.

The maximum and minimum displacements on the boundary in the  $x$  direction are approximately  $0.015m$  and  $-0.02m$ , respectively, while in the  $y$  direction they are around  $0.002m$  and  $-0.05m$ . Furthermore, it is important to observe that the regions with the maximum displacements coincide precisely with the areas primarily composed of clay material, which has the lowest elasticity modulus among the constituents. Therefore, this complex example based on a real-life structure employs a variety of techniques in a single simulation, such as h-refinement, subregions, and Galerkin vector to include the domain term. As demonstrated, it shows a very satisfactory agreement with the FEM analysis via ANSYS, validating the code implementation.

The techniques outlined and applied herein allow further studies in cases where different materials need to be considered. Furthermore, in scenarios where the influence of body forces is crucial for analysis, the Galerkin vector strategy is a very suitable tool, as it transforms a domain integral into a boundary one, facilitating the analysis.

## REFERENCES

- [1] SIMPSON, R. N. et al. A two-dimensional isogeometric boundary element method for elastostatic analysis. *Computer Methods in Applied Mechanics and Engineering*, Elsevier, v. 209, p. 87–100, 2012.
- [2] Procházka, P. (1992). The BEM applied to optimization and contact problems in geotechnics. *Acta Montana IGt CSAS*, 21-32.
- [3] Panji, M., & Ansari, B. (2017). Modeling pressure pipe embedded in two-layer soil by a half-plane BEM. *Computers and Geotechnics*, 360-367.
- [4] CHEN, S.-C.; LIN, T.-W.; CHEN, C.-Y. Modeling of natural dam failure modes and downstream riverbed morphological changes with different dam materials in a flume test. *Engineering Geology*, Elsevier, v. 188, p. 148–158, 2015.
- [5] RAVEENDRA, S.; CRUSE, T. BEM analysis of problems of fracture mechanics. *Developments in Boundary Element Methods: Industrial applications*, CRC Press, p. 182, 1989.

- [6] LEONEL, E. D.; VENTURINI, W. S.; CHATEAUNEUF, A. A BEM model applied to failure analysis of multi-fractured structures. *Engineering Failure Analysis*, Elsevier, v. 18, n. 6, p. 1538–1549, 2011.
- [7] ALIABADI, M. H. The boundary element method, volume 2: applications in solids and structures. [S.l.]: John Wiley & Sons, 2002. v. 2.
- [8] ITAIPU. Principais características técnicas. Av. Tancredo Neves, 6702 - CEP 85866-900 - Foz do Iguaçu - PR, 2023. Available in <[https://www.itaipu.gov.br/sites/default/files/af\\_df/2202\\_023\\_revista\\_aspectos\\_tecnicos\\_bizuarios\\_018.pdf](https://www.itaipu.gov.br/sites/default/files/af_df/2202_023_revista_aspectos_tecnicos_bizuarios_018.pdf)>, accessed in March 2023.
- [9] Brebbia CA, Dominguez J, “Boundary elements: An introductory course”. McGraw Hill, Southampton, UK, 1989.
- [10] PIEGL, L.; TILLER, W. The NURBS book. [S.l.: s.n.]: Springer Science & Business Media, 1996.

### RESPONSIBILITY NOTICE

The author(s) is (are) the only responsible for the printed material included in this manuscript.

## ON THE OBTAINANCE OF DAMAGE EVOLUTION LAWS FOR COMPOSITE LAMINATES VIA CYCLIC TESTING

Gabriel S. C. Souza<sup>a</sup>, Behzad V. Farahani<sup>b</sup>, Rui M. Guedes<sup>c</sup>, Eduardo Gerhardt<sup>d</sup>,  
Sandro C. Amico<sup>d</sup>, Volnei Tita<sup>a,c</sup>

<sup>a</sup>University of São Paulo, São Carlos School of Engineering, Aeronautical Engineering Department  
Av. João Dagnone, 1100, São Carlos, SP, Brazil, 13563-120  
gabrielsales@usp.br, voltita@sc.usp.br

<sup>b</sup>Ghent University, Department of Electromechanical Systems and Metal Engineering  
Technologiepark 46, 9052 Zwijnaarde, Gent, Belgium  
behzad.vasheghanifarahani@ugent.be

<sup>c</sup>University of Porto, Faculty of Engineering, Mechanical Engineering Department  
Rua Dr. Roberto Frias, Porto, Portugal, 4200-465  
rmguedes@fe.up.pt, voltita@sc.usp.br

<sup>d</sup>PPGE3M, Federal University of Rio Grande do Sul  
Porto Alegre, RS, Brazil, 91501-970  
eduardo.gerhardt.eng@gmail.com, amico@ufrgs.br

**Keywords:** fiber-reinforced composites, continuum damage mechanics, cyclic testing, parameter identification, damage evolution laws.

### 1. INTRODUCTION

Continuum damage mechanics (CDM) have been used to describe damage development in fiber-reinforced plastic (FRP) composite materials since the end of the 1970s and the beginning of the 1980s. CDM considers the emergent effects of intra and interlaminar mechanisms in the material behavior in a lamina. Commonly, deterioration quantification is made via the introduction of damage variables and its kinetics (i.e., evolution or accumulation) predicted by empirical hardening equations obtained from experimental data of quasi-static cyclic testing. From the thermodynamic viewpoint, damage variables ( $d_{ij}$ ) are state variables having a conjugate thermodynamic force ( $Y_{ij}$ ) driving their growth. Furthermore, at the meso and macro scales, this translates as a loss of stiffness. Several authors have presented over the years many different CDM-based material models used to describe damage onset and progression for composites. The most comprehensive models are those that consider the different modes present in composites' failure that, in its turn, are dependent on the material stress state. Hence, for each mode, one can expect to exist an evolution law. In particular, during the past 30 years, Ladevèze and contributors [1-3] published several works and developed a constitutive model that describes damage evolution in the composite until final failure. Inspired by these, the present work proposes a different approach to obtain the evolution of damage via cyclic testing for the coupled in-plane shear ( $\tau_{12} \neq 0$ ) and transverse tension ( $\sigma_{22} \geq 0$ ) case. Instead of the traditional [ $\pm 45$ ] and [ $\pm 67.5$ ] cross-ply tensile specimens used by Ladevèze and summarized by Herakovich [4], this work proposes utilizing off-axis tensile specimens for this purpose. Also, as already pointed out by Ribeiro [5], the current work supports the finding that for the stress state under study, there exists one damage evolution law for each damage variable that is dependent on the fiber orientation  $\theta$ , i.e.,  $d_{22} = f(\theta)$  and  $d_{12} = f(\theta)$  in which those are damage variables associated with transverse tension and in-plane shear, respectively.

## 2. EXPERIMENTAL CAMPAIGN

### 2.1. Material Set and Specimens' Characteristics

A material set from TORAYCA T700S-12K-50C carbon fiber combined with a UF3369 TCR epoxy resin system is used for all the samples. Manufacture is made by filament-winding (FW) using an MF Tech Kuka robot arm and a flat mandrel, allowing high-quality sample obtaining. Two off-axis orientations (20° and 45°) are selected to be tested under tensile loading. These are chosen due to the existence of low and high coupling between transverse tension and in-plane shear damage mechanisms, as discussed by Sandhu [6]. Specimens' geometry follows recommendations from ASTM D3039 transverse tension sample dimensions, i.e., 175x25x1.85 mm for 20° and 175x25x3.74 mm for 45°. The latter is thicker to avoid fracture at the grips, and, as a rule of thumb, it is recommended a sample thickness of 3.0 to 4.0 mm for all orientations bearing in mind that this is an empirical observation made for laminates with tabs' thickness of 1.5 to 2.0 mm. Herakovich's [4] recommendation that the fibers must not go from one grip to the other for off-axis specimens is respected. Also, the average aspect ratio of the coupons,  $h/l$ , equals 14.22, making the global shear stress  $\tau_{xy}$  negligible, as desired. These are needed for the validity of the considered governing equations and boundary conditions (BCs) of the problem.

### 2.2. Off-Axis Cyclic Testing

Firstly, to perform cyclic tests, it is necessary to plan these by executing monotonic ones. For this purpose, it was performed three preliminary tests for the 20° and 45° orientations. Also, a maximum of five cycles is permitted to avoid the occurrence of low-cycle fatigue. An INSTRON 5985 universal testing machine and a CANON EOS 350 digital camera are used in all tests to obtain stress and strain histories. The digital camera usage is to analyze the images with the GOM Correlate software of digital image correlation (DIC). All tests are done via machine crosshead displacement control of 0.5 mm/min. Denoting  $m = \cos \theta$  and  $n = \sin \theta$ , and knowing that the experimental setup provides  $\sigma_x$ ,  $\varepsilon_x$  and  $\varepsilon_y$ , it is possible to obtain all local stress components by:

$$\sigma_1 = m^2 \sigma_x, \quad (1a)$$

$$\sigma_2 = n^2 \sigma_x, \quad (1b)$$

$$\tau_{12} = -mn \sigma_x, \quad (1c)$$

and, for the local strain components:

$$\varepsilon_1 = m^2 \varepsilon_x + n^2 \varepsilon_y + mn \gamma_{xy}, \quad (2a)$$

$$\varepsilon_2 = n^2 \varepsilon_x + m^2 \varepsilon_y - mn \gamma_{xy}, \quad (2b)$$

$$\gamma_{12} = -2mn \varepsilon_x + 2mn \varepsilon_y + (m^2 - n^2) \gamma_{xy}. \quad (2c)$$

To obtain the global shear strain  $\gamma_{xy}$ , it follows that:

$$\gamma_{xy} = \bar{S}_{16} C_2 - \bar{S}_{66} C_0 h^2, \quad (3)$$

where  $h$  is half the laminate width,  $C_0$  and  $C_2$  are coefficients derived from the solution of the governing equations with constrained BCs. Derivation of these coefficients can be found in [4]. The shear stress in the global coordinate system is given by,

$$\tau_{xy} = \frac{\gamma_{xy} - \bar{S}_{16} \sigma_x}{\bar{S}_{66}}, \quad (4)$$

where in Eqs. (3) and (4),  $\bar{S}_{ij}$  are the components of the transformed reduced compliance matrix.

### 3. DAMAGE EVOLUTION LAWS

Stiffness loss is accounted for damage calculation by,

$$d_i = 1 - \frac{E_i}{E_0}, \quad (5)$$

in which  $E_i$  is the stiffness measured in the  $i$ -th cycle,  $E_0$  is the elastic modulus and  $d_i$  is the damage variable value obtained in the  $i$ -th cycle. The thermodynamic forces  $Y_i$  associated with each internal damage variable are given as,

$$Y_i = \frac{\sigma_i^2}{[2E_0(1 - d_i)^2]}. \quad (6)$$

From the best fit of experimental data, it is possible to notice that  $d_i$  and  $\sqrt{Y_i}$  have a linear relationship, i.e.,  $d_i = a_0\sqrt{Y_i} + a_1$  for each orientation. Denoting by  $\sqrt{Y_0}$  and  $\sqrt{Y'_0}$  the damage onset thresholds for  $d_{12}$  and  $d_{22}$ , respectively, these are obtained by imposing  $d_{ij} = 0$ . Also, the inverse angular coefficients  $\sqrt{Y_C}$  and  $\sqrt{Y'_C}$  for the in-plane shear and transverse tension are given as  $1/a_0$ . By doing this, it is possible to retrieve the damage evolution laws by simply,

$$d_{ij} = \frac{\langle \sqrt{Y_{ij}} - \sqrt{Y_0} \rangle}{\sqrt{Y_C}}, \quad (7)$$

where the bracket operator simply means that the value inside must be greater than 0. Now, two additional cyclic tests must be executed. These are the pure transverse tension and pure in-plane shear cases and are used to serve as a basis to create four new parameters used to obtain the damage evolution laws for any given angle  $\theta$ . These are defined as,

$$\alpha'_0 = \frac{\sqrt{Y'_0}|_\theta}{\sqrt{Y'_0}|_{\theta=90}}, \quad (8a)$$

$$\beta'_C = \frac{\sqrt{Y'_C}|_\theta}{\sqrt{Y'_C}|_{\theta=90}}, \quad (8b)$$

$$\alpha_0 = \frac{\sqrt{Y_0}|_\theta}{\sqrt{Y_0}|_{shear}}, \quad (8c)$$

$$\beta_C = \frac{\sqrt{Y_C}|_\theta}{\sqrt{Y_C}|_{shear}}, \quad (8d)$$

with Eq. (8a) and (8b) for transverse tension and Eq. (8c) and (8d) for in-plane shear. For each case, a best fit of  $\alpha_0$  and  $\beta_C$  vs.  $\theta$  is done where, the pure shear result is considered to be  $\theta = 10$ , since this test can be used to assess shear properties [7]. The parameters dependency with  $\theta$  are given as:

$$\alpha'_0 = -7.5718 * 10^{-4}\theta^2 + 8.5397 * 10^{-2}\theta - 0.5751, \quad (9a)$$

$$\beta'_C = -2.7417 * 10^{-4}\theta^2 + 4.0035 * 10^{-2}\theta - 0.3814, \quad (9b)$$

$$\alpha_0 = -2.0162 * 10^{-4}\theta^2 + 3.0809 * 10^{-3}\theta + 1.3192, \quad (9c)$$



$$\beta_C = -3.4225 * 10^{-4}\theta^2 + 2.0842 * 10^{-2}\theta + 0.8894. \quad (9d)$$

Also, Tab. 1 shows the results obtained along with Fig. 1.

Table 1 – Parameters values for each case.

Orientation	Transverse tension				In-plane shear			
	$\sqrt{Y'_0}$	$\sqrt{Y'_C}$	$\alpha'_0$	$\beta'_C$	$\sqrt{Y_0}$	$\sqrt{Y_C}$	$\alpha_0$	$\beta_C$
Shear (10°)	n/a	n/a	0	0	0.14412	1.03681	1	1
20°	0.05987	0.38377	1.15488	0.29612	0.26351	1.31763	1.82845	1.27084
45°	0.08244	1.12938	1.59037	0.87143	0.11746	1.12939	0.81500	1.08929
90°	0.05184	1.29602	1	1	n/a	n/a	0	0

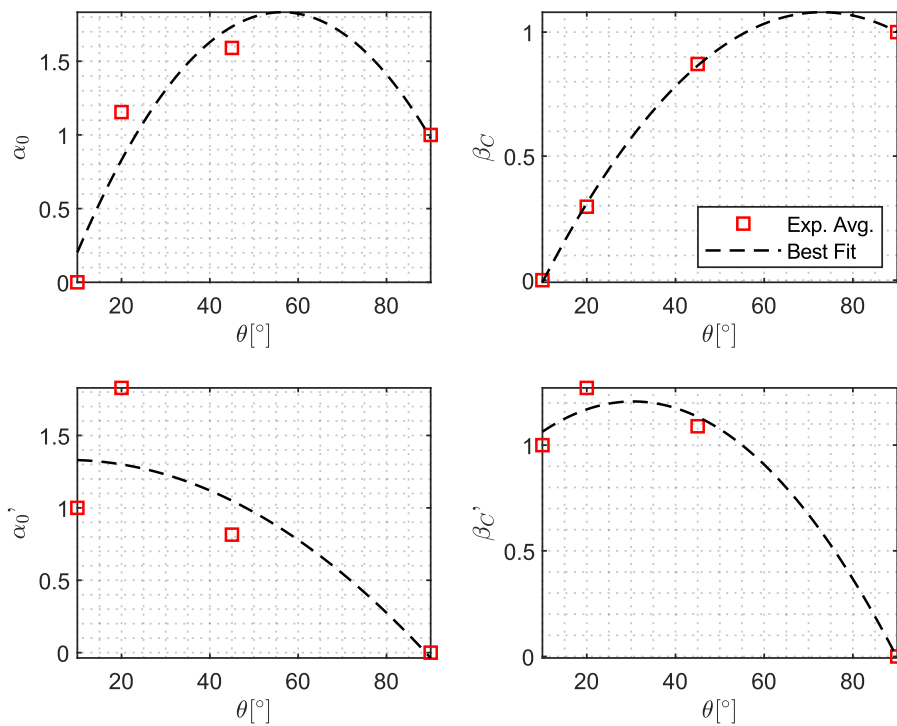


Figure 1 – Experimental data of  $\alpha_0, \alpha'_0, \beta_C, \beta'_C$  vs.  $\theta$  and best fit.

Therefore, for any given  $\theta$  it is possible to obtain the  $\alpha$  and  $\beta$  parameters from Eq. (9). Now, using Eq. (8), the damage onset thresholds and the inverse angular coefficients are obtained and using Eq. (7) it is possible to predict the damage variable value of interest, and, consequently, to obtain its damage evolution law as depicted in Fig. 2.

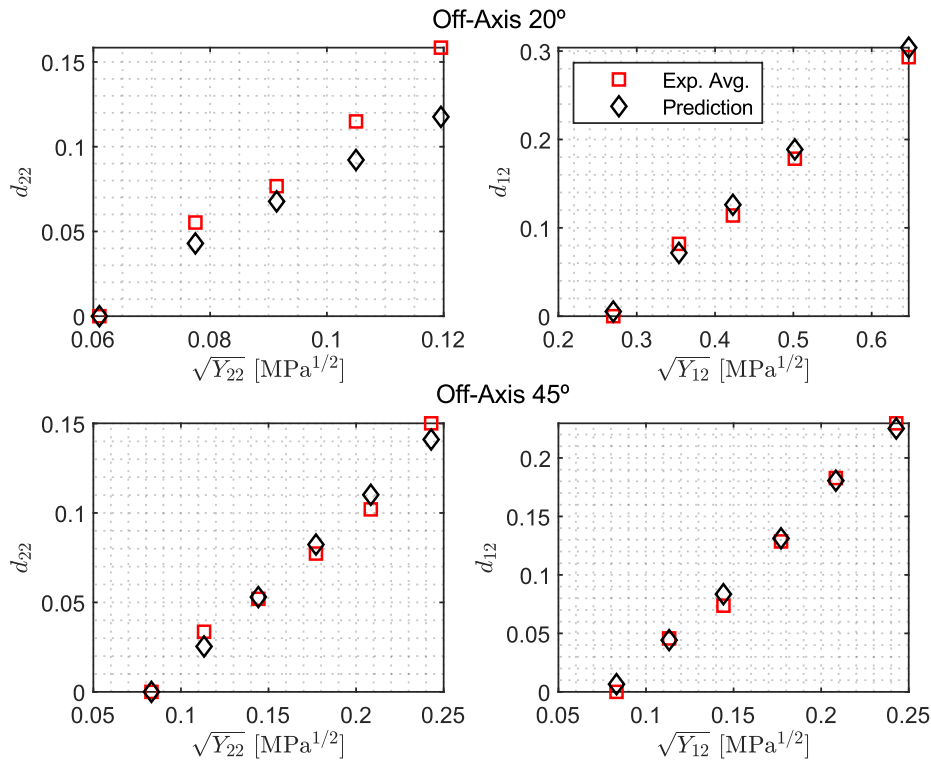


Figure 2 – Decoupled damage evolution for tensile off-axis laminates: experimental results and prediction.

#### 4. FINAL REMARKS

The present work objective was to derive the damage evolution relations for any fiber angle  $\theta$  from a few cyclic tests considering the coupling between transverse tension and in-plane shear mechanisms. To accomplish this, four cyclic tests are necessary, two of these on off-axis laminates that, in this study, are chosen to be with 20° and 45° orientation. The other two remaining tests are for the pure transverse tension and in-plane shear cases used for the definition of four new parameters used to predict the damage evolution law for an arbitrary orientation. After applying the step-by-step approach to retrieve the damage variables values, is observed a good behavioral and quantitative agreement for all case studies, the worst one being for  $d_{22}$  in the 20° case. It is also noticeable that the damage evolution is not the same for different angles, which is supported by Ladevèze et al. [1-3] but dealt in a different manner, and in agreement with observations of Ribeiro [5]. Recommendations for the specimens' geometry are made based on the necessity to perform more tests on thicker 20° laminates due to failure at the tab area, a feature observed on thinner 45° laminates too. The main advantage of the present approach is the simplicity of tests and the ease to manufacture laminates without adding many experiments in comparison with other methodologies. Furthermore, the present approach needs to be tested for different damage mechanisms, for example, in the  $\sigma_{22} < 0$  portion of the  $\sigma_{22} - \tau_{12}$  envelope.

#### ACKNOWLEDGEMENTS

The authors acknowledge the financial support of the Coordination for the Improvement of Higher Education Personnel (CAPES numbers 88887.608253/2021-00, 88887.817120/2023-00 and 88887.729128/2022-00). Volnei Tita is thankful for the support of CAPES (CAPES-FCT: AUXPE 88881.467834/2019-01) – Financial Code 001. The FAPESP-FAPERGS project (process number: 2019/15179-2 and 19/2551) is also acknowledged.

## REFERENCES

- [1] P. Ladevèze, E. LeDantec. Damage modelling of the elementary ply for laminated composites. *Composites science and technology*, v. 43, n. 3, p. 257-267. (1992).
- [2] O. Allix, P. Ladevèze. Interlaminar interface modelling for the prediction of delamination. *Composite Structures*, Elsevier, v. 22, n. 4, p. 235-242. (1992).
- [3] O. Allix, P. Ladevèze, A. Corigliano. Damage analysis of interlaminar fracture specimens. *Composite Structures*, Elsevier, v.31, n. 1, p. 61-74. (1995).
- [4] C. T. Herakovich. *Mechanics of fibrous composites*. John Wiley & Sons. (1998).
- [5] M. L. Ribeiro. *Damage and progressive failure analysis for aeronautic composite structures with curvature*. PhD Thesis. University of São Paulo. (2013).
- [6] R. Sandhu. Nonlinear behavior of unidirectional and angle ply laminates. *Journal of Aircraft*, v. 13, n. 2, p. 104-111. (1976).
- [7] M. Merzkirch, T. Foecke. 10° off-axis testing of CFRP using DIC: A study on strength, strain and modulus. *Composites Part B: Engineering*, v. 196, p. 108062. (2020).

## RESPONSIBILITY NOTICE

The author(s) is (are) the only responsible for the printed material included in this manuscript.

# REDUCTION OF PLATE FLEXIBILITY BY THE PROGRESSIVE APPLICATION OF REINFORCEMENTS WITH OPTIMIZED PATHS

Eduardo da Rosa Vieira<sup>a</sup>, Daniel Milbrath de Leon<sup>b</sup>, Rogério José Marczak<sup>b</sup>

<sup>a</sup>Federal Institute of Rio Grande do Sul – IFRS – Campus Rio Grande  
475 Eng. Alfredo Huck St, Rio Grande, 96201-460, Brazil  
vieira.r.eduardo@gmail.com

<sup>b</sup>Federal University of Rio Grande do Sul – UFRGS – PROMEC  
425 Sarmento Leite St, Porto Alegre, 90040-001, Brazil  
daniel.leon@ufrgs.br; rato@mecanica.ufrgs.br

**Keywords:** Optimization, Reinforced Plates, Stiffeners, VAT, Linear Programming

## 1. INTRODUCTION

The elaboration of equipment projects using plates and shells as structural elements is very common in the mechanical industry, especially in shipbuilding and aircraft. However, as these elements are generally thin, their ability to withstand high loads without collapsing is relatively low [1,2]. Therefore, one of the solutions to improve the mechanical properties is to increase its thickness. This design suitability ends up causing a significant increase in structural weight, reducing the ratio between weight and resistance and designing low energy efficiency systems. Another solution is the insertion of reinforcements in the plates, which improve the structure's performance, mainly increasing the stiffness and critical buckling load, in addition to reducing tension and deformation [2,3].

Generally, most of the structural elements are constructed of steel or other metals, as well as the reinforcements, which are normally attached to the surface of the plates by welding. These reinforcements are also called stiffeners [2]. The more traditional stiffeners are produced in geometries that allow their positioning orthogonal to the plate, with rectilinear lengths and equidistant positioning from each other [4]. These reinforcements provide considerable improvement in mechanical properties, with relatively low insertion of material, developing structures with lower cost and better ratio between weight and strength [5].

The replacement of metallic materials by composites is a reality in the mechanical industry, and some aircraft models already have more than 50% of composites in their structure. This is because these materials have excellent reliability and a high weight-to-strength ratio. In this context, fiber-reinforced polymer matrix composites are the most prominent [3,6]. In addition, the development of manufacturing techniques that allowed the construction of curvilinear fibers made possible the applications of these composites. The ability to build plates with independent reinforcements in each layer, the Variable Angle Tow (VAT), made it possible to explore the anisotropy of composites in order to design structures that are more adapted to each project [7,8]. Furthermore, in order to obtain the best positioning of the reinforcements, it is essential to apply an optimization method. In this way, excellent results can be achieved without an increase in the volume of reinforcements [9].

Plates with stiffeners made of fibrous composite materials - with a polyester matrix and fiberglass reinforcement - were designed and experimentally validated, demonstrating the possibility of using these materials as stiffeners. In several cases tested, an increase of between 38% and 110% was observed in its resistance to flexion load in relation to plates without stiffeners [5]. Alhajahmad and Mittelstedt (2020) successfully employed path optimization of plate stiffeners, which resulted in curvilinear reinforcements. However, these reinforcements were external to the matrix and their trajectories were not mutually independent, resulting in parallel and equidistant paths [10]. In turn, Esposito *et al.* (2019) studied plates built with an epoxy resin matrix and carbon fiber reinforcements, which were internal to the plate. It should be noted that, in these experiments, the authors used an unrestricted number of fibers, which occupied almost the entire area of the structure. In one of the case studies of the work, a cantilever

plate with optimized reinforcement trajectories, under a point load, reduced flexibility by 56.03% in relation to a quasi-isotropic plate, which had the same geometry and the same boundary conditions [11].

As new manufacturing technologies make it possible to manufacture reinforcements with considerable variation in cross-sectional area, it is possible to build stiffeners that remain internal to the structure. Thus, using a reduced number of filaments, which when they have optimized paths, enable a significant reduction in flexibility [11,12]. Therefore, this work aims to reduce the flexibility of a plate containing a limited number of reinforcements. These stiffeners are progressively deposited and optimized, until the increase in the number of reinforcements does not present significant results for minimizing the total flexibility of the structure.

## 2. METHODOLOGY

The aim of this work is to reduce the flexibility of an epoxy resin plate reinforced by carbon fibers. The plate used has the same geometry and boundary conditions used by Esposito *et al.* (2019), which had a height of 200 mm, length of 500 mm and thickness of 2.24 mm. In addition, it was fixed on one of the vertical edges and on the other edge a vertical load of 1 kN was applied. The structure can be seen in Figure 1(a). Before applying reinforcements, the plate will have its compliance calculated. After that, reinforcement with a square cross section will be applied. The edge of the cross-section has the same dimension as the plate thickness. This fiber has a horizontal initial direction, is located between the upper and lower ends of the plate and its center coincides with the median plane. This structure can be seen in Figure 1(b).

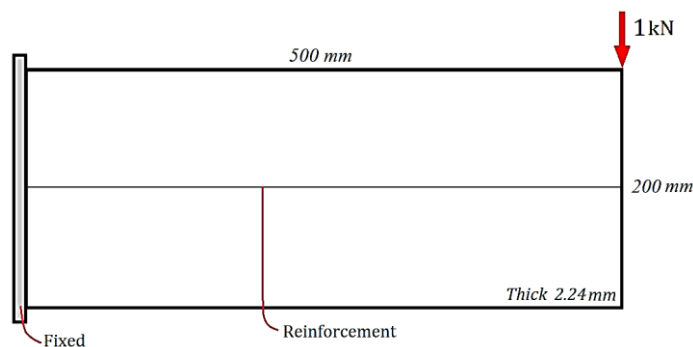


Figure 1 – Plate with boundary conditions and a reinforcement at the starting position

The reinforcement paths are represented by B-Splines and have their trajectory optimized by Linear Programming. The flexibility of the structure will be measured by its total strain energy, which is calculated by the Finite Element Method.

The applied process starts with the deposition of this rectilinear reinforcement on the plate, followed by the optimization of its trajectory. After this reinforcement has been optimized, it is kept in the position obtained and a new straight reinforcement is applied in the same initial horizontal position and is also optimized. This process is repeated until the insertion and optimization of new fibers does not cause significant improvement in reducing the flexibility of the structure.

## 3. RESULTS AND DISCUSSION

First, before the implementation of reinforcements, the deformation energy of the plate without any reinforcement was calculated. Based on the assessment of the non-reinforced plate, the stiffeners were implemented in the standardized initial position and at each insertion and subsequent optimization of the fiber, the strain energy was recorded. Then, in order to compare the effects caused by the application of more filaments, the percentages of reduction of the strain energy in relation to the structure composed only of epoxy resin were calculated. These results are shown in Figure 2.

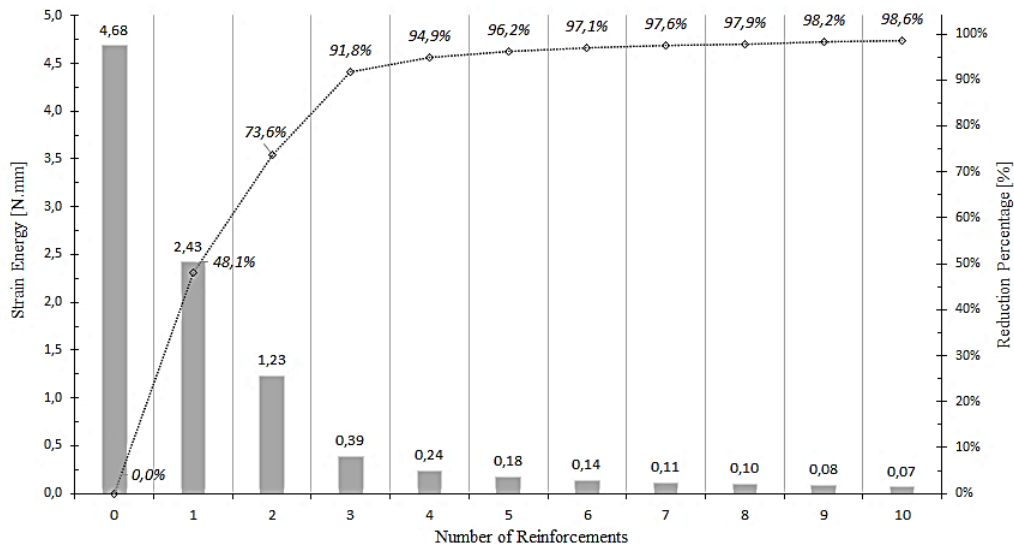


Figure 2 – Strain energy and percentage reduction for each number of reinforcements applied

As can be seen in the graph, the board without reinforcements has compliance equal to 4.68 Nmm. When a single reinforcement is placed and optimized, the strain energy has a value equal to 2.43 Nmm, which represents a percentage reduction of 48.1% in the flexibility of the structure. After that, the insertion of the second stiffener has a significant effect, but less than the previous reinforcement. The third reinforcement also exhibits a relatively large minimization of strain energy. In turn, the fourth reinforcement still develops a considerable reduction in the flexibility of the plate, however, its percentage reduction is only 3.1%. This minimization is low compared to the second and third stiffeners, which reduced by 25.5 and 18.2% respectively.

From the fifth reinforcement, there is no justification for implementing a greater number of reinforcements. This occurs because, in the observed cases, there is no percentage reduction in strain energy greater than 1.3%, and the increase in the number of reinforcements no longer produces significant effects on the flexibility of the structure. Furthermore, the fibers begin to occupy equal or very close positions on the plate. Added to this, it is possible to notice that a very high number of crossings between the fibers begins to occur, which may cause greater difficulty in the fabrication of the structures. Figure 3 presents the results of the plate with four and ten stiffeners.

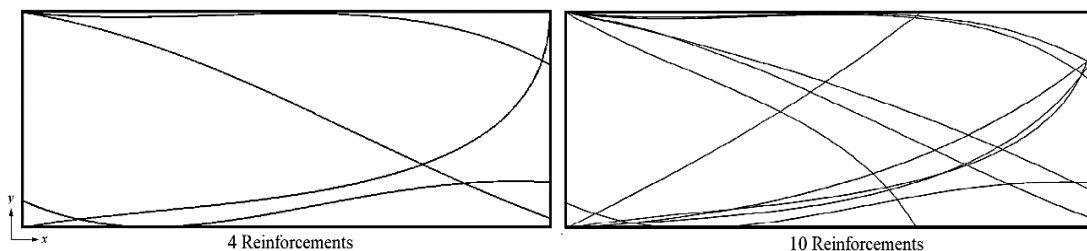


Figure 3 – Path of optimized reinforcements on plates with four and ten stiffeners

According to the results obtained, it is possible to understand that for the structure studied under the imposed boundary conditions, there is no justification for using a number greater than four reinforcements. It is important to highlight that this number of reinforcements is specific to the case study investigated in this work. Therefore, in other structures, materials or boundary conditions, it is necessary to verify the ideal number of stiffeners. Since, due to the anisotropic characteristics of these materials, it is possible that a different number of reinforcements is more appropriate.

#### 4. CONCLUSIONS

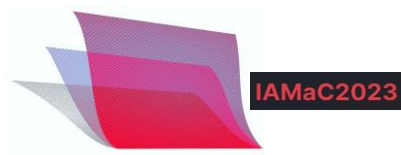
- It is possible to greatly reduce the flexibility of plates using a relatively low number of reinforcements with optimized paths.
- The capacity to reduce the strain energy is inversely proportional to the number of reinforcements inserted in the plate, that is, the greater the number of reinforcements applied, the lower the capacity to reduce the strain energy.
- In the studied structure, the application of more than four reinforcements is not indicated, a number equal to or greater than five reinforcements do not cause a significant effect on the plate.
- High amounts of stiffeners, in addition to not producing a significant reduction in flexibility, also cause many crossings between the fibers, which can make it difficult to manufacture structures.

#### ACKNOWLEDGEMENTS

This study was financed in part by the Coordenação de Aperfeiçoamento de Pessoal de Nível Superior – Brasil (CAPES) – Finance Code 001. This study was carried out with the support of the Conselho Nacional de Desenvolvimento Científico e Tecnológico (CNPq), under the grant number 140478/2020-5, and Fundação de Amparo à Pesquisa do Estado do Rio Grande do Sul (FAPERGS), under the grant number 19/2551-0001255-1.

#### REFERENCES

- [1] M. M. Alinia. A study into optimization of stiffeners in plates subjected to shear loading. *Thin-Walled Structures*, v.43, December. (2005).
- [2] R.S. Shirazi, M.M. Alinia. On the design of stiffeners in steel plate shear walls. *Journal of Constructional Steel Research*, v.65, June. (2009).
- [3] S. Kesarwani. Polymer Composites in Aviation Sector. *International Journal of Engineering Research*, v.6. (2017).
- [4] D.J. Mead. Plates with regular stiffening in acoustic media: Vibration and radiation. *The Journal of the Acoustical Society of America*, v.88. (1990).
- [5] T. I. Think, T. H. Quoc. Finite element modeling and experimental study on bending and vibration of laminated stiffened glass fiber/polyester composite plates. *Computational Materials Science*, v.49. (2010).
- [6] J. Konieczny, K. Labisz. Materials Used in The Combat Aviation Construction. *Transport Problems*, v.16. (2021).
- [7] S.B. Aragh. et al. Manufacturable Insight into Modelling and Design Considerations in Fibre-Steered Composite Laminates: State of the Art and Perspective. *Computer Methods in Applied Mechanics and Engineering*, v. 379. (2021).
- [8] Z. Wu, G. Raju, P.M. Weaver. Optimization of Postbuckling Behaviour of Variable Thickness Composite Panels with Variable Angle Tows: Towards “Buckle-Free” Design Concept. *International Journal of Solids and Structures*, v.132, September. (2018).
- [9] S. Nikbakt, S. Kamarian, M. Shakeri. A Review on Optimization of Composite Structures Part I: Laminated Composites. *Composite Structures*, v.195, March. (2018).
- [10] A. Alhajahmad, C. Mittelstedt. Design Tailoring of Curvilinearly Grid-Stiffened Variable-Stiffness Composite Cylindrically Curved Panels for Maximum Buckling Capacity. *Thin-Walled Structures*, v.157. (2020).
- [11] L. Esposito, et al. Topology Optimization-Guided Stiffening of Composites Realized through Automated Fiber Placement. *Composites Part B*, v.164, September. (2019).
- [12] M.A. Albazzan, et al. Efficient Design Optimization of Nonconventional Laminated Composites using Lamination Parameters: A State of the Art. *Composite Structures*, v.209. (2019).



## RESPONSIBILITY NOTICE

The author(s) is (are) the only responsible for the printed material included in this manuscript.



## STUDY OF FILAMENT WOUND CYLINDERS WITH VAT IN ELASTIC CONDITIONS

**Maísa Milanez Ávila Dias Maciel<sup>a</sup>, Bruno Cristhoff<sup>a</sup>, Sandro Amico<sup>b</sup>, Eduardo Gehardt<sup>b</sup>, Nuno Viriato Ramos<sup>c</sup>, Paulo Tavares<sup>c</sup>, Rui Miranda Guedes<sup>c</sup>, Volnei Tita<sup>a</sup>**

<sup>a</sup>University of São Paulo  
Sao Carlos School of Engineering, Brasil, 13563-120  
maisa.madm@usp.br, brunogch@gmail.com, voltita@usp.br

<sup>b</sup>Federal University of Rio Grande do Sul  
Porto Alegre, Brasil, 90040-060  
eduardo.gerhardt.eng@gmail.com, 00146425@ufrgs.br

<sup>c</sup>Porto University, Faculty of Engineering  
Porto, Portugal  
nviriato@inegi.up.pt, ptavares@inegi.up.pt, rmguedes@fe.up.pt

**Keywords:** variable angle tow, variable stiffness, VIC 3D, elastic testing, radial compression

### 1. INTRODUCTION

Carbon fiber reinforced polymers (CFRP) have been widely used not only in secondary structures, but also as primary structures in aircraft [1,2]. On the other hand, the maximum potential of composites is still not utilized, since the only factor considered for composite designs is the high specific strength and stiffness. However, the opportunity to design the structural components considering factors such as anisotropy and the dependence of the fiber architecture on fracture resistance is lost [3].

Traditionally, CFRP are manufactured with an almost isotropic behavior [4]. However, this type of conventional architecture does not fully exploit its anisotropy. Thus, placing the fibers in a continuous and smooth curved path [5–8] can optimize the use of CFRP. These fiber laminates with a curved trajectory are denominated as variable angle tow (VAT), which shows fibers that vary their orientation according to their coordinates in the plane of the lamina [6,9,10].

VAT have shown promising uses in the aeronautical and aerospace industry, due to the increase in resistance to buckling and behavior against vibrations due to their ability to redistribute loads from critical regions to the interior of the laminate [9,11–15]. However, due to the heterogeneous and anisotropic characteristics, different types of occur, leading to very complex mechanical behavior [9]. As the only way to use these materials in primary structures in a safe way is by knowing the initiation and propagation of damage, it becomes essential to study the mechanisms of initiation, propagation, and prediction of damage. VAT present two types of imperfections arising from processing methods, which are resin pockets (gaps) and overlapping reinforcements (overlaps). These imperfections can be hotspots for damage nucleation from mechanical deformations. Within the context of the aeronautical and aerospace industry, this proposal therefore aims to contribute to the development of advanced composite structures without interfering with aircraft safety. The use of VAT laminates can reduce the weight of structures, allowing energy savings for aircraft.

### 2. METODOLOGY

In this work cylindrical shells of variable stiffness were manufactured by FW using the KUKA KR 140 L100 robot integrated with the MF-Tech control system. The towpreg used is by TCR

composites, in which the filaments are by Toray T700-12K-50C with UF3369 resin system. Unidirectional resistance values were previously obtained and are found in references [21,22]. The cylinders are 130 mm in diameter and the angle variation is  $52^\circ/62^\circ(\alpha_0)/52^\circ$  ( $\alpha_1$ , with two of the three cylinders having a length of 150mm and one of them having a length of 200mm. In addition, they have different winding tension, with 75% and 50%, these variations being in order to reach a more suitable processing condition.

## 2.1. Radial Compression

The static tests performed is radial compression within the elastic regime with a load ratio of 20 N/min up to a maximum load of 110 N. The test was carried out in two stages, firstly the loading ramp, which presented a pre – load of 0.5 N and ending with 110 N. After the ramp there was a landing where the load is maintained at 110 N for 30 s. The test lasted 6 min in total. The testing was accompanied by digital image correlation 3D due to the materials curvature [23]. The software, Vic3D, performed the acquisition at 45 Hz, but the images were selected later. Spatial resolution was  $06 \mu\text{m}/\text{pixel}$  with objective lenses of 60 mm focal length.

## 2.2. Simulation parameters

The material has 4 layers and approximately 2 mm, and was assumed to have an orientation of  $57^\circ$  (the average between the two maximum angle variations). 3 integration points were used for each layer. At the bottom of the cylinder the following degrees of freedom were restricted  $u_2 = u_1 = u_3 = 0$ . A displacement of 0.07mm and 0.5mm was applied to the nodes at the top of the cylinder. The value of 0.07 mm is related to 10% of the maximum displacement of the  $90^\circ$  compression test performed on unidirectional samples of the same material. After that, the displacement was increased until a limiting condition given by the Hashin criterion was found. To determine when a material would be 'degraded', the damage initiation model for FRP based on Hashin's theory [24,25] was used, which considers 4 failure modes, fiber traction, fiber compression, traction, and matrix compression, and is already implemented in the ABAQUS distribution. Thus, by using a damage variable, a value of 1.0 or higher indicates that the initiation criterion has been met, so that the propensity of the material to suffer damage can be evaluated without modeling the damage evolution process, considering thus the first ply failure instead of the last ply failure.

## 3. RESULTS AND DISCUSSIONS

It was obtained that the maximum force for 1 mm of displacement was 179 N in the direction of  $52^\circ$ , which would be on the edge of the cylinder, and the maximum value of the Hashin coefficient was in the direction of traction of the matrix and its value was of 0.017. In the tests, the value of 110 N will be used for the maximum load, and the load application rate will be approximately 22 N/min. Figure 1 show the strain map in the 2 (y) direction and the Hashin coefficients map in matrix compression mode, which was the most severe condition found in the simulation. These are the first maps that will be compared with the values obtained by the DIC.

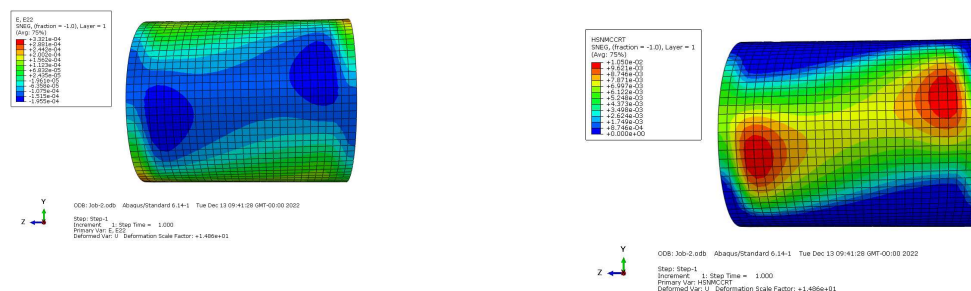


Figure 1. Strain map in direction 2, in side view (y-z plane) and the Hashin coefficients map in compression mode for matrix in side view (y-z plane)

The observed displacements obtained experimentally were close to the one obtained by the simulations for the predicted load in the test. With the 200:75 cylinder having a final displacement of 1.0mm and the 150:50 cylinder having a final displacement of 1.3mm.

Figure 2 shows the final states of deformation in the Y direction, for cylinders 150:50, 150:75 and 200:75, obtained by DIC 3D

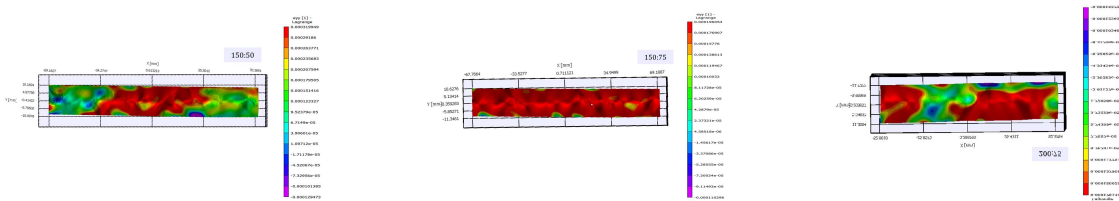


Figure 2 Deformation maps in the Y direction for cylinders 150:50, 150:75 and 200:75

Firstly, it is important to note that only for the 200:75 cylinder, the map only represents half of the cylinder because the length of 200 mm did not allow framing by the lens. At first, there was no correlation between the images, but the observation tracks were made at different points of the cylinder, which may have led to different effects being present in the deformation map, since, according to the literature, the winding pattern of the cylinder can considerably increase the stresses along the length [26]. Furthermore, the literature suggests that winding patterns change stress distributions to non-linear distributions and alter fracture processes of regions [26–28]. It is observed that for cylinder 150:75 the analysis was performed almost to the center of the pattern and for cylinders 150:50 and 200:75 the analysis was displaced from the center of the winding patterns.

#### 4. CONCLUSIONS

Cylinders manufactured with a winding of 52° at the ends and 62° at the center were analyzed in the elastic region by finite elements and with a radial compression test. Simulation analyzes showed a maximum flexion of 1 mm for a load of 110 N which was very close to that obtained for all cylinders 1.0 mm, 1.3 mm and 1.3 mm for cylinders 150:50, 150:75 and 200:75 respectively. The simulation also resulted in a deformation map in the y direction, showing mostly compressive deformations. The experimental radial compression tests, however, show that the cylinders present mainly tensile deformation in the y direction, but that the winding pattern together considerably influences the pattern of the deformation map, which may have affected the results for comparison.

#### ACKNOWLEDGEMENTS

We would like to acknowledge the founding of FAPESP/FAPERGS and CAPES/FCT number 88887.660187/2021-00. The first author would also like to acknowledge the CAPES PROEX number 88887.817112/2022-00.

#### REFERENCES

- [1] Okabe T. Recent studies on numerical modelling of damage progression in fibre-reinforced plastic composites. *Mechanical Engineering Reviews* 2015;2:14-00226-14-00226. <https://doi.org/10.1299/mer.14-00226>.

- [2] Djabali A, Toubal L, Zitoune R, Rechak S. An experimental investigation of the mechanical behavior and damage of thick laminated carbon/epoxy composite. *Compos Struct* 2018;184:178–90.
- [3] Fanteria D, Lazzeri L, Panettieri E, Mariani U, Rigamonti M. Experimental characterization of the interlaminar fracture toughness of a woven and a unidirectional carbon/epoxy composite — ScienceDirect. *Compos Sci Technol* 2017;142:20–9.
- [4] Uhlig K, Tosch M, Bittrich L, Leipprand A, Dey S, Spickenheuer A, et al. Meso-scaled finite element analysis of fiber reinforced plastics made by Tailored Fiber Placement. *Compos Struct* 2016;143:53–62.
- [5] Tornabene F, Fantuzzi N, Baccocchi M. Foam core composite sandwich plates and shells with variable stiffness: Effect of the curvilinear fiber path on the modal response. *Journal of Sandwich Structures and Materials* 2019;21:320–65
- [6] Gürdal Z, Tatting BF, Wu CK. Variable stiffness composite panels: Effects of stiffness variation on the in-plane and buckling response. *Compos Part A Appl Sci Manuf* 2008;39:911–22.
- [7] Gürdal Z, Olmedo R. In-plane response of laminates with spatially varying fiber orientations: Variable stiffness concept. AIAA/ ASME/ASCE/AHS/ASC 33rd Structures, Structural Dynamics, and Materials Conference, vol. 31, Dallas: 1993, p. 751–8.
- [8] Blom AW, Abdalla MM, Gürdal Z. Optimization of course locations in fiber-placed panels for general fiber angle distributions. *Compos Sci Technol* 2010;70:564–70.
- [9] Soriano A, Díaz J. Failure analysis of variable stiffness composite plates using continuum damage mechanics models. *Compos Struct* 2018;184:1071–80.
- [10] Montemurro M, Catapano A. A general B-Spline surfaces theoretical framework for optimisation of variable angle-tow laminates. *Compos Struct* 2019;209:561–78.
- [11] Sousa CS, Camanho PP, Suleman A. Analysis of multistable variable stiffness composite plates. *Compos Struct* 2013;98:34–46.
- [12] Almeida JHS, Bittrich L, Jansen E, Tita V, Spickenheuer A. Buckling optimization of composite cylinders for axial compression: A design methodology considering a variable-axial fiber layout. *Compos Struct* 2019;222:110928.
- [13] Uhlig K, Bittrich L, Spickenheuer A, Almeida JHS. Waviness and fiber volume content analysis in continuous carbon fiber reinforced plastics made by tailored fiber placement. *Compos Struct* 2019;222:110910.
- [14] Yazdani S, Ribeiro P, Rodrigues JD. A p-version layerwise model for large deflection of composite plates with curvilinear fibres. *Compos Struct* 2014;108:181–90.
- [15] Yazdani S, Ribeiro P. A layerwise p-version finite element formulation for free vibration analysis of thick composite laminates with curvilinear fibres. *Compos Struct* 2015;120:531–42.
- [16] Almeida Júnior JHS, Staudigel C, Caetano GLP, Amico SC. Engineering properties of carbon/epoxy filament wound unidirectional composites. 16th European Conference on Composite Materials, ECCM 2014, Seville: 2014, p. 22–6.
- [17] Almeida Júnior JH, Maciel MMÁ dias, Tita V. Effect of Imperfect Fiber/Matrix Interphase: a Micromechanical Model for Predicting Failure in Composite Materials. ABCM International Congress of Mechanical Engineering, Uberlândia: 2019. <https://doi.org/10.26678/abcm.cobem2019.cob2019-0623>.
- [18] Gu Y, Zhang D, Zhang Z, Sun J, Yue S, Li G, et al. Torsion damage mechanisms analysis of two-dimensional braided composite tubes with digital image correction and X-ray micro-computed tomography. *Compos Struct* 2021;256:113020..
- [19] Hashin Z. Failure Criteria for Unidirectional FibreComposites. *J Appl Mech* 1980;47:329–34.
- [20] Hashin Z, Rotem A. A Fatigue Failure Criterion for Fiber Reinforced Materials. *J Compos Mater* 1973;7:448–64.
- [21] Morozov E v. The effect of filament-winding mosaic patterns on the strength of thin-walled composite shells. *Compos Struct* 2006;76:123–9.
- [22] Mian HH, Rahman H. Influence of mosaic patterns on the structural integrity of filament wound composite pressure vessels. *International Journal of Structural Integrity* 2011;2:345–56.
- [23] Stabla P, Lubecki M, Smolnicki M. The effect of mosaic pattern and winding angle on radially compressed filament-wound CFRP composite tubes. *Compos Struct* 2022;292.

## RESPONSIBILITY NOTICE

The author(s) is (are) the only responsible for the printed material included in this manuscript.

# A TECHNIQUE FOR STRUCTURAL FINITE ELEMENT MODELING OF FIBER-REINFORCED RUBBER COMPOSITE USED IN FLEXIBLE COUPLINGS

**Bruno Cavalli Vieceli<sup>a</sup>, Katulo Rossi De Martini Moraes<sup>a</sup>, Daniel Pacheco e Silva<sup>a</sup>, João Moreira Lopes<sup>a</sup>, Lourenço de Siqueira Daudt<sup>a</sup>, Filipe Paixão Geiger<sup>a</sup>, Rogério José Marczak<sup>a</sup>**

<sup>a</sup>Federal University of Rio Grande do Sul – UFRGS  
Av. Paulo Gama, 110, Porto Alegre 90040-060, Brazil  
bruno.vieceli@ufrgs.br  
00288467@ufrgs.br  
00318380@ufrgs.br  
00323852@ufrgs.br  
lourenco.daudt@ufrgs.br  
filipe.geiger@ufrgs.br  
rato@mecanica.ufrgs.br

**Keywords:** fiber-reinforced elastomer, tire coupling, anisotropic hyperelasticity

## 1. INTRODUCTION

Fiber-reinforced elastomer composites see a wide range of applications in today's industry. One of the most common for these types of composites are seen in tires, as they contain several reinforcements made of steel wires and fiber plies, along with the rubber. Other applications may be seen on aerospace sectors [1] but also on the analysis of biological soft tissues [2-3], as they tend to be well represented by a soft matrix which is strengthened by internal fibers. The focus, however, will be on the analysis of a tire or tyre coupling, which consists of a fiber-reinforced rubber part which is vulcanized together with a steel flange. The flange is typically joined with a steel hub via a bolted connection, as per Fig. 1. The main function of such component is to transmit power and torque between two shafts that have some radial and/or angular misalignments between them.

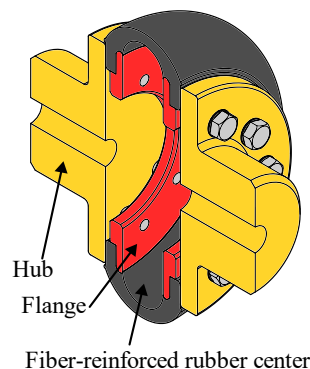


Figure 1 – View cut of isometric drawing of tire coupling.

In order to develop a structural analysis for this component, one must consider the hyperelastic behavior of the rubber matrix, as well as the linear elastic, anisotropic behavior of the fiber reinforcement. Some works have been done on the subject, mainly to develop a hyperelastic model

which accounts for internal fiber direction. [4] managed to utilize overlay “rebar” finite elements in the context of large strains to represent the reinforcements in a composite material. [5] managed to implement a transversely isotropic hyperelastic constitutive model in small to moderate strains in a finite element simulation, requiring traction, shear and two compression tests for calibration. [6-7] also developed anisotropic hyperelastic models, but with applications for textile fabrics in forming simulation and shape memory composites, respectively. [8] proposed another model, but with applications to coord-rubber composites (mainly tires) with good agreement to experimental data. [9] performed a numerical simulation in a fiber-reinforced rubber V-belt through an adaptation of the Mooney-Rivlin model, to include the transverse effects.

All the works presented have been used for simple geometry cases or are not yet available in a commercially viable solution, requiring complex and time-consuming implementations. In this regard, this work aims to perform a structural finite element analysis in a tire coupling through simple assumptions, considering different techniques for modelling its behavior, which impacts the CAD drawings, hyperelastic model choice and methodology for calibration of hyperelastic model. The results are subsequently compared to experimental tests, in order to assess the validity of the numerical analysis.

## 2. METHODOLOGY

### 2.1. Finite elasticity and hyperelastic formulation

When dealing with structures characterized by large displacements, rotations, and deformations, as it is common for hyperelastic problems, formulations for finite elasticity must be considered. In the more general sense, consider an undeformed body  $\Omega_0$ , as per Fig. 2(a), which lies in a stress-free configuration and in the absence of body forces. The body is mapped by a material point vector  $\mathbf{X} \in \Omega_0$ . Under the action of a traction field  $\mathbf{t}_0$  and displacement field  $\mathbf{u}_0$ , the body encounters a deformation map  $\chi : \Omega_0 \rightarrow \Omega$  that establishes a deformed configuration  $\Omega$  with displacements  $\mathbf{u}(\mathbf{X})$ , seen in Fig. 2(b), and is now defined by the material point vector  $\mathbf{x} = \chi(\mathbf{X})$ . This leads to the definition of a deformation gradient field  $\mathbf{F} = \partial \mathbf{x} / \partial \mathbf{X}$  and the right Cauchy-Green strain tensor  $\mathbf{C} = \mathbf{F}^T \mathbf{F}$ .

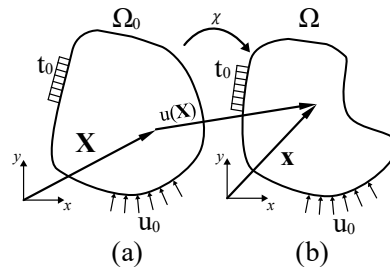


Figure 2 – Schematic drawing of a body in (a) undeformed configuration; (b) deformed configuration.

The strain energy  $\Psi$  can be defined as a function of  $\mathbf{C}$ , as in  $\Psi = \Psi(\mathbf{C})$ . In hyperelasticity, it is common to also write this function in terms of the invariants  $I_1$ ,  $I_2$  and  $I_3$ , for an isotropic material. However, since anisotropy is present, one must also add at least one pseudo-invariant,  $I_4$ , which accounts for fiber direction.

Many models aim to define the strain function  $\Psi$ . The Holzapfel-Gasser-Ogden (HGO) model [10] is a known anisotropic model which also includes the  $I_6$  pseudo-invariant. In Abaqus® implementation, however,  $I_6$  is discarded and  $\Psi$  takes the form of Eq. (1), with  $\bar{E}_\alpha$  defined in Eq. (2).

$$\Psi = C_{10}(\bar{I}_1 - 3) + \frac{1}{D} \left( \frac{J^2 - 1}{2} - \ln J \right) + \frac{k_1}{2k_2} \sum_{\alpha=1}^N \left( \exp \left\{ k_2 \left[ \frac{1}{2} (|\bar{E}_\alpha| + \bar{E}_\alpha) \right]^2 \right\} - 1 \right) \quad (1)$$

$$\bar{E}_\alpha = \kappa(\bar{I}_1 - 3) + (1 - 3\kappa)(\bar{I}_{4(\alpha\alpha)} - 1) \quad (2)$$

$C_{10}$ ,  $D$ ,  $k_1$ ,  $k_2$  and  $\kappa$  are material parameters to be calibrated,  $N$  is the number of families of fibers,  $\bar{I}_1$  is the first invariant of  $\bar{\mathbf{C}} = J^{-\frac{2}{3}}\mathbf{C}$ ,  $J = \det \mathbf{F}$  is the Jacobian and  $\bar{I}_{4(\alpha\alpha)}$  are the fourth pseudo-invariant of  $\bar{\mathbf{C}}$  and  $\bar{I}_{4(\alpha\alpha)} = \mathbf{a}_\alpha \cdot \bar{\mathbf{C}} \cdot \mathbf{a}_\alpha$ , where  $\mathbf{a}_\alpha$  are a set of unit vectors in the direction of fibers in the reference configuration.

## 2.2. Hyperelastic model calibration

The tire coupling has two sets of reinforcements embedded in the rubber in the form of woven fabrics, each set containing a fabric at the 45° and 135° angles relative to the toroidal surface of the coupling (that is, four fabrics in total).

To fit the data, MCalibration® software is used. The HGO model requires at least two curves to calibrate the entire set of material parameters. This is typically done with a sample with the fibers in the 1-direction and the other at the 2-direction. This is not possible in this case since there are multiple reinforcements in different directions. To overcome such a problem and fit the elastomer-reinforcement material to the Holzapfel-Gasser-Ogden form, a set of tensile test coupon specimens are created, one of which contains the fabric in the [0/90]<sub>2</sub> configuration, and the other at [45/135]<sub>2</sub> configuration. The stress-strain curves for the specimens are obtained with no prior hysteresis tests done to them, as it was detected that permanent deformation of the fabric was happening in these cases.

Two hypotheses are made in order to properly fit the data. It is assumed that the first specimen at the [0/90]<sub>2</sub> configuration is equivalent to a sample at the 1-direction. This may be seen as acceptable, as most of the load will be held up by the fabric at the 0° angle. The second assumption presumes that the sample in the [45/135]<sub>2</sub> configuration is equivalent to a simple shearing test. The reliability of this hypothesis may not be as sufficient as the first one, but since the stress levels are low for this test, in comparison to the first one, it is deemed adequate.

## 2.3. CAD and finite element model

Three modelling techniques were developed regarding the CAD drawings, as seen in Fig. 3. The first one assumes that the entirety of the rubber center has fiber-reinforced rubber properties. The second presumes that half the center contains fiber-reinforced rubber properties and the other half, only the elastomer properties. The third one has the assumption that two sets of reinforcements represented by surfaces S1 and S2 have the fabric material properties, while the rest of it have the pure elastomer material characteristics.

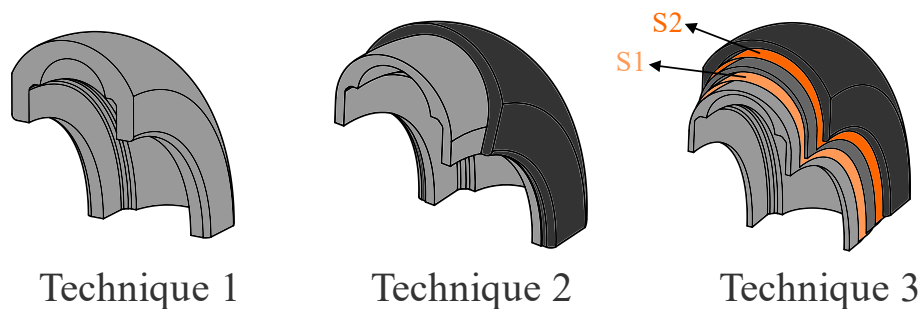


Figure 3 – Visualization for different CAD modelling techniques

Abaqus® software is employed in the finite element analysis. A prescribed displacement is implemented on both hubs, in order to force them against the rubber part, to simulate the bolt clamping force. Then, a torque of 500 Nm is applied to the model, while being clamped on one of the hubs' end surfaces. Tie restrictions are also applied between each part to restrain rigid body motion, while the bolts are modelled using Kinematic Couplings and Multi-Point Constraints (MPC). Figure 4(a) shows the clamped boundary condition and Fig. 4(b) presents the loads and the rest of the boundary conditions.

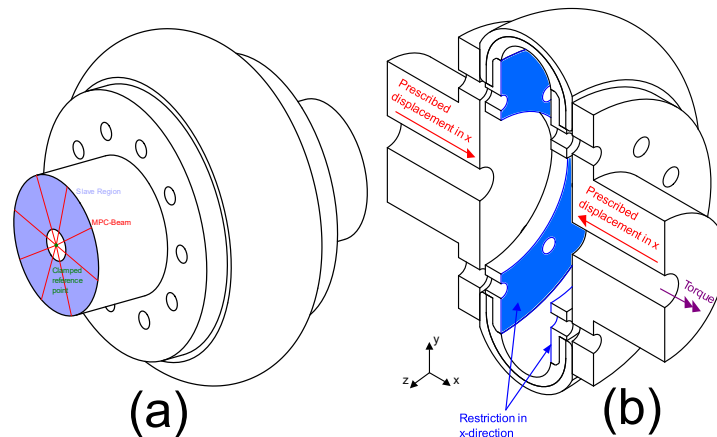


Figure 4 – (a) Clamped conditions for the model; (b) Prescribed displacements and torque.

A simple mesh study is carried out to assess the quality of the results. Figure 5 shows how the stress values taken from a critical area of the coupling vary with different mesh refinements. A medium-sized mesh is utilized, which is not as computationally intensive as the fine mesh but is also able to properly present the results.

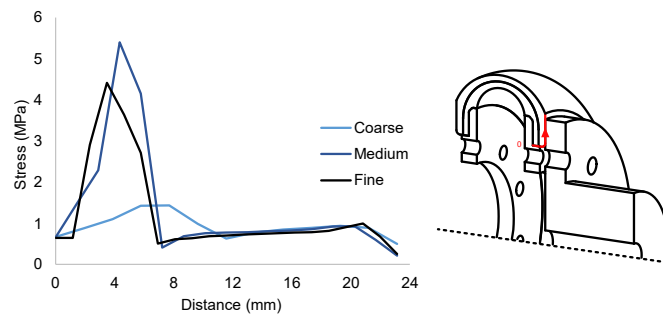


Figure 5 – Mesh study taken in a critical area.

### 3. RESULTS

Figure 6 shows the comparison between each employed technique along with the experimental results, which are made in a tire coupling subjected to a torque done by a universal testing machine through a special device. It is seen that Technique 2 can more precisely replicate the experimental behavior, although care should be taken, as the error becomes substantially greater the more torque is applied to the model. Nevertheless, there is good agreement with the experimental data up until values of approximately 300-400 Nm.

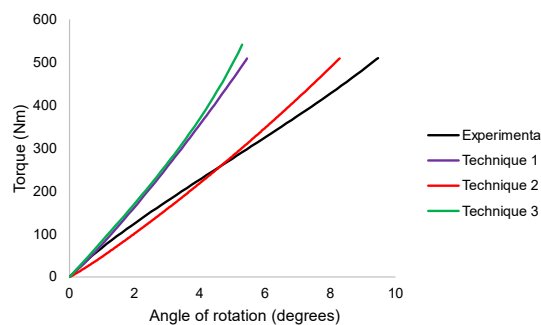


Figure 6 – Torque vs angle graph for experimental results and the three numerical techniques employed.



When looking at the values for stress, particularly from Fig. 7, one can see that the internal center area bears the highest values of stress. From a qualitative perspective, this is coherent, because the internal area is the one with the reinforced rubber properties, in which the calibration data included higher values of stress, when compared to only the pure elastomer experimental data. Also, the torque applied is expected to impose higher strains in the center of the toroidal structure.

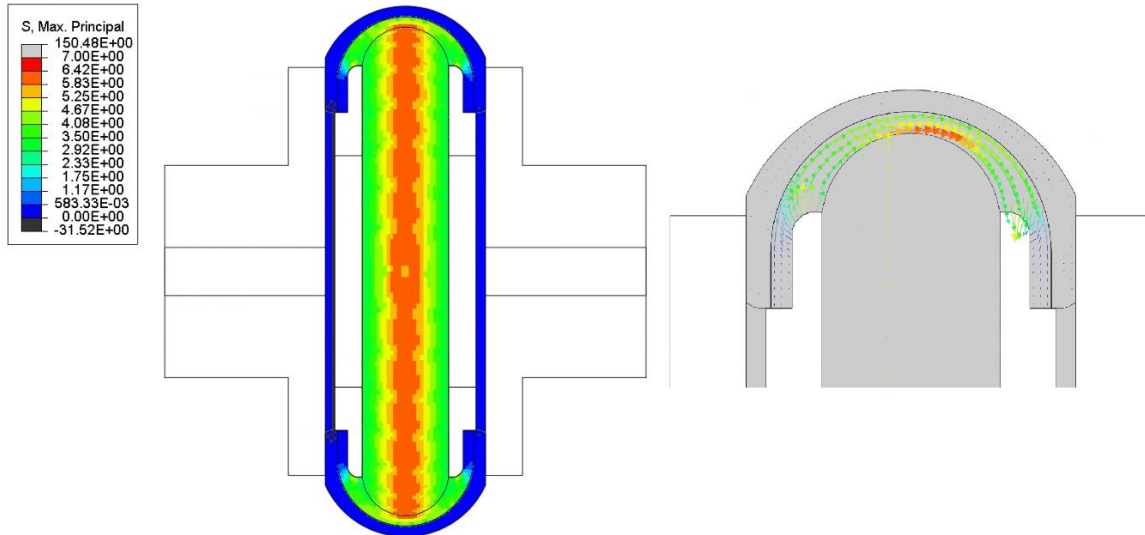


Figure 7 – Maximum principal stresses in the rubber center

In addition to it, from Fig. 8, the behavior observed in high torque values (in this case, 900 Nm or more) is also partially replicated in the numerical environment. The formation of what seems to be a local buckling from Fig. 8(c) is seen on both the stress and displacement simulation results.

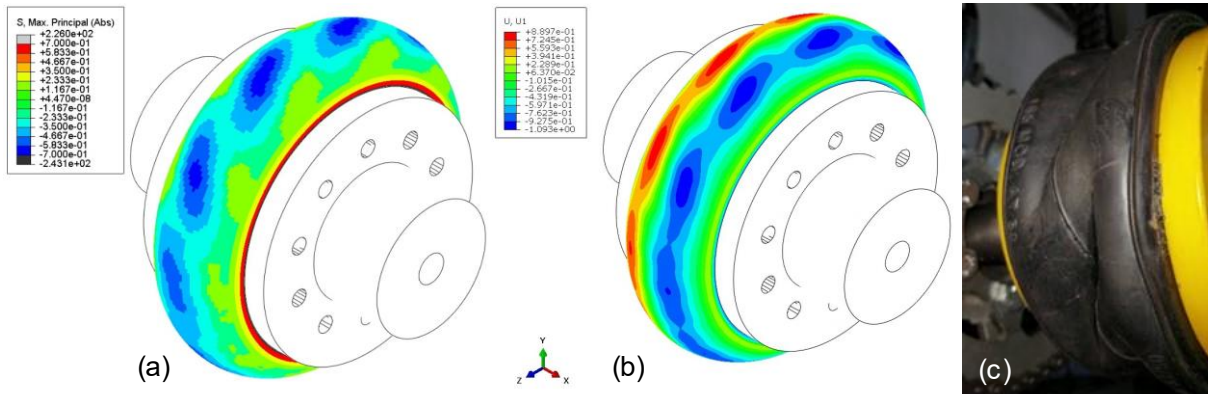


Figure 8 – (a) Maximum principal stress for high torque simulation, (b) Displacements in x-direction for high torque simulation and (c) Local buckling in flexible coupling obtained through application of high torque values.

#### 4. CONCLUSIONS

In this work, several assumptions were made to evaluate the structural behavior of a fiber-reinforced rubber utilized in a tire coupling assembly. It was detected that, even though many simplifications had to be made in order to reach the results, the second modelling technique was able to depict the experimental behavior well within the same order of magnitude.

Finally, one can replicate the methodology used here to have an initial structural assessment of a fiber-reinforced elastomer component, as to how it might behave regarding its displacements and possible critical areas which may bear high stress sections.

## ACKNOWLEDGEMENTS

This study was financed in part by the Coordenação de Aperfeiçoamento de Pessoal de Nível Superior – Brasil (CAPES). The authors would also like to thank Antares Acoplamentos LTDA for providing the materials and financial support that made this research possible.

## REFERENCES

- [1] R. D. Vocke III, C. S. Kothera, B. K. S. Woods, et. al. Development and Testing of a Span-Extending Morphing Wing. *Journal of Intelligent Material Systems and Structures*, v. 22, p. 879-890. (2011).
- [2] M. Abbasi, M. S. Barakat, K. Vahidkhah, et. al. Characterization of three-dimensional anisotropic heart valve tissue mechanical properties using inverse finite element analysis. *Journal of the Mechanical Behavior of Biomedical Materials*, v. 62, p. 33-44. (2016).
- [3] P. Ciarletta, P. Dario, F. Tendick, et. al. Hyperelastic Model of Anisotropic Fiber Reinforcements within Intestinal Walls for Applications in Medical Robotics. *The International Journal of Robotics Research*, v. 28, p. 1279-1288. (2009).
- [4] G. Meschke, P. Helnwein. Large-strain 3D-analysis of fibre-reinforced composites using rebar elements: hyperelastic formulations for cords. *Computational Mechanics*, v. 13, p. 241–254. (1994).
- [5] L. W. Brown, L. M. Smith. A Simple Transversely Isotropic Hyperelastic Constitutive Model Suitable for Finite Element Analysis of Fiber Reinforced Elastomers. *ASME. J. Eng. Mater. Technol.*, v. 133(2), 021021. (2011).
- [6] X. Peng, Z. Guo, T. Du, et al. A simple anisotropic hyperelastic constitutive model for textile fabrics with application to forming simulation. *Composites Part B: Engineering*, v. 52, p. 275-281. (2013).
- [7] Y. Wang, H. Zhou, Z. Liu, et al. A 3D anisotropic visco-hyperelastic constitutive model for unidirectional continuous fiber reinforced shape memory composites. *Polymer Testing*, v. 114, 107712. (2022).
- [8] X. Peng, G. Guo, N. Zhao. An anisotropic hyperelastic constitutive model with shear interaction for cord–rubber composites. *Composites Science and Technology*, v. 78, p. 69-74. (2013).
- [9] S. Ishikawa, A. Tokuda, H. Kotera. Numerical simulation for fibre reinforced rubber. *Journal of Computational Science and Technology* v. 2(4), p. 587-596. (2008).
- [10] G. A. Holzapfel, T. C. Gasser, R. W. Ogden. A new constitutive framework for arterial wall mechanics and a comparative study of material models. *Journal of elasticity and the physical science of solids*, v. 61, p. 1-48. (2000).

# A 3D COMPUTATIONAL HOMOGENIZATION APPROACH FOR PREDICTING THE EFFECTIVE ELASTIC CONSTITUTIVE TENSOR OF PERIODIC POROUS MATERIALS

Wanderson Ferreira dos Santos<sup>a</sup>, Sergio Persival Baroncini Proença<sup>a</sup>

<sup>a</sup>Department of Structural Engineering, Sao Carlos School of Engineering, University of Sao Paulo  
Av. Trabalhador Sao-Carlense, 400, ZIP 13566-590, Sao Carlos, SP, Brazil  
e-mail: [wanderson\\_santos@usp.br](mailto:wanderson_santos@usp.br), [persival@sc.usp.br](mailto:persival@sc.usp.br)

**Keywords:** computational homogenization approach, periodic porous materials, effective elastic constitutive tensor, extrapolation strategy based on posteriori error estimation, results with accuracy

## 1. INTRODUCTION

Porous materials have been used in a wide range of industrial and engineering applications due to their interesting physical and mechanical properties. In this sense, porous solids are suitable materials in structures designed for lightweight materials, impact energy absorption, vibration and acoustic energy damping, for instance. Cellular and lattice materials are examples of porous structures with particular characteristics, including low density and large surface area. However, the effective constitutive behavior of porous solids can be complex due to the heterogeneity created by the voids. Therefore, the design of porous media requires detailed studies to obtain the desired properties.

The study of the effective elastic properties of periodic structures can be important for the design of porous media. In particular, approaches based on computational homogenization are interesting to predict the effective elastic properties of porous materials [1]. In this context, the present work presents a computational homogenization framework for investigating the effective elastic constitutive tensor of periodic porous materials. In order to improve the accuracy of the computational approach, a strategy based on posteriori error estimation proposed by Szabó and Babuška [2] is explored to extrapolate the results from numerical simulations to estimate the components of the effective elastic constitutive tensor. The homogenization procedure is implemented in ANSYS® Mechanical-Release 18.0 using the Ansys Parametric Design Language (APDL). The consistency and applicability of the computational strategy is evaluated through the investigation of periodic porous materials. The numerical analyses are performed for RVEs composed of: (i) cubic cells with unidirectional voids of circular cross-section; (ii) cubic cells with unidirectional voids of square cross-section. The assessment of the void morphology can be of particular interest in the design of porous materials to obtain improved constitutive properties.

## 2. COMPUTATIONAL HOMOGENIZATION APPROACH

This section describes the 3D computational homogenization approach for predicting the effective elastic constitutive tensor of periodic porous media. The framework is implemented using the APDL language in ANSYS® Mechanical-Release 18.0. Constraint equations are explored to impose the periodic boundary condition given by

$$\mathbf{u} = \mathbf{E}^* \cdot \mathbf{x} + \tilde{\mathbf{u}} \quad \forall \quad \mathbf{x} \in \partial V \quad (1)$$

where  $\mathbf{u}$  is the displacement vector,  $\mathbf{E}^*$  is the macroscopic strain tensor imposed on the RVE contour ( $\partial V$ ),  $\tilde{\mathbf{u}}$  is the portion called periodic fluctuation, and  $\mathbf{x}$  indicates the positions.

The solution of the Boundary Value Problem is obtained by solving the linear system of equations of the RVE through 3D numerical analyses performed with the Finite Element Method. The homogenized or macroscopic fields of stress ( $\underline{\Sigma}$ ) and strain ( $\underline{E}$ ) are calculated by:

$$\underline{\Sigma} = \frac{1}{V} \sum_{i=1}^{nelem} \underline{\sigma}_i V_i \quad (2)$$

$$\underline{E} = \underline{E}^* \quad (3)$$

where  $nelem$  is the number of finite elements;  $\underline{\sigma}_i$  is the average stress on the element  $i$  calculated from the values at its integration points;  $V_i$  is the volume of the element  $i$ ;  $V$  is the total initial volume of the RVE (considering the hypothesis of small displacements). The macroscopic stress and strain tensors are linearly correlated by the effective constitutive tensor ( $\underline{C}$ ):

$$\underline{\Sigma} = \underline{C} : \underline{E} \quad (4)$$

The macroscopic constitutive behavior is assumed to be linear elastic obeying an orthotropic law. Different loading programs must be conveniently imposed on the RVE considering the homogeneous macroscopic strain tensor ( $\underline{E}^*$ ) to determinate the components  $C_{ijkl}$ . Due to the symmetry of the problem:  $C_{2222} = C_{1111}$ ;  $C_{2233} = C_{1133}$ ;  $C_{2323} = C_{1313}$ . Therefore, the number of independent elastic components can be reduced to 6. In this context, each RVE is subject to 6 loading conditions: (1)  $E_{11}^* = 1.0$ ; (2)  $E_{22}^* = 1.0$ ; (3)  $E_{33}^* = 1.0$ ; (4)  $2E_{12}^* = 1.0$ ; (5)  $2E_{23}^* = 1.0$ ; and (6)  $2E_{13}^* = 1.0$ .

The strategy proposed by Szabó and Babuška [2] is explored to estimate the effective elastic properties from the numerical results in order to improve the predictive ability of the computational approach. This strategy was initially proposed for a posteriori estimation of error in energy norm. However, the initial idea can be extended for predicting the effective properties. In this context, an effective elastic component ( $C_{ijkl}$ ) can be obtained from three numerical simulations ( $p$ ,  $p-1$  and  $p-2$ ) solving the following non-linear equation:

$$\frac{C_{ijkl} - C_{ijkl}^{(p)}}{C_{ijkl} - C_{ijkl}^{(p-1)}} \approx \left( \frac{C_{ijkl} - C_{ijkl}^{(p-1)}}{C_{ijkl} - C_{ijkl}^{(p-2)}} \right)^Q \quad (5)$$

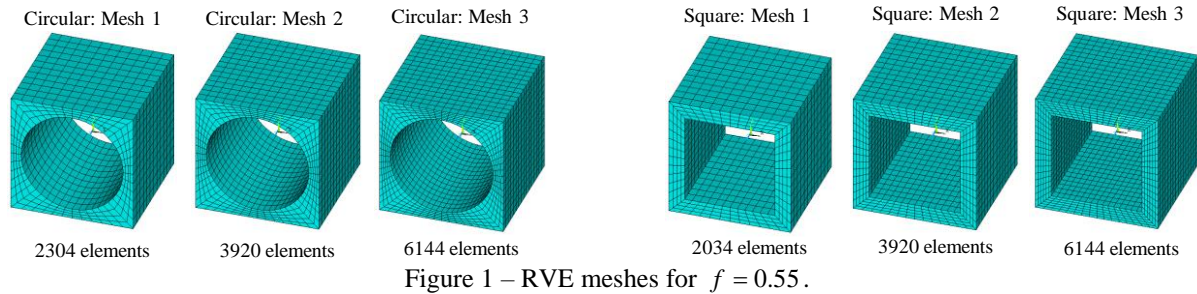
where

$$Q = \frac{\log\left(\frac{N^{(p-1)}}{N^{(p)}}\right)}{\log\left(\frac{N^{(p-2)}}{N^{(p-1)}}\right)} \quad (6)$$

where  $N$  is the total number of degrees of freedom (D.F.) of each numerical simulation.

To illustrate the applicability of the computational framework, the influence of the void morphology on the effective elastic constitutive tensor of porous materials is assessed for cubes with unidirectional voids considering circular cross-section and square cross-section. Comparisons are performed for five porosity values: (i)  $f = 0.15$ ; (ii)  $f = 0.25$ ; (iii)  $f = 0.35$ ; (iv)  $f = 0.45$ ; (v)  $f = 0.55$ . Therefore, the analyses comprise a wide range of porosities. The microscopic constitutive behavior of the matrix is linear elastic, and the values for the modulus of elasticity ( $Y$ ) and the Poisson coefficient ( $\nu$ ) are adopted according to Christoff et al. [1]:  $Y_m = 70$  GPa and  $\nu_m = 0.3$ . Three numerical

simulations must be performed for each RVE to estimate a component of the effective elastic constitutive tensor by Eq. (1). For instance, Fig. 1 shows the simulated meshes in this paper for  $f = 0.55$ . The 20-node hexahedral finite element (H20) was used in numerical simulations.



### 3. RESULTS AND DISCUSSION

Initially, a comparative analysis was performed to assess the accuracy of the results extrapolated by Eq. (5) when compared to the analytical solution proposed by Rodríguez-Ramos et al. [3] and the numerical results in ABAQUS® software obtained by Christoff et al. [1]. Table 1 presents the comparisons performed for the RVE with a circular cross-section void and  $f = 0.55$ . The effective results obtained by the computational homogenization approach are close to the compared works. The proximity of the homogenized results with the analytical solution proposed by Rodríguez-Ramos et al. [3] indicates the consistency of the computational strategy herein proposed.

Table 1 – Results of the effective elastic stiffness tensor components compared with Rodríguez-Ramos et al. [3] and Christoff et al. [1] for the RVE with a circular cross-section void and  $f = 0.55$ .

	Rodríguez-Ramos et al. [3]	Christoff et al. [1]	Authors	Relative differences in module	
Component	(1)	(2)	(3)	(2) to (1)	(3) to (1)
$C_{1111}$ (GPa)	20.4986	20.5519	20.5015	0.2602%	0.0141%
$C_{3333}$ (GPa)	35.7979	35.8392	35.7986	0.1155%	0.0020%
$C_{1122}$ (GPa)	3.3787	3.3881	3.3783	0.2782%	0.0127%
$C_{1133}$ (GPa)	7.1632	7.1820	7.1650	0.2627%	0.0251%
$C_{1212}$ (GPa)	1.8088	1.8276	1.8101	1.0431%	0.0708%
$C_{1313}$ (GPa)	7.4591	7.4795	7.4605	0.2739%	0.0182%

The extrapolated results for the components of the effective stiffness tensor considering different RVE morphologies are shown in Fig. 2. The results are presented for porosities between  $f = 0.15$  and  $f = 0.55$ , in which 180 numerical simulations were computed for predicting the effective properties. For lower porosity values, in general, the RVE with a unidirectional void of circular cross-section provides more stiffness when compared to the RVE with a unidirectional void of square cross-section. The biggest relative differences occur for the component  $C_{1212}$ , which is directly associated with the shear modulus in plane of the void cross-section. It is also worth mentioning the differences in the case of component  $C_{1122}$ . In relation to component  $C_{1212}$ , the differences are more evident with the increase in porosity. Furthermore, the differences are also sensitive for the component  $C_{1133}$  considering lower porosity values. On the other hand, except for  $C_{1122}$  and  $C_{1212}$ , the component results are closer for high porosity values. Therefore, the void morphology and the porosity level can strongly influence the effective constitutive tensor of the porous material with periodic behavior.

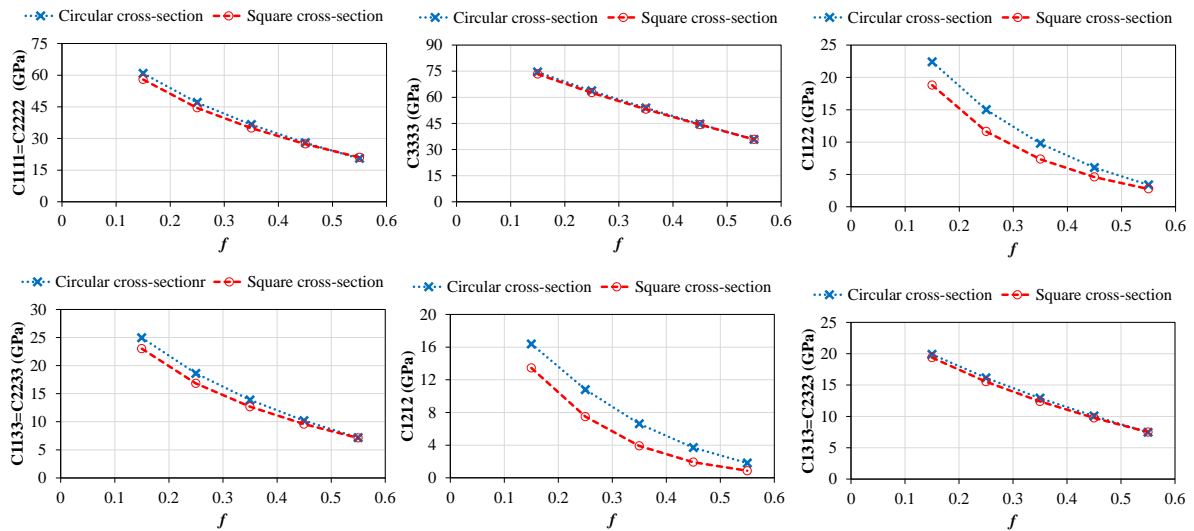


Figure 2 – Effective elastic stiffness components for the RVEs with different void morphologies and porosities.

#### 4. CONCLUSIONS

In this paper, a computational homogenization approach was proposed for predicting with good accuracy the effective elastic constitutive tensor of periodic porous materials. In particular, an extrapolation strategy was explored to better estimate the final homogenized results from the numerical results computed by a computational homogenization procedure implemented using the APDL language in ANSYS® Mechanical, Release 18.0. The applicability of the computational strategy was investigated by a study considering the influence of the void morphology on the effective elastic constitutive tensor of porous materials with periodic structure. The study was performed for unidirectional voids of circular and square cross-sections with different porosity values.

The accuracy of the approach based on computational homogenization was assessed by means of comparisons with other works in the literature, including analytical and numerical studies. In this context, the final results showed good agreement with the compared works for unidirectional voids of circular cross-section, evidencing the consistency of the computational strategy. In particular, the effective results were very close to the results of the compared analytical approach, where the differences were minimal. The comparison between the different void morphologies showed interesting conclusions. In general, significant differences were observed for the components of the effective elastic constitutive tensor associated with the shear in the plane that cuts the void cross-section. Finally, it is worth mentioning that the computational homogenization framework herein described is an interesting strategy for the design of periodic porous materials with improved and/or specific effective properties, including applications in cellular and lattice structures.

#### REFERENCES

- [1] B.G. Christoff, H. Brito-Santana, R. Talreja, et al. Development of an ABAQUS plug-in to evaluate the fourth-order elasticity tensor of a periodic material via homogenization by the asymptotic expansion method. *Finite Elements in Analysis and Design*, v.181, p. 1-13. (2020).
- [2] B. Szabó, I. Babuška. *Finite element analysis*. Wiley-Interscience. New York. 1<sup>st</sup> ed. (1991).
- [3] R. Rodríguez-Ramos, R. Medeiros, R. Guinovart-Díaz, et al. Different approaches for calculating the effective elastic properties in composite materials under imperfect contact adherence. *Composite Structures*, v.99, p. 264-275. (2013).

#### RESPONSIBILITY NOTICE

The authors are the only responsible for the printed material included in this manuscript.

## ON THE USE OF A NOVEL ALL-SOLID-STATE BATTERY AS A COMPOSITE STRUCTURE DAMAGE SENSOR

Denys Eduardo Teixeira Marques<sup>a</sup>, Bruno Guilherme Christoff<sup>b</sup>, Maísa Milanez Maciel<sup>a</sup>, Pouria Ataabadi<sup>c</sup>, João Paulo Carmo<sup>d</sup>, Maria Helena Braga<sup>c</sup>, Rui Guedes<sup>b</sup>,  
Marcílio Alves<sup>c</sup>, Volnei Tita<sup>a,b</sup>

<sup>a</sup>University of São Paulo, São Carlos School of Engineering  
Aeronautical Engineering Department, Av. João Dagnone 1100, São Carlos, SP, Brazil  
[denysmarques@gmail.com](mailto:denysmarques@gmail.com), [voltita@sc.usp.br](mailto:voltita@sc.usp.br), [maisa.madm@usp.br](mailto:maisa.madm@usp.br)

<sup>b</sup>University of Porto, Faculty of Engineering of the University of Porto  
Mechanical Engineering Department, Rua Dr. Roberto Frias s/n, Porto, Portugal  
[bchristoff@fe.up.pt](mailto:bchristoff@fe.up.pt), [rmguedes@fe.up.pt](mailto:rmguedes@fe.up.pt)

<sup>c</sup>University of São Paulo, Engineering School of the University of São Paulo  
Mechanical Engineering Department, Av. Prof. Mello Moraes 2231, São Paulo, SP, Brazil  
[pouriabrahmi@usp.br](mailto:pouriabrahmi@usp.br), [maralves@usp.br](mailto:maralves@usp.br)

<sup>d</sup>University of São Paulo, São Carlos School of Engineering  
Electrical Engineering Department, Av. Trabalhador São Carlense 400, São Carlos, SP, Brazil  
[jcarmo@sc.usp.br](mailto:jcarmo@sc.usp.br)

<sup>e</sup>University of Porto, Faculty of Engineering of the University of Porto  
Department of Engineering Physics, Rua Dr. Roberto Frias s/n, Porto, Portugal  
[mbraga@fe.up.pt](mailto:mbraga@fe.up.pt)

**Keywords:** All-Solid-State Battery, Piezoelectricity, Vibrational Test

### 1. INTRODUCTION

In the last decades, the use of battery technologies, especially lithium-ion (Li-ion), has been a very important trend for numerous electrical applications. The combination of high energy and power density makes it a substantial solution in applications such as portable electronic devices and vehicles. This type of battery has, however, a couple of limitations, such as slow charging, and a flammable electrolyte [1].

Aiming at greener energy storage, and more efficient and safer types of batteries, companies and governments have invested great amounts of money in developing newer technologies for energy storage [2]. Thus, the development, production, and use of environmentally friendly batteries are the key to achieving a sustainable, and climate-neutral technology [3].

An alternative to the well-established Li-ion battery is the use of solid-state electrolytes, which have been attracting significant attention due to their advantages, such as non-flammability, higher thermal stability, no leakage risk, and non-volatile materials. In addition, this alternative also demonstrates better mechanical properties and a higher electromechanical window of stabilities in comparison to the Li-ion counterpart, making it an interesting alternative in energy technology [4].

Considering the aforementioned aspects, the present study considers a novel all-solid-state battery to investigate the possibility of using it as a piezoelectric sensor. Figure 1(a) shows a depiction of the battery used, in which the electrodes are made of Zinc and Copper, and the electrolyte is formed by a Sodium solution. The battery is coated with a polymeric protective film, as shown in Figure 1(b).

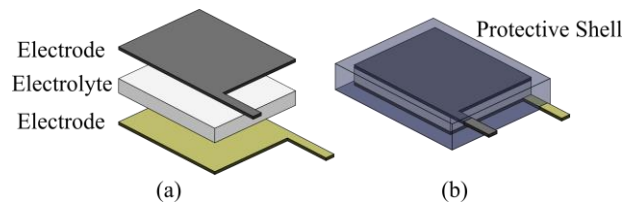


Figure 1 – Schematics of the all-solid-state battery: (a) electrodes and electrolyte; (b) battery assemble and protective polymeric shell.

In this work, the objective is to use an all-solid-state battery as a piezoelectric sensor and to discuss the potentialities and limitations of this type of battery for such applications. Thus, vibrational tests are performed using this battery coupled to a composite beam and a shaker. The battery signal variation is obtained when the battery is subjected to constant vibration. This type of test seeks to understand the potential of applying this type of battery as a sensor, which can be very promising in several engineering applications.

## 2. EXPERIMENTAL SETUP

To evaluate the piezoelectric response of the battery, a case study is examined using a composite carbon fiber beam. The geometry is that of a cantilever beam with 2.2 mm thickness, 30 mm width, and 150 mm long. The battery is attached to the beam and it is positioned close to the clamp device, as schematically shown in Figure 2.

The beam is clamped to a rigid grip, which is then mounted on an electrodynamic shaker, subjecting the specimen to a base excitation condition. The shaker is set to produce a constant frequency sine wave signal, and the response of the battery at different excitation frequencies is examined. It should be noted that the first bending mode of the beam is located at around 90 Hz, while the second bending mode is found only at 350 Hz. The base-acceleration load is applied in the  $z$ -direction (as shown in Figure 2), and in some tests, an added mass is glued to the free tip of the beam, thus increasing its vibration amplitude.

The battery is connected to a circuitry mounted directly into a breadboard, which is designed to remove its DC output voltage but allowing the passage of the voltage oscillations expected to happen during the vibration tests. The signal is then sent to a Kistler LabAmp 5167A data acquisition system.

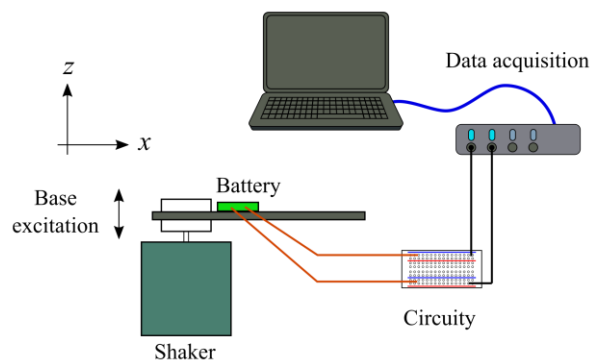


Figure 2 – Setup of the vibration test.

The battery is attached to the beam using a rapid curing, single component adhesive, and it is positioned close to the clamp device, as schematically shown in Figure 3. In addition, two accelerometers are used for comparison measures. The first accelerometer is attached to the rigid grip to measure the base acceleration. The second accelerometer is attached to the tip of the beam, and its signal is compared to the battery signal.



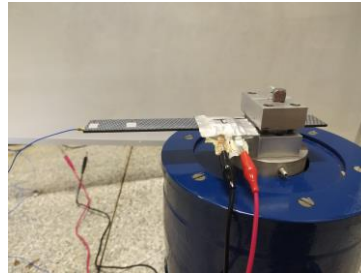


Figure 3 – Depiction of the battery attached to the composite beam mounted to the shaker.

### 3. RESULTS AND DISCUSSION

In a preliminary study, the battery behavior under a constant base excitation of the system is investigated. An excitation frequency of 25.0Hz is chosen for the vibrational tests since this frequency is sufficiently distant from the natural frequencies of the system. The vibrational test is initiated with the shaker off, and then it is suddenly turned on, and after a few seconds, it is turned off again. The time signal of the battery and the highlights of the regions in which the shaker is off and on are shown in Figure 4.

In the region where the shaker is turned on, it is noticed that the battery is capable of generating a variation in the electrical potential difference at the same excitation frequency as the system, that is, 25.0Hz. Another characteristic noted in the test is that in regions where the shaker is turned off, the battery signal oscillates at a frequency of 60.0Hz, due to electromagnetic interference from the electrical network.

It is important to note that the amplitude of the battery signal when the shaker is on is about 10 times greater than the amplitude of the signal when the shaker is off. In this way, the battery can generate a representative electrical signal for the analyzed case, even with the noise coming from the electrical network.

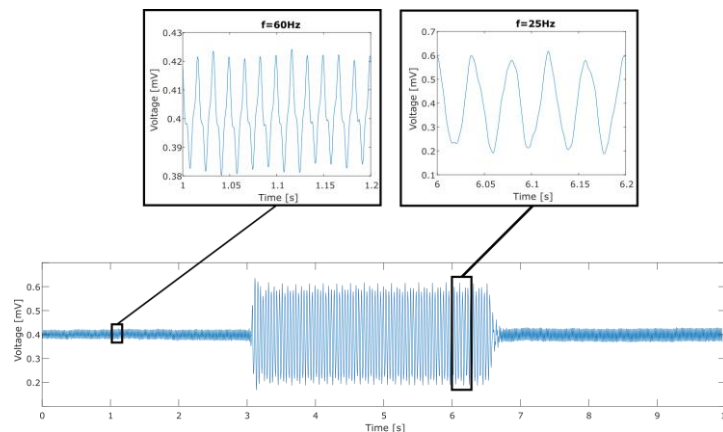


Figure 4 – Battery signal in the time domain under a constant base excitation of 25.0Hz - shaker is suddenly turned on and then turned off after a few seconds, and highlights of the regions where the shaker is off and on.

In a following analysis, the battery signal in the frequency domain is investigated. Thus, the Fast Fourier Transform (FFT) is used to convert the signal in the time domain to the frequency domain. Figure 5 shows the battery signal in the frequency domain, as well as the signal of the accelerometer on the tip of the beam. It can be seen that both the battery and the accelerometer can detect signal peaks at the working frequency of the system (25.0Hz), as well as its harmonics (multiples of 25.0Hz). In addition, it can be seen that the battery presents signal peaks in frequencies multiple of 60.0Hz, due to electromagnetic interference due to the electrical network.

As initial conclusions, it can be said that there are possibilities of using the battery as a piezoelectric sensor since it generates a potential difference when excited at a constant frequency. Also,

the amplitude of the signal generated by the battery when excited is much higher than the amplitude of the signal due to electromagnetic noise.

For future work, the battery will be excited at different frequencies to investigate the limit of battery usage. The higher the excitation frequency of the system, the smaller the signal amplitude generated by the battery. Thus, we have to investigate at what working frequency level the signal amplitude generated by the battery is equal to or less than the electrical network noise, which implies the impossibility of using the battery at these frequencies.

Hereafter, we will use a sweep-type excitation signal, to find the natural frequencies of the system through the signal generated by the battery. Finally, aiming at applications in Structural Health Monitoring (SHM), the battery will be used to compare systems using an intact beam and a damaged beam. With this investigation, it will be possible to determine if the signal generated by the battery is capable of detecting variations in the natural frequencies of the system, due to damage to the composite beam.

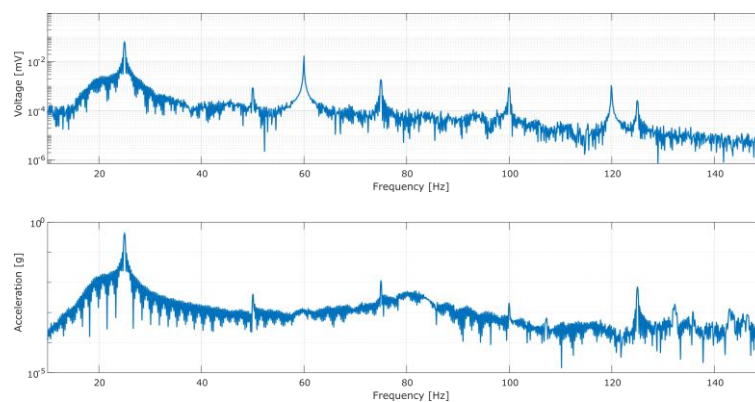


Figure 5 – Battery and accelerometer signals in the frequency domain.

## ACKNOWLEDGEMENTS

Volnei Tita acknowledges the financial support of the National Council for Scientific and Technological Development (CNPq process number: 310656/2018-4). The authors are thankful for the support of the Coordenação de Aperfeiçoamento de Pessoal de Nível Superior – Brasil / Finance Code 001, and for the support of Dean’s Office of Researcher of the University of São Paulo via “PIPAAE - PROJETOS INTEGRADOS PARA PESQUISAS EM ÁREAS ESTRATÉGICAS”.

## REFERENCES

- [1] F. Danzi, P.P. Camanho, and M.H. Braga. An all-solid-state coaxial structural battery using sodium-based electrolyte. *Molecules*, v.26(17), p.5226. (2021).
- [2] F. Danzi, R.M. Salgado, J.E. Oliveira, et al. Structural batteries: A review. *Molecules*, v.26(8), p.2203. (2021).
- [3] F. Danzi, M. Valente, S. Terlicka, et al. Sodium and potassium ion rich ferroelectric solid electrolytes for traditional and electrode-less structural batteries. *APL Materials*, v.10(3), p.031111. (2022).
- [4] M.C. Baptista, H. Khalifa, A. Araújo, et al. Giant Polarization in Quasi-Adiabatic Ferroelectric Na<sup>+</sup> Electrolyte for Solid-State Energy Harvesting and Storage. *Advanced Functional Materials*, p.2212344. (2022).

## RESPONSIBILITY NOTICE

The author(s) is (are) the only responsible for the printed material included in this manuscript.

## VERTICAL TWO-PHASE FLOW WITH A NON-NEWTONIAN PHASE IN LAMINAR HETEROGENEOUS POROUS MEDIA

Lucas Constantino Mendonça<sup>a</sup>, Panters Rodríguez-Bermudez<sup>a</sup>, Alexandre Santos  
Francisco<sup>a</sup>, Isamara Landim Nunes Araujo<sup>b</sup>, Jorge A. Rodríguez Durán<sup>c</sup>

<sup>a</sup>PPG-MCCT, Universidade Federal Fluminense (UFF)  
Av. dos Trabalhadores 420 Vila Sta. Cecília, Volta Redonda -RJ 27255-125, Brasil  
lucasconstantino@id.uff.br  
pantersrb@id.uff.br  
afrancisco@id.uff.br

<sup>b</sup>IMECC/UNICAMP  
Rua Sérgio Buarque de Holanda 651, Campinas-SP 13083-859, Brasil  
Isamara-landim@hotmail.com

<sup>c</sup>Universidade Federal Fluminense (UFF)  
Av. dos Trabalhadores 420 Vila Sta. Cecília, Volta Redonda -RJ 27255-125, Brasil  
jorgedurán@id.uff.br

**Keywords:** flow in porous media, heterogeneous porous media, two-phase flow, non-Newtonian fluids, gravity

### 1. INTRODUCTION

In the oil and gas industry, natural production mechanisms allow for the recovery of an average of 20 to 40% of the total oil contained in the reservoir. In view of this, secondary and enhanced recovery methods are used aiming at a greater oil recovery or maintenance of reservoir pressure [1]. The most used methods in secondary recovery are waterflooding (immiscible water injection) and immiscible gas injection. During the application of the immiscible water injection method, if the displaced fluid is a very viscous oil, it may possess rheological attributes characteristic of that of a non-Newtonian fluid, while in enhanced oil recovery, some methods utilize surfactant, alkaline, or polymer solutions, which can impart non-Newtonian behavior to the injected fluid [4]. The great frequency in the use of such methods becomes a motivation for carrying out several studies aimed at simulating the flow of Newtonian and non-Newtonian fluids in porous media. A variety of physical phenomena such as the two-phase immiscible flow of fluids in porous media, for example, can be modeled through conservation laws and the well-known Riemann problems (piecewise constant initial data). For heterogeneous porous media, obtaining Riemann solutions analytically can be a very tough task, so numerical methods have been increasingly used to obtain approximate solutions to a given problem. In problems involving conservation laws with piecewise constant data, the methods of Godunov, Lax-Wendroff, MacCormack and Lax Friedrichs are highlighted [5].

### 2. MATHEMATICAL MODEL

The present research proposes the study of a mathematical model for vertical two-phase immiscible flow in heterogeneous porous media with a non-Newtonian phase of Bingham plastic type based on an extension of the Buckley-Leverett equation [6]. The heterogeneous rock is assumed to be a composite porous material composed by a periodic-laminar structure with two types of rocks, one of

them as a matrix while the other is a refill. In parallel, the finite difference numerical schemes of Lax-Friedrichs and Lagrangian-Eulerian developed by [2] were implemented.

## 2.1. Darcy's law and apparent viscosity for Bingham plastic

In order to carry out a phenomenological description of the flow of non-Newtonian fluids, such as Bingham plastic, through porous media, it is necessary to take into account the apparent viscosity of the rheological model in question within Darcy's Law. A modified version of Darcy's Law for non-Newtonian fluids of the Bingham plastic type is presented as follows:

$$u = \begin{cases} \left(\frac{-K}{\mu_B}\left(1 - \frac{G}{|\nabla\Phi|}\right)|\nabla\Phi|\right), & \text{if } |\nabla\Phi| > G, \\ 0, & \text{if } |\nabla\Phi| \leq G, \end{cases} \quad (1)$$

where

$$|\nabla\Phi| = |\nabla P| \pm \rho g. \quad (2)$$

The apparent viscosity can be obtained by rearranging Eq. (1) and after some algebraic manipulations, the following expression is achieved:

$$M(\nabla\Phi^*, S_{Ne}) = \frac{\mu_{Ne}}{\mu_{nN}} = \begin{cases} \frac{1}{m_\alpha}\left(1 - \frac{G^*}{|\nabla\Phi^*|}\right)|\nabla\Phi^*|, & \text{if } |\nabla\Phi^*| > G^*, \\ 0, & \text{if } |\nabla\Phi^*| \leq G^*, \end{cases} \quad (3)$$

where  $u$  is the Darcy velocity vector,  $\mu_B$  is the consistency index of the rheological model,  $G$  is the minimum pressure gradient,  $G^* = G/\gamma_{nN}$  is the dimensionless minimum pressure gradient,  $K$  is the absolute permeability of the rock,  $\nabla P$  is the pressure gradient,  $\nabla\Phi$  is the flow potential gradient,  $\nabla\Phi^*$  is the dimensionless flow potential gradient (see [6]),  $\rho$  is the fluid density,  $\mu_{Ne}$  is the dynamic viscosity of Newtonian phase,  $\mu_{nN}$  is the apparent viscosity of non-Newtonian phase,  $m_\alpha = \mu_B/\mu_{Ne}$  and  $g$  is the gravitational constant. Once the variables are defined, it is important to mention that if  $G^*$  equals zero, the problem goes back to the Newtonian case.

## 2.2. Two-phase flow with a non-Newtonian phase in heterogeneous porous media

For a laminar flow in a porous medium composed of two rocks with distinct absolute permeabilities, we should define:

$$\begin{aligned} & \frac{\partial S}{\partial t} + \frac{\partial f_l(S)}{\partial Z}, \text{ if } Z < 0; \quad \frac{\partial S}{\partial t} + \frac{\partial f_r(S)}{\partial Z}, \text{ if } Z > 0, \\ & S(Z, 0) = \begin{cases} S_l, & \text{if } Z < 0, \\ S_r, & \text{if } Z > 0, \end{cases} \text{ with } f_l(S_l) = f_r(S_r) \end{aligned} \quad (4)$$

Here  $f_l, f_r: [0, 1] \rightarrow \mathbb{R}$  are the flux functions assumed to be twice differentiable such that  $f_l(0) = f_r(0)$  and  $f_l(1) = f_r(1)$ ,  $S$  is the fluid saturation and  $Z$  is the vertical coordinate. The flux function for the Newtonian phase, considering it as the displacing phase (the phase that displaces the non-Newtonian phase) for vertical flow (with gravity), can be represented in the following manner:

$$f_{NeL} = \frac{1}{1 + \frac{(1-S_{Ne})^2}{S_{Ne}^2} M(\nabla\Phi^*, S_{Ne})} [1 + N_g(1 - S_{Ne})^2], \quad (5)$$

and

$$f_{NeR} = \frac{1}{1 + \frac{(1-S_{Ne})^2}{S_{Ne}^2} M(\nabla\Phi^*, S_{Ne})} [1 + K_f N_g(1 - S_{Ne})^2], \quad (6)$$

with  $K_f = K_r/K_l$ , where  $K_r$  is the absolute permeability of the right rock layer,  $K_l$  is the absolute permeability of the left rock layer and  $N_g(\nabla\Phi^*, S_{Ne})$  is a gravitational parameter [6].

## RESULTS AND DISCUSSION

In the present research, two cases are presented. For the first case,  $|\nabla\Phi^*|$  was considered greater than  $G^*$ , while for the second case,  $|\nabla\Phi^*|$  was considered less than or equal to  $G^*$ . For Case I, the following dimensionless parameters associated with  $\nabla\Phi^*$  were considered: node number = 5000, CFL = 0.6,  $T = 1$ ,  $S_l = 0.3$ ,  $S_r = 0.7$ , number of time steps = 1027,  $m_\alpha = 4$ ,  $\eta = 2.5$ ,  $G^* = 0.375$ ,  $\gamma^* = 1.25$ ,  $\omega^* = 5$ , and  $K_f = 0.5$ . As for Case II, the following parameters were considered: node number = 5000, CFL = 0.6,  $T = 2$ ,  $S_l = 0.8165$ ,  $S_r = 0$ , number of time steps = 246,  $m_\alpha = 0.1$ ,  $\eta = 0.025$ ,  $G^* = 0.625$ ,  $\gamma^* = 1.25$ ,  $\omega^* = 0.125$ ,  $K_f = 2$ ,  $S_{liml} = 0.8165$  and  $S_{limr} = 0.5773$ . The results are presented in Fig. 1, 2, and 3.

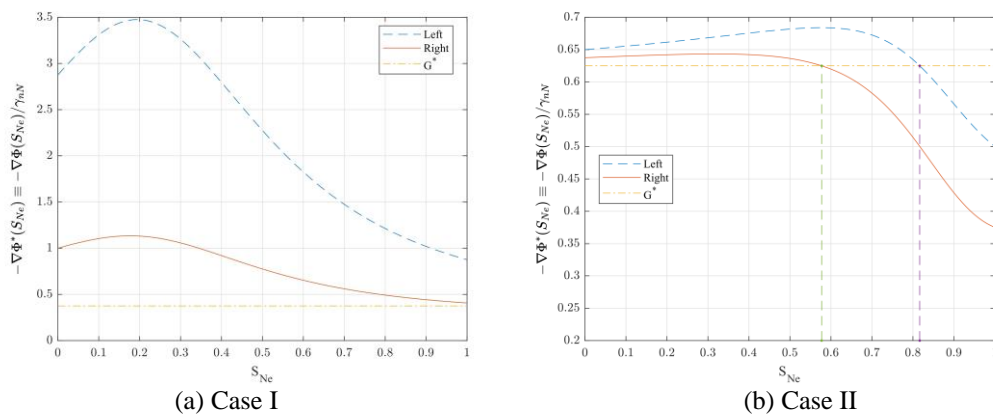


Figure 1 – Flow potential gradient.

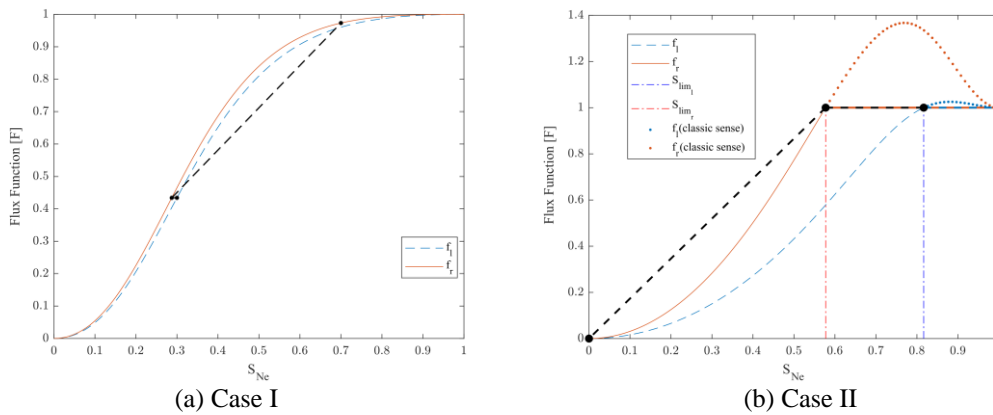


Figure 2 – Flux functions.

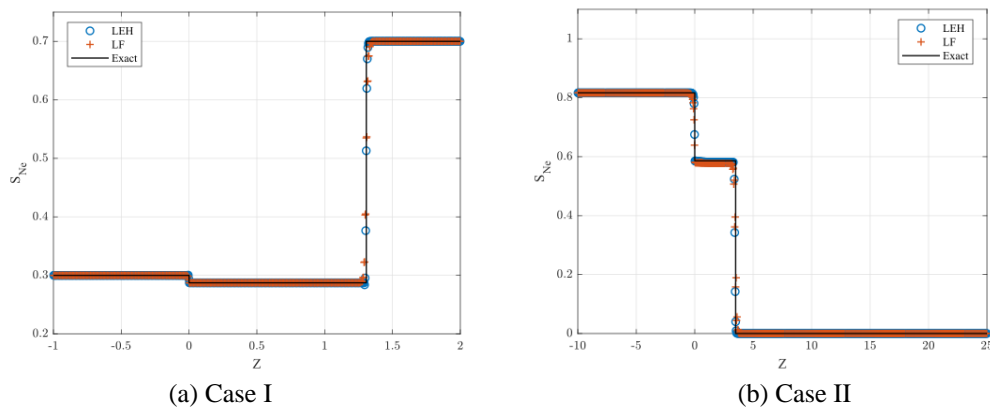


Figure 3 – Analytical and numerical solutions.

The numerical solutions obtained were compared with the analytical solutions determined through the extension of Oleinik’s geometric construction to discontinuous flux functions emerged as a consequence of the heterogeneity in the rock. The numerical results were satisfactory when compared with the exact solutions that consist of the combination of shock waves, with the presence of a stationary shock at the point of discontinuity (interface between the two types of rocks) of spatial variable.

The solutions of both cases consist of a positive-speed shock wave and a stationary shock wave. What differentiates the solutions is the existence of a limiting saturation, which determines the maximum Newtonian-phase saturation value at which the fluid continues to behave as a liquid. This phenomenon is observed in Case II, which presents a limiting saturation of 0.8165 for the rock layer on the left side. This behavior is due to the rheological model, as for saturations above the limiting saturation, the apparent viscosity becomes infinite, and the fluid does not flow.

## REFERENCES

- [1] A. Bahadori. *Fundamentals of enhanced oil and gas recovery from conventional and unconventional reservoirs*. Gulf Professional Publishing, 1<sup>st</sup> edition. (2018).
- [2] E. Abreu and J. Pérez. *A new locally conservative lagrangian eulerian method for hyperbolic and balance laws*. In: VIII Pan-American Workshop Applied and Computational Mathematics. (2014).
- [3] L. C. Mendonça. *Mathematical and computational modeling of biphasic flow in heterogeneous porous media under gravitational effect and the presence of non-Newtonian phase*. Master Thesis. Federal Fluminense University. (2023).
- [4] N. El-Khatib. Immiscible displacement of non-Newtonian fluids in communicating stratified reservoirs. *SPE Reservoir Evaluation & Engineering*, v.9, n. 04, p. 356-365, August. (2006).
- [5] R. J. LeVeque. *Numerical Methods for Conservation Laws*. Basel: Birkhäuser. (1992).
- [6] Y. S. Wu. *Multiphase fluid flow in porous and fractured reservoirs*. Gulf Professional Publishing, 1<sup>st</sup> edition. (2015).

## RESPONSIBILITY NOTICE

The author(s) is (are) the only responsible for the printed material included in this manuscript.